THE UNIVERSITY OF CHICAGO

NEUTRINO AND ASTROPARTICLE PHYSICS WITH P-TYPE POINT CONTACT HIGH PURITY GERMANIUM DETECTORS

A DISSERTATION SUBMITTED TO
THE FACULTY OF THE DIVISION OF THE PHYSICAL SCIENCES
IN CANDIDACY FOR THE DEGREE OF
DOCTOR OF PHILOSOPHY

DEPARTMENT OF PHYSICS

BY

PHILLIP S. BARBEAU

CHICAGO, ILLINOIS
DECEMBER 2009

For Sarah, you are my compass

and

for my parents

ABSTRACT

The recent development of large mass, low noise P-type point contact (PPC) high purity germanium detectors has opened up a number of new opportunities for experiments in neutrino and astroparticle physics. Several of these experiments have been performed with the earliest prototypes. They are described in this thesis. A measurement for the quenching factor for sub-keV nuclear recoils in germanium detectors is presented. Also discussed is an assessment of the low energy backgrounds at a nuclear power reactor along with the progress that has been achieved towards a measurement of coherent neutrino-nuclear scattering. Using the brief exposure of the detector to a high flux of reactor neutrinos, a limit is placed on the magnitude of a neutrino magnetic moment and a projected limit that can be achieved with a more complete experiment is discussed. A limit is also placed on the magnitude of a continuous energy deposition by reactor neutrinos in the germanium detector. Using the low background data that were obtained at the reactor, limits on light WIMPs as well as dark galactic pseudoscalars are presented, which constrain the physical explanation for a claimed observation of dark matter by the DAMA collaboration. As PPC detectors have been chosen as the preferred detector for the 60 kg Majorana demonstrator double beta decay experiment, projected limits on light WIMPs and dark pseudoscalars are also presented. Finally, bounds are placed on the lifetime of the electron for "invisible" decays that occur via $e^- \rightarrow \nu_e \bar{\nu_e} \nu_e$, and projected limits for such a search using the 60 kg Majorana demonstrator are also presented.

ACKNOWLEDGMENTS

There are many heros that deserve my appreciation for their contribution to this dissertation and to my education.

First and foremost, I thank my beautiful wife for her constant support, understanding and insight. Also for her patience and tolerance, of which she has an enormous supply. I would also like to express my appreciation to my parents and my brother for all of their support.

I have an enormous amount of gratitude for everything my advisor, Juan Collar, has done for me these last seven years. My education with him has been of unrivaled quality, depth and breadth; the best I could have hoped for. His intensity, quantity, quality and diversity of research will always be a model for me.

I am indebted to Orren Tench, Jim Colaresi and Mike Yocum for their tireless work towards the development of the PPC detectors. I would like to thank our many collaborators within the CoGeNT and Majorana collaborations. Most especially Dave Reyna, Nathaniel Bowden, Craig Aalseth, Steven Dazeley and Lorraine Sadler, for their assistance and their time. To everyone involved at Sandia National Laboratories in Livermore, and Lawrence Livermore National Laboratory, thank you.

I thank all of my other Professors, teachers and mentors at the University of Chicago. I first thank the other members of my committee, Professors Ed Blucher, Jon Rosner and Bruce Winstein for their good advice, assistance and attention during this process. I would also like to express thanks to Professors Dietrich Muller and Simon Swordy for exposing a teenage kid to the wonders of experimental physics. To Dr. Florian Gahbauer for teaching me how to survive in a physics lab. To Gary Kelderhouse, Gene Drag, Wayne "Skip" Johnson and Rich Northrop for taking the time to listen and explain. I would especially like to thank the fabricators in the machine shop at the University of Chicago, for their never ending strive for perfection, their invaluable input, their tolerance of the innumerable last minute jobs and their willingness to answer ridiculous questions; to Dave Plitt, Ernie Mendoza, Bob Metz, Gordon Ward and Larry Fiscelli, thank you. And of course, I must thank those who really know how to make things happen: Pat Plitt, Helen Pates, Valeri Galtsev, Sandy Heinz and Nobuko McNeill.

Finally I would like to acknowledge all of the undergraduate, graduate and other students at the University of Chicago that I have had the great pleasure of working with on this project. In approximate chronological order: Taylor Aune, Kevin O'Sullivan, Aza Raskin, Julia Rasmussen, Keith Crum, Chris Passolano, Hannes Schimmelpfennig, Luke Goetzke, Barnabas Kipapa, Jacob Claussen and most especially Charles Greenberg for his tireless work on the radiation shield. I am also indebted to Aaron Plasek, Nathan Riley, Jillian Mislinski and my good friend Dante Nakazawa.

TABLE OF CONTENTS

LIST OF FIGURES

LIST OF TABLES

PREFACE

The road travelled for the preparation of this dissertation has been a long and winding one. As the title suggests, the end result has very broad applications in several areas of neutrino and astroparticle physics. The work began with our attempt to build a detector that was simply capable of detecting coherent neutrino-nucleus scattering. There have been many attempts to develop such a detector. Indeed, while we have achieved great strides toward that goal, it has yet to be realized. Despite this, using the detector that we have developed, a number of physics experiments have been performed. This dissertation describes the work from a topical point of view, but the actual timeline of events differs slightly from the order in which it is presented. This preface attempts to provide some clarity by giving an alternative, historical perspective of the work.

I began my work with Professor Collar in the summer of 2002 with the goal of building a detector capable of measuring coherent neutrino-nucleus scattering. The experimental signature has long been predicted, but has never yet been measured because it requires the detection of sub-keV nuclear recoils. The initial designs involved the use of micropatterned gas detectors in order to take advantage of the high internal amplification that can be obtained and to achieve sensitivity to single electrons for ionization deposited in the detector [Barbeau et al., 2003a]. Several thousand Gas Electron Multipliers (GEMs) were soon produced for us by 3M utilizing their roll-to-roll lithographic etching technique, which is used primarily for the production of flex circuits. These GEMs from 3M were characterized in collaboration with colleagues at Purdue University [Barbeau et al., 2003b] and were found to perform excellently. I quickly achieved our first goal of single electron sensitivity in low pressure (1 atm) gas; however, very little progressed beyond this point as new avenues of research developed that promised to lead to larger mass detectors.

About this time, we began work to determine if the experiment could be performed with conventional inorganic scintillators. The intention was to search for anomalously high relative scintillation efficiencies for low energy nuclear recoils. I was involved in the design, construction and characterization of a 24 keV neutron beam to test this. The beam was installed at the Kansas State University TRIGA Mark II experimental reactor [Barbeau et al., 2007a]. I performed the analysis for a few of these characterizations, in particular some preliminary tests with a small plastic scintillator. The work with the inorganic scintillators was put aside with the eventual development of the first P-Type Point Contact (PPC) HPGe detector.

The large mass, low energy threshold and low backgrounds achievable with the PPC-1 detector made it the ideal detector technology for this experiment. We exposed the detector to the 24 keV neutron beam and measured the quenching factor for sub-keV nuclear recoils, for which I performed the analysis [Barbeau et al., 2007b]. I then built a low background radiation shield and muon veto located at a depth of 6 m.w.e. at the University of Chicago. The results of the deployment of the PPC-1 detector in this shield indicated that there were prohibitively high backgrounds from the aluminum parts in the detector. At the same time, it was determined that the electrode structure of PPC detectors made them ideal for identifying multiple site interactions within a single crystal. I performed the first such analysis with a PPC detector. The resulting optimal rejection of multiple-site gamma interactions made the detector an excellent candidate for the Majorana $0\nu\beta\beta$ decay experiment, for which it was quickly proposed. I assisted with or performed several more detector characterizations in support of the campaign that led to the decision to make PPCs the preferred detector technology for the Majorana demonstrator experiment. This included measurements of the charge trapping profile, an approximated mapping of the depleted volume versus voltage, and measurements of the detector capacitance as a function of voltage.

During the intervening period, the dirty aluminum was replaced in the PPC-1 detector. In support of the effort to measure coherent neutrino-nucleus scattering, I designed, fabricated, built, tested and performed background simulations for a new radiation shield for the next deployment. I then deployed the PPC-1 detector and all of its shielding to a laboratory in the Tunnel and Reservoir Project (TARP) outside of Chicago (∼300 m.w.e.). The intention was to establish the backgrounds from the detector away from cosmogenic sources present at 30 m.w.e at the nuclear reactor. We took advantage of the low background deployment, the large mass and the low threshold of the detector to perform two powerful searches for dark matter candidates [Aalseth et al., 2008].

With the first results obtained at the TARP facility, it was determined that the detector backgrounds and threshold were not sufficient to perform a coherent neutrino-nucleus scattering measurement at a power reactor, instigating a campaign to reduce both. Eventually, the PPC-1 detector and its shielding were installed in the "Tendon" Gallery at the San Onofre Nuclear Generating Station (SONGS), with the invaluable assistance of the members of the CoGeNT collaboration from Sandia National Laboratories in Livermore and Lawrence Livermore National Laboratory. Unfortunately, the detector had been severely activated by thermal neutrons, and no measurement was possible due to the high level of backgrounds that resulted. PPC-1 was returned to Chicago to be upgraded and also to let the ^{71}Ge decay away.

In the meantime, a different style of PPC detector was obtained and deployed to the reactor. The detector, a version of the Canberra BEGe that included a number of upgrades which were incorporated in order to reduce backgrounds, was installed on November 12, 2008. I analyzed the data that was obtained (∼50 kg–days) in parallel with Professor Juan Collar, from which we determined that a measurement of coherent neutrino-nucleus scattering was still unlikely. However, with the same data, I improved upon some of the dark matter results obtained from the deployment at the TARP facility. In addition, because these searches will also be performed with the 60 kg Majorana demonstrator experiment, I produced an approximate background spectrum for that experiment which is based on the estimated level of cosmogenic activation that the germanium crystals are likely to receive. I analyzed the simulated spectra with the same dark matter analysis routines and projected the sensitivity that the searches are likely to achieve. I also analyzed the data in an attempt to constrain the magnitude of a neutrino magnetic moment from ν_e–e^- scattering, and projected the sensitivity of such a search for a longer and more complete experiment. Also, I was able to place a limit on the continuous energy deposition of neutrinos in the BEGe-1 detector, which resulted in a significant improvement on existing bounds. Finally, using the measured background spectra at the reactor, I placed a limit on the lifetime of the electron. This limit is not competitive with other experiments; however, I have also estimated the sensitivity of the 60 kg Majorana demonstrator experiment for such a search, showing that it will likely result in a dramatic improvement on the limit.

While the primary goal of our work remains unfulfilled, a great deal of progress has been made. Detectors with capacitances on the order of 1 pF could potentially have thresholds as low as ∼50 eV, which is much lower than has currently been achieved. There is an ongoing effort to discover the source of electronic noise in the detectors. Within the Majorana collaboration, there is also significant work towards improving the preamplifiers that are used. Along the way, we have performed many significant physics experiments.

CHAPTER 1

INTRODUCTION

It is often the case in physics that the arrival of a detector technology opens up new avenues of research. This is undoubtably true for the recently developed P-type Point Contact (PPC) high purity germanium detectors (HPGe). The electronic noise and sub-keV energy threshold is unprecedented in semiconductors of this size ($\sim$1 kg). This dissertation describes the early development of P-type Point Contact detectors as well as several measurements in neutrino and astroparticle physics that were performed with the first detectors. The primary results that are presented in this dissertation are derived from a deployment of the detector and its radiation shield to the San Onofre Nuclear Generating Station (SONGS).

The deployment of this unique instrument to such a unique location enables a number of searches for new physics. The primary purpose for the deployment of this detector to the SONGS reactor was an attempt to measure coherent neutrino-nucleus scattering, the status of which is presented. In support of this, a measurement of the low energy quenching factor for nuclear recoils in germanium was performed, and is presented as well. Using the results of the deployment, a limit is placed on the electron-neutrino magnetic moment and projections are made for the sensitivity of a dedicated experiment with PPC detectors. Also, a bound is placed on the continuous energy deposition ($\frac{dE}{dx}$) by neutrinos in matter that is an improvement over a previous limit by more than two orders of magnitude. In addition to the work with reactor anti-neutrinos, experiments were performed that took advantage of the low background deployment of this new detector technology. There are two different searches for dark matter reported in this dissertation (for light WIMPs and dark pseudoscalars) as well as a search for the violation of charge conservation via electron decay. All of these measurements make use of either the low energy threshold or the excellent resolution at low energies of PPC detectors.

There is one aspect of the PPC detector technology that instead benefits experiments that are performed at much higher energies, such as the Majorana $0\nu\beta\beta$ experiment. As a direct result of the geometry of the point contact electrode, which is responsible for the low capacitance of the detectors ($\sim$1 pF), it is possible to identify multiple site interactions from Compton scattered background gammas in the detector volume. This Pulse Shape Discrimination (PSD) capability and the excellent resolution at high energies ($\sim$2 MeV) make PPCs an ideal detector technology for the 60 kg Majorana demonstrator. The role of PPC detectors within this experiment is briefly described. The experiments discussed in this dissertation that do not utilize the reactor neutrinos, but instead only take advantage of the low background location, can all be reproduced and improved upon with the Majorana demonstrator. With this in mind, low energy background spectra for the expected deployment of the demonstrator are estimated. Using these estimates, the projected sensitivity for searches for dark matter and electron decay, which are previewed with the results from the SONGS reactor, are calculated.

As a result of the diverse nature of the experiments presented in this dissertation, the chapters discussing each topic are fairly self contained. A description of the PPC style detector, along with characterizations of a number of the earliest detectors, is presented in chapter 2. The details of the Majorana experiment, and the role of the PPC detector technology in it, are described in chapter 3, providing context and some perspective for a number of measurements that are described later. A measurement of the quenching factor for low energy nuclear recoils in germanium detectors is presented in chapter 4 because a number of the experiments and background estimates discussed later demand an accurate knowledge of it. The deployment of the detector to the SONGS reactor and the analysis of the raw data are described in chapters 5–6. The three experiments using reactor anti-neutrinos, specifically the coherent neutrino scattering experiment, the limit on the neutrino magnetic moment and the limit on the continuous energy deposition of neutrinos in matter, are described in chapter

7. The two dark matter searches, for light WIMPs and dark pseudoscalars, are presented in chapter 8. These searches are placed into the larger context of the 60 kg Majorana demonstrator experiment in this chapter as well, where the estimated background spectra and projected limits for the demonstrator experiment are also presented. Finally, the results from the search for electron decay and the projected limits that can be obtained with the Majorana demonstrator are discussed in chapter 9.

The measurements and experiments described in this thesis do not exhaust the possibilities that are presented by the development of this detector, but they are a good representation of the breadth of experiments that can be performed.

CHAPTER 2

LARGE MASS ULTRA LOW NOISE HPGE DETECTORS

This chapter describes the P-type Point Contact detector concept for high purity germanium semiconductor detectors. To date, PPC detectors represent a significant technological step towards the development of a detector capable of measuring coherent neutrino-nucleus scattering. The detector design is a further development of a concept originally developed by Paul Luke and collaborators for an experimental search for the Cosmion [Luke et al., 1989], a hypothetical particle since ruled out [Caldwell et al., 1990]. A germanium crystal was modified to have an electrode structure which reduced the detector capacitance, and thus the electronic noise, below typical levels for large mass germanium detectors. The choice of a germanium semiconductor detector seems a natural one for a low threshold experiment when one considers that the energy required to produce electron-hole pairs is of the order of 3 eV, much less than in detectors such as gas ionization or inorganic crystal scintillators. The detector is comparable in size to a standard HPGe detector ($\sim$ 1kg), having a very similar construction. There are a number of low background techniques that have been developed for dark matter and $\beta\beta$ decay searches that can be incorporated in a deployment of this detector as well. As such, it is possible that very low backgrounds can be achieved.

For this experiment, we have used two incarnations of the PPC detectors, both of which are described below. A brief discussion of the source and characterization of electronic noise in semiconductors and the characterization of this noise in the PPC detector is presented.

2.1 Electronic Noise in Semiconductor Detectors

The electronic noise and threshold of semiconductor detectors is dependent on several characteristics of the crystal and the signal amplification chain. Typically, when characterizing the noise of semiconductor detectors, no consideration is made for pickup from external sources of noise nor for the contribution to the energy resolution due to charge creation statistics. These are either controllable by the experimenter, or are a fundamental limit imposed by the nature of the semiconductor. It is the careful control of the detector parameters, primarily the detector capacitance, but also the leakage current, the quality of the field effect transistor (FET), the nature of the preamplifier and the filtering characteristics of the amplifier that are responsible for the success of the P-type Point Contact detectors.

It is well known that the ratio of the signal to noise of a detector-amplifier system is optimized when the capacitances of the detector and FET are small and well matched [Radeka, 1988]. Through the years, one way that the FET noise has been reduced has been by reducing the level of impurities in the FET channel. These impurities create generation-recombination centers which can lead to an elevated noise level. The use of a quality FET, preferably with a high transconductance g_m, and a correspondingly low noise voltage V_n, can have dramatic effects on the noise. An example of such a FET is the EuriFET ER105 which has a capacitance $C_F = 0.9$pF and $V_n = 1.6nV/\sqrt{Hz}$ at 295° and 10 kHz. The idealized electronic series noise in a germanium detector as measured by the width of a pulser peak is [Radeka, 1988]:

$$FWHM = (41\ eV)V_n(C_F + C_D)/\sqrt{\tau} \tag{2.1}$$

where C_D is the detector capacitance and τ is the characteristic time of the shaping amplifier used to condition the signal from the preamplifier. For the EuriFET ER105, with a $C_D = 1$ pF and a shaping time of 8 μs, the full width at half maximum (FWHM) of a pulser peak is calculated to be $\sim$ 45 eV. This is far below the measured value for PPC detectors (see 2.3) because several other sources also contribute to the electronic noise, but gives an idea of the potential reduction in noise brought about by a $\sim$1 pF detector capacitance.

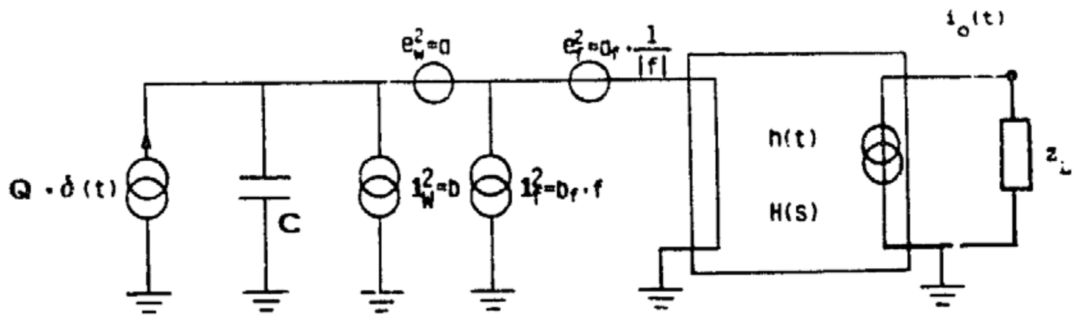

Figure 2.1: A schematic representation of the equivalent noise circuit for a detector-amplifier system. Components of the electronic noise are represented as current (double circles) or voltage (single circles) generators: these are the series and parallel white noise (subscript w) as well as the series and parallel non-white components (subscript f). The figure was obtained from [Gatti et al., 1990].

2.1.1 Equivalent Noise Circuit

It is possible to describe the electronic noise of a detector-amplifier system as consisting of four main components. This is illustrated in the simplified equivalent noise circuit in figure 2.1, obtained from [Gatti et al., 1990]. In the figure, $Q\delta(t)$ is a theoretical test charge input at the detector, C is the sum of the detector, stray and FET capacitances. The four components of the electronic noise are modeled as either voltage or current generators. The usefulness of this simplification becomes evident in the ability to quantify these sources by measuring the Equivalent Noise Charge (ENC) at several characteristic shaping times and capacitances. The coefficients of the noise that are given below contribute to the ENC^2, which can be seen in equation 2.4.

The first component, labeled with a spectral density a, is the white series noise. Conceptually, it is caused by charge fluctuations in the FET channel from random thermal noise. Following the notation of [Bertuccio & Pullia, 1993], it is defined as:

$$a = \alpha \frac{2kT}{g_m} \tag{2.2}$$

where T is the temperature of the FET, k is Boltzmann's constant and g_m is the transconductance of the FET. The value of α is usually between 0.5–0.7 for JFET's [Radeka, 1988].

The second component is the parallel white noise, labeled as b. It is a shot noise, occurring only in the direction of the leakage current and is a function of the quality of the germanium detector and the front end electronics. It is caused by the feedback resistor (if a resistor feedback preamplifier is used) as well as a small leakage current to the JFET gate, where:

$$b = qI_L + \frac{2kT}{R_f} \tag{2.3}$$

I_L is the leakage current of the detector diode, q is the charge of an electron and R_f is the feedback resistance. When the detector leakage current does not dominate, the white parallel noise is easily reduced by eliminating the feedback resistor and using a pulsed-reset preamplifier. The charge that is then built up on the FET gate is not drained with a resistor, but instead is periodically removed using either an optical diode or transistor. The sacrifice made is a reduced throughput of the detector; oftentimes an unimportant consideration for low background experiments.

There are also two non-white components of the noise. The first is the series 1/f noise, $a_f \frac{1}{|f|}$. The source is usually charge trapping in the FET channel. Its counterpart, parameterized as b_f, is the parallel f noise and is often referred to as the dielectric noise. As is discussed in more detail in section 2.3, currently the dominant noise in PPC detectors under optimal operating conditions is from non-white components.

It is possible to characterize the components by filtering with a shaping amplifier and varying the characteristic shaping time τ. Using the notation of [Bertuccio & Pullia, 1993], the Equivalent Noise Charge can be parameterized as:

$$ENC^2 = \left(\frac{aA_1}{\tau} + 2\pi a_f A_2\right) C_{tot}^2 + \left(b\tau A_3 + \frac{b_f}{2\pi} A_2\right) \tag{2.4}$$

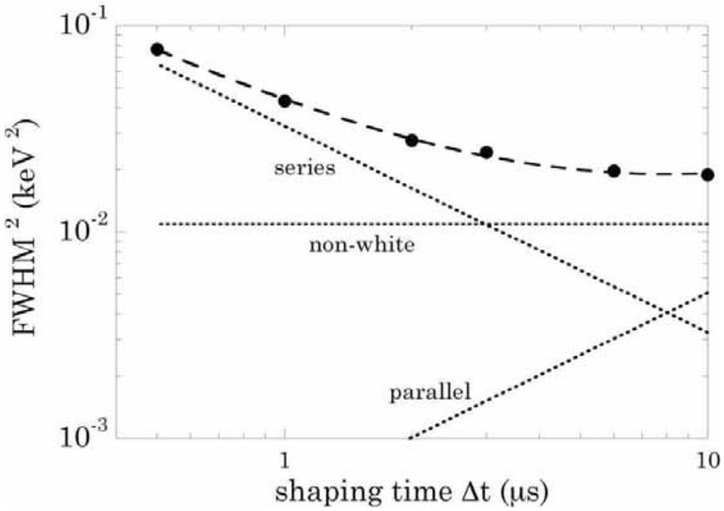

Figure 2.2: The noise of the PPC-1 detector, as measured with a pulser, is plotted for several shaping times. A fit is performed to determine the three noise components (also plotted). Figure courtesy of J. I. Collar.

where ENC is the root mean square of the noise in electrons, C_{tot} is the total capacitance and A_1, A_2 and A_3 are weighting coefficients that depend on the nature of the filtering in the shaping amplifier. The contribution from the series noise increases with detector capacitance, while it is apparent that it also decreases with increasing shaping time. On the other hand, the white parallel noise is a function of the leakage current and increases with the shaping time. For detector systems where the two white components dominate, there is an optimum shaping time τ where the noise is a minimum. It is referred to as the noise corner in the graph of ENC^2 versus τ. An example of such a graph can be seen in figure 2.2. The two non-white noise contributions to the flat line in the figure are independent of τ. Methods to disentangle the contributions can be found in Bertuccio & Pullia [1993].

2.1.2 Noise Filtering

Electronic noise is filtered by integrating and differentiating the preamplifier traces with a shaping amplifier. The result depends on the characteristic shaping time τ of the amplifier.

The specific components that are affected (series white, parallel white, or the non-white components) depend on the nature of the shaping. This is reflected in the coefficients A_1, A_2 and A_3 in equation 2.4. While there is an optimum filter for the suppression of noise in the presence of 1/f noise, known as the cusp filter [Gatti et al., 1990], it is best applied in software because it must be adjusted for each detector and is not easily realized. In place of this, there are several commonly used sub-optimal filters for which the parameters are presented in table 2.1 [Gatti et al., 1990]. These include the RC-CR, trapezoid, gaussian, and the triangular filter. Of these, the RC-CR, gaussian and triangular are commonly used with NIM analog electronic modules, while like the cusp filter, the trapezoidal is most often implemented digitally on the preamplifier traces. The minimum noise achievable with these sub-optimal filters, as a function of the noise parameters a, a_f, b, b_f and the total capacitance C_{tot} is:

$$ENC_{min}^2 = 2(ab)^{1/2}(A_1A_3)^{1/2}C_{tot} + \left(2\pi a_f C_{tot}^2 + \frac{b_f}{2\pi}\right) \tag{2.5}$$

The minimum will occur at the bottom of the noise corner. If the flat (non-white) noise components dominate then a wide range of shaping times can achieve this minimum noise. A brief inspection of table 2.1 shows that of the filters achievable with analog electronics, the triangle filter is the best, followed by the gaussian, then the RC-CR filter. It is the triangular filter implemented in the Ortec 672 NIM module that is used for all of the low energy measurements that are described in this thesis. The optimal filter is only marginally better for these detectors than a triangular filter. Separately, for measurements of the time structure for the arrival of charge at the electrode (chapter 3), a Timing Filter Amplifier, which implements an RC-CR filter, was used with very short shaping times (10 ns) which are necessary for experimenting with the arrival time of charge, which can span ~700 ns.

With the A_{1-3} parameters for triangular filtering in hand, it is a trivial matter to complete the fitting function for determining the components of ENC (see equation 2.4).

Table 2.1. Noise Component Parameters for a Selection of Sub-Optimal Filters

	Parameters			
Shaping	A_1	A_2	A_3	$\sqrt{A_1 A_3}$
indefinite cusp	1	1	0.64	1
triangular	2	0.88	0.67	1.15
gaussian	0.89	1	1.77	1.26
RC-CR	1.85	1.18	1.85	1.85
trapezoidal[a]	2	1.38	1.67	1.83

[a] The rising edge, falling edge and flat top durations equal to τ.

Following the notation of [Bertuccio & Pullia, 1993], the Equivalent Noise Charge can be parameterized as follows:

$$ENC^2 = \frac{h_1}{\tau} + h_2 + h_3\tau \tag{2.6}$$

where the fitted values of h_1, h_2 and h_3 are:

$$h_1 = 2aC_{tot}^2$$

$$h_2 = 0.88\left(2\pi a_f C_{tot}^2 + \frac{b_f}{2\pi}\right)$$

$$h_3 = 0.67b$$

It is possible to directly determine the white series and white parallel components, though the components of the non-white noise remain convoluted. The noise of PPC detectors is measured in terms of the FWHM of a pulser peak, in keV, using the average energy per electron-hole pair creation at 77 K, 2.96 eV.

2.1.3 Detector Noise and Threshold

So far, the discussions have been focused on characterizing the electronic noise, while it is the electronic threshold that is important for many of the applications of this detector. A simplistic method for describing the threshold is to assign it to be 5σ from the centroid of the electronic noise pedestal, if it can be approximated by a normal distribution. This can be difficult to implement if the entire pedestal is not recorded, as is usually the case. It is also an arbitrary designation making no stipulation on the rate of noise events above threshold. The threshold of the experiment is not a well defined level, but must be determined from the desired background rate. A more appropriate method for choosing the threshold is encapsulated in equation 2.7, which describes the rate of random excursions above a specified threshold from noise fluctuations when integrated with a shaping amplifier [Statham, 1977]. To a very good approximation, for a noise described by the rms (σ), the rate of spurious events above the threshold d is calculated to be:

$$R \sim N_{\circ} e^{-d^2/2\sigma^2} \tag{2.7}$$

$$N_{\circ} \sim 1/4\tau$$

As an example, for a detector noise of 160 eV FWHM (σ=68 eV) with a 10μs shaping time and a DAQ threshold of 400 eV, an approximate trigger rate of ~65 cpd is expected from the noise pedestal alone. The noise fluctuations are described by a gaussian distribution that is centered around zero, and thus the threshold of the detector changes linearly with the noise.

2.2 The P-Type Point Contact Detector Concept

The starting point for the development of the P-type Point Contact Detector is the seminal work by Luke et al. [1989], on what was described as the shaped field germanium detector.

The intention was to develop a large mass, low threshold detector. Conventional coaxial electrode detectors have a large central-core electrode that serves to minimize charge drift distances, allowing the construction of large volume detectors. In contrast, the shaped field detector had a small, "point-like" electrode in order to reduce the electrode capacitance and thus the electrical noise of the detector. See figure 2.3 for an example of the comparison to a standard coaxial HPGe detector geometry. In the limit where the size of the central electrode is much smaller than the outer diameter of the detector, the capacitance is assumed to be a function only of the size of the central electrode. Approximating the contact to be hemispherical, with the outer electrode estimated to be at infinity, the capacitance is then:

$$C = 2\pi K \epsilon_{\circ} r \tag{2.8}$$

where K is the dielectric constant of germanium, r is the approximate radius of the hemispere, and $\epsilon_{\circ} = 8.85 \times 10^{-12}$ farad m^{-1}. The shaped field detector had an estimated and measured capacitance of 1 pF. It relied on the electric field produced by space charge impurities to drift charge to the electrode because of the small electric fields produced by the electrode geometry. It is this gradient of impurities, which is a result of germanium detector manufacture, that makes these detectors possible.

The electronic noise of the N-type shaped field detector was 270 eV FWHM, measured with a pulser. This is not sufficient to measure coherent neutrino scattering. Fortunately, the cause of the high noise is the poor quality of the FET's available at the time. The 2N4416 JFET that was used had both a high capacitance and was poorly matched to the detector. The JFET also had a large voltage noise ($C_F = 4.2$ pF, $V_n = 2nV/\sqrt{Hz}$ at 295 °K and 10 kHz). In addition, the shaped field detector also suffered from extremely poor charge collection. This was because the detector was N-type and therefore collected electrons at the central electrode, which are more likely than holes to get trapped over long drift distances or

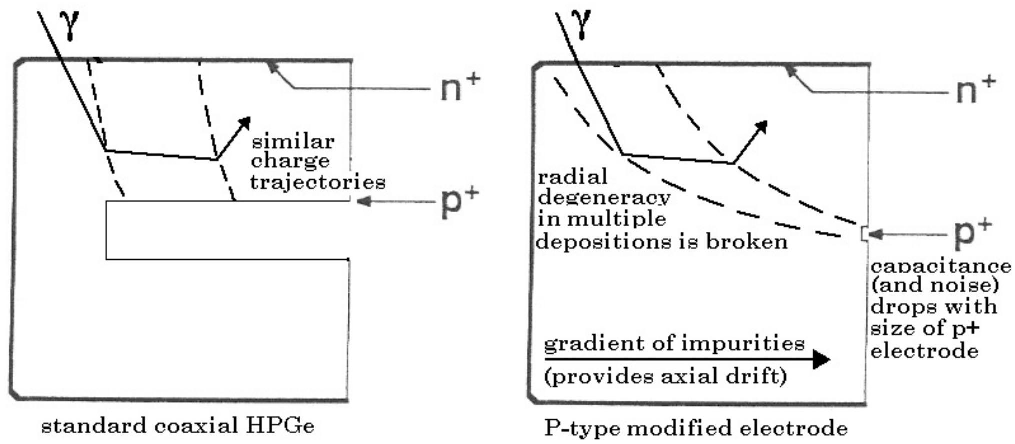

Figure 2.3: The geometry of a standard coaxial HPGe detector is compared to that of a P-type Point Contact detector. Reducing the size of the electrode has the effect of lowering the detector capacitance and thus the series component of the electronic noise. It also extends the range of charge drift lengths within the detector volume, providing a simple mechanism for separating out individual interaction sites.

in low field regions. The energy resolution of the detector was comparable to that achieved with scintillators (∼15%), which is significantly worse than is typical for a HPGe detector (∼0.1%). Unfortunately, the poor charge collection of this N-type crystal excluded it from further consideration in spectroscopy applications. On the positive side, the low fields and long drift times prolonged the arrival of the charge at the electrode from the far recesses of the crystal. Investigations of these extended pulse shapes suggested that it was possible to differentiate between single and multiple-site interactions of high energy gammas within a single crystal. This is a quality the can be put to use in the Majorana 60 kg demonstrator experiment to reduce backgrounds, for example. This is now possible with the development of the P-type Point Contact detector, which have excellent charge collection and are capable of being used in a $0\nu\beta\beta$ decay experiment.

The first PPC detector was the modern incarnation of the shaped field detector, initially having the same geometry as the original [Barbeau et al., 2007b]. There were two main changes made to the design: the detector was changed from an N-type to a P-type germanium detector; and the front end electronics and preamplifier were upgraded with their modern equivalents. The FET was upgraded to a EuriFET ER102, which has a lower noise voltage $V_n = 1.6nV/\sqrt{Hz}$ at 195 °K and 10 kHz, though there are several high quality FET's that can be used with this detector. The reduced FET capacitance (C_n = 0.9 pF) is a better match for the capacitance of the detector. The immediate impact is an increase of the signal-to-noise ratio, which incorporates a reduction in the white series component of the noise. Also, the standard resistor feedback preamplifier was replaced with a transistor pulsed-reset preamplifier, eliminating the leakage current through the feedback resistor. The change also reduced the energy throughput of the system, which is fortunately not a problem for low background experiments. With the great skill of the detector fabricators at Canberra, the detector leakage current was reduced to ∼1 pA, lowering the white parallel component of the noise even further. Careful attention is paid to the construction materials around the detector and FET to eliminate possible source of electronic noise.

The switch to a P-type crystal had a dramatic effect on the performance of the detector. The P-type detectors have a ∼1 mm thick layer of Li-drifted germanium which serves as the outer electrode. This layer of "dead" germanium shields the active germanium volume from low energy betas and x-rays, which can be a significant background for a low threshold detector. As will be discussed later, in some cases partial energy deposition can lead to a background from low energy interactions near the boundary of the dead layer. In addition, handling of the crystals on the dead layer is far less damaging to the crystal, as it requires only a few simple precautions (see figure 2.4).

Finally, the point contact electrode collects holes in the P-type configuration, which is less susceptible to trapping and therefore sees little effect of charge losses within the crystal. Some attention must be paid to the gradient of impurities in the crystal so that the shaped field continues to assist in charge collection. The long drift times that result make it possible

Figure 2.4: The bare PPC-1 germanium crystal is shown, after it was dismounted in a class 1000 clean room. The crystal is safely gripped on the n+ lithium-drifted layer. The borehole electrode of a standard coaxial HPGe crystal is replaced with the boron implanted point contact, which can be seen at the center of the passivated surface.

to differentiate single from multiple-site interactions with these detectors by analyzing the preamplifier pulse shapes (see figure 2.3). The arrival time of charge from different sections of the crystal can span at least up to 1 μs, requiring a long shaping time to fully integrate the energy. Normally this would result in a ballistic deficit effect, where late arriving charges are not properly integrated. The desire for short charge collection times is one reason for the geometry of coaxial HPGe detectors; the long shaping times needed to reduce the electronic noise coupled with the fact that pulsed reset preamplifier traces do not decay at longer time scales make this point moot. Charge collection in the P-type Point Contact detectors is excellent, leading to energy resolutions at $\sim$MeV energies comparable to or better than standard coaxial HPGe detectors. At the same time, thresholds are achieved which are characteristic of small ($\sim$1 g) x-ray detectors.

2.3 PPC Detector Characterizations

Characterizations of three P-type point contact detectors are presented. They are the first such detector, and two more recent incarnations, respectively referred to as PPC-1, BEGe-1 and BEGe-2.

2.3.1 PPC-1

The PPC-1 germanium detector has a total mass of 475g, with an active mass of 450g. The cylindrical detector is 4.42 cm long and 5.07 cm diameter. A picture of the bare crystal, as it looked from the factory, can be seen in figure 2.4. A lithium-drifted dead layer surrounds three sides of the crystal and is $\sim$0.05 cm thick. A thin layer of aluminum coats most of the dead layer. The crystal was originally mounted in an aluminum holder, which was attached to a cold-finger inside a right angle vacuum cryostat. A geometry that was used for Monte Carlo simulations can be seen in figure 2.5. After the germanium quenching factor was measured (chapter 4) the internals of this cryostat were replaced with low background aluminum parts, and then later replaced again with OFHC copper parts to further reduce backgrounds. Several other small internal parts were also replaced to reduce backgrounds.

The noise of the detector was characterized using the method described in section 2.1 and equation 2.4. The noise corner, measured with a pulser and using the triangular shaping setting of an Ortec 672 shaping amplifier can be seen in figure 2.2. The optimal energy resolution is 140 eV FWHM, measured with a shaping time of 10 μs. From the best fit value for the white parallel noise, the leakage current was determined to be 1 pA, which agreed well with some measurements from the reset time of the preamplifier. The series noise is what is expected from the detector capacitance and the FET characteristics. It is apparent that at the optimal shaping time, the dominant source of noise is from a non-white component, the absence of which would give an energy resolution comparable to that achieved with small

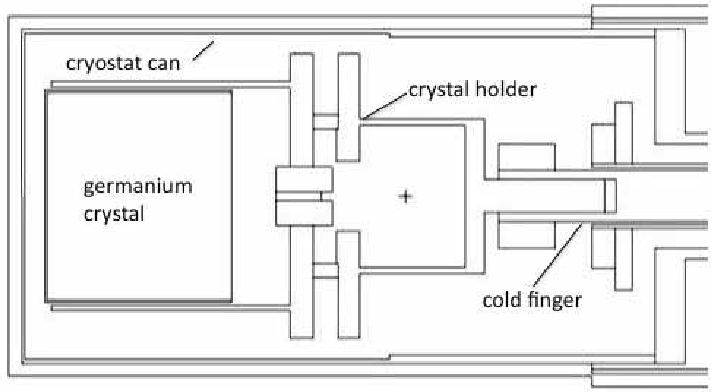

Figure 2.5: A cross-section of the geometry used for MCNP [Briesmeister, 1993] simulations involving the PPC-1 detector.

(few g) semiconductor X-ray detectors. This fact alone suggests that significant improvement of the electronic noise threshold may be able to be achieved. Presently, progress is being made towards understanding the origin of the non-white noise. The noise pedestals of PPC-1 and a conventional coaxial HPGE are compared in figure 2.6 (solid line) where the improved threshold of PPC-1 is evident. Also depicted are two pulser peaks (dotted lines) with the pedestal subtracted, demonstrating the superior electronic noise of this detector. It should be noted that stable operation of the detector noise and threshold were observed over a period of five months in a temperature controlled underground laboratory.

The level of charge trapping in PPC-1 was measured by scanning a collimated ^{241}Am source axially, along the edge of the detector. The 59.5 keV gamma rays interact very near to the surface via the photo-electric effect, leading to point-like energy depositions. The measurements are shown in figure 2.7, where the variation of the mean and FWHM of the 59.5 keV peak versus location can be seen. The charge collection in PPC-1 varies by less than 0.15%, a dramatic improvement compared to the 3% shift in the N-type shaped field detector in Luke et al. [1989]. This is consistent with measurements of the energy resolution of peaks from a ^{60}Co source at 1,333 keV (1.82 keV FWHM), which is comparable to coaxial

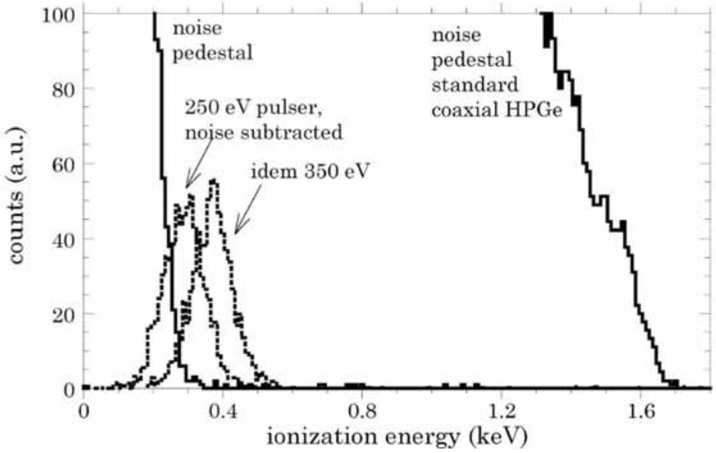

Figure 2.6: The thresholds of the PPC-1 detector and a conventional coaxial HPGe detector are compared; the effect of the improved electronic noise is evident. Also shown are peaks produced by a test pulser, with the noise pedestal subtracted, which demonstrate the quality of the energy resolution of PPC-1. Figure courtesy of J. I. Collar.

HPGe spectrometers. This contrasts with the measured energy resolution of 15 keV FWHM in the N-type shaped field detector. At this energy, the dominant interaction type is via Compton scattering, implying that the majority of signals under the 1,333 keV peak are from multiple site interactions; thus good energy resolution implies good charge collection from different locations in the crystal.

Measurements were also made of the average pulse shape from signals produced with the collimated ^{241}Am source. Figure 2.8 shows a comparison of the risetime of the preamplifier trace as a function of the position of the source between PPC-1 and a standard coaxial HPGe detector. The pulse risetimes in the standard coaxial HPGe detector are uniform for most of the length of the detector until the source is placed at the endcap at the closed-off end of the crystal. In contrast, the risetimes for signals in PPC-1 vary continuously along the length of the crystal, a result of the long drift distances through the crystal for events occurring further along the detector edge. The effect has a dramatic impact on pulse shapes from events involving energy deposition in multiple locations within the crystal providing a method to

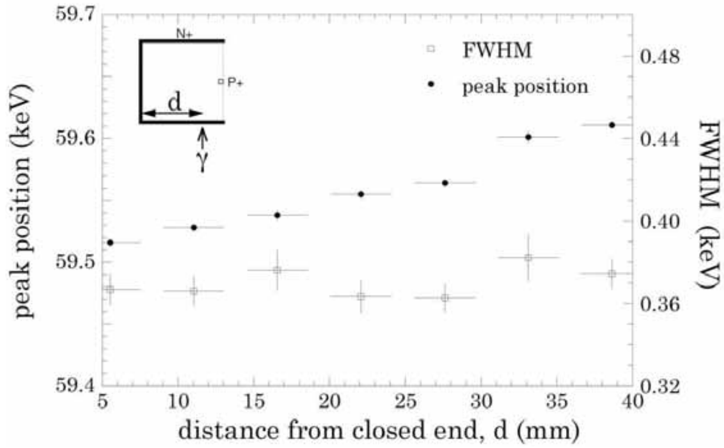

Figure 2.7: The PPC-1 detector was determined to have excellent charge collection, as is illustrated in the figure. A collimated ^{241}Am source was scanned along the edge of the crystal. There is only a minor change (<0.15%) in the charge collection efficiency from the 59.5 keV x-rays.

differentiate them from single site interactions. This characteristic of the detector is put to good use as a method of rejecting gamma backgrounds for the MAJORANA experiment (see chapter 3).

2.3.2 BEGe-1

The BEGe-1 detector is modeled after a commercial product (the Broad Energy germanium detectors) already produced by Canberra Industries, a quasi-planar PPC crystal. The standard BEGe detector sold by Canberra has the same electrode structure and shaped field as P-type Point contact detectors, but this option was not offered to us by the manufacturer during the design phase of PPC-1. The crystal is wider than it is thick to optimize the surface area for collecting low energy x-rays. The BEGe-1 detector (6 cm in diameter and 3 cm thick) has a significantly different aspect ratio than the PPC-1 detector. A geometry used for Monte Carlo simulations can be seen in figure 2.9. The commercial P-type detector crystal has a thinner n+ lithium-drifted layer on the front face to allow more penetration by

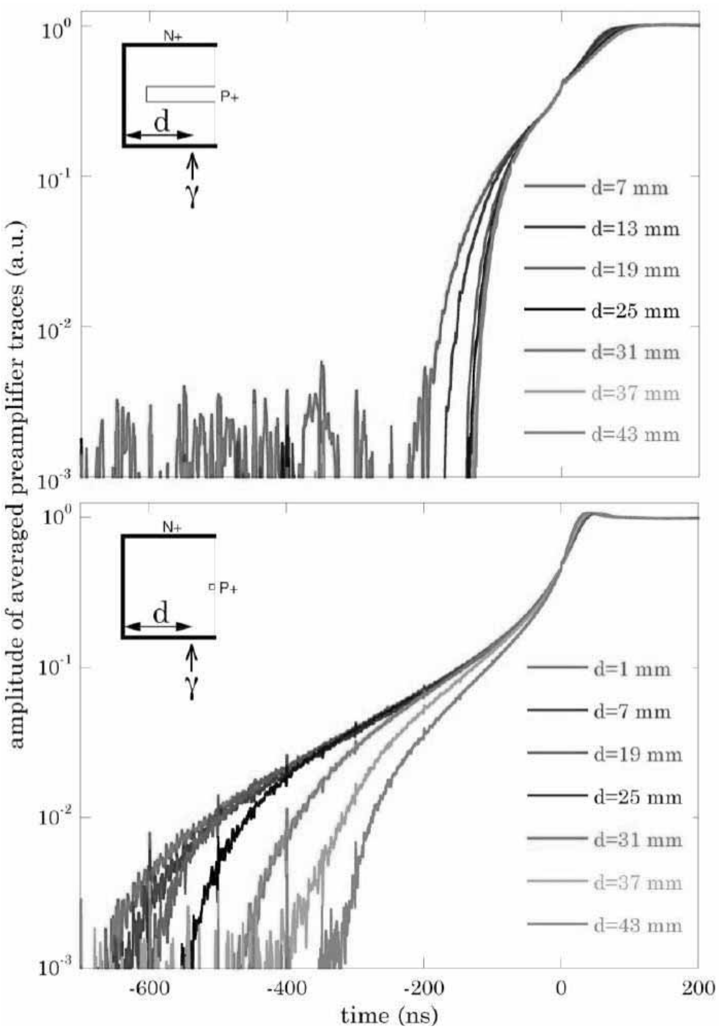

Figure 2.8: Pulser risetimes of a conventional coaxial HPGe detector (top) and the PPC-1 detector (bottom) are compared. The waveforms are averages of ∼1000 events from an ^{241}Am source scanned along the edges of the detectors at several locations. The extended range of pulse shape risetimes is due to the modified electrode structure.

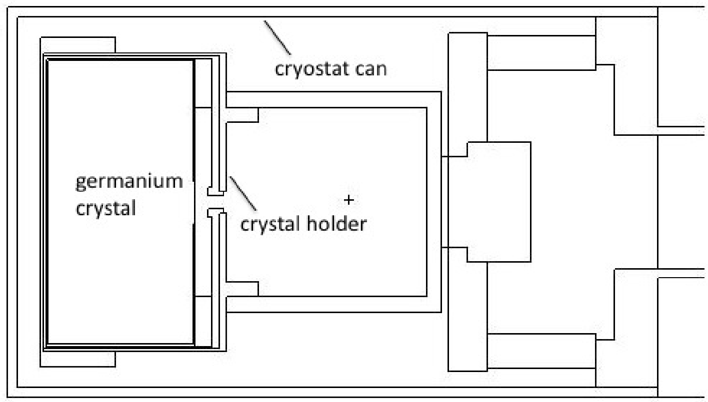

Figure 2.9: A cross-section of the geometry used for MCNP [Briesmeister, 1993] simulations involving the BEGe-1 detector is shown.

low energy x-rays. Unlike the standard BEGe detectors, the dead layer has a uniform thickness (0.05 cm) around the crystal, to reduce the sensitivity to low energy x-ray backgrounds, and has an active mass of 422 g. Also, unlike the original configuration of the PPC-1 crystal, the dead layer wraps around the back face of the crystal. This significantly lowers the total exposed surface area of passivated surface, further reducing the backgrounds from nearby low energy x-rays and betas. While the electrode size is the same as that on PPC-1, it is surrounded by a guard ring in order to help reduce the leakage current to the the FET gate in the BEGe-1 detector. Also, the crystal is enclosed in a low background OFHC can, which was produced at the University of Chicago.

Noise characterizations were also performed for BEGe-1 and can be seen in figure 2.10. The optimal noise resolution, measured with a pulser, was determined to be 140 eV FWHM. The leakage current is 0.9 pA, as determined by the manufacturer.

Typically, the energy resolution of BEGe detectors at 1,333 keV is $\sim$ 2 keV or better, suggesting the impurity profile in the crystal is sufficient to efficiently collect charge. However, it is the aspect ratio of the BEGe style detector that is primarily responsible for the quality of the energy resolution because of the reduced charge drift distances involved.

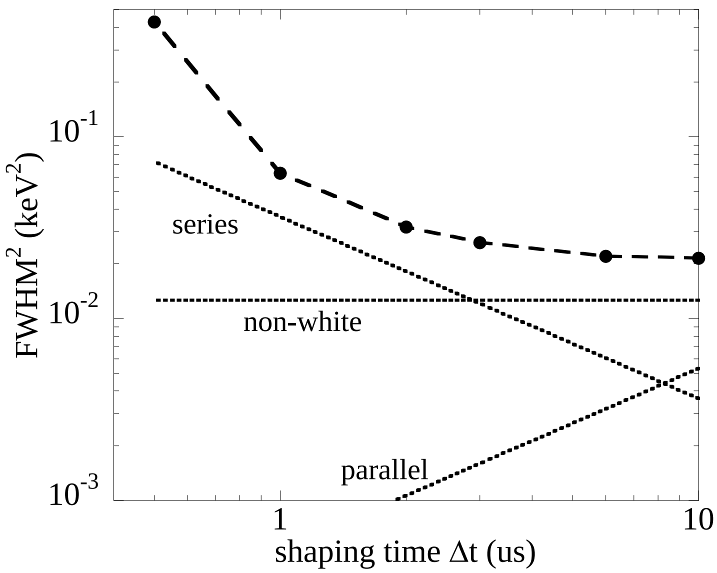

Figure 2.10: The components of the electronic noise of the BEGe-1 detector are depicted. The non-white components dominate for this detector as well. The anomalously high point at τ=0.5 μs has not been reproduced in other detectors and is not included in the fit for the noise parameters. Figure courtesy of J. I. Collar.

2.3.3 BEGe-2

The BEGe-2 detector, purchased by the anti-neutrino group at Sandia National Laboratories as part of the CoGeNT collaboration, is similar to BEGe-1. The detector has a larger mass of ∼800 g, with a diameter of 8 cm and a thickness of 3 cm. The point contact electrode and wrap around n+ lithium-drifted outer contact are identical to BEGe-1. The crystal mount was constructed and cleaned at the University of Chicago and delivered to Canberra Industries for the assembly of the detector. The optimal electronic noise of the detector is 141 eV FWHM, demonstrating that the P-type Point Contact detectors are capable of increasing in mass (×2) without loss of their low noise characteristics. Steps were taken to alleviate a potential source of the flat component, which may have succeeded, as can be seen in figure 2.11. There is some uncertainty as to the validity of the result because of the high leakage current and the poor leverage for the fit at high shaping times. Unfortunately, the leakage

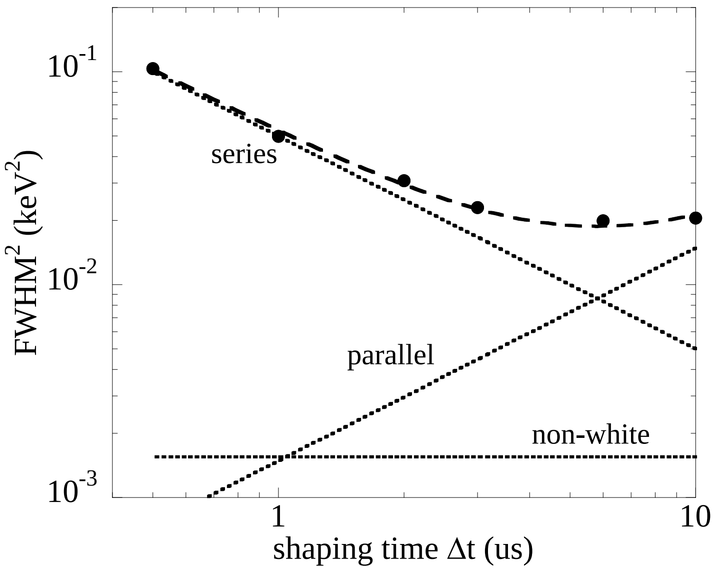

Figure 2.11: The components of the electronic noise in the BEGe-2 detector are depicted. The white series is as expected. The white parallel noise (related to the leakage current) is high compared to previously produced crystals, possibly obscuring a dramatic improvement in the non-white noise. The BEGe-2 measurements were performed by David Reyna and Belkis Cabrera-Palmer at Sandia National Laboratories in Livermore.

current of the detector was initially higher than the previous two detectors, increasing the noise and compensating for this potential improvement in non-white noise. By reworking the detector at Canberra Industries, a drop in the leakage current to the level achieved by previous detectors is expected, meaning that the 0.8 kg detector could potentially have an even lower electronic noise of FWHM.

CHAPTER 3

THE ROLE OF PPC DETECTORS IN THE MAJORANA EXPERIMENT

With the resolution of the Solar neutrino problem and the measurements from atmospheric and long baseline neutrino experiments, the hypothesis of neutrino oscillation is now confirmed. Thus it is known that neutrinos have a finite mass; however, the absolute scale and ordering of the neutrino mass eigenstates is still unknown. As a result, experiments searching for zero neutrino double beta decay are more important than ever. The observation of the decay would identify the neutrinos as their own anti-particles (i.e., Majorana neutrinos). Also, because the decay rate is proportional to the effective mass of the electron neutrino, the scale and hierarchy of the neutrino masses could potentially be set. The matter is more urgent as there exists a controversial claim for the observation of the decay [Klapdor-Kleingrothaus et al., 2001], which must be explored.

The MAJORANA demonstrator experiment is one of several next generation $0\nu\beta\beta$ experiments that proposes to do this. The experiment will consist of 60 kg of ^{76}Ge enriched germanium semiconductor detectors [Elliott et al., 2009]. The purpose is to demonstrate the control of backgrounds for a 1-ton scale experiment. It will use several technology upgrades that aim to improve the sensitivity of the measurement over previous germanium experiments. One of the most important upgrades is the use of the P-type Point Contact HPGe detectors. An alternative that was considered by the MAJORANA collaboration, prior to the development of the PPCs, was the use of highly segmented N-type germanium detectors. This chapter describes the role that PPC detectors play and the advantages that they bring to the experiment compared to the highly segmented detectors.

To begin with, PPC detectors themselves improve on two background rejection techniques. The first is an improved rejection of the background from ^{68}Ge that is a result of the sub-keV threshold. Also, PPCs are superior to other germanium detectors at rejecting multiple-scatter gamma backgrounds using Pulse Shape Discrimination (PSD). This is due to the unique electrode structure and complete charge collection capabilities of the detectors, as was discussed in Chapter 2.

Perhaps most significantly the use of the PPC detector technology results in an enlargement of the physics capabilities of the 60 kg MAJORANA demonstrator. The intention was always to take advantage of the significant mass of germanium crystals to perform a dark matter search [Majorana, 2003]; the large exposure enables a search for the characteristic annual modulation effect expected from the standard isothermal dark matter WIMP halo hypothesis. Unfortunately, the advantages end with the large mass of the detector, as conventional germanium detectors cannot compete in sensitivity with modern dark matter detectors, which typically separate or suppress gamma related backgrounds from the nuclear recoil signatures of WIMP interactions [Ahmed et al., 2009a]. However, as was demonstrated in [Aalseth et al., 2008], the first dark matter experiment with PPC detectors, the low threshold of PPC detectors provides a sensitivity to models that are out of reach of all other experiments. For low mass WIMP candidates, specifically 1–10 GeV c^{-2}, the projected sensitivity of the MAJORANA demonstrator (presented in chapter 8.4), is on par with the best projections of conventional dark matter experiments for higher WIMP masses. In addition to searches for supersymmetric WIMP candidates for the dark matter, PPC detectors also excel in searches for pseudoscalar candidates due to their excellent energy resolution. Also presented in chapter 8.4 is the projected sensitivity for the MAJORANA demonstrator for such searches. It is shown there that it will be possible, for the first time, to impose limits that will exceed those from astrophysical arguments. The potential ancillary searches do not end here. For example, another search that was also planned for the MAJORANA experiment was an effort to place bounds on the decay of the electron [Majorana, 2003]. The superior energy resolution of PPC detectors at low energies ($\sim$ 10 keV) increases the ratio of the signal to background for the measurement, while the reduced threshold increases the potential number of electrons whose decay can be recorded in comparison to an experiment constructed with conventional detectors. The improved reach of this measurement, as well as the potential dark matter experiments, is described in chapter 8.4. As a preview, these three measurements are demonstrated with the current deployment of a PPC style detector to the SONGS reactor in chapter 8.

The importance of PPC detectors to Majorana for the $0\nu\beta\beta$ measurement cannot be overemphasized. Neither can the importance of the ancillary measurements, especially the fact that the results would be the leading measurements in the various fields. It is important to point out that very large deployments of low background HPGe detectors are very expensive propositions. While the use of PPC detectors will also reduce the cost of deployment (per kg of germanium), the additional physics applications rightly play a role in the justification of the overall cost.

3.1 The Majorana Experiment

The Majorana experiment is a large mass, low background array of intrinsic germanium detectors which was designed with the primary purpose of searching for the $0\nu\beta\beta$ decay of ^{76}Ge. The initial goal will be to verify or refute the existing controversial claim for observation of the decay. The full experiment will attempt to measure the decay rate in order to pin down the effective mass scale of the neutrinos. Barring a positive measurement, it may identify the hierarchy of the three known neutrino mass eigenstates. Any measurement of the decay would also indicate that neutrinos are their own antiparticles.

3.1.1 The ν Mass Problem

Since its proposal by Pauli in 1930 the neutrino has been taken to have a tiny mass, if it was assumed to have a mass at all. In fact, within the framework of the Standard Model, the neutrino is massless. It was the eventual resolution of the Solar neutrino deficit problem along with measurements of atmospheric neutrinos and long baseline reactor experiments which upended this paradigm [Araki et al., 2005; Eguchi et al., 2003; Aharmim et al., 2005; Ahmad et al., 2002; Aliu et al., 2005; Ashie et al., 2005]. The problem was grounded in the fact that the charged current measurements of the flux of Solar and atmospheric neutrinos were less than what was expected from Solar models. The issue was resolved when the SNO collaboration measured both the charged current and neutral current interactions from Solar neutrinos. When a global analysis of neutrino experiments is performed with the addition of the KamLAND results, the clear conclusion has been that neutrinos oscillate between flavors.

The most immediate consequence is that neutrinos must have a finite mass, as neutrino oscillation is otherwise impossible. While a non-zero mass was not incorporated into the Standard Model, its inclusion is a minor extension. In addition to neutrino oscillations, other interesting neutrino phenomena also become possible because of a finite neutrino mass. One example is the manifestation of an electromagnetic interaction with a non-zero magnetic moment $\mu_\nu \neq 0$. Another is neutrino decay, $\nu_l \rightarrow \nu_k + \gamma$. The oscillation of neutrinos between flavors, and these more exotic phenomena, are characterized by the neutrino mixing matrix, which describes the relationship between the three neutrino mass and flavor eigenstates.

By studying neutrino oscillations the square of the differences between mass eigenstates can be determined; however, neither the ordering of the masses nor the mass scale can be determined. The possible mass hierarchies are:

$$m_1 \sim m_2 \ll m_3 \tag{3.1}$$

for the normal hierarchy,

$$m_3 \ll m_1 \sim m_2 \tag{3.2}$$

for the inverted hierarchy, and

$$m_1 \sim m_2 \sim m_3 \tag{3.3}$$

for the degenerate hierarchy, where $m_{1,2,3}$ represent the neutrino mass eigenstates. It should be noted that the masses cannot be truly degenerate, because then neutrino oscillation would not occur. It is, however, possible to directly bound the mass of the neutrinos with other experiments. The most constraining come from ^{3}H beta decay experiments ($m_{\nu_e} < 2.3$ eV) that look for spectral deviations at the endpoint of the beta decay spectrum that would result from a non-zero mass [Weinheimer et al., 1999; Kraus et al., 2005]. The limits on ν_μ [Assamagan et al., 1996] and ν_τ [Barate et al., 1998] are much less constraining at: $m_{\mu_e} < 170$ keV and $m_{\tau_e} < 18.2$ MeV.

There are two theories of the nature of the neutrino: they are described as either Dirac neutrinos or Majorana neutrinos. A Dirac neutrino is the conventional description. The theory states that there are four types of neutrinos: left and right-handed neutrinos, as well as left and right-handed anti-neutrinos. Lepton number is always conserved in interactions of Dirac neutrinos. If neutrinos are Majorana particles, then they are their own antiparticles and the theory then contains two neutrino types: left-handed and right-handed neutrinos. Interactions with Majorana neutrinos do not conserve lepton number. The true nature is currently unknown. It may be possible to determine if neutrinos are Majorana particles with $0\nu\beta\beta$ experiments because the process occurs if neutrinos are their own anti-particles. If it is observed, it also is possible to determine the effective neutrino mass from the decay rate. Depending on the measured decay rate, there is also the potential to determine the mass hierarchy of the neutrino mass eigenstates.

3.1.2 Zero Neutrino Double Beta Decay

Double beta decay results in the simultaneous emission of two electrons (or two positrons) for even-even nuclei. Experiments searching for the decay use nuclei where the granddaughter nucleus has a lower binding energy than the parent, but also where the single beta decay is forbidden on energetic arguments or because of selection rules. For example, the decay scheme for ^{76}Ge is shown in figure 3.1, where the double beta decay to ^{76}Se is allowed, but the single beta decay to ^{76}As is not. There are a number of isotopes other than ^{76}Ge that are often used in experiments, such as ^{82}Se, ^{100}Mo, ^{116}Cd,^{128}Te ,^{130}Te, ^{150}Nd and ^{136}Xe (see [Majorana, 2003] and references therein). The choice of a specific isotope usually depends on the choice of detector technology. It also is affected by the Q-value of the reaction and the expected sensitivity of a particular isotope. Some Q-values are so large that they are well separated from most backgrounds (>2.6 MeV), while others have much higher probabilities for decay.

There are several possible types of double beta decay including two neutrino double beta decay ($2\nu\beta\beta$), zero neutrino double beta decay ($0\nu\beta\beta$) and double beta decay with the emission of a majoron. This last will not be further discussed here. The first, $2\nu\beta\beta$, is a second order process that is allowed within the framework of the standard model. The decay includes the emission of two neutrinos and conserves lepton number. For example:

$$2n \rightarrow 2p + 2e^- + 2\bar{\nu_e} \tag{3.4}$$

In this case, the energy from the Q value of the decay is split between the recoiling nucleus,

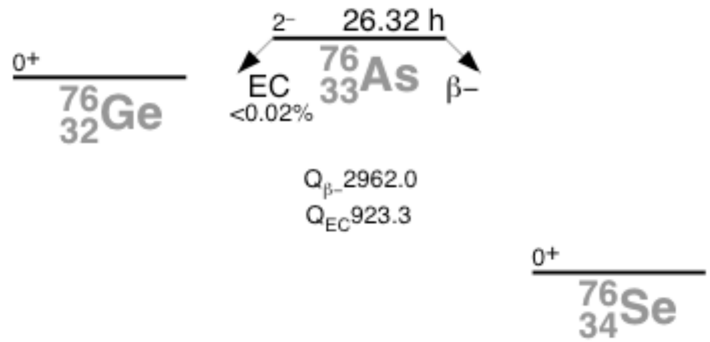

Figure 3.1: Relative energy levels of isotopes near the double beta decay isotope of ^{76}Ge. Single beta decay to ^{76}As is prohibited on energy arguments, but double beta decay is allowed. This figure was obtained from Firestone [1996]
.

the electrons and the escaping neutrinos. A particle detector attempting to measure this process would observe a continuum in the energy spectrum below the Q value, where the missing energy is carried away by the neutrinos. An example spectrum is illustrated in figure 3.2. The other type of beta decay, $0\nu\beta\beta$ decay, is not allowed within the framework of the Standard Model. If the neutrino is a Majorana particle, this decay can occur such that:

$$2n \rightarrow 2p + 2e^{-} \tag{3.5}$$

where instead of emitting two neutrinos, only electrons are emitted. The process occurs because the neutrinos are not in pure helicity states, allowing the exchange of a virtual Majorana neutrino between the nucleons. The Feynman diagrams of the two types of decay are shown in figure 3.3. In $0\nu\beta\beta$ decay, there is no missing energy that is carried away by neutrinos, thus the primary experimental signature is a peak in the detected energy spectrum at the Q value of the decay. Figure 3.2 illustrates the advantage of using detectors with very narrow energy resolution, where backgrounds are less likely to enter the region of interest

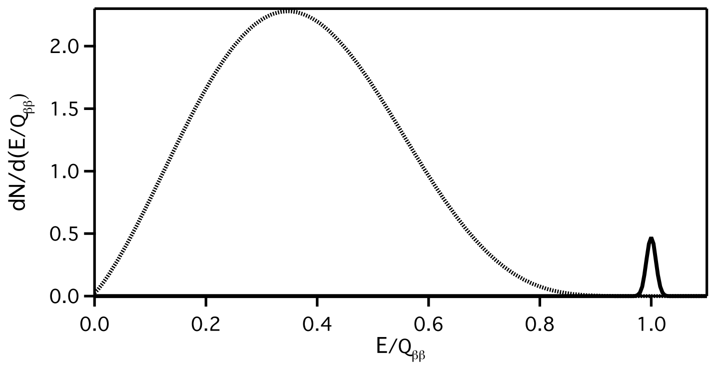

Figure 3.2: Representations of the energy spectra expected from $2\nu\beta\beta$ and $0\nu\beta\beta$ decay. In the two neutrino case the neutrinos can carry energy away from the reaction resulting in a continuous spectrum. This is not the case for the zero neutrino case, as it results in an energy deposition equal to the Q value of the reaction. The spectra are broadened in this figure by a hypothetical detector energy resolution and normalized in energy to the Q value. Figure credit: [Avignone et al., 2008a].

(ROI) and obscure the measurement.

The decay rates of $0\nu\beta\beta$ and $2\nu\beta\beta$ are unrelated. If one assumes $0\nu\beta\beta$ decay occurs by the exchange of a Majorana neutrino, the decay rate can be written as:

$$\lambda^{0\nu}_{\beta\beta} = G^{0\nu}(E_0, Z)\langle m_\nu \rangle^2 |M^{0\nu}_f - (g_A/g_V)M^{0\nu}_{GT}|^2 \tag{3.6}$$

where $\lambda^{0\nu}_{\beta\beta}$ is the measured decay rate, $G^{0\nu}$ is the two-body phase space factor which includes the coupling constants, $M^{0\nu}_f$ is the Fermi matrix element and $M^{0\nu}_{GT}$ is the Gamow-Teller matrix element [Majorana, 2003]. The effective neutrino mass, $\langle m_\nu \rangle$, can be written in terms of the nuclear structure factor and the measured half-life as:

$$\langle m_\nu \rangle = m_e (F_N T^{0\nu}_{1/2})^{-1/2} eV, \tag{3.7}$$

where m_e is the mass of the electron and $T^{0\nu}_{1/2}$ is the half life of the decay, measured with a specific isotope. The structure function $F_N = G^{0\nu}|M^{0\nu}_f - (g_A/g_V)M^{0\nu}_{GT}|^2$, depends on the

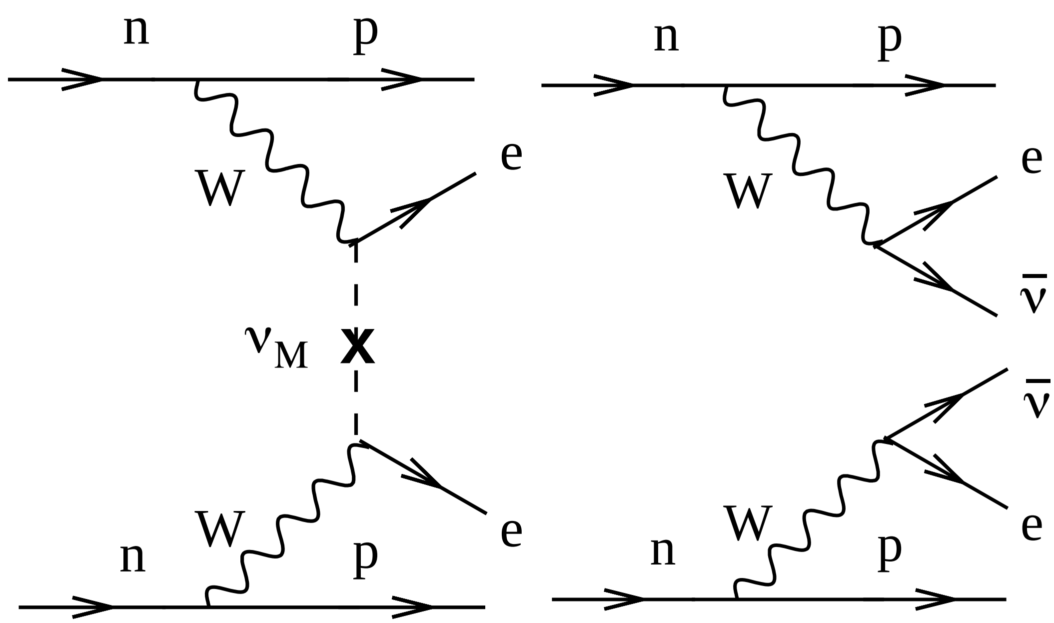

Figure 3.3: The Feynman diagrams for $0\nu\beta\beta$ decay (left) and $2\nu\beta\beta$ decay (right). $0\nu\beta\beta$ can occurs with the exchange of a virtual Majorana neutrino, which is only possible if the neutrino is its own anti-particle. Figure credit: [Avignone et al., 2008a].

isotope in question and is highly model dependent.

The effective neutrino mass is a convoluted parameter that takes into account the neutrino mass mixing matrix.

$$m_\nu^2 = |\sum_i^3 U_{ei}^2 m_i|^2 \tag{3.8}$$

Depending on the measured value of the effective neutrino mass, it may be possible to determine the mass hierarchy of the neutrino mass eigenstates. This is best represented in figure 3.4, which is a plot of the bound on the minimum neutrino mass, versus the effective neutrino mass as measured in a $0\nu\beta\beta$ experiment and is based on the current understanding of the neutrino mass mixing matrix. There are three important regions in this graph. If the neutrino mass eigenstates are nearly degenerate, then both the effective neutrino mass and the minimum neutrino bound are large, and it would not be possible to determine the hierarchy of the eigenstates. It may be possible, however, for low values of the effective

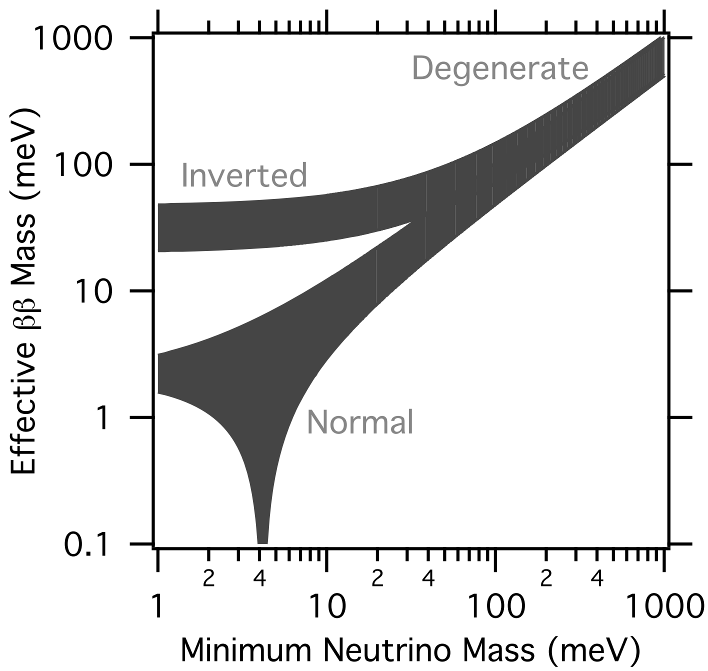

Figure 3.4: The allowed region of phase space, based on neutrino oscillation measurements, of the effective neutrino mass as a function of the minimum neutrino mass. The three named regions relate to the three hierarchy possibilities of the neutrino mass eigenstates. Double beta decay experiments measure or place limits on the effective neutrino mass. Figure credit: [Avignone et al., 2008a].

neutrino mass. It should be noted that for the inverted hierarchy, the effective neutrino mass obtains a value that is potentially within the reach of the Majorana experiment. However, within the allowed region for the normal hierarchy, it is possible that the terms in equation 3.7 cancel, leading to a vanishing effective neutrino mass, as can be seen in figure 3.4. Even if the neutrino were a Majorana particle, the effect would not be able to be measured.

There is a controversial claim for the observation of $0\nu\beta\beta$ decay which would put the effective neutrino mass in the degenerate region [Klapdor-Kleingrothaus et al., 2001]. The experiment consisted of 11.5 kg of germanium, which were operated for approximately 10 years. This will likely be tested very soon with the current deployments of the next generation of $0\nu\beta\beta$ decay experiments.

3.1.3 Experimental Technique

Double beta decay experiments have a long history. The earliest searches studied the ratio of isotopes in old ores in order to determine a small total $\beta\beta$ decay rate over geological timescales. Modern searches use particle detection techniques in an attempt to separate a potential $0\nu\beta\beta$ signal from a background of $2\nu\beta\beta$ decay and radioactive backgrounds. To put it simply, the name of the game is background suppression. In order to maximize the efficiency for detecting the $\beta\beta$ decay events, many detectors enrich a specific detector technology with a $\beta\beta$ decay isotope so that the source and the detector are the same material.

The most common technique is to utilize detector technologies with excellent energy resolution around the energy of the Q-value of the reaction. The narrower the region of interest (ROI) for accepting signals, such as around the peak energy in figure 3.2, the fewer backgrounds counted. This includes the irreducible $2\nu\beta\beta$ signals as well as signals from radioactive backgrounds that often show up as a continuum surrounding the ROI. Modern experiments use ultra clean materials to minimize the introduction of radioactive backgrounds from gamma or alpha emitting isotopes (e.g. ^{60}Co, ^{232}Th, ^{210}Pb). Most often, ultra pure copper is used. Also, exposure to Rn in the air, which can be deposited on detectors and give rise to an alpha background, is kept to a minimum. A common technique for reducing backgrounds is to utilize the spatial information of an interaction to throw out events from multiple-site events. The important point here is that the energy deposited from the betas is often a point-like interaction ($\sim$ 1 mm), except in a gas detector, where the actual straggling of the electron is discernible. Backgrounds from gammas at these energies involve Compton or pair-production interactions, which have multiple energy deposition sites. The high Q-value (>2 MeV) of the decays also typically places the ROI in the portion of the energy spectrum that is least dominated by gamma backgrounds.

Nearly every modern detector uses some form of these techniques. A few experiments are discussed in order to illuminate some of the different approaches for this measurement. For example, the CUoRE/CUoRICINO experiment uses a bolometer detector to obtain good energy resolution in the ROI of the decay [Arnaboldi et al., 2008]. The detectors use ^{130}Te which has a Q-value well beyond the 2.6 MeV line from ^{208}Tl; above this there are few naturally occurring gamma backgrounds. Another experiment, the EXO detector, uses liquid xenon (LXe) detector enriched in ^{136}Xe [Danilov et al., 2000]. The energy resolution is not as good, but it is very easy to make the detector volume clean because the LXe is a bulk material. While spatial information also is used to reject some backgrounds, the final goal is to identify and tag the granddaughter ^{136}Ba ion with each interaction to eliminate all backgrounds that are not $\beta\beta$ decay events. The SNO+ experiment aims to utilize the very large and very low background environment that was the SNO Solar neutrino detector, doping a liquid scintillator with ^{150}Nd [SNO+, 2007]. The matrix elements for Nd are very favorable, but the main strength of the experiment comes from the sheer bulk of the deployment, which is necessary as the energy and spatial resolution will be relatively poor. Just as with these experiments, the Majorana [Majorana, 2003] and Gerda [Bettini, 2007] experiments will use high purity germanium (HPGe) detectors enriched in ^{76}Ge as the source and detector. Germanium is superior to other detector materials used in double beta decay experiments for several reasons. The excellent energy resolution of the detectors leads to good separation of the expected double beta decay signal from the background. Germanium also has a favorable matrix element for the $0\nu\beta\beta$ decay. In addition, because the source and target are the same, the efficiency for the detection of the decay is $\sim$100%.

The Majorana demonstrator module will be a deployment of 60 kg of HPGe PPC detectors. It is currently estimated that approximately 2/3 of the module will be composed of enriched crystals. The experiment will have very good energy resolution in the ROI, which is typical of HPGe detectors. In addition to using very clean construction materials and detectors the Majorana experiment aims to make as much use of the spatial information of the background interactions as possible. By using an array of ∼1 kg germanium detectors the experiment will be able to eliminate backgrounds from Compton-scattered photons that interact with multiple detectors. In addition, by using the information encoded in the arrival time of the charge carriers, backgrounds that involve multiple scatters in a single detector will be reduced. It is estimated that PPC detectors have a spatial resolution of 1–2 mm. The experiment will be located deep underground at the Homestake mine (4850 m.w.e.), to reduce cosmic ray induced backgrounds. One of the most important considerations is to minimize the exposure of the germanium detectors and construction materials (electroformed Cu) to cosmogenic activation on the surface. The activation of the unstable isotopes can lead to decays that can be a significant background in the ROI [Majorana, 2003]. The deployment will serve as an important demonstration of the technology that is intended to be used for a much larger ∼1 ton deployment.

3.2 Improved Rejection of ^{68}Ga Background

Aside from gamma backgrounds from natural radioactivity, which are reduced by using clean shielding materials, one of the more important backgrounds for the Majorana detector is due to the cosmogenic activation of the germanium crystals with ^{68}Ge. The long half-life (270 days) of the isotope makes it difficult to wait for the detector backgrounds to decay. ^{68}Ge occurs via electron-capture. The result is an energy deposition that totals 10.36 keV due to the cascade of low energy x-rays and Auger electrons following the filling the K-shell in the daughter gallium atom. It is not this first decay which is a background for $\beta\beta$ measurement. It is the decay of the daughter isotope of ^{68}Ga which can cause backgrounds in the region of interest. The largest branching ratio of ^{68}Ga decay involves the emission of a positron with a maximum energy of 1.9 MeV. The maximum energy deposited increases to ∼2.9 MeV when combined with the full energy deposited from the two 511 keV gammas emitted from the

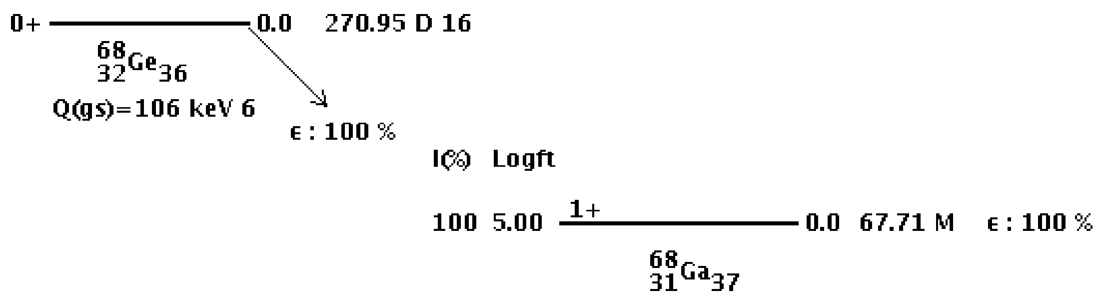

Figure 3.5: The electron capture decay of ^{68}Ge. The resulting energy deposition from the cascade of x-rays and Auger electrons is equal to the binding energy of the captured electron of the daughter atom (10.4 keV and 1.3 keV for the K and L-shells respectively). About 8% of the daughter nuclei decay via electron capture and result in the 9.6 keV peak from the Cu K-shell cascade; the balance decay via β^+ emission. This plot was obtained from the Table of Isotopes at [Nuc, 2009]

positron annihilation. The resulting continuum of energy depositions invades the $\beta\beta$ ROI (at 2,039 keV for ^{76}Ge), causing a significant background at the level of ∼15 ton^{-1} y^{-1} in the ROI [Majorana, 2003].

According to the background estimate, this would be the dominant contributor to the background. However, there are two main techniques that have been developed to reduce this to manageable levels. The first is to utilize the capabilities of the germanium crystals, along with the germanium detector array, to identify events that involve multiple-site interactions. Without the interaction of at least one of the annihilation 511 keV gammas, there would be no contribution to the background at 2,039 keV. By eliminating events that are characterized as multiple-site interactions a significant reduction in background can be achieved. A second cut utilizes the short 67 m half-life of ^{68}Ga, looking backwards in time (4–5 half-lives) for indications of the decay of the parent isotope, which is only possible in ultra low background experiments. For typical (higher threshold) germanium detectors, this only involves looking for the 10.36 keV K-shell peak of atomic gallium. This identifies, at best, ∼90% of the ^{68}Ge decays because the L-shell electron-capture signature occurs below threshold. However, the low electronic noise and correspondingly superior peak resolution (160 eV FWHM) of a PPC at these energies make it possible to identify nearly all of the parent decays. It should be noted that the improved rejection capability is expected to be unnecessary, because the projected backgrounds from this decay should already be sub-dominant ($\sim$0.1 ton^{-1} y^{-1} in the ROI at 2,039 keV [Majorana, 2003]). Nevertheless, it may prove useful if the germanium crystal suffers more cosmogenic activation than is currently estimated.

3.3 Multiple Site Rejection of High Energy Backgrounds

The Majorana experiment aims to achieve an unprecedented level of background in the $0\nu\beta\beta$ ROI for germanium detector experiments. Even though it will be constructed with radioclean materials (electroformed copper, hyper-pure germanium, etc.) there will still be some background nuisance sources from gamma emitting isotopes contaminating the detector and its shielding. Such sources from natural and cosmogenic radioactivity can lead to Compton scatters in the detectors, depositing only a fraction of their energy, and potentially contaminate the ROI. Many of these events involve energy depositions in more than one location, where the electron range is usually 1–2 mm. In addition to this, some contributing backgrounds involve beta decays where multiple-site interactions are expected. This is especially true of positron decays, as the two resulting 511 keV annihilation gammas have a very high likelihood of interacting at different locations. An important example of such a background from the positron decay of ^{68}Ga was discussed in section 3.2. Two analysis methods will be used to reduce the background by attempting to identify events which have multiple interactions: the identification of events in multiple detectors and within individual detector volumes.

The primary method for reducing backgrounds from multiple scattered gamma backgrounds is to eliminate events that interact in more than one germanium crystal. This "granular cut" works best when the crystals, each $\sim$0.4–1 kg, are packed as closely together as possible within the cryostat. The configuration will likely consist of three to four detectors stacked in vertical columns. The columns are then close-packed in a hexagonal geometry. The materials used to hold the crystals will be minimized to reduce the probability that a Compton scattered gamma is absorbed in them.

The second method for the rejection of background events involves the analysis of the event waveforms using Pulse Shape Discrimination (PSD), which identifies events that are due to multiple-site interactions. By recording the shape of the event pulse, it is often possible to determine when an event involves more than one interaction site within a single crystal. For PPC detectors, the technique relies of the spread of arrival time of charge produced in different locations within the crystal. It should be pointed out that it does not necessarily provide any significant spatial information for the event. Similar techniques have been put to good use in several other experiments [Petry et al., 1993; Petry, 1994; Hellmig & Klapdor-Kleingrothaus, 2000; Elliott et al., 2006; Budjas et al., 2008; Smith et al., 1988; Gonzalez et al., 2003; Blair et al., 1999], usually involving standard coaxial HPGe detectors, removing some of the multiple scatter events while attempting to avoid eliminating single site events. For standard coaxial detectors, this is something of an unnatural act, considering the crystals are typically designed to minimize differences in the arrival time of the charge at the electrodes from different location within the crystal. This uniformity is imposed in order to minimize the burden on the Data Acquisition electronics, to reduce charge losses over long drift distances, and to minimize pile-up in high rate experiments. PPC detectors were not designed with these considerations in mind. In fact, the small electrode which was designed to reduce the detector capacitance, and thus the electronic noise, maximizes the drift distance between locations in the crystal. The result is that arrival time of charge from different locations within the crystal can span at least $\sim 1\mu$s (figure 2.8), while charge losses are nearly non-existent (figure 2.7). The accuracy and efficiency for the identification of multiple site events is much improved in comparison to earlier detector technologies. It is also relatively trivial to implement.

It is also possible to identify multiple site interaction events using a Pulse Shape Analysis (PSA) technique [Smith et al., 1988], which identifies single or multiple-site interactions within the crystal and is implemented for more complicated segmented detectors that have many electrodes. The event location can be specifically located within the crystal. An example of such a detector that was considered for deployment as part of the Majorana experiment are the highly segmented N-type crystals [Avignone, 2008]. With independent readout channels in 60 segments of the germanium crystals, the position of events can be fairly accurately reconstructed. Unfortunately, for the highly segmented N-type crystals, many more signal cables are required to instrument similar mass detectors. These cables introduce a significant level of radioactive contamination and account for a significant amount of the background budget. The ability of PPC detectors to reject multiple site interactions while keeping single site interactions is superior to the highly segmented style (see 3.3.1). Simulations have shown that PPC detectors will achieve the same background rejection goals, if not better, while introducing less background.

3.3.1 Pulse Shape Discrimination Technique

Some experiments that attempt to discriminate against multiple-site interaction backgrounds in germanium detectors split the signals from the charge preamplifier. The data acquisition system then measures the energy of the event with one channel and uses the second for PSD analysis [Budjas et al., 2008; Gonzalez et al., 2003; Barbeau et al., 2007b]. In this parallel path, the signal is sent through an amplifier with a very short shaping time ($<$100 ns) compared to the characteristic shaping times used for energy determination (> 1 μs). The difference is due to the fact that the energy determination focuses on the final integration of the energy, while the PSD technique derives its power from the differentiation of arrival times for different locations within the crystal.

For these tests, a Timing Filter Amplifier (TFA) NIM module was used which utilizes an RC-CR shaping amplifier. The characteristic time constants of the integration and differentiation of the amplifier are controllable between 10 ns and 500 ns. The output waveforms from the TFA module were recorded in tandem with the energy of the event for analysis off-line. An example trace for a standard coaxial HPGe detector can be seen in figure 3.6 (top), along with the signal from the preamplifier. The waveform from the TFA essentially traces the arrival of the charge at the electrodes. It can be very difficult to determine if a given waveform represents a multiple site interaction because coaxial detectors are designed to collect all of the charge as rapidly as possible. Sophisticated analysis routines are often used. One technique that has had significant success measures several parameters of the peaks, such as the width, the front-back asymmetry and the moment of the pulse [Elliott et al., 2006], similar to a moment of inertia. Some success has also been achieved using neural networks for the same purpose [Majorovits & Klapdor-Kleingrothaus, 1999]. For the tests described here, a method similar to that reported in [Gonzalez et al., 2003] is used, where multiple site interactions are identified by counting the number of peaks and lobes in the trace from the TFA. The technique takes advantage of the fact that the multiple-site interactions are essentially encoded in the arrival time of charge at the electrode. For PPC detectors, this is dramatically extended with respect to the coaxial detectors used in [Gonzalez et al., 2003], resulting in dramatically improved capabilities. All of these techniques provide a measure of the likelihood of any single event being the result of a single or multiple site interaction.

There will always be some elimination of good $0\nu\beta\beta$ signals whichever discrimination method is used. There is a standard benchmark that is typically used in germanium experiments that characterizes the misidentifications of a given technique for a given detector [Elliott et al., 2006; Gonzalez et al., 2003; Majorovits & Klapdor-Kleingrothaus, 1999]. A comparison is made for two nearby gamma peaks that involve either mostly single site or mostly multiple site events. This is easily achieved with a thorium source, where there is a gamma line at 1588 keV from ^{228}Ac and a double escape peak (DEP) from the 2,614 keV gamma from ^{208}Tl at 1,592 keV. The 1,588 keV peak consists of mostly multiple scattered events from Compton-scattering. On the other hand, the DEP is due to a pair production interaction where two 511 keV annihilation gammas escape the crystal, resulting in an energy deposition in a single location. The peaks are close enough in energy that it is unlikely to find any energy-dependent effects that skew the comparison. Methods are compared by measuring the effectiveness for eliminating the ^{228}Ac peak and the simultaneous reduction in the ^{208}Tl DEP.

3.3.2 Pulse Shape Discrimination with PPC-1

The basics of this analysis were performed with traces from the PPC-1 detector in order to characterize the multiple-site rejection capabilities of PPC detectors. The results, using the standard PSD benchmark, indicate that PPC detectors are superior to other detector technologies for rejecting multiple-site interactions. Both the simplicity of the analysis and the exceptional discrimination are due to the extended arrival time of charge at the central electrode in PPC detectors.

For these tests, the PPC-1 detector was exposed to a ^{208}Th source that bathed the entire germanium crystal as uniformly as possible. The preamplifier signal was sent through an amplifier with a 10 μs shaping time and the waveform was recorded on an 8-bit DAQ card. This signal served as a trigger as well as providing a reasonable measurement of the energy of the events. Unfortunately, while the energy resolution was sufficient for this demonstration,

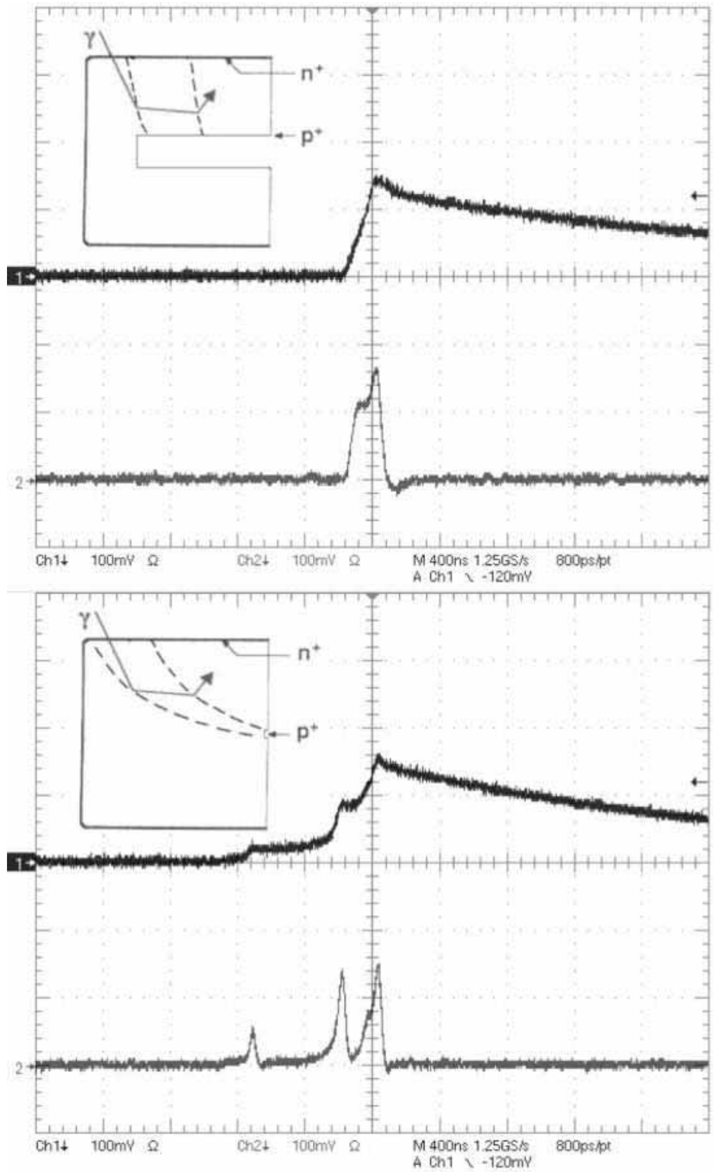

Figure 3.6: In this figure, oscilloscope traces are compared from high energy events in a conventional coaxial detector (tope two figures) and a PPC detector (bottom two figures). For each pair, shown are the preamplifier traces (top trace) and the same signal passed through a Timing Filter Amplifier (bottom trace) with 10 ns integration and differentiation. A simple peak finding algorithm is used on the filtered traces to eliminate signals from multiple site interactions. Charge drifting scenarios, arising from the same gamma interaction, are depicted in the insets. The field lines, indicated by the dashed lines, closely follow calculations of the PPC detectors by David Radford. It should be noted that decay in the shape of the preamplifier trace from the PPC-1 detector is a result of AC-coupling the scope input, as it does not occur for a pulsed reset preamplifier. Figure courtesy of J. I. Collar.

it suffered because of the lack of dynamic range of the card (8 bits). The signal from the preamplifier was split off into the TFA with the integration and differentiation set to 10 ns. This waveform was also recorded on the DAQ card. An example TFA trace from the PPC-1 detector can be seen in figure 3.6 (bottom). It is interesting to calculate the expected noise with this particular RC-CR shaping. It is clear from the noise corner graph for this detector, in figure 2.2, that for a characteristic shaping time of 10 ns, the equivalent noise will be dominated by the series contribution. After accounting for the change in the type of shaping, the noise of the PPC-1 detector is calculated to be 2.35 keV FWHM, corresponding roughly to a threshold of 5 keV.

Comparing the two traces in figure 3.6, the advantages of PPC detectors for eliminating multiple site interactions become apparent. Where the typical coaxial germanium detector requires sophisticated analysis techniques to determine the nature of the event in the example trace, it is a trivial matter to characterize the event in the PPC detector as being due to a multiple-site interaction. An analysis was performed using a simple LabVIEW application: The waveform was searched for peaks with a pre-existing peak-finding subroutine. A minimum peak half-width at half maximum of 20 ns was required to reduce picking out false peaks from digitizer noise. Similarly, a minimum peak height threshold was chosen to be 5σ from the baseline, characterized by the baseline root mean square (RMS) earlier in the waveform trace. Any event where more than one peak was found within a 4μs window (to avoid issues with pileup) was identified as a multiple scatter event. An additional cut on the falltime of the peak was applied to assist in identifying peaks that were too near together to be separated. The cut is similar to some of the more sophisticated analysis techniques used with other detectors. If there is another, smaller, peak that occurs immediately after the primary one, this cut is efficient at identifying it. A similar cut cannot be used on the rising edge of the peaks in the TFA trace because of slow risetime of some pulses. While this cut does enhance the discrimination capabilities of the technique, it is susceptible to

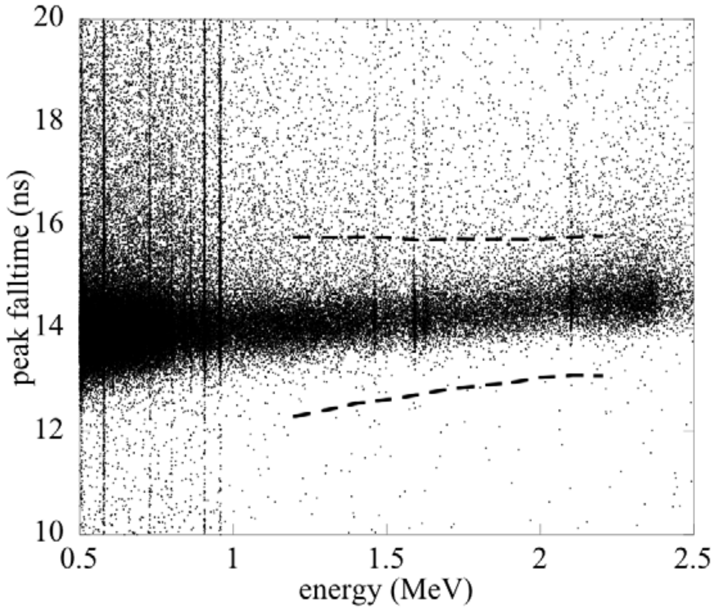

Figure 3.7: The measured fall time of traces from the TFA versus the total measured energy. A cut is performed which enhances the discrimination capabilities against multiple site interactions. The dotted lines are an energy dependent 3σ window about the mean falltime of single site events. While a mild energy dependence is accounted for here, a full study was delayed for a more thorough analysis.

energy-dependent effects. These do not bother the quality of discrimination at $\sim$1,600 keV; however, it will likely affect the capabilities of this method at higher energies. A scatter plot of the falltime versus the event energy for single site events illustrates this nicely in figure 3.7. A slight energy dependence on the falltime cut was accounted for by placing a 3σ window about the band of events that can be assumed to be due to single scatter interactions.

3.3.3 Results

A histogram of event energies around 1,600 keV from the ^{208}Th source for the PPC-1 detector is displayed in figure 3.8. Evident in the unfiltered spectrum are the 1,588 and 1,592 keV peaks. A multiple-site background rejection of 88% was achieved, with a single-site signal acceptance of 93%. The reduction of several other peaks, due mostly to multiple scatters, is

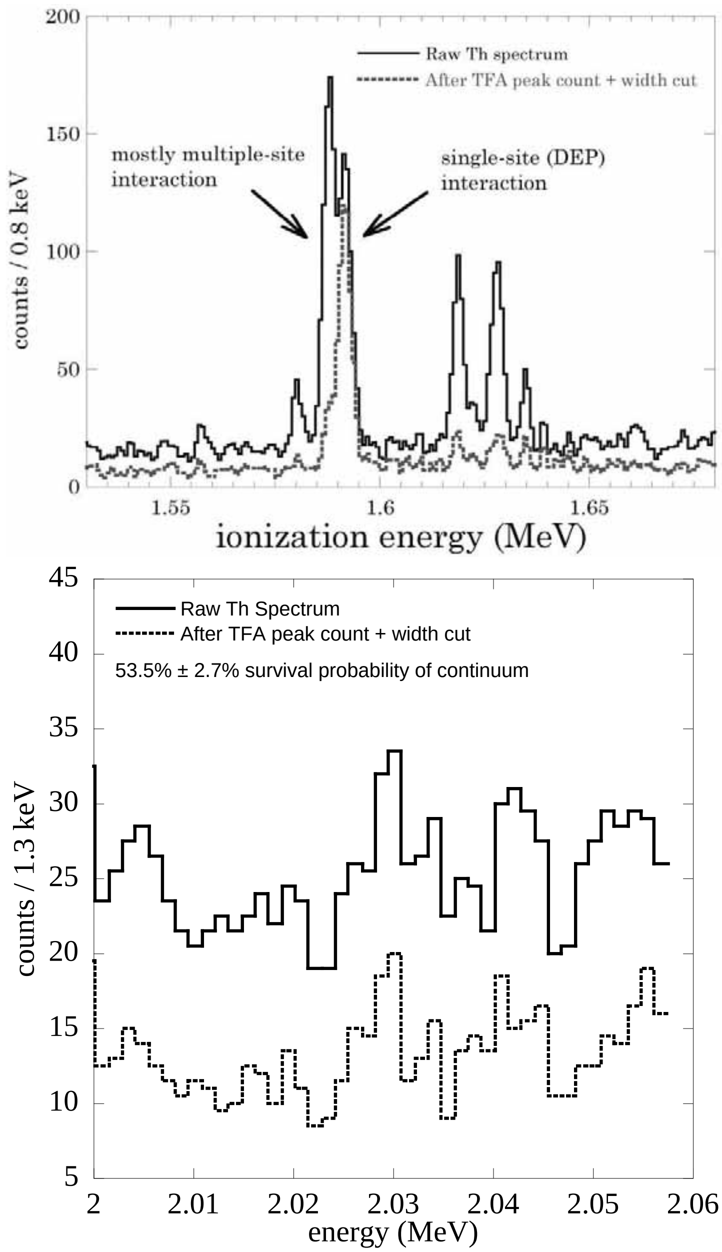

Figure 3.8: The efficacy of the simple multiple site rejection algorithm is determined by comparing its effect on peaks composed primarily of multiple or single interaction sites. A thorium source was used which produced a primarily multiple site event at 1,588 keV from ^{228}Ac, as well as single site events from the double escape peak of the 2,614 keV ^{208}Tl line (top). A rudimentary test of the energy dependence of the cuts is performed at $\sim$2 MeV (bottom), where ratio of single-site to multiple-site events for this specific source-detector configuration, is shown to be in reasonable agreement with what is expected from a Monte-Carlo simulation (55%).

also apparent.

Similar cuts were applied, using the modified value for the falltime cut, at the higher energy near the $0\nu\beta\beta$ decay ROI. This is also displayed in figure 3.8. The survival probability of 53.5% $\pm$ 2.7% is in agreement with the expected value of 55%, determined with an MNCP-Polimi simulation, which is able to generate the multiplicity of each interaction. While this is not iron-clad evidence for the energy independence of this cut, the reduction of the continuum is consistent with expectations from a Monte Carlo simulation.

3.3.4 Discussion

The multiple-site rejection capabilities for a single PPC detector fare better than the other detector types that have been considered for the 60 kg MAJORANA demonstrator experiment: the P-type coaxial and N-type highly segmented detectors. The simplicity of this approach is a direct result of the encoding of the interaction position information in the time structure of the signal pulse. The method used here to demonstrate the capabilities is not optimal, but it is sufficient to demonstrate the appropriateness of PPC detectors for the 60 kg MAJORANA demonstrator experiment in terms of their ability to reject multiple scattered backgrounds.

3.4 Expansion of the MAJORANA Physics Program with PPC Detectors

With PPC detectors the 60 kg MAJORANA demonstrator experiment can place strong limits on Light WIMP and pseudoscalar dark matter candidates. They also improve limits on the lifetime of the electron, beyond what would be capable with other HPGe detector technologies that have been considered (P-type coaxial, N-type highly segmented).

The energy region of interest for a conventional WIMP search is typically 10–100 keV (ionization energy). Experiments search for the low energy nuclear recoils in detectors which

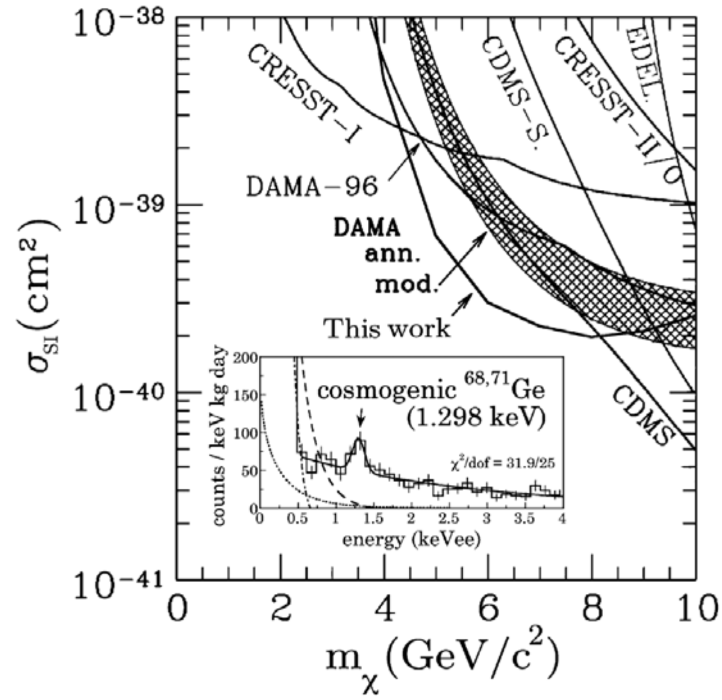

Figure 3.9: The results of a light WIMP search using the first deployment of a PPC detector. The detector and its shielding where located at the TARP facility (300 m.w.e.) outside Chicago. The results rule out a standard isothermal WIMP hypothesis as the source of the DAMA annual modulation, assuming no untested or hypothetical detector response modes are invoked (i.e. channeling). Results for an improved search are reported in this dissertation, as are projected limits for the MAJORANA demonstrator experiment. This figure is reproduced from [Aalseth et al., 2008]. Figure courtesy of J. I. Collar.

are the signatures of WIMP interactions. Unlike most modern direct WIMP searches, the germanium crystals in the 60 kg Majorana demonstrator will not have the ability to distinguish nuclear recoils from the most prevalent backgrounds that are from minimum ionizing particles (MIPs). That is, the background sources lead to interactions involving the scattering off electrons in the detector. The CDMS experiment, one of the leading dark matter experiments, deploys hybrid germanium bolometer detectors that are also ionization detectors in order to discriminate against this unwanted background. Unlike MIPs, nuclear recoils deposit only a fraction of their energy as ionization in the detector, where the balance is deposited in the form of heat. This difference provides the discrimination mechanism for these bolometer experiments. Another, the COUPP experiment, uses bubble chambers that can be made insensitive to minimum ionizing events, while at the same time being sensitive to nuclear recoils. The only way for the Majorana experiment to compete in sensitivity would be to construct a massive detector ($\sim$ 500 kg) and search for an annual modulation of the event rate. A claim for the observation of a modulated signal has been made by the DAMA collaboration (see chapter 8). However, with the use of PPC detectors, the threshold of the Majorana 60 kg demonstrator experiment would be far below that of any conventional dark matter experiment. The detectors do not need any MIP discrimination capability to provide strong limits on light mass WIMP candidates for which other experiments have no sensitivity. This is because the lighter the mass of the WIMP, the lower the energy of the recoil. Also, a light WIMP concentrates the signal into a small energy region which leads to a larger differential rate than in a typical dark matter experiment and thus a larger signal to background ratio. PPC detectors are sensitive to models for the dark matter in a region of phase space that no other experiment can reach. This is demonstrated in figure 3.9, which is a reproduction of the first dark matter limits obtained with PPC detectors [Aalseth et al., 2008]. It should be noted that a second light WIMP search has been performed with PPC detectors, benefiting from a reduced background, as part of the deployment of the detec-

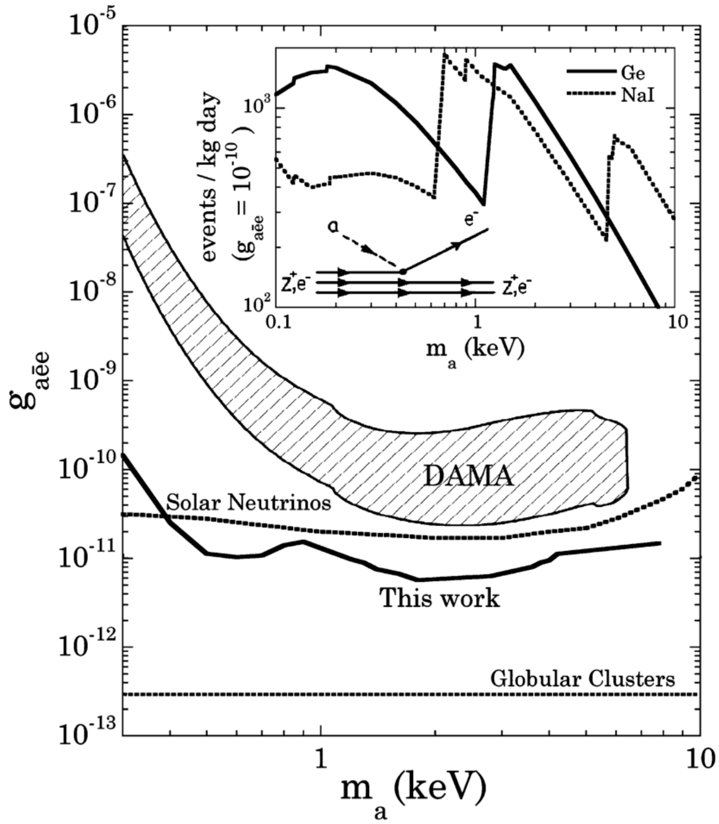

Figure 3.10: Results of a search for axion-like dark pseudoscalars with the first deployment of a PPC detector at the TARP facility. A significant improvement to these results is reported in this dissertation, as are projected limits for the MAJORANA demonstrator experiment. This figure is reproduced from [Aalseth et al., 2008]. Figure courtesy of J. I. Collar.

tors to the SONGS nuclear reactor. See chapter 8.2 for these improved results and a more complete discussion of the topic. These new limits will be part of a future publication.

PPC detectors have also been used to search for pseudoscalar dark matter candidates. Limits for this were also reported in Aalseth et al. [2008]. The interaction signature for this form of dark matter is not a nuclear recoil, but instead the pseudoscalars interact via the axioelectric effect. The process is similar to the photoelectric effect; it is proportional to the product of the mass of the particle and the photoelectric cross section in the germanium crystal. The energy deposited in the detector is equivalent to the mass of the incoming pseudoscalars. The signature is a peak in the spectrum. The expected masses of these dark matter candidates are in the few keV. The corresponding limits are obtained after searching for any anomalous peaks in the low energy region (<10 keV). As a result of the excellent resolution at these low energies, PPC detectors are very sensitive for these measurements. The limits obtained in the first such measurement with a PPC detector are reproduced in figure 3.10. A more complete discussion of this topic is also covered in chapter 8.3, where stronger limits are obtained as part of the deployment of a PPC detector to the SONGS nuclear reactor.

In addition to these two new dark matter searches, the experimental search for the "invisible" decay of the electron via the process $e^- \rightarrow \nu_e \nu_e \bar{\nu_e}$, can also be dramatically improved with the use of PPC detectors. The experiment would have been sensitive to the decay of an electron in the K-shell of germanium with normal detectors, for which the resultant signature is a cascade of x-rays and Auger electrons with a total energy equal to the binding energy at the K-shell. The search for this decay is a search for an anomalous peak at $\sim$11.1 keV. Just as with the pseudoscalar dark matter search, the excellent peak resolution of PPC detectors at these low energies provides an increased sensitivity for this measurement. In addition, the low threshold of PPC detectors allows a search for the decay of electrons from the L-shells as well ($\sim$1.1 keV), where there are $\times$4 as many electrons that can potentially decay. Thus, PPC detectors will provide an improvement on the limits on the lifetime of the electron compared to previous experiments. A full discussion of this topic can be found in chapter 9, where modest limits are obtained for the current deployment at the SONGS reactor, limited by the backgrounds obtained in a shallow underground site.

The common link between these three physics applications is that they result from an analysis of the low energy spectrum from PPC detectors. A brief discussion of the expected level of background from the usual sources, those from neutron interactions as well as from gamma sources, demonstrates that they are sub-dominant for the Majorana demonstrator experiment below 15 keV (chapter 8.4). It is also pointed out that a potential background from the coherent scattering of Solar neutrinos in the detector is negligible as well. The most important backgrounds are from the cosmogenic activation of ^{3}H, as well as a handful of other isotopes that decay via electron capture. Conservative backgrounds from an expected minimum of 15 days of cosmogenic activation above ground during detector fabrication and transportation are presented. The expected sensitivity of the Majorana experiment to light WIMPs is calculated. Limit projections are also generated for the sensitivity of the Majorana experiment in a pseudoscalar search, suggesting that for the first time an experiment will be able to exceed the limits imposed from cosmological arguments. The projected bounds on the electron decay for the Majorana experiment are also a dramatic improvement over the current leading results.

3.5 Other Advantages of PPC Detectors for Majorana

Several of the advantages of PPC detectors in a germanium $\beta\beta$ decay experiment have been discussed. These include the enhanced rejection of the background from cosmogenic activation of ^{68}Ge; the excellent capabilities for discriminating against multiple site interaction backgrounds from gammas within the germanium crystals; the correspondingly minimal introduction of radioactive backgrounds from signal cables; and, most interestingly, an expanded research program for dark matter searches (WIMP and pseudoscalar) and electron decay modes that can be achieved with low threshold, low noise PPC detectors.

One of the major backgrounds for the $0\nu\beta\beta$ aspect of the experiment is from alphas with degraded energy from natural radioactivity in materials near the detectors that can invade the ROI. The highly segmented N-type detectors are very sensitive to these alphas because of the lack of any significant dead layer on the surface of the crystals. While these detectors should be able to identify the location of these alphas as occurring on or near the surface, the

0.25 mm thick dead layer makes PPC detectors insensitive to this background over most of their surface area and no rejection is necessary. There is a passivated surface of germanium that spans the gap between the detector electrodes which can be very thin and therefore sensitive to these alphas; however, it is very small in the BEGe style PPC detectors due to the wrap around geometry of the lithium-drifted layer.

The lithium-drifted layer also allows for relatively easy handling as is illustrated in figure 2.5. The same cannot be said for N-type detectors. PPC detectors are far simpler in a number of ways than the highly segmented N-type detectors. The manufacture of PPC detectors is also less expensive per kilogram of germanium. The characterization of individual detectors is easier and requires less time. The data acquisition is simpler for PCC detectors, requiring only one channel, compared to as many as 60 for the highly segmented N-type detectors. Also because of the dramatic reduction in the number of channels, the thermal load that is introduced by the electronics is far less with PPC detectors. All of these advantages make the choice of PPC detectors for the Majorana experiment a natural one.

CHAPTER 4

MEASUREMENT OF THE QUENCHING FACTOR FOR SUB-KEV GERMANIUM RECOILS

This chapter describes a direct measurement of the quenching factor for individual nuclear recoils in a high purity germanium (HPGe) detector. It is the first such measurement for sub-keV recoils. Knowledge of the quenching factor, defined as the fraction of the nuclear recoil energy that is detectable as ionization, is of vital importance for experiments for which the primary signature is a low energy nuclear recoil. The measurement described below was performed in support of the coherent neutrino scattering experiment, as well as the light WIMP search, for which there is a large dependence of the detectable interaction rate on the value of the quenching factor. While there are previous measurements of the quenching factor in germanium detectors, they are either for higher energy recoils [Shutt et al., 1992; Benoit et al., 2007], or use indirect techniques that may be subject to systematic effects [Chasman et al., 1968; Jones & Kraner, 1975; Chasman et al., 1967; Jones & Kraner, 1971]. A review of these measurements is presented. Also covered is the design, construction and characterization of a facility at the Kansas State University Triga Mark II research reactor that was used to produce low energy nuclear recoils [Barbeau et al., 2007a]. The resulting direct measurements of the quenching factor for individual sub-keV nuclear recoils are presented.

4.1 The Quenching Factor for Nuclear Recoils

4.1.1 Lindhard Theory

For nuclear recoils in the energy range of 1 keV to 1 MeV the ionization deposited in a germanium semiconductor is significantly less than the total energy lost by the particle.

Typically, the fraction of recoil energy that is deposited as ionization is of the order of 10–25%, where the balance is dissipated in the form of heat. The loss of energy by ions in matter as modeled by the Lindhard theory [Lindhard & Scharff, 1961] is described by the equation:

$$E_{ioniz} = \frac{E_{rec}\ k\ g(\epsilon)}{1 + k\ g(\epsilon)} \tag{4.1}$$

with

$$\epsilon = 11.5\ E_{rec}\ Z^{-7/3},$$

$$g(\epsilon) = 3\epsilon^{0.15} + 0.7\epsilon^{0.6} + \epsilon$$

$$k = 0.133\ Z^{2/3} A^{-1/2}$$

$$Q = \frac{E_{ioniz}}{E_{rec}}$$

where E_{ioniz} is the ionization energy deposited (in keV), E_{rec} is the recoil energy in keV, Q is the quenching factor, Z is the atomic number and A the atomic mass. For germanium semiconductor detectors, the value of k is calculated to be 0.157. In regions where the quenching factor is not well known, the relationship has been parameterized by letting the value of k float to provide a local fit to data over selected energy windows [Jones & Kraner, 1975]. This approximation is sufficient for regions that are not thoroughly studied or understood, such as for sub-keV recoils.

4.1.2 Previous Measurements

Several measurements have been made for germanium recoils in germanium detectors. Most are at high energies, above 10 keV recoil energy, which is well outside the region of interest for the proposed low energy experiments for PPC detectors. Some of these are plotted in figure 4.17. The highest energy points, from [Messous, 1995], were directly measured by using elastic neutron scattering. The measurement suffers when the ionization produced from indirect recoils is insufficient to surpass the detector threshold. To get around this limitation, experiments using compound interactions have been performed that measure the extra ionization deposited from a process involving a high energy coincident gamma ray. The measurement from [Jones & Kraner, 1971, 1975] used inelastic neutron scattering, detecting the sum of the ionization produced from the recoiling nucleus and the emitted gamma. The lowest energy point in figure 4.17 is also a compound measurement [Jones & Kraner, 1975]. In this case, thermal neutrons were captured on ^{73}Ge nuclei, which subsequently decay with the emission of a 68.8 keV gamma. The nucleus recoils with 254 eV, depositing energy in the germanium crystal along with the gamma. The quenching factor is determined by measuring the shift in the position of the peak. While these two indirect measurements probe the quenching factor at low energies, they may be prone to systematics errors. These uncertainties were avoided by performing a new quenching factor measurement that exposed the low threshold PPC-1 detector to a monochromatic 24 keV neutron beam, extending the low energy reach of direct neutron elastic scattering measurements.

4.2 The 24 keV Neutron Beam

A direct measurement of the quenching factor for low energy nuclear recoils has been difficult because of the kinematics of neutron scattering. For the usual toolbox of neutron sources (AmBe, ^{252}Cf, D-D or D-T guns) one must measure extremely forward scattered neutrons in order to produce low energy recoils with narrow scattering angles. The measurements are also complicated by using sources with a broad spectrum of neutron energies. The best way to perform the measurement is to use a high flux, mono-energetic neutron beam, where low energy recoils can be produced for large neutron scattering angles.

This was achieved with the construction of a 24 keV neutron beam by building a neutron

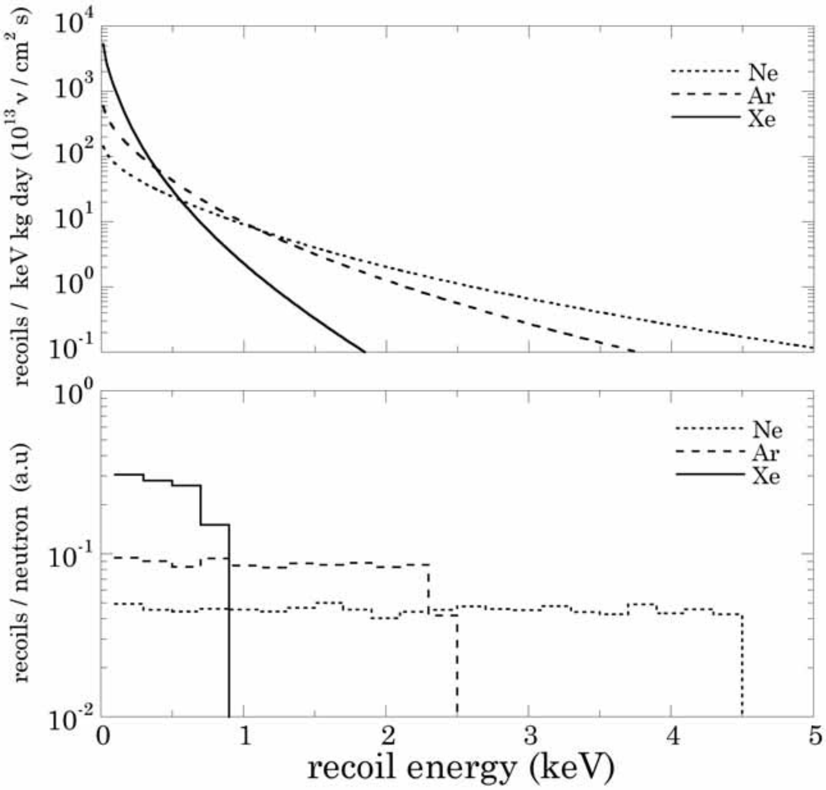

Figure 4.1: Comparison of the nuclear recoil spectra from coherent scattering of reactor anti-neutrinos (top) and from from the 24 keV neutrons (bottom) for several targets. The neutron scattering spectra were produced using MCNP-polimi [Pozzi et al., 2003]. The beam was designed to mimic the energy range of recoils from neutrinos in order to calibrate the quenching factor at low energies. Figure courtesy of J. I. Collar.

transmission filter at the Kansas State University Triga Mark II research reactor. The beam was fully characterized using a variety of detectors in order to build confidence in the purity of the neutron energy and the quality of the collimation. The full facility utilizes a goniometric table and a 95% ^{6}Li enriched ^{6}LiI(Eu) scintillator, allowing the selection of neutron scattering angles, and providing a robust measurement of individual neutron scatters. It is described below.

4.2.1 The Fe Filter

The transmission filter technique takes advantage of narrow anti-resonances in the neutron cross-sections, for materials like Si or Fe [Nilsson, 1983], to produce beams of monochromatic neutrons. These "dips" are a result of zeroes in the s-wave scattering amplitude from the Ramsauer-Townsend effect; an example can be seen for ^{56}Fe in figure 4.2. The filters are typically used with high flux neutron sources that have a broad range of neutron energies, such as research reactors. Only neutrons with energies at the anti-resonances pass through the filter without scattering, resulting in a beam of neutrons with narrowly defined energies at the anti-resonances. In the case of Fe filters there is a dominant band at 24 keV ($\pm$ 2 keV FWHM), although there are also a few sub-dominant bands at slightly higher energies. The 24 keV component of the resulting neutron beam is ideal for producing nuclear recoils that mimic those produced from coherent neutrino-nucleus scattering, as depicted in figure 4.1. In addition, Fe is a good material for shielding the copious number of gammas from the reactor core, alleviating any gamma contamination of the beam. Aluminum post-filters are commonly used with Fe to reduce the contamination of the beam from neutrons that pass through the higher energy "dips" by utilizing the higher neutron scattering cross-section in aluminum at these energies. For this experiment a Ti post filter was also used which has a higher cross section near 24 keV than at other energies (figure 4.2). It works in the opposite manner as the Al filter, preferentially removing the 24 keV neutrons, while leaving the other components relatively untouched and provides a method to "turn off" the 24 keV component of the beam. This capability is used to perform residual measurements by subtracting the signal measured with the beam "off", such that the remaining signal is due only to 24 keV neutrons.

The filter design was centered around an Fe rod with a very low impurity concentration. Impurities in the Fe have the effect of reducing the transmission of the 24 keV neutrons and,

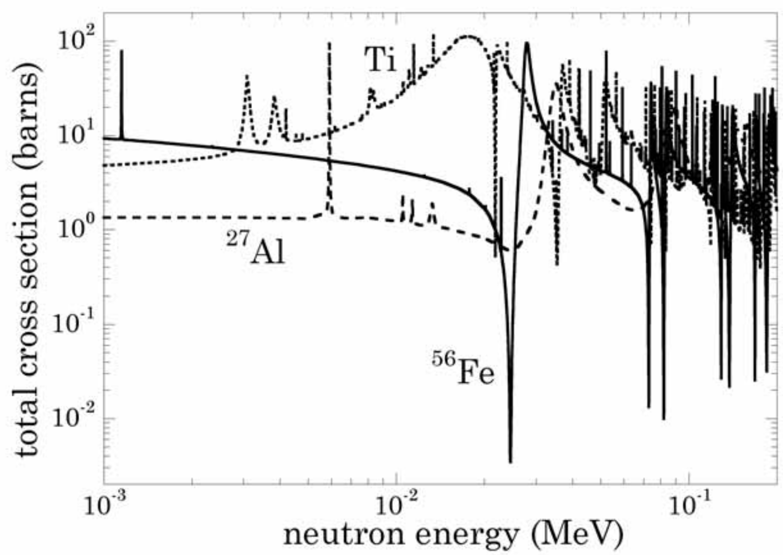

Figure 4.2: Neutron cross sections that are important for the 24 keV Fe transmission filter are shown. The prominent "dip" in the ^{56}Fe scattering cross section (Ramsauer-Townsend effect) produces the 24 keV beam of neutrons, while the high cross section of Aluminum at higher energies serves to improve the purity of the beam. A thin titanium post-filter is used to "turn off" the 24 keV component while leaving other neutron energies and gamma backgrounds unaltered [Nilsson, 1983].

therefore, the total flux from the beam. This increased transmission allowed the rod to be long and narrow, in comparison to typical neutron filters [Nilsson, 1983], while maintaining a large neutron throughput resulting in a more collimated beam. The rod (2.5 cm diam. 60 cm long) was tapered to prevent streaming along the seams of the beam pipe. It is surrounded by borated polyethylene, Pb gamma shielding and Cd neutron absorber, encased in a steel liner (figure 4.3). The neutron moderator and absorber prevent the scattered neutrons from exiting the port, while the Pb shield reduces gamma backgrounds from reactor and (n_{th}, γ) backgrounds. The steel liner facilitates rapid installation or removal of the filter.

The filter is used in a tangential port, aimed away from the center of the reactor core. This has the effect of softening the spectra of the incident neutrons and gammas, increasing the neutron flux from the beam while also reducing backgrounds from gammas. Simulations of the filter using MCNP4b [Briesmeister, 1993] were performed based on measurements of the spectral neutron flux at the exit of the unfiltered port. The simulation results, seen in figure 4.3, indicate that a high flux of 24 keV neutrons can be achieved with this filter at a relatively low power reactor (240 kW maximum). It should be noted that an unforeseen high gamma background (50 mRem/hr) was measured at the concrete wall. The origin of these gammas is from neutrons scattered in the back of the filter that moderate near the outside edge of the concrete wall. This background was overcome by the addition of 50 cm of concrete and Pb shielding around the beam exit.

4.2.2 Beam Characterization

The beam was characterized using several detector technologies that include measurements with a "Benjamin" spherical proton-recoil spectrometer, a 95% ^{6}Li enriched ^{6}LiI(Eu) scintillator, a ^{3}He ionization tube, and a standard HPGe detector. The proton-recoil spectrometer is an avalanche wire chamber filled with hydrogen gas used for measurements of low energy

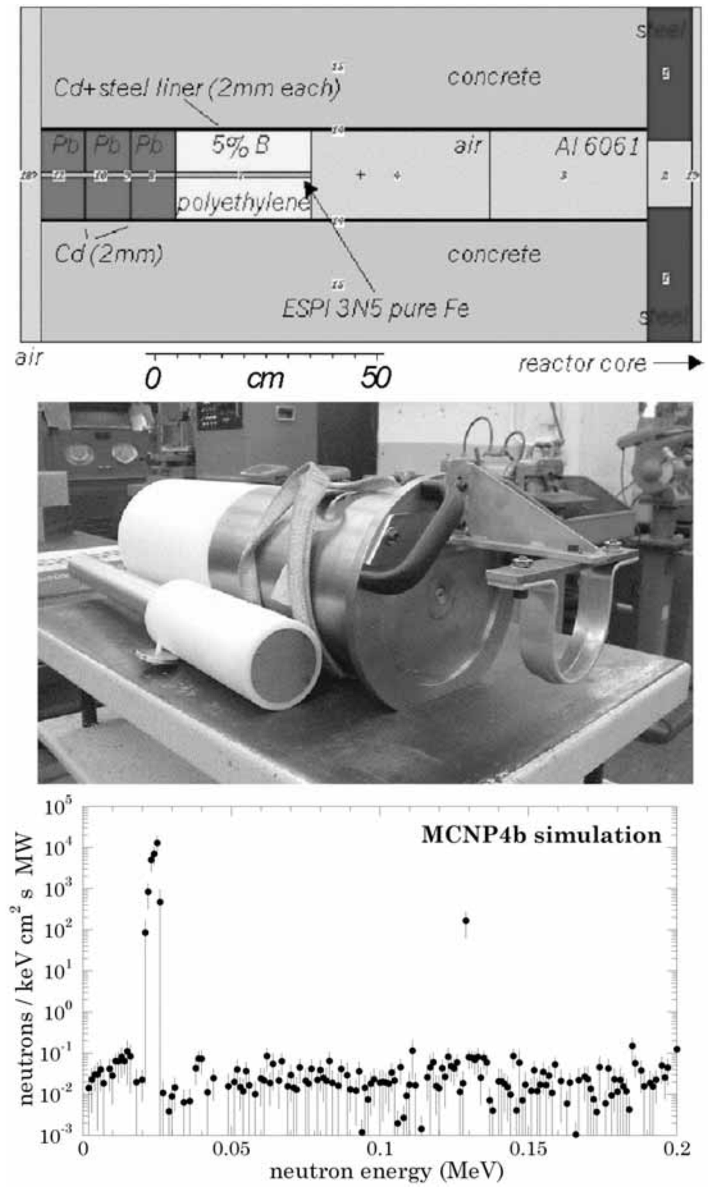

Figure 4.3: The Fe filter, shown in the picture, was built at the University of Chicago and used at the Kansas State University Triga Mark II research reactor. The geometry of the filter situated in the tangential neutron port is shown (top). The filter, shown with the titanium post-filter (middle), is easily removable from the port. A laser pointer can be attached to assist in alignment of the beam with the detector under test. An MCNP4b [Briesmeister, 1993] simulation of the neutron flux (bottom) is shown as well. Figures courtesy of J. I. Collar.

neutrons. Neutrons scatter, producing proton recoils which ionize the gas and deposit energies up to that of the incoming neutron. While this is not a direct measurement of the neutron spectrum, it is possible to de-convolve the spectral response using the SPEC-4 code [RSICC, SPEC-4]. Recoils as low as 1 keV are identifiable without encroachment of gamma backgrounds. The device is ideal for measurements in these environments because of its response to low energy neutrons its and minimal sensitivity to environmental gammas. The ^{6}LiI(Eu) scintillator, approximately 1 cm^{3}, allows fine spatial measurement of the neutron flux. Neutrons moderate in the scintillator until they are captured via the ^{6}Li(n, α) reaction. The resulting reaction deposits 4.78 MeV, of which 3.1 MeV is observed as scintillation. The ^{3}He detector is an ionization chamber filled with 3 bar of gas. In this case, the neutron interaction is via the ^{3}He(n, p) capture process. The decay products, a proton and tritium nucleus, ionize the gas in the chamber depositing 765 keV. The HPGe detector is a portable P-type coaxial detector that was used to measure gamma rays emanating from the beam port. It was also used to help characterize the neutron flux by way of (n, γ) reactions in the detector. Care was taken not to expose the germanium crystal to a large fluence of neutrons to limit damage to the crystal, which can harm charge collection.

Beam Profile and Flux

Measurements of the angular divergence of the beam were made with the proton-recoil spectrometer. The neutron interaction rate was measured at locations along the beam axis from which it was determined that the 24 keV neutron beam diverges with an equivalent point source located at -36 cm $\pm$ 4.8 cm into the filter, with the exit point defined as the origin. This is in good agreement with the estimate from neutron optics of -35.9 cm, derived based on the filter geometry. The maximum beam intensity at the exit point of the Fe filter, as measured by the proton-recoil spectrometer, is 7.9×10^{4}($\pm$10% stat. $\pm$15% sys.) n cm^{-2}

s^{-1} MW^{-1} for the full spectrum of neutron energies.

The detector irradiation point, where the detector to be calibrated is positioned, is at +110 cm from the exit point of the filter. The proton-recoil spectrometer was also placed at several off-axis lateral positions at +110 cm to determine the spread of the beam (6 cm FWHM). A similar, more precise, measurement was also performed with the 95% ^{6}Li enriched ^{6}LiI(Eu) scintillator. The scintillator was surrounded by 0.5 cm of Cd to reduce the sensitivity of the detector to ambient thermal neutrons. Neutron flux measurements of the 24 keV component were performed on a 10×10, 2-D grid by counting the rate difference between runs with the Ti filter on and off. The results, displayed in figure 4.4, confirm the measurements with the proton-recoil spectrometer with a measured spread of 5.9 cm FWHM. The flux was determined by comparing the measured rates to simulated detection efficiencies for 24 keV neutrons using an MCNP4b [Briesmeister, 1993] simulation. The measured 24 keV neutron flux and spread are used in simulations for the interpretation of the quenching factor measurements.

Beam Contaminations

The optimal thickness of the aluminum post-filter, which maximized beam purity while maintaining a high flux of 24 keV neutrons, was determined using the proton-recoil spectrometer. Measurements performed at the detector irradiation point (+110 cm) can be seen in figure 4.5, both with and without a 10.7 cm Al filter. Recoils from neutrons with energies greater than 24 keV are clearly reduced with the application of the aluminum. The relationship between the purity and intensity of the beam is depicted in the inset for increasing thickness. For the calibrations that follow, the aluminum post-filter thickness was chosen to be 2.5 cm, which resulted in a 24 keV beam that was 88% pure. The proton-recoil spectrometer was also used to measure the capability of the 1.25 cm Ti post-filter for "turning off" the 24

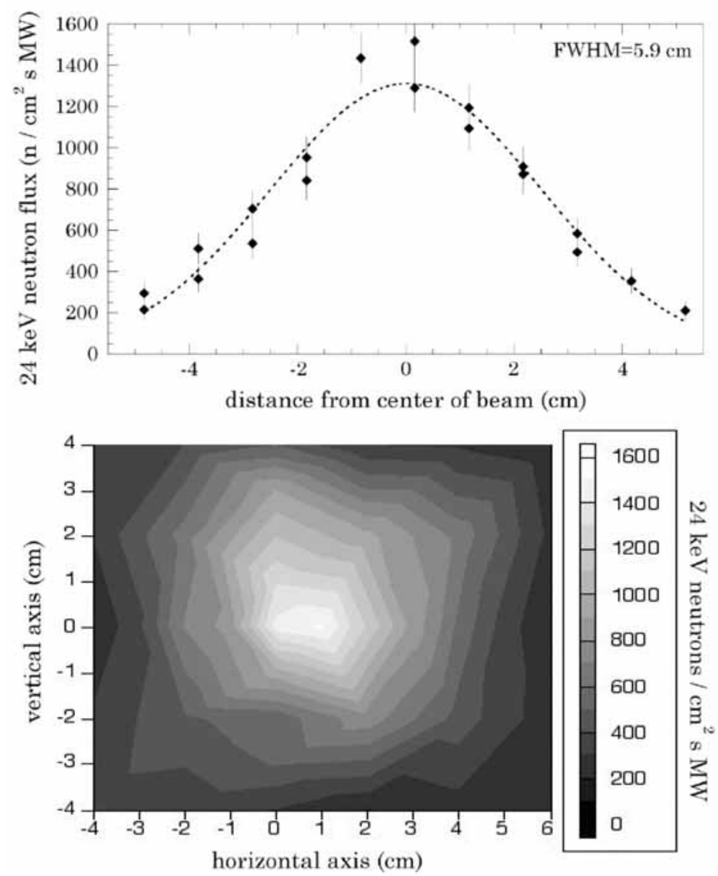

Figure 4.4: The profile of the 24 keV component of the neutron beam was measured at the detector irradiation point by a 1 c.c. enriched ^{6}LiI(Eu) scintillator. The flux and profile are used for Monte Carlo simulations of the quenching factor measurements.

keV neutron component of the beam, see figure 4.6 (top). Shown are the spectra with and without the Ti post-filter, as well as their de-convoluted spectra, illustrating the factor of 20 reduction in the number of recoils from the 24 keV neutrons and the minimal effect on the other beam components. This reduction was in good agreement with expectations from simulations. Also included is a renormalized spectrum from a 3 mCi ^{88}Y gamma source demonstrating the absence of significant gamma backgrounds that would get in the way of the de-convolution. The Ti post-filter only affects the 24 keV component of the spectra, neither changing the high energy neutrons nor the gamma backgrounds.

A similar measurement was performed with the ^{3}He detector, using it as a rudimentary neutron spectrometer. This is made possible by the still significant neutron capture cross-section at 24 keV. The ionization energy deposited in the helium gas is the sum of the release from the capture reaction and the kinetic energy of the neutron. The effect can be seen in figure 4.6 (bottom) both with and without the Ti post-filter. A renormalized spectrum from the ^{3}He(n, p) reaction for a field of pure thermal neutrons is also overlaid to illuminate the effect. The inset is a plot of the neutron energy spectrum after the exothermic energy of the reaction has been subtracted, leaving only the contribution from the kinetic energy of the neutrons in the beam. Evident is the capability of the Ti post-filter for removing only the 24 keV component of the neutron beam, while leaving the rest of the neutron energies untouched. The unfolded spectra from the proton-recoil spectrometer and the ^{3}He detector with the Ti filter removed also illustrate the monochromatic nature of the beam. Other peaks at 72 keV and 128 keV, which are typical of Fe filters, do not constitute a large fraction of the neutrons in the beam. Nevertheless, it is important that they are untouched by the Ti post filter so that residual measurements can be performed.

The effect of the Ti post-filter on the gamma contaminations of the beam was measured with the HPGe detector, located at the detector irradiation point. The overall gamma flux was reduced by only 6%, as seen in figure 4.7, as is expected for Ti that is only 1.25 cm

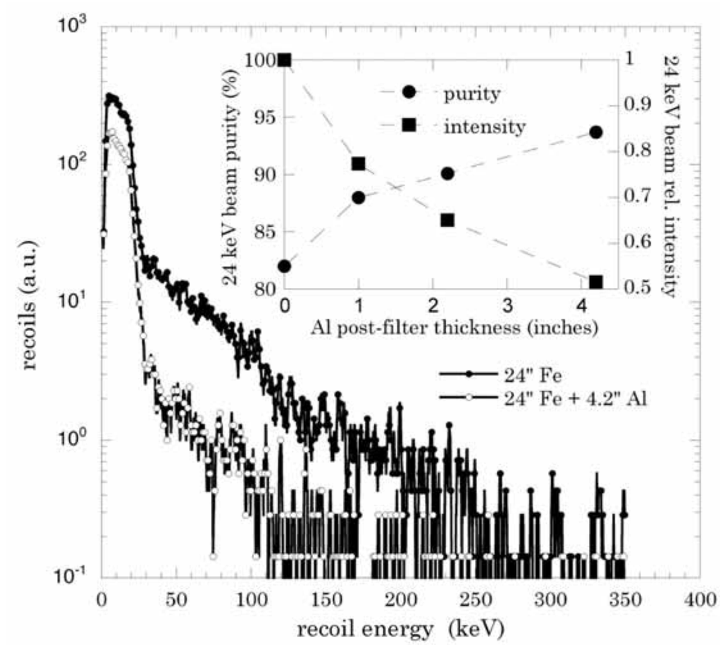

Figure 4.5: Spectra from a spherical "Benjamin" proton-recoil spectrometer exposed to the beam from the Fe filter is shown with and without an Al post-filter. The effect of increasing purity on the component >24 keV is evident. The inset quantifies the increasing purity, as well as the loss of 24 keV neutrons, with increasing Al thickness. Figure courtesy of J. I. Collar.

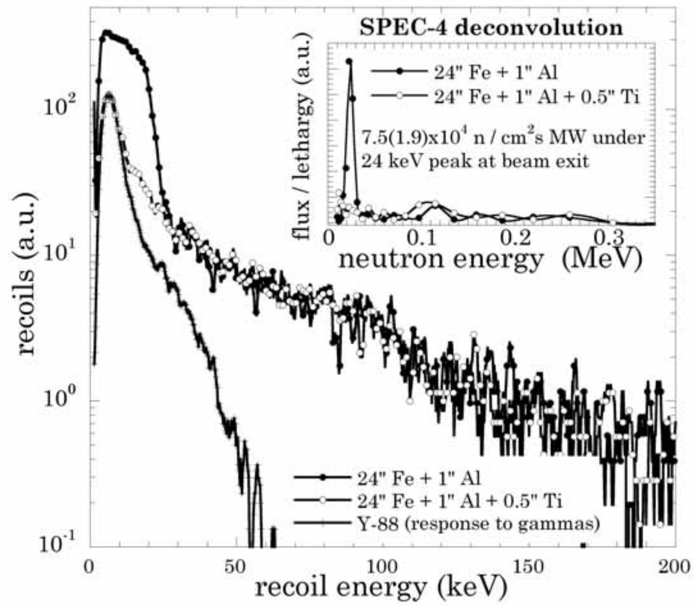

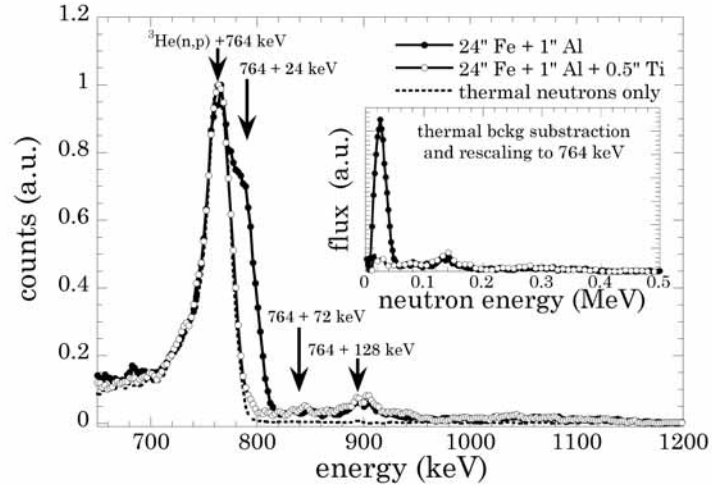

Figure 4.6: These figures primarily show the effect of the Ti post-filter on the 24 keV component of the neutron beam. Top: the spectrum from a proton-recoil spectrometer with the Ti filter (open circles) and without the Ti filter (closed circles). The effect of reducing only the 24 keV neutrons can be seen in the de-convoluted spectrum (inset). Bottom: similar measurements were performed with a ^{3}He ionization tube. Again, the inset depicts the unfolded spectra of neutron energies, showing the effect on the 24 keV component. Figure courtesy of J. I. Collar.

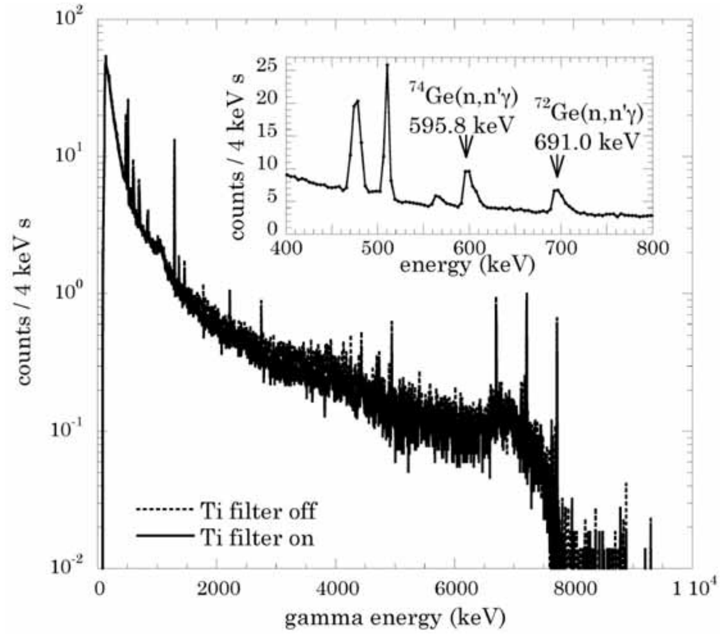

Figure 4.7: Spectrum measured by a HPGe at the detector irradiation point (+110 cm) indicating a slight reduction (<6%) of gammas with the application of the Ti post-filter. This is also used to measure neutron fluxes at thermal energies via a (n_{th}, γ) peak and energies > 691 keV via an inelastic neutron scattering peak. Figure courtesy of J. I. Collar.

thick. The asymmetric peak in the spectrum at 691.0 keV from inelastic neutron scattering, ^{72}Ge(n, n'γ), indicates that the neutron flux at energies >691 keV is less than 100 n cm^{-2} s^{-1} MW. Also, using the thermal neutron capture peak in Ge at 139.9 keV, the thermal neutron flux was found to be $\sim$ 30 n cm^{-2} s^{-1} MW. Finally, the gamma dose at the detector irradiation point was measured with a Geiger counter to be 0.3 mRem/hr when the reactor was at full power (240 kW), demonstrating the good gamma shielding property of the filter.

4.2.3 The Neutron Scattering Facility

The quenching factor measurement isolates specific recoil energies by selecting events with scattered neutrons that have a recoil angle θ_n. A large, ^{6}Li enriched, ^{6}LiI(Eu) scintillator was mounted on a goniometric table and used to detect the scattered neutrons as well as trigger the data acquisition of the target detector being tested. A picture of the setup can be seen in figure 4.8 (top). The scintillator is thick enough to moderate low energy neutrons and efficiently detect them via the ^{6}Li(n, α) reaction. A simulation of the depth of the capture reaction for 24 keV neutrons is shown in 4.8 (bottom) for the larger ^{6}LiI(Eu) scintillator, illustrating the high efficiency for detecting these moderate energy neutrons. At the same time, the peak energy of the capture reaction is large enough (3.1 MeV) that events from reactor related gammas are rarely confused for neutrons. Because these crystals are very sensitive to thermal neutrons, which are prevalent in the reactor bay, they were surrounded by borated silicon (Boron-Flex). This was sufficient to reduce the background neutron capture rate in the scintillator to $\sim$100 Hz with the reactor at full power (240 kW). While Boron-Flex does not significantly attenuate the 24 keV neutrons, it is nevertheless accounted for in the Monte Carlo simulations of the neutron scattering experiment.

There were two ^{6}Li enriched, ^{6}LiI(Eu) scintillators used to capture the scattered neutrons. The first, a refurbished crystal (5 cm diam. $\times$ 7.5 cm long) was used for most of the initial characterizations of the scattering experiment. A second, custom-grown, thinner crystal (5 cm diam. $\times$ 1.5 cm length), was purchased and used for the measurements of the germanium quenching factor because it had an improved energy resolution. The narrower energy window for thermal neutron captures, combined with the smaller crystal size, reduced the number of background triggers from gammas. Unlike the earliest detector, which was appropriated and refurbished from another experiment, the level of ^{6}Li enrichment was well known to be 95% for the second crystal, an important handle for accurately predicting the total interaction rate. A brief inspection of figure 4.8 (bottom) indicates that the smaller crystal is about half as efficient, though the significant drop in gamma backgrounds more than makes up for the loss in rate.

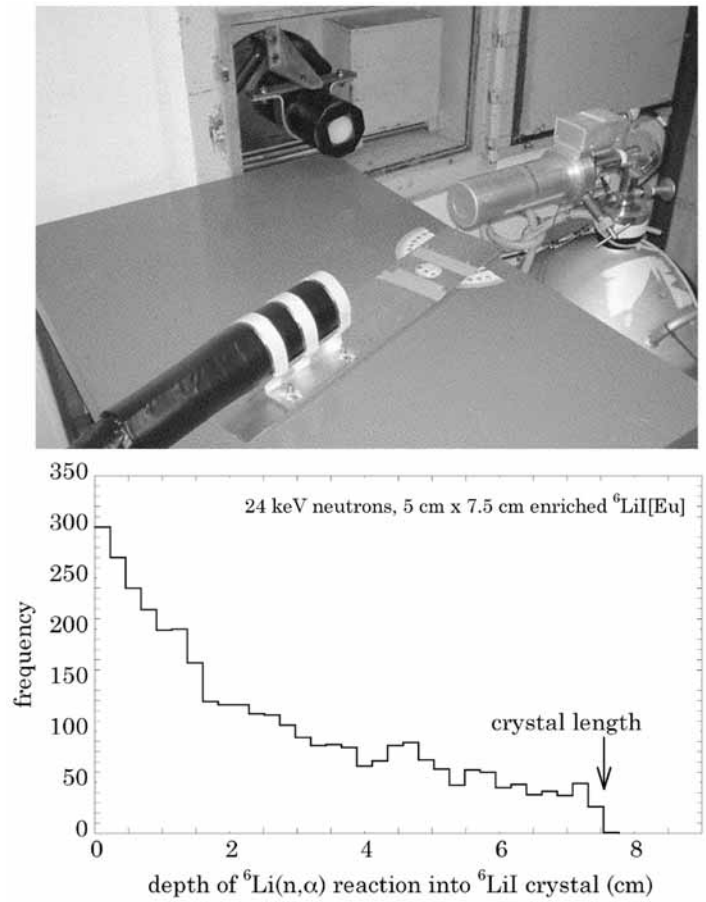

Figure 4.8: Top: neutron scattering setup, with detector, goniometric table, and ^{6}LI enriched ^{6}LiI(Eu) scintillator, which selects neutron scatters at chosen recoil angles and triggers the DAQ. Bottom: a simulation of the depth of interaction for ^{6}Li(n, α) of 24 keV neutrons in the ^{6}LiI(Eu) scintillator. Figure courtesy of J. I. Collar.

4.2.4 Tests with Plastic Scintillator

The neutron scattering setup was tested by repeating the classic measurement of the quenching factor for low energy proton recoils in plastic scintillator that validated the MACRO experiment as a potential monopole detector [Ficenec et al., 1987]. For this test, a small cube (0.5 cm^3) of BC-404 plastic scintillator, with the highest light yield available, was attached directly to a PMT and placed at the detector irradiation point. The data acquisition was triggered by events in the ^{6}LiI(Eu) scintillator for several scattering angles. Several important characteristics of the scattering experiment are able to be identified.

When a signal in the ^{6}LiI(Eu) scintillator triggers the data acquisition, the amplitude of the signals in both scintillators as well as the time difference (Δt) between the two signals are recorded. A scatter plot of the time separation versus ^{6}LiI(Eu) amplitude for these events with the Ti post-filter in place (bottom), and removed (top), can be seen in figure 4.9. The diffuse distribution of points is caused by spurious events between the detectors. It is apparent that the vast majority of events are from gamma interactions, but a population of neutron captures can be seen at 3.1 MeV in the Ti-off plot. A slight excess can also be seen in the Ti-on plot which are likely either from higher energy neutrons that are not removed by the post-filter or from thermal neutrons in the reactor bay. Also apparent in both the Ti-on and Ti-off scatter plots is the band of true coincidences between the detectors centered around Δt = 0. It is clear from the Ti-on scatter plot that there are a large number of gamma coincidences which are likely due to Compton scattering off the plastic into the ^{6}LiI(Eu) crystal. In the analysis, a cut is placed on the energy of events in the ^{6}LiI(Eu) so that only those within a 3σ energy window about the neutron capture peak are accepted. However, there are still coincident gamma interaction accidental gamma coincidences that are not removed with this cut.

Histograms of the time separation between proton scatters in the plastic and the capture

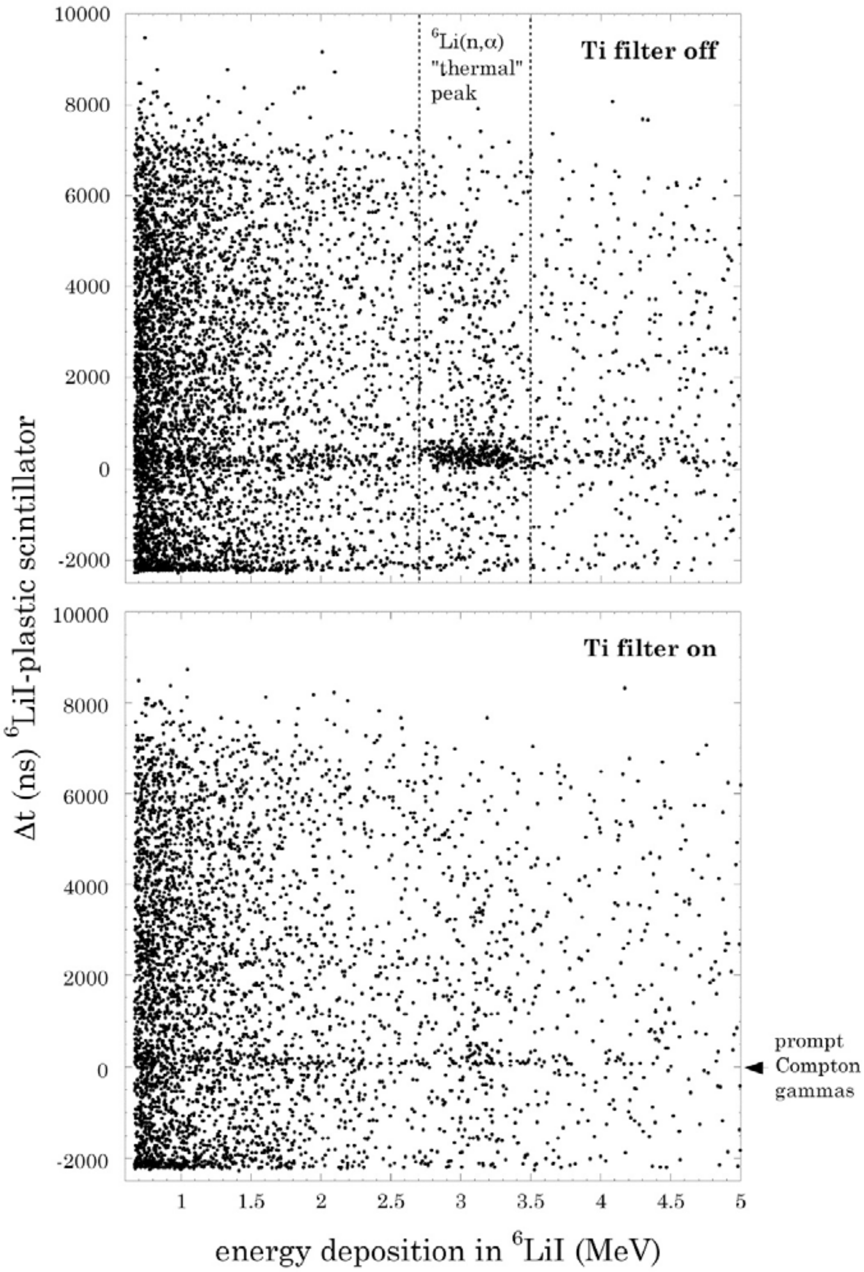

Figure 4.9: The time separation between events in a plastic scintillator and the ^{6}LiI(Eu) neutron detector is plotted versus the energy deposition that was measured in the neutron detector. The excess population of coincidences at ~ 3.2 MeV with the Ti filter is a nice demonstration of the facility. A population of coincidences from Compton scattered gammas is also evident.

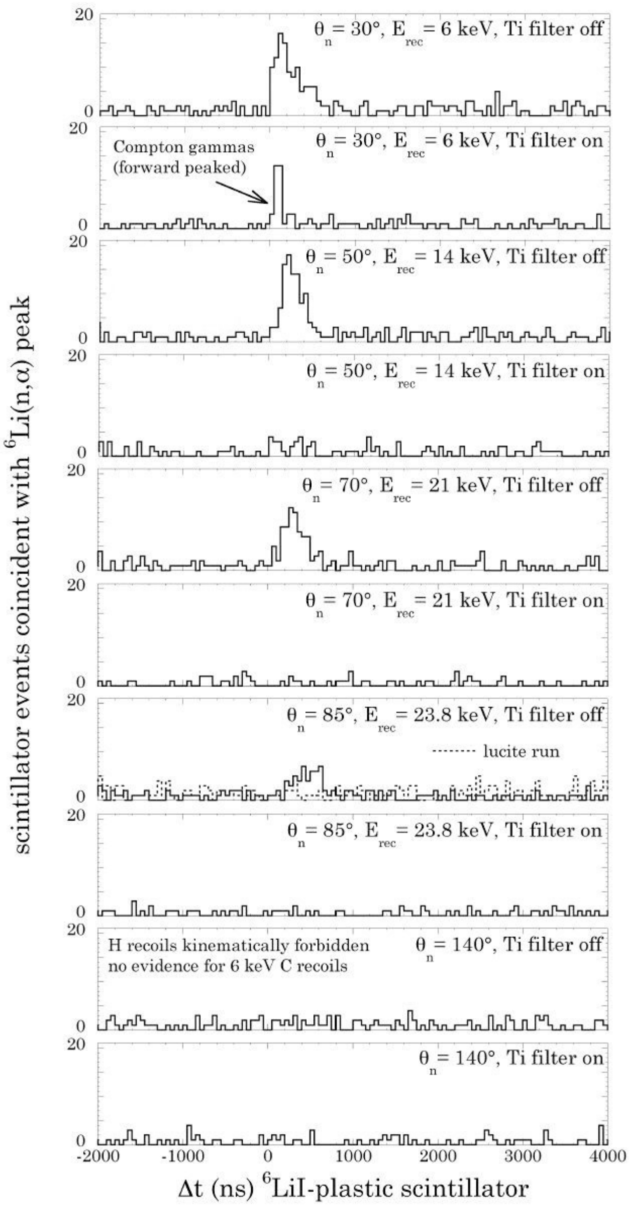

Figure 4.10: Histograms of the time separation of events between a small plastic scintillator and the ^{6}LiI(Eu) neutron detector for several recoil angles. The effect of the Ti filter at reducing neutron scatter coincidences is clear. Also, for small recoil angles, a population of forward peak Compton scattered photon events can be seen. For recoil angles $>90°$, single neutron scatters off hydrogen is kinematically forbidden. Also depicted, for an angle of 85°, was a measurement performed with a non-scintillating acrylic target of the same dimensions as the actual scintillator, demonstrating that the neutron scatter coincidences are indeed recoils off the plastic scintillator and not the Cerenkov light emission in the PMT glass envelope.

of the neutron for several neutron scattering angles θ_n can be seen in figure 4.10. Much of the physics of this setup is represented in these histograms. To begin with, the excess events between Δt = 0–1000 ns defines the time window for coincidences for this target. It is clear by the uniformly scattered background that there are still plenty of accidental coincidences that fall within this coincidence window. By selecting only events that fall within the time coincidence window we can suppress this accidental background. In addition, it is possible to characterize it with events that are outside the coincidence window (anti-coincidences) to account for those that contaminate the coincidence window see 4.3.2. The only significant difference between the Ti off/on, configurations is the existence of 24 keV neutrons. Clearly then, the broad excesses of events within the coincidence window at the various recoil angles θ_n are a result of 24 keV neutron scatters. For $\theta_n = 30°$ a sharp excess of events remains in the Ti-on histogram when the 24 keV neutron scatters have been removed. The prompt nature of these coincidences suggests that they are Compton scattered gammas between the two detectors. The source is likely the beam port where the small gamma component of the beam is forward peaked at the smaller recoil angles, a characteristic of Compton scattering. The dominant scattering is likely off the glass envelope of the PMT which produces only a handful of photons via Cherenkov radiation, as only the most forward scattered photons in the plastic scintillator would cause the signal to be out of range of the DAQ. While it is possible to eliminate these events by a judicious reduction of the coincidence window for the plastic scintillator, this may not be possible for detectors which have slower developing signals. Therefore, it is wise to characterize these events separately from the accidental backgrounds.

Returning to the 24 keV neutron scatter coincidences, it can be seen in 4.10 that the mean Δt increases with increasing θ_n, a result of the slower velocities of the neutrons after scattering. Also folded into the Δt distribution for coincident scatters is the effect of the neutron straggling time in the ^{6}LiI(Eu) scintillator. This last effect is demonstrated in figure

4.11, which shows the good agreement of the measured straggling to that expected from an MCNP-Polimi simulation [Pozzi et al., 2003]. Also, for scattering angles larger than 90°, no population of excess coincidences is measured, a result of the kinematics of neutron-proton scattering. Because plastic scintillator consists of both hydrogen and carbon nuclei, carbon recoils could in principle be observed, but this is very unlikely given the extremely low energy recoils. As a further check, the plastic scintillator was replaced by an identical sample of Lucite for a recoil angle of $\theta_n = 85°$, with Ti-off. As expected, there are no 24 keV neutron coincidences because the Lucite does not scintillate, instilling confidence that the excess coincidences are due to neutron recoils in the plastic scintillator. Finally, good agreement was found between the measured rate for hydrogen recoils compared to the expected rate from the Monte Carlo (figure 4.11 inset). The simulation input includes the beam intensity and profile, as derived from the beam characterization discussed earlier in this chapter.

There are a few characteristics of the neutron scattering experiment which are key for a robust background-free measurement of quenching factors. Firstly, candidate events for 24 keV recoil coincidences must be selected by placing a 3σ window about thermal neutron capture peak in the ^{6}LiI(Eu) spectrum. For the germanium measurement, the number of gamma backgrounds included in this cut was reduced by replacing the neutron detector with the thinner crystal, dramatically improving the energy resolution. Second, a suitable time coincidence for Ti-off runs must be chosen based on the time response of the target detector. Any accidental coincidences included in this time window can be characterized and removed using anti-coincident time windows. Finally, contributions from true coincidences that are not from 24 keV neutron scattering, such as gammas or higher energy neutrons, can be subtracted using the Ti-on data.

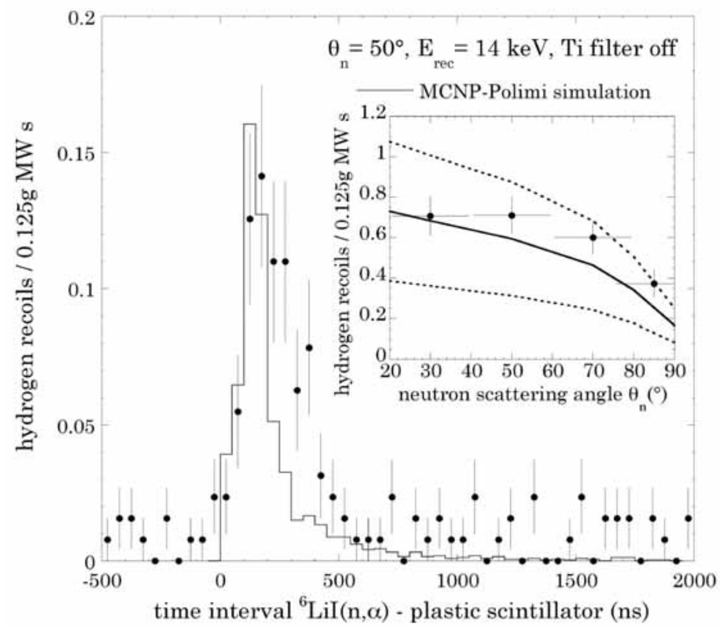

Figure 4.11: The simulated straggling time of 24 keV neutrons in the enriched ^{6}LiI(Eu) scintillator is compared to measured data. Good agreement is found. Also shown, in the inset, is a comparison of the expected number of recoils to what was measured, also finding good agreement. The simulations take into consideration the beam intensity and profile, as derived from the beam characterization described in this chapter. Figure courtesy of J. I. Collar.

4.3 Quenching Factor Measurement

The quenching factor was measured with the PPC-1 germanium detector at the UofC-KSU facility for recoil energies between 0.6 keV–1.2 keV. The quenching factor was determined by comparing the expected recoil energy at specific neutron scattering angles to the ionization measured for neutron scattering coincidences from 24 keV neutrons. MCNP-Polimi [Pozzi et al., 2003] simulations were used to determine the energies deposited for coincident scatters. The signal from the 24 keV excess is contaminated by several backgrounds related to the operation of the neutron beam; the removal of these backgrounds is described below. One of these backgrounds, from isotropic scattering of the 24 keV neutrons that are accidentally coincident with the trigger, is useful as a composite measurement of the quenching factor for the full range of recoil energies. The spectrum of these recoils was compared to that expected from a simulation, providing a final crude measurement of the quenching factor for the lowest energy recoils.

4.3.1 Description of Data

In order to optimize the noise performance of PPC-1, the signals from the detector preamplifier were sent through a spectroscopy amplifier with triangular shaping and a 10 μs shaping time. The raw PMT signals from the ^{6}LiI(Eu) detector were preamplified and sent through a spectroscopy amplifier with a characteristic shaping time of 12 μs, reflecting the long decay time of the scintillation (6 μs) of ^{6}LiI(Eu). Both signals were digitized and recorded by a National Instruments scope card, in 400 μs traces. The digitizer was triggered by a discriminator placed on the ^{6}LiI(Eu) scintillator signal, with a threshold placed just below the thermal neutron capture peak at 3.1 MeV. The DAQ trigger rate was $\sim$4 Hz, which is much larger than the expected rate of neutron recoils, suggesting that there are many backgrounds that must be accounted for.

Data taken for recoil angles of 121° and 151°, where the scintillator was placed 18 cm from the center of the germanium crystal in PPC-1. This was changed to 15 cm for a measurement at 99° recoil angle to increase the solid angle for detecting neutron recoils, and thus the rate of scatters. The reactor was operated at 10% of maximum power in order to reduce the rate of spurious coincidences from reactor related backgrounds and avoid damage to the germanium crystal lattice. Data was recorded at each angle for 170 minutes with the Ti post-filter off and then repeated with the Ti-filter in place.

There were several short runs taken with the signal from a pulser sent through both preamplifiers test inputs in order to establish the appropriate time window for coincidences between detectors. The pulser data also serves as an in-situ measurement of the PPC-1 detector noise and characterization of the pedestal position and width.

4.3.2 Analysis Overview

The goal of this experiment is to measure the ionization produced by 24 keV neutrons at several scattering angles, comparing it to the total energy of the nuclear recoil. The first step in the analysis is to identify neutron recoils between the detectors. This is achieved by selecting only events within a 3σ window about the thermal neutron capture peak in the ^{6}LiI(Eu) scintillator. The signals are required to be coincidences, therefore the signal amplitude is taken as the maximum height above the baseline of the PPC-1 waveform within a time window of 12 μs about the DAQ trigger position.

Unfortunately, even after the data reduction from the thermal neutron peak cut, there are still many spurious backgrounds that must be eliminated. The vast majority of events under the thermal peak are not from true neutron scatters, but are instead from the capture of environmental neutrons or from gammas that deposit energy within the 3σ window. It must be kept in mind that the experimental site, a reactor bay, is a high-background environment, and that it is impossible to shield the ^{6}LiI(Eu) detector beyond the addition of Boron-Flex. Most triggers occur when there is no radiation induced signal in the germanium detector. Therefore, all that is recorded is the noise pedestal. The noise pedestal was easily characterized and accounted for when the beam was off by fitting it with a gaussian function for random triggers from a pulser. There are, however, a large number of interactions from gammas and high energy neutrons (> 24 keV) which remain. These spurious high energy neutron and gamma backgrounds are accounted for by measuring the spectrum of events in seventeen different 12 μs windows, which are anti-coincident with the trigger. This is done with the Ti-filter in place so as to avoid contamination from 24 keV neutron scatters. This spectrum, which contaminates the spectra from all other configurations, is subtracted from them.

There are also many coincident backgrounds from high energy neutrons and environmental gammas. The most likely to deposit energy in the region of interest are the high energy neutrons from the beam. They interact with the germanium detector and scatter into the ^{6}LiI(Eu) scintillator in the same manner as the 24 keV neutrons. As these are true coincidences, they are characterized by including only events within the 12 μs window and for data runs with the Ti-filter on. This is not a pure measurement of the high energy neutron coincident background because it is contaminated by accidental backgrounds. While the accidental backgrounds could be subtracted from this spectra, it is enough that the spectra of both of these backgrounds combined are subtracted from the spectra with the titanium filter removed.

Removing the Ti post-filter "turns on" the 24 keV neutron beam, leaving any other backgrounds untouched. When the Ti post-filter is removed, another background arises from isotropically scattered 24 keV neutrons which are accidentally coincident with events in the ^{6}LiI(Eu) scintillator. These background events are identified, just as in the case of the previously mentioned accidental backgrounds, by measuring the spectrum of events in 12μs windows that are anti-coincident with the trigger. This spectrum of events is contaminated by the previously measured spectrum of spurious high energy neutrons and gammas, which are subtracted from it. The background of isotropically scattered 24 keV neutrons is then easily characterized.

The spectrum of 24 keV neutron scatter coincidences is measured for events within the 12 μs coincidence window for data runs with the Ti post-filter removed. It is contaminated by three backgrounds which have already been characterized. These are the accidental gamma and high energy neutron backgrounds, the coincident gamma and high energy neutron backgrounds, and the accidental isotropically scattered 24 keV neutron backgrounds. All contaminating spectra are subtracted and the leftover spectrum is fit by a function for single and multiple neutron recoils as well as a fit for the noise pedestal. The expected recoil spectra for single and multiple scatters is determined by an MCNP-Polimi [Pozzi et al., 2003] simulation of the detector in the beam setup. The electronic noise is folded into the quenching factor fits because the angular resolution of the neutron scatters is of comparable magnitude.

The triple signature requirement for this experiment provides for a robust measurement of the 24 keV neutron recoils. Only the excess recoils that occur in coincidence with the ^{6}LiI(Eu) scintillator are measured when the Ti post-filter is removed, and only for events that occur under the thermal neutron capture peak. A nice consistency check is performed by repeating the above analysis only for events that lie outside the thermal neutron capture peak. The lack of any coincident signals when the Ti post-filter is removed indicates that any excess measured must be from 24 keV neutrons interacting in the germanium detector under test (PPC-1).

The analysis outlined above was performed for the three recoil angles indicated obtaining a measurement of the quenching factor for low energy recoils in a germanium detector. Another data point was included that is based on the spectra of isotropically scattered 24 keV neutrons that were measured in anti-coincidence with the ^{6}LiI(Eu) scintillator. The measured spectrum is fit with a function for single and multiple recoils for isotropically scattered 24 keV neutrons based on an MCNP-Polimi [Pozzi et al., 2003] simulation. It does not benefit from a selection of a narrow recoil angle and, therefore, should be considered a crude measurement of the quenching factor.

4.3.3 In-situ Determination of Detector Parameters

Several of the detector and signal parameters are measured in-situ in order to avoid problems from changes that arise due to the local environment. The first of these is the determination of the energy acceptance window for thermal neutron capture in the ^{6}LiI(Eu) scintillator. The peak is fit with a gaussian distribution on a linear background for each scattering angle to account for changes in PMT gain with the orientation. The FWHM of the thermal neutron capture peak was measured to be 0.39 MeV. Any event within a 3σ window of the centroid of the peak, illustrated in figure 4.12, is considered a potential neutron capture event. Events outside this window are due to gamma interactions.

Also measured in-situ, but with the reactor off, were the electronic noise and the noise pedestal of the PPC-1 detector. It is important to have an accurate measurement of the electronic noise in order to perform the quenching factor fits because of the proximity of the signals to the threshold. It is also important to measure the electronic noise because it contributes to the energy resolution of recoil signals. It was measured by determining the width of a peak produced by a precision pulse generator and was found to be 166 eV FWHM. This is similar to measurements performed at the University of Chicago, indicating good control of microphonics and electromagnetic noise in the reactor bay. For this measurement, the data acquisition was triggered by an auxiliary output from the pulser, and the pulser signals were measured for the same coincidence window used for the experiment.

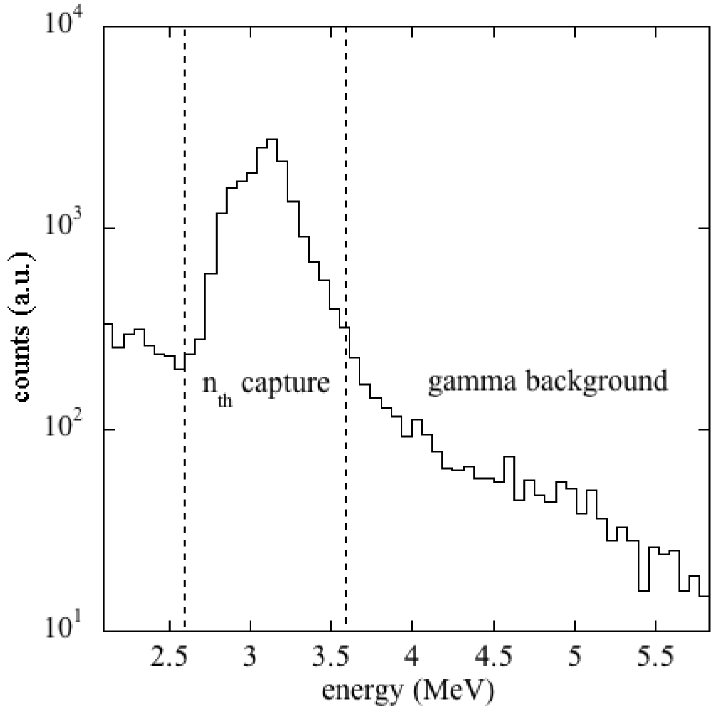

Figure 4.12: The spectrum of signals are shown from the enriched ^{6}LiI(Eu) scintillator, which serves as the neutron detector. The peak at 3.2 MeV is due to the capture reaction on ^{6}Li from moderated neutrons. The dotted lines indicate the energy window that was used to identify potential neutron scatter events in the analysis. The background continuum from gamma interactions can also be seen.

The noise pedestal, which appears in all fits for the quenching factor, can also be well described by a gaussian distribution. The pedestal was isolated, with the reactor off, for signals in anti-coincident windows of the waveforms stored from the pulser measurements. The pedestal position and width were 0.0285 keV and 0.0569 keV, respectively.

4.3.4 MCNP-Polimi Simulation

The primary purpose of simulating the neutron scatters is to determine the energy of recoils produced for the different configurations. Ideally the measured recoils consist of neutrons that scattered only once within the germanium crystal. This is not the case for the size of the germanium detector used. While the energy resolution of single scatters is excellent, the spread in the total energy deposited from multiple scatters is much larger. Complicating this is the fact that the total energy measured from a multiple scatter is the sum of many lower energy neutron scatters. As such, the portion of the spectrum from multiple scattering probes a broad range of quenching factors. Thus, it is important to have a good understanding of the relative populations of single and multiple scatters, as well as the energies and spread of the recoils produced.

A detailed geometry was used that included all of the necessary components (Ge and ^{6}LiI(Eu) detectors), as well as construction materials surrounding the detectors which can scatter or absorb neutrons. Previous characterizations of the beam were used as the basis of the intensity and spread of the simulated beam (figure 4.4). The recoil distributions, which are composed of single and multiple scatter distributions, can be seen in figure 4.13. Both distributions of single and multiple scatters are fit with gaussian functions to determine their mean and width (table 4.1), which will be used in the analysis of the measured recoil spectra. Also listed are the simulated rates of neutron scatters, which are used as a final check on the accuracy of the simulations. The uncertainty quoted for the rates is a conservative 15%,

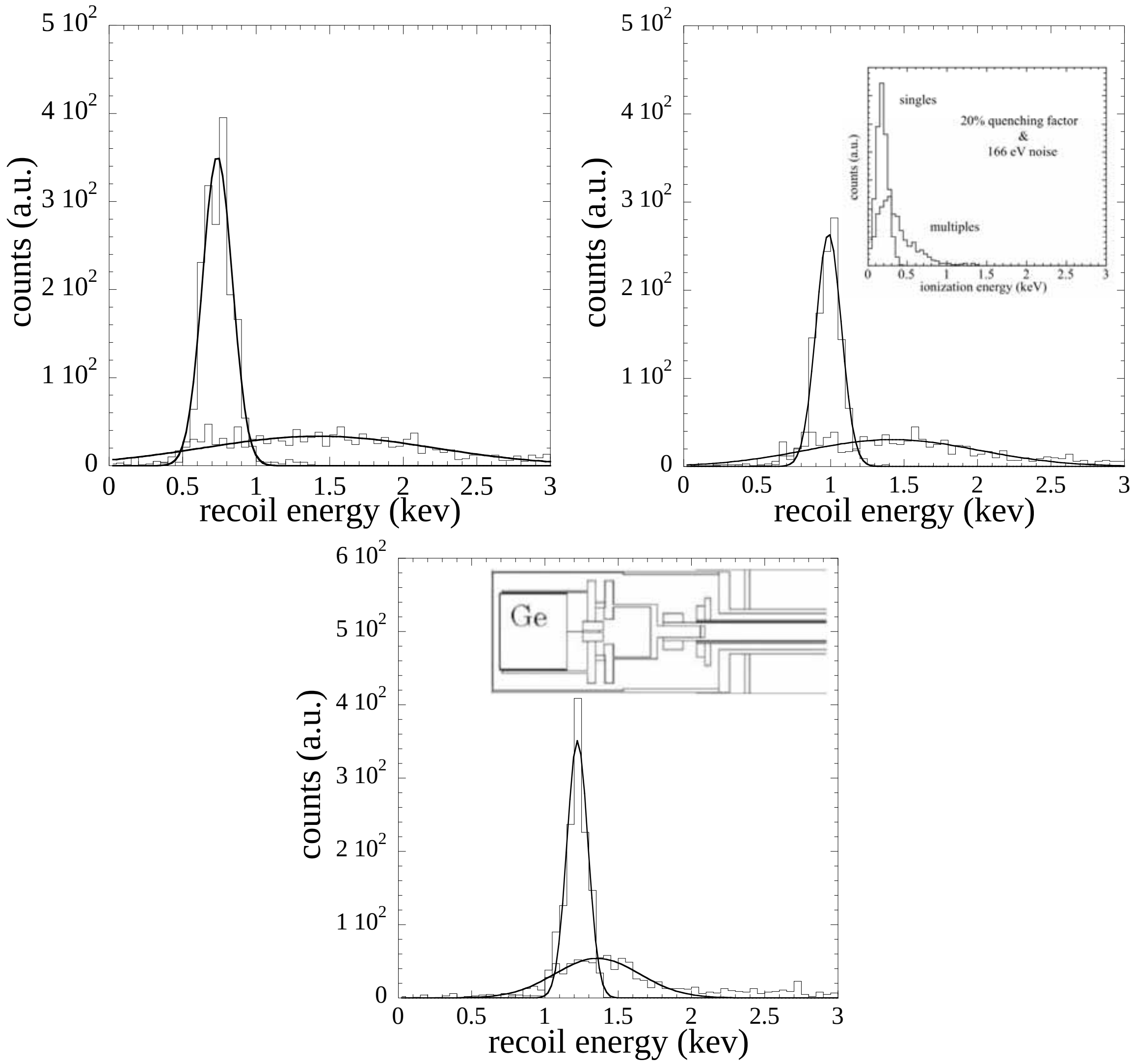

Figure 4.13: Simulated spectra for neutron scatter coincidences at three recoil angles (99°, 121° and 150°) are shown. The spectra are decomposed into single scatters (narrow distributions) and multiple scatters (broad distributions) and are fit with gaussian curves (solid lines) for use in the analysis. The inset in the top right figure depicts the expected shape of the recoil spectrum for 121°, assuming a quenching factor of 20%. The detector geometry used in the MCNP-Polimi [Pozzi et al., 2003] Monte Carlo simulations can be seen in the bottom inset.

typical for such a Monte Carlo simulation. An inspection of the simulated spectra suggests that the multiple scatter distribution does not appear to play a dominant role; however, there is a significant effect on the shape of the spectrum when the quenching factor and electronic noise are accounted for. This effect can be seen in the inset of figure 4.13, where the results of a simulation for 121° scattering angle have been folded in with a quenching factor of 20% and broadened by the measured electronic noise of 166 eV FWHM. Because the contribution from multiple scatters can play a significant role in any fit, it is important to know the approximate energy of the recoils that are being probed by this population of events. For each neutron scatter involving more than one recoil in the germanium detector the average energy of the constituent recoils was determined. The mean of these $<E_{rec}>$ distributions is also listed in table 4.1. While this is a rough estimation of the energy and, therefore, the quenching factors probed by multiple scatters, it is sufficient to know that it is nearly identical for all scattering angles. Indeed, the average energy per recoil for the multiple scattered component is about 0.7 keV, which is very near to the 0.74 keV probed by the single scatters for 99°. This proves useful when determining the effect of the multiple scatters on the fits of the measured recoils spectra.

A simulation was also performed of the distribution for recoils from isotropic neutron scattering. The distributions, broken down into single and multiple scatters, can be seen in figure 4.14. The flat distribution of single scatters was fit with a function composed of two error functions, while the multiple scatter distribution was fit with a gaussian to determine its relative position and width. The energy cutoff of the flat component, along with the characteristic width of the error functions is recorded in table 4.1. The position and width of the multiple scatters is also listed. These approximations are then used to determine the approximate quenching factor for the measured recoil spectrum of isotropic scatters over the broad range of energies probed by the beam. Isotropic scattering produces recoils of all energies up to 24 keV, but the inclusion of multiple scatters favors the production of recoils

Table 4.1. Fit Parameters from a MCNP-Polimi Simulation for the PPC-1 Quenching Factor Measurement

	Single Scatters		Multiple Scatters			
Scattering Angle	μ (keV)	σ (keV)	μ (keV)	σ (keV)	$< E_{rec} >$ (keV)	Rate[a] (counts / 170 min)
99°	0.737	0.097	1.428	0.782	0.71	677.3 ± 101.6[b]
121°	0.988	0.086	1.422	0.586	0.71	455.3 ± 68.3
150°	1.224	0.071	1.358	0.289	0.675	470.5 ± 70.5
isotropic	1.279[c]	0.151	1.41	0.792	0.647 ± 0.325	...

[a]At 10% of 170 kW reactor power, as used in the experiment.

[b]The ^{6}LiI(Eu) scintillator was placed at 15 cm, instead of the normal 18 cm.

[c]The maximum energy of the plateau for the error function fit.

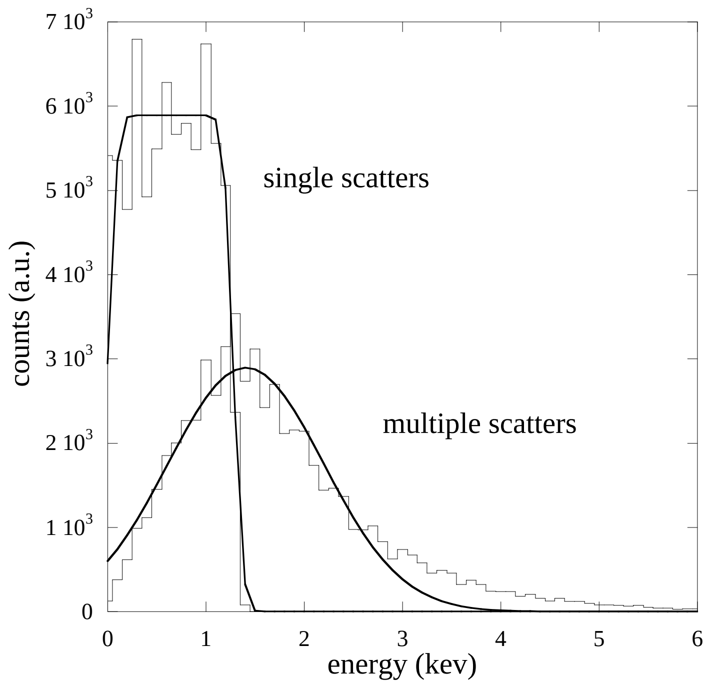

Figure 4.14: The simulated spectra due to 24 keV neutrons from single and multiple scatters for neutron recoils that scatter into all angles. The distributions are also fit in order to incorporate these events into the analysis. These accidental neutron scatters represent a background that must be characterized to properly measure the quenching factor; it can also be used as a crude measurement of the quenching factor for a large range of neutron recoil energies.

with moderate energies. While the energy range of recoils probed by "isotropic" scatters is broad, it is possible to assign an average energy and width, listed in table 4.1, to the distribution seen in figure 4.14. This should be considered representative of the broad range of the recoil energies measured by this distribution.

4.3.5 Selected Neutron Scattering Angles

The neutron scattering experiment was performed for the scattering angles of 99°, 121°, and 151°. The experiment was performed for only a few angles in order to avoid damaging the germanium crystal lattice [Sudarshan & Singh, 1991]. The total fluence was kept below 10% of the level that would damage the crystal. According to MCNP-Polimi [Pozzi et al., 2003] simulations, these correspond to nuclear recoil energies of 0.73 keV, 0.99 keV and 1.22 keV, respectively. The required triple signature makes for a robust measurement: the nuclear recoils must be measured in coincidence with a second detector, only for coincidences that correspond to neutron capture events, and only when the Ti post-filter is removed so that 24 keV neutrons are measured. These three handles on the data significantly suppress the backgrounds.

99° scattering angle

The first background removed is from the accidental coincidences from high energy (>24 keV) neutron and gamma scattering. They are measured by selecting only events that are anti-coincident with the trigger, when the Ti post-filter is in place. The spectra of spurious coincidences that contaminates the final spectrum of 24 keV neutron scatter coincidences (open circles) can be seen in figure 4.15. Also included is a fit for the noise pedestal (dashed line) which was characterized separately. The excellent statistical uncertainty on these points is a result of the fact that the accidental backgrounds are sampled from seventeen windows

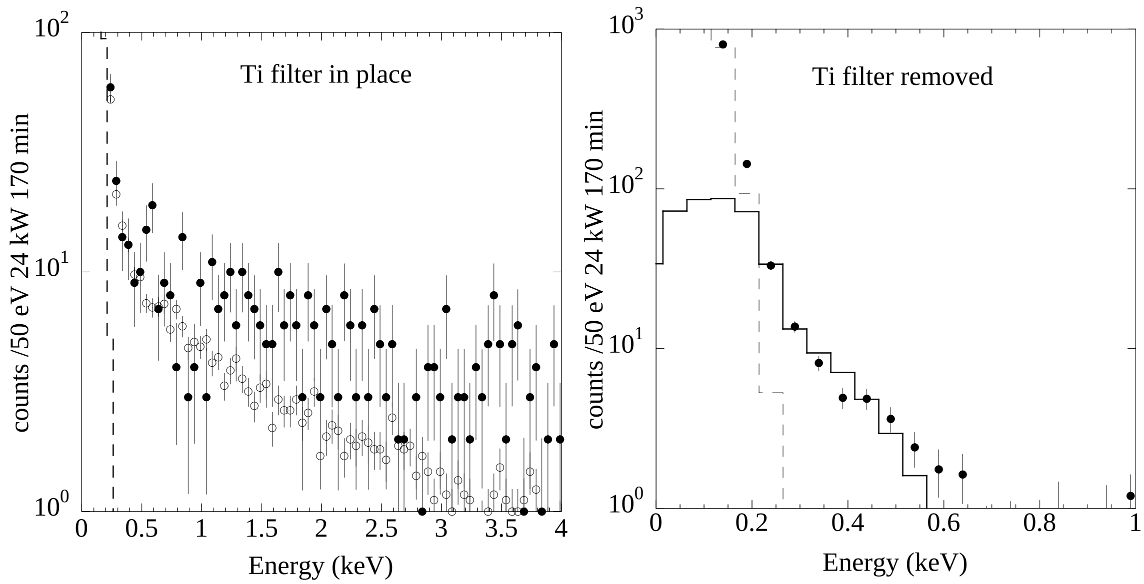

Figure 4.15: Characterization of several backgrounds that obscure the measurement of the 24 keV neutron recoils. Two backgrounds unrelated to the 24 keV component of the neutron beam are shown (left), which are characterized with the Ti filter on. The data are: accidental backgrounds (open circles), high energy neutron and gamma scatters (filled circles) and the noise pedestal (dotted line). With the Ti filter removed, the accidental coincidences from 24 keV neutrons scattering into all angles are shown (right). The filled circles are the measured spectrum. The fit for single and multiple scatters, the spectral shape of which is based on Monte Carlo simulations (solid line) is also shown. The threshold of the noise pedestal appears small ($\sim$0.25 keV) because the data acquisition electronics record some random triggers of the noise baseline.

in the recorded waveform.

Also depicted in figure 4.15 are the true coincident scatters between the two detectors for high energy neutrons and gammas. These are measured in the coincidence window, with the Ti post-filter in place and are contaminated by the spurious backgrounds. While the statistics for the measurement of this background are poor, the excess number of events that are coincidences between detectors over the spurious backgrounds is evident.

The third background measured is from accidentally coincident isotropic scattering of 24 keV neutrons. These are measured in seventeen anti-coincidence windows in the recorded waveform, for data sets with the Ti post-filter removed. This spectrum is contaminated by

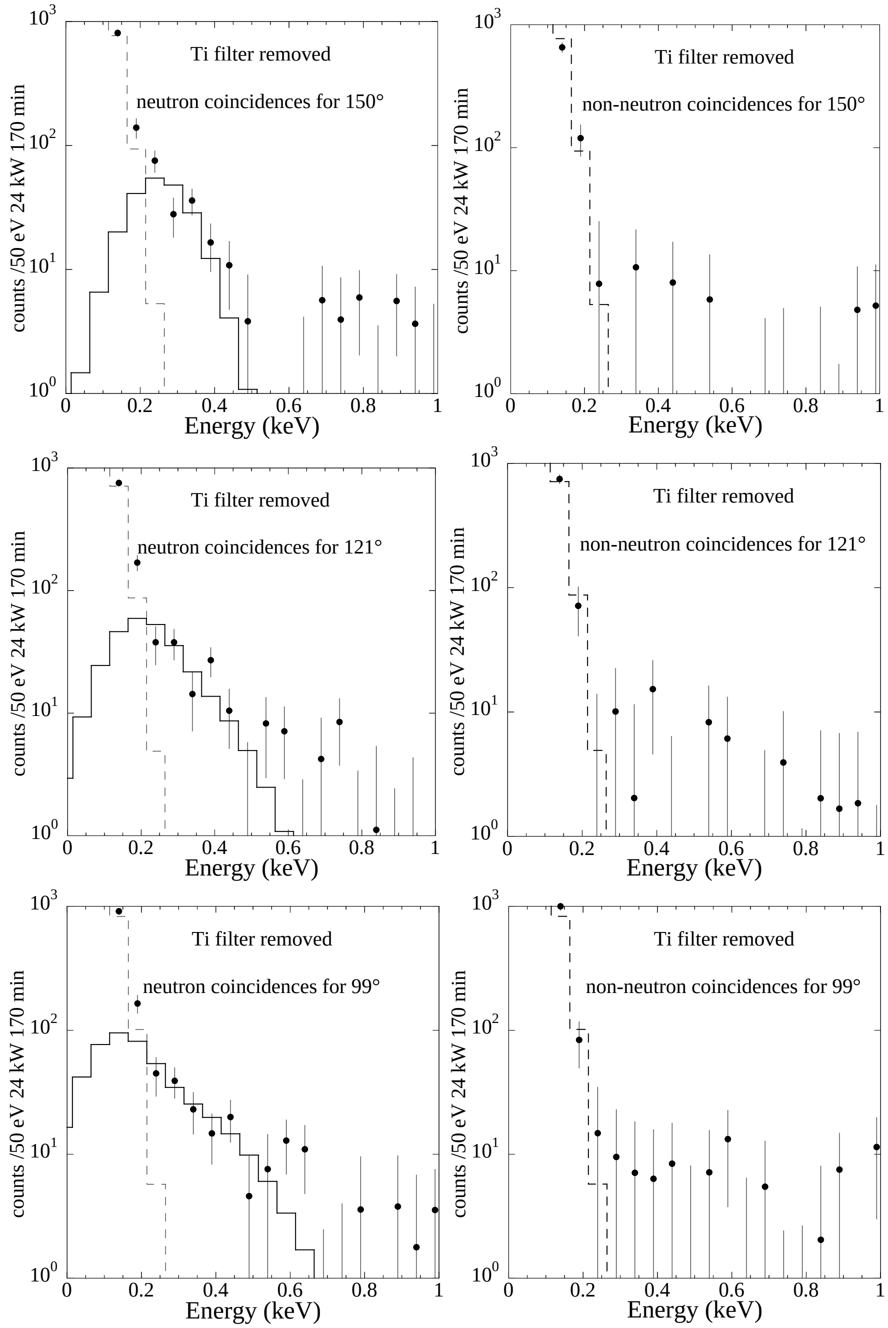

Figure 4.16: Recoil spectra from 24 keV neutrons at three recoil angles (left column). All backgrounds have been removed and the fits to the data are shown (solid line). The noise pedestal is also included (dashed line). The data are compared to the results of the same analysis performed on events that are from gamma interactions (right column) in the ^{6}LiI(Eu) scintillator, demonstrating that the signal arises only for neutron recoils. The threshold of the noise pedestal appears small ($\sim$0.25 keV) because the data acquisition electronics record some random triggers of the noise baseline.

the previously measured accidentally coincident backgrounds from high energy neutrons and gammas, which are therefore subtracted from it. The resulting spectrum of isotropic 24 keV neutron scatters is seen in figure 4.15. The excellent statistics for this measurement are a result of the fact that it is measured in seventeen non-coincident portions of the waveform. The plot is an average of these spectra for all three measured angles to further improve the statistics; a legitimate operation, as the background does not change with the placement of the ^{6}LiI(Eu) detector. A fit for the single and multiple scatters is shown based on Monte Carlo simulations along with a fit for the noise pedestal. This will be revisited in section 4.3.6.

Finally, the spectrum of 24 keV neutron scatters for 99° is shown in figure 4.16, with the three backgrounds removed. A fit for the single and multiple scatters, as well as the noise pedestal was performed to determine the quenching factor. The fit was based on the Monte Carlo simulations, with the quenching factor and amplitudes as free parameters, and also folding in the electronic noise of 166 eV FWHM. Essentially, the following substitutions are made to the two gaussian functions used on the Monte Carlo output:

$$\mu \rightarrow Q\mu$$

$$\sigma^2 \rightarrow (Q\sigma)^2 + \sigma_{noise}^2$$

where μ is the mean value of the simulated single or multiple scattered distributions; Q is the quenching factor, σ is the width of simulated single or multiple scattered distributions and σ_{noise} is the standard deviation of the electronic noise (70.6 eV) as determined by the pulser measurements. The folding in of the quenching factor occurs such that Qμ is the position of the distribution mean in terms of ionization energy. Also included is the contribution of the electronic noise to the width of the transformed peaks, which adds in quadrature. For the 99° scattering angle, the effect of the multiple scattering peak on the measurement is minimal because both the single and multiple distributions are effectively probing the same energy recoils, which cannot have vastly different quenching factors. For this angle, the quenching factor was measured to be 18.4% ± 2.7%, where the errors are statistical. This is consistent with the Lindhard theory (section 4.1.1), indicating that the quenching factor is well behaved in this region. A conservative estimate of the systematic uncertainty resulting from the inclusion of multiple scatters is obtaineds by estimating the effect of their spread in energy on the measurement of the quenching factor. In this energy region, the quenching factor drops by about 3.4% keV^{-1} according to the Lindhard theory. Using the standard deviation of multiple scatters determined by Monte Carlo of 0.187 keV, a conservative systematic uncertainty of ± 0.64% is estimated.

As a final double check, the same analysis was performed for events in the ^{6}LiI(Eu) detector that occur outside the thermal neutron capture peak and are therefore not due to neutron scatters. The resulting spectrum of coincidences with the Ti post-filter off, and all of the same backgrounds removed, is shown in figure 4.16. The statistics are worse than the neutron capture result because of the scarcity of triggers outside the thermal neutron capture peak; however, a similar fit to the one performed for the neutron coincidences indicates that the data are consistent with zero excess events. This is recorded in table 4.2.

121° and 150° scattering angles

A similar analysis was performed on the data sets from the other two angles. The backgrounds are essentially the same, though there is a slight change in the apparent spectrum of coincident high energy neutrons and gammas, as can be expected from the displacement in the position of the ^{6}LiI(Eu) detector. The 24 keV isotropic scatters are unchanged, which justifies averaging the spectra that were obtained from the data sets for the three recoil angles, the results of which are shown in figure 4.15. The resulting spectra of 24 keV neutron scatters with the backgrounds removed are shown in figure 4.16. The spectra are fit with similar functions as for the 99° data set, for the single and multiple scatters, as well as the noise pedestal. The only change is in the centroids of the energies as determined by the Monte Carlo simulations. Again, the quenching factor and amplitudes were taken as free parameters and the electronic noise was folded in. For 121°, the quenching factor was measured to be 19.2% ± 2.4%, and for 150°, 19.8% ± 1.4%. For both of these angles, the effect on the measurement from the multiple scatters is potentially larger than it was for 99°. The largest energy difference of individual recoils is between the centroid of the single scatter peak and average recoil energy ($<E_{rec}>$) for the multiple scatters. This energy span is used to estimate systematic uncertainties for the quenching factor to be ± 0.96% for 121°, and ± 1.89% for 150° scattering angles.

Double-checks were performed for both angles, by "turning off" the neutrons using events selected outside the thermal neutron capture peak in the ^{6}LiI(Eu) scintillator. They are shown in figure 4.16. Fits using the same functions on these spectra are also consistent with zero excess signal. This is also recorded in table 4.2.

4.3.6 Spectrum of Isotropically Scattered 24 keV Neutrons

Returning to the spectrum of accidentally coincident scatters from 24 keV neutrons, an additional rough measurement is made of the quenching factor for low energy recoils. This excess, after the accidental gamma and high energy neutron backgrounds are removed, is present only when the Ti post-filter is removed. Because no selection of a recoil angle is made, the spectrum consists of contributions from single and multiple recoils in the germanium from neutrons that scatter into all directions. A fit for the single and multiple scatters, as well as the noise pedestal, is shown in figure 4.15. As in the fits for the recoil angles, the fit for the pedestal uses previously measured characteristics. The fit for the single and multiple scatters is based on the Monte Carlo simulation, where the quenching factor and amplitudes were free parameters. The fit parameters from the simulation were transformed, similar to the previous substitutions, as follows:

$$E_{max} \rightarrow QE_{max}$$

$$\mu_{mult} \rightarrow Q\mu_{mult}$$

$$\sigma^2 \rightarrow (Q\sigma)^2 + \sigma_{noise}^2$$

where E_{max} is the end point energy of the flat single scatter distribution (figure 4.14) which was fit with two error functions, μ_{mult} is the mean of distribution of multiples and σ is the width of the multiple scatter distribution, or the characteristic width of the error functions. Note that the quenching factor and electronic noise impacts the endpoint of the single scatters in a similar manner to the way that it affects the position of the mean of the multiple scatters. The quenching factor was determined to be 17.4% $\pm$ 1.6%, where the uncertainty is statistical. The systematic uncertainties due to the spread of the recoil energies probed for this measurement of the quenching factor are not included. Instead, this spread is reported as an error on the recoil energies probed, as can be seen in figure 4.17.

4.4 Results

The measured quenching factors for all three recoil angles and the isotropic scatters are plotted in figure 4.17. For the recoil angle measurements, the recoil energies are determined by the calculated centroid of single neutron scatters based on the MCNP-Polimi [Pozzi et al., 2003] simulations. The horizontal error bars represent the spread in recoil energy of the single scatters, while the vertical error bars represent the statistical and systematic uncertainties,

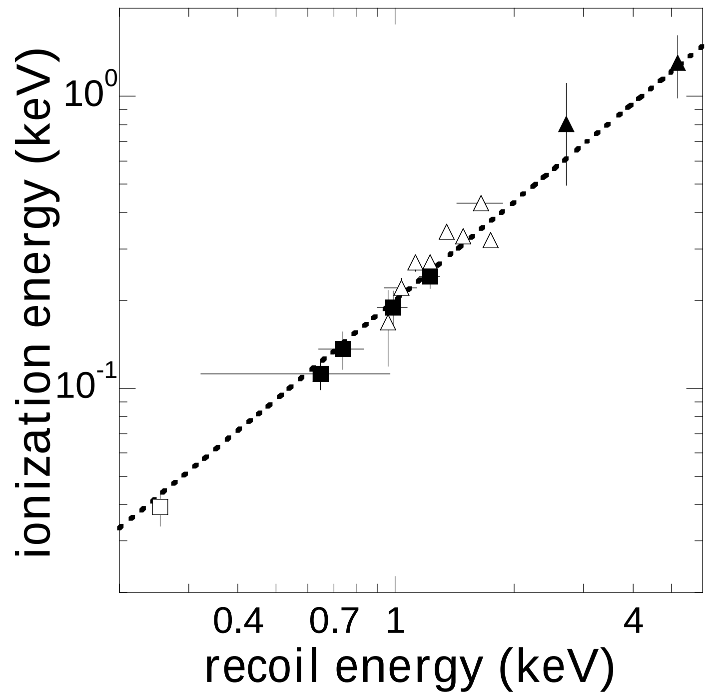

Figure 4.17: The measured quenching factor for nuclear recoils from the analysis described here (filled squares) is compared to results performed at higher energies (filled triangles)[Messous, 1995], or with indirect measurement methods (open square and triangles) [Jones & Kraner, 1975, 1971]. The dotted line is the expected response from the Lindhard theory (k=0.2).

added in quadrature. The data point for the isotropic scattering is located at the mean recoil energy of single and multiple scatters. The horizontal error bars are indicative of the broad range of recoil energies probed by this measurement, while the vertical error bars are statistical. The lowest energy point, from isotropic scattering, is indicative of the quenching factors at these energies, but is by no means a direct measurement.

A comparison of the expected and measured neutron scattering rates for the three recoil angles can be seen in table 4.2. It is important to point out that the measured rates from 24 keV neutron scatter coincidences is consistent with zero when the Ti post-filter is in place. Also recorded are the measured rates of the excess for the non-neutron capture analysis

Table 4.2. Comparison of the Simulated and Measured Rate of 24 keV Neutron Scattering

Scattering Angle	Simulated Rate[a] (counts / 170 min)	Measured Rate[a] (counts / 170 min)[b]	Non-Neutron Captures Rate (counts / 170 min)
99°[c]	677.3 ± 101.6	871.4 ± 170.7	9.2 ± 165.2
121°	455.3 ± 68.3	514.3 ± 107.7	52.1 ± 92.53
150°	470.5 ± 70.5	386.3 ± 65.8	-52.9 ± 55.23

[a]At 10% of 170 kW reactor power.

[b]Corrected for the live time.

[c]Measured at 15 cm, instead of the normal 18 cm.

double checks. These values have been corrected for the DAQ live time ($\sim 50\%$), measured separately with a pulser. The effect on the live time was a result of regular resets of the germanium preamplifier that prohibited measurement of the waveform because it caused the trace to be out of range of the NI scope card. It is important to note that the rates for the 99° runs are larger than for other angles because the ^{6}LiI(Eu) crystal was moved close to the germanium detector, increasing the solid angle for detecting scattered neutrons.

4.5 Discussion

This measurement has demonstrated the sensitivity of these detectors to sub-keV nuclear recoils. The results for the quenching factor are in good agreement with the Lindhard theory, as well as previous direct and indirect measurements in the vicinity of this low energy region. Some of these are shown in figure 4.17, where the dashed line represents a parameterization of the Lindhard theory for nuclear recoils. Recalling equation 4.1, a value of k = 0.2 is seen to fit the data well in the low energy region. This description will be used for all other estimates of the ionization produced from low energy nuclear recoils in germanium such as in the simulation of neutron backgrounds, or for the expected spectra from coherent neutrino nucleus scattering or dark matter WIMPs. The measurement itself is very robust as events are only considered if they are coincident with the ^{6}LiI(Eu) scintillator, if the energy deposited in the scintillator is consistent with neutron captures, and only for the excess of events that occur when the Ti post-filter is removed.

If the electronic noise and threshold of PPC detectors continue to improve, more measurements of the low energy quenching factor will be warranted. Indeed, the lowest plotted point from these measurements, at 0.647 keV recoil energy, is not of the highest quality. If such a measurement were to be undertaken, a smaller detector should be used to minimize multiple scattering. Simulations demonstrating the potential reach with germanium and NaI detectors are shown in figure 4.18.

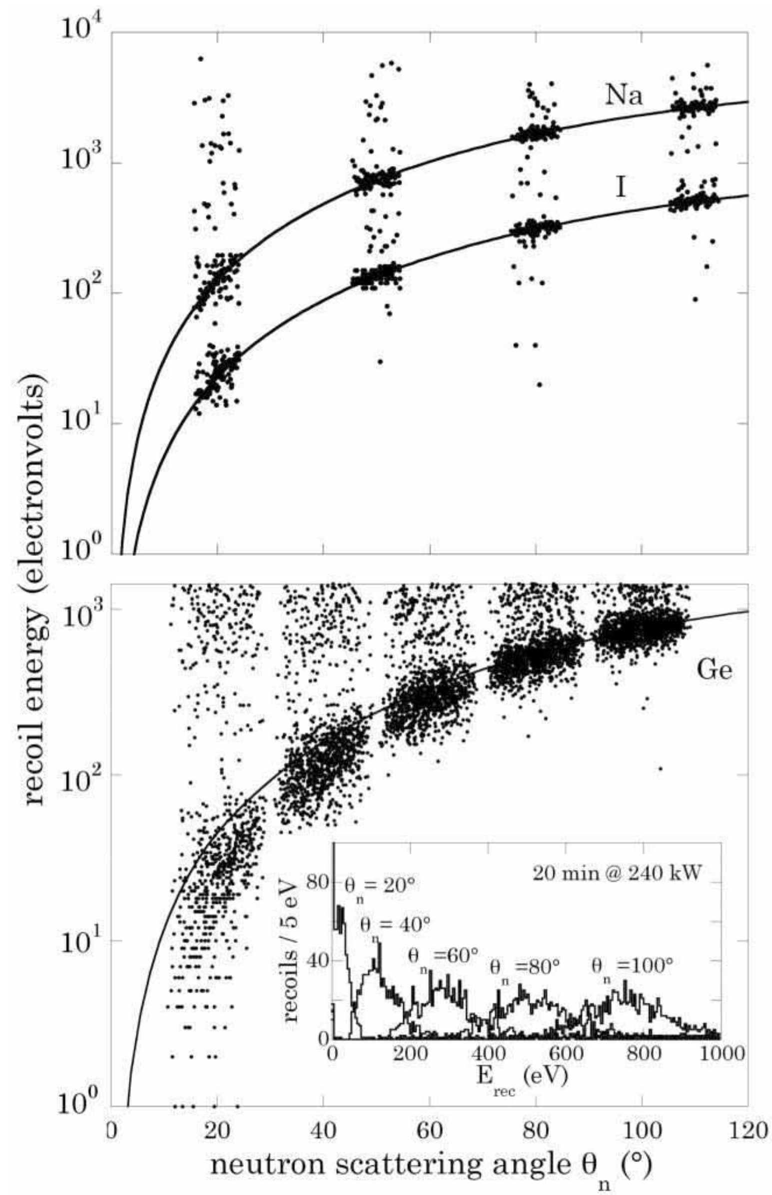

Figure 4.18: The results of an MCNP-Polimi [Pozzi et al., 2003] simulation, for NaI (top) and Ge (bottom) illustrate the potential reach of the 24 keV neutron beam facility. Figure courtesy of J. I. Collar.

CHAPTER 5

THE COGENT EXPERIMENT AT THE SONGS NUCLEAR REACTOR

The control and reduction of backgrounds is critically important in any low background experiment. Therefore, the description of the experiment at the SONGS nuclear reactor is almost entirely a discussion of the reduction of backgrounds. For this deployment, the acceptable background level is higher than in a typical low background experiment because the primary goal is to measure coherent neutrino scattering. Most experiments operate in deep underground sites to eliminate backgrounds from cosmic rays, while this experiment operates near the surface and close to the reactor to enjoy the highest possible neutrino flux, where higher backgrounds are expected. However, the experiment does benefit from a modest overburden as it is located in a Tendon Gallery (30 m.w.e.), which is underneath a concrete dome and slightly below ground. This reduces the effect of cosmic secondary neutrons. Also, the expected signal region from coherent neutrino scattering is highly concentrated at low energies, where the contributions from typical background sources are diluted. Even so, great care must be taken to eliminate or identify as many background events as possible. These backgrounds do not always result from radiation, They are often due to electronic effects like detector noise or microphonic signals from detector vibration [Morales et al., 1992]. Efforts to reduce backgrounds and estimates of the surviving rates are described below. Most of the sources are well known. However, because this is the first low background, large mass, germanium experiment with a sub-keV threshold, it must be acknowledged that some backgrounds may have been forgotten, and that this is by no means a complete list.

5.1 Experimental Description

5.1.1 Shielding

The germanium detector is surrounded by several layers of passive shielding and active vetoes. Their primary purpose is to reduce or identify radiation backgrounds without introducing new sources near the detector. Listed from the inside out, the shielding elements are: a refurbished, low background, NaI(Tl) anti-Compton Veto; 5 cm of low background lead followed by 15 cm of regular lead for gamma shielding; 0.3 cm boron-carbide and cadmium sheet for thermal neutron absorber; a 5 cm plastic scintillator muon veto, which is here referred to as the internal muon veto; 25 cm of Polyethylene neutron moderator; and a 1 cm plastic scintillator external muon veto.

Refurbished NaI(Tl) Anti-Compton Veto

The anti-Compton veto consists of a NaI(Tl) crystal scintillator that is 8 cm thick encompassing the germanium detector. It is in two parts: an annulus that is coaxial with the germanium detector cryostat and a plug that sits in the annulus in front of the germanium to provide more complete coverage.

The primary purpose of the anti-Compton detector is to veto gammas from internal sources of contamination that Compton scatter in the detector and subsequently interact with the NaI(Tl) crystal. The gammas are mostly from small contaminations of ^{238}U, ^{232}Th and ^{40}K in construction materials near the detector. It also vetoes or attenuates Bremsstrahlung photons from ^{210}Pb in the shield wall. The energies of these photons are very large compared to the energy region of interest of this experiment, so their contribution to the background in the coherent neutrino scattering region of interest (ROI) must be due to forward scattering. In addition, the NaI(Tl) detector can be used to veto energetic neutrons that survive the

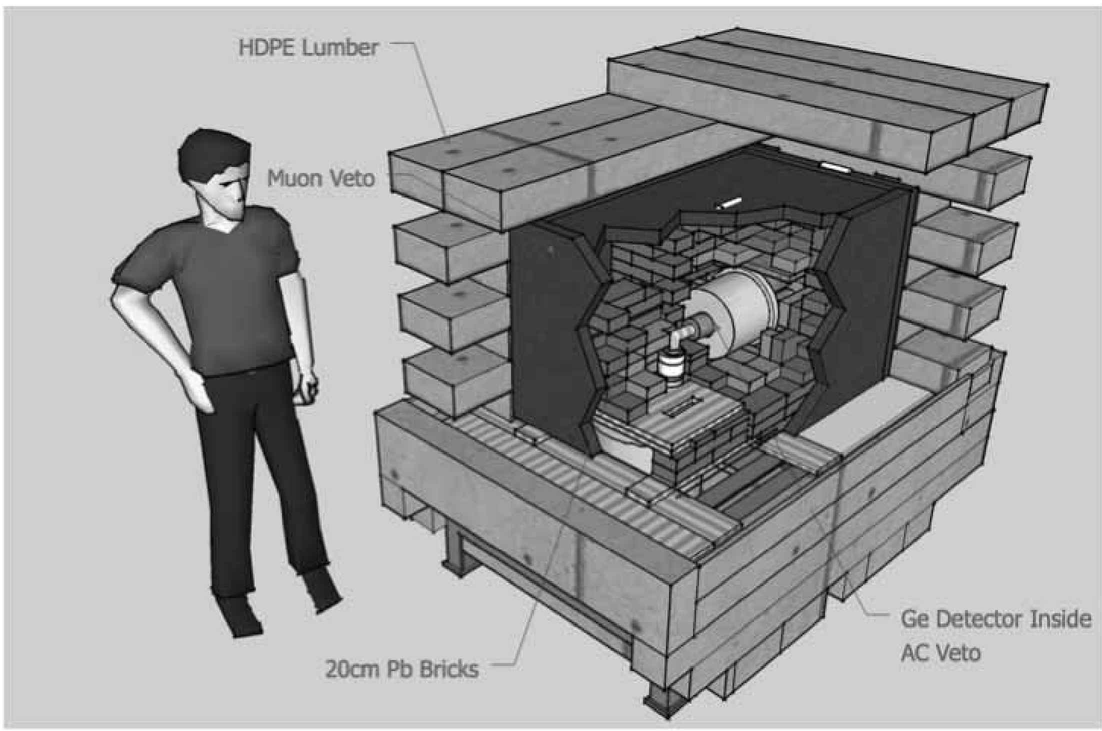

Figure 5.1: A rendering of the germanium detector cryostat surrounded by the many layers of passive shielding and anti-coincidence vetoes for the deployment to the SONGS nuclear reactor. The external muon veto is not pictured.

neutron moderator. These neutrons deposit very little energy in the veto and the germanium detector and are thus the most important and difficult radioactive backgrounds to attenuate. A fraction can be vetoed if the neutron scatters off a sodium atom, transfering enough recoil energy to produce a detectable level of scintillation. The kinematics of the neutron scattering make it unlikely that any iodine recoils will be energetic enough to produce scintillation.

The NaI(Tl) crystal is surrounded by a Teflon liner and a Magnesium powder reflector to facilitate collection of scintillation photons. Because NaI(Tl) is hygroscopic, the scintillator and reflector are encapsulated in a steel casing. To minimize attenuation of gammas that enter the veto, the inner wall of the annulus and the front face of the plug are very thin, 0.6 mm and 0.3 mm respectively. The annulus has 6 quartz windows (the plug has one) that have 3" low background PMTs affixed with fixtures made of low background Teflon rings, OFHC clamps, and Nylon screws.

To avoid introducing radioactive sources near the Germanium detector, all efforts were made to use low background materials in the construction of the NaI(Tl) vetoes. The Teflon reflector, steel casing and quartz window of the plug all have low levels of ^{238}U, ^{232}Th and ^{40}K. Though steel can sometimes have high levels of ^{60}Co, it is far better than the alternative of aluminum. The plug was purchased with these specifications in mind. The annulus, on the other hand, was refurbished to improve an already existing anti-Compton veto by making it match our low background specifications. First, the old aluminum inner liner was replaced with one made of low background steel. Where possible, mostly on the inner diameter of the annulus, the magnesium powder reflector was replaced with low background Teflon. Finally, the old Pyrex windows, which typically have notoriously high levels of ^{40}K, were replaced with low background Spectrasil 2000 quartz. The PMTs each have less than 60 ppm K, 30 ppm Th and 30 ppm U. The PMT bases, which are a possible source of background, are sufficiently far away from the detector and blocked by the anti-Compton veto itself, making it unlikely that they will contribute.

Lead Shielding

The next layer of shielding consists of 20 cm of lead. There are three types, which are characterized by their levels of contamination of ^{210}Pb. Ultra low background ancient lead bricks were used in a few areas very near the germanium detector crystal where there is a direct line of sight to it. These bricks (2.5 cm $\times$ 10 cm $\times$ 20 cm), most recently used in the CAST experiment, have < 0.02 Bq/kg of ^{210}Pb. These are used primarily in the region near the neck of the cryostat, where it would have been difficult to build an anti-Compton veto. They are not included when accounting for the total thickness of lead shielding. In areas where the veto blocks the line of sight to the detector, a 5 cm layer of low background lead bricks (5 cm $\times$ 10 cm $\times$ 20 cm) were used. These bricks, stamped "Low Radioactivity Lead", are from a less successful casting of the same "old" lead and are estimated to have $\sim$14 Bq/kg of ^{210}Pb (see A.3). The final 15 cm of lead bricks are standard commercial bricks (5 cm $\times$ 10 cm $\times$ 20 cm) with approximately 100 Bq/kg of ^{210}Pb. The shielding must surround the anti-Compton veto, and thus the lead bricks must span a distance of 30 cm above it. Low background OFHC copper plates, 2.5 cm thick, form a roof above the detector that supports 20 cm of low background and commercial lead bricks.

The sole purpose of the lead shielding is to passively reduce backgrounds from external sources of gamma rays. It has been shown that 20 cm is sufficient for this task [Shizuma, 1989]. Unfortunately, the production of lead suffers from a contamination of the bricks by ^{210}Pb, which has a half-life of 22.2 years. This means that the lead bricks themselves are a source of Bremsstrahlung photons due to the beta decay of the daughter isotope ^{210}Bi. The best solution to shield these gammas is to use an inner layer of old lead, as was done here, which has been through many half-lives and does not produce much background of its own.

Another potential source of backgrounds is from Rn daughters that have been implanted on the surfaces of the lead bricks and the copper pieces, along with other dirt and dust that has been ground into them over time or in fabrication. To eliminate this, all of the lead bricks and OFHC copper pieces were cleaned and etched in acidic solutions, removing the top layers of material, according to an already established recipe [Hoppe, Pacific Northwest National Laboratory]. They were immediately placed in clean 8 mil thick polyethylene bags, where they remained during storage and shipment until the construction of the shielding.

This lead shield (nearly 4,700 kg) was supported on a preexisting steel table that was designed and built at the University of Chicago. Where possible, the gaps between lead bricks were interlaced so as to prevent streaming of gammas into the interior.

Thermal Neutron Absorber

The thermal neutron absorber is mounted immediately outside the walls of the lead castle. It consists of two types of absorber: a 0.3 mm thick cadmium sheet beneath the lead bricks and boron-carbide powder made into 3 mm thick plates that surround the castle on the sides and top.

It is common practice to eliminate thermal neutrons with materials containing Cd or ^{10}B fillers, both of which have very high absorption cross sections. Gammas produced via the (n_{th},γ) reaction near the detector can contribute to the background and need to be attenuated. Thermal neutrons can also cause a background if they capture in the detector, creating ^{71}Ge, which decays via electron-capture with an 11.43 day half-life. The background from this particular decay is explored later (5.2.4). It is particularly important to incorporate thermal neutron absorber immediately outside the lead, as most of the outer layers are dedicated to moderating higher energy neutrons, adding to the existing population of environmental thermal neutrons. The absorber is located outside of the lead shield because the process typically emits many gammas, which need to be attenuated by the lead shield.

In this experiment there are two types of boron absorber plates. The first set were made by sandwiching loose boron-carbide powder between two thin aluminum sheets and sealing the edges with vinyl tape. To avoid any shifting of the powder that may create gaps these plates were mounted horizontally on top of the lead castle. The second type consists of boron-carbide powder suspended in a hard urethane epoxy that was poured into the desired shape and thickness. While these were preferred to the type with the loose powder, they were mounted vertically around the lead castle but nowhere else because they were in limited supply.

Internal Muon Veto

The internal muon veto is mounted outside the thermal neutron absorber. It consists of five panels of 5 cm thick plastic scintillator, coupled to a total of 13 PMTs.

The purpose of the veto is to identify when cosmic ray muons pass through the lead shielding, which can produce background neutrons via a spallation reaction. This is especially important as the process is enhanced for larger nuclei, when there is a large quantity of lead in close proximity to the detector. Neutrons are the dominant background to this experiment as they produce nuclear recoils in the germanium detector with energies that can mask the expected signal. At the depth of the SONGS Tendon Gallery, the dominant source of neutrons are from muon induced spallation reactions. An extra benefit of the muon veto is that the 5 cm of plastic scintillator serves as additional neutron moderator.

The scintillation light from each veto panel is piped through short right angle light guides that are coupled to the PMTs. This configuration was chosen for purposes of compactness. It is not the optimal configuration in regards to the uniformity of light collection by the PMTs, but it is sufficient for a muon veto because of the copious amount of scintillation light produced and collected from a muon passing through 5 cm of scintillator ($\sim$2.0 MeV cm^{-1}), regardless of the distance of the interaction to a PMT. The efficiency of the veto is ∼99.9%. It is possible that gaps can form between the veto panels, allowing muons to stream through and go unvetoed. Therefore, great care was always taken when assembling the veto.

Neutron Moderator

The penultimate layer of shielding is made up of high density polyethylene logs (HDPE), approximately 28 cm thick, that serve as neutron moderator. The total mass of the HDPE moderator is approximately 3,800 kg.

Cosmic secondary neutrons are an important background consideration for any experiment situated so close to the surface. While they do not play a dominant role for the deployment described here, they are by far the most important backgrounds for one with less overburden. The hydrogen in the polyethylene logs efficiently moderates the sources of background neutrons. As an added benefit, the 28 cm of HDPE also serves as additional gamma shielding. While it adds minimally to the efficacy of the lead shield, it helps reduce the rate of environmental gammas interacting in the internal muon veto, which reduces the rate of misidentified vetoes that were not from muons. This helps improve the live time fraction of the experiment.

The HDPE logs that surround the experiment are stacked on top of each other and the support table. The only exception to this are the logs located beneath the table, which are bolted to it and serve as the floor beneath which the detector's liquid nitrogen Dewar rests. The logs, originally designed to replace wood lumber for outdoor commercial construction, are extruded with soft corners and imprecise dimensions. This can lead to gaps in the neutron moderator that might allow some neutrons to stream through. The gaps are minimized by utilizing an adjustable steel frame along with 5 heavy duty freight straps that encircle the neutron moderator and cinch the logs together. This also provides a measure of safety in an area of the country prone to earthquakes. The effect of the irregular shape of the logs is also mitigated by the presence of 5 cm of plastic scintillator located immediately inside the neutron moderator, whose gaps do not overlap with those from the logs.

External Muon Veto

The outermost layer of shielding is the external muon veto. It consists of 10 panels, approximately 1 m^2 and 1 cm thick. Each panel has a single PMT attached in the center of the panel with a short, right angle light pipe to reduce the profile of the vetoes. The panels sit on top of the experiment, or are hung on the sides, but do not efficiently cover the geometry. The estimated veto efficiency is approximately 80%.

The purpose of this extra muon veto is two-fold. First, it provides an extra measure of confidence that muons that intersect the lead shielding are vetoed. Second, while HDPE is used as neutron moderator because it contains a lot of hydrogen, it also has a large quantity of carbon. Thus, muon induced neutrons can be produced in the neutron moderator close to the lead castle. While carbon nuclei are not as large as lead nuclei, and are thus less prone to produce neutrons via spallation, there is enough carbon in the 3,800 kg of HDPE and a large enough flux of muons at the depth of this experiment to be a cause for concern. This potential source of neutron backgrounds is ameliorated with the external muon veto. Simulations were performed to estimate the contribution of these neutrons to the background spectrum (see section 5.2.2).

5.1.2 Power and Data Acquisition

For the SONGS deployment, the detector systems are powered by NIM standard electronics. The signals produced in the germanium detector and the vetoes are also conditioned by NIM modules and are recorded as waveforms on two synchronized 8-bit National Instruments (NI) scope cards installed on a local computer. The waveforms are 400 μs long, with 0.4 μs per point resolution.

To minimize ground loops, the entire DAQ and control system is powered off a single 1 kW line. This is the maximum power available per line in the SONGS Tendon Gallery. Special care was taken in the selection of the line because conditions at the reactor have caused some to have floating grounds, which is particularly bad for the integrity of the HPGe detector. An un-interruptable power supply was used to filter the power, as well as provide a very modest safety margin in case of a power loss–a surprisingly regular occurrence in a power generation nuclear plant.

The germanium detector preamp has two signal outputs, which are used to drive two shaping amplifiers with 6 μs and 10 μs shaping times. The ratio of these amplitudes is used to remove anomalous signals (see 5.3) that are not radiation induced events. The amplifiers also receive the reset inhibit signal from the pulse-reset preamplifier, but this is not sufficient to prevent anomalous pulses caused by the reset mechanism from triggering the scope cards. Therefore, the amplified 6 μs signal is passed through a linear gate that prohibits passage of the signal upon receipt of the reset inhibit. The 6 μs signal (noisiest of both channels) triggers the data acquisition and is recorded on channel 0 (Ch0) by the NI cards. This prevents the reset pulses from triggering the DAQ at a rate higher than the NI cards can handle. The maximum energy measurable in Ch0 is approximately 3.3 keV. The signal from the 10 μs amplifier is recorded on channel 1 (Ch1) and has a similar energy range, up to 3 keV. The disparity is a function of a small difference in gain of the amplifiers, which were matched by hand. The 10 μs signal is also recorded on channel 2 (Ch2) in the NI cards, but with a maximum measurable energy of 15 keV. An example of a recorded waveform can be seen in figure 6.1.

The number of available channels is limited, which means all of the veto signals are recorded on channel 3 (Ch3) in the NI cards. They are encoded such that it is still possible to determine the time and type of veto from the recorded waveform. The signals from the PMTs of the three vetoes are amplified, discriminated, combined and sent through gate generators. There are three gate generators, set to produce a 10 μs pulse when a veto occurs of each type. The pulses are combined using a Fan-in/Fan-out NIM module. The pulses from the anti-Compton veto are doubled by splitting with a Fan-out, and then recombined with a Fan-in. The pulses from the internal muon veto are then combined at their normal magnitude with these doubled pulses. The pulses from the external muon veto are attenuated to half the normal magnitude, and then combined with the other two. Ch3 records the output, a series of pulses corresponding to three different vetoes, or combinations thereof, for which it is possible to decode and determine when each veto fired, based on the amplitude of the logic pulse.

The data acquisition also incorporates a precision pulser that sends a signal to the germanium preamplifier test input. It is used periodically to measure the stability of the rate of accidental vetoes. It also provides a method for measuring the stability of the gain and the electronic noise. The pulser is turned on several times a day by the data acquisition software, but to avoid creating ground loops, its control is isolated from the controlling computer with an opto-coupler. The amplitude of the pulser is set just below 3 keV, so that it can be measured in all of the signal channels, and is set at a high rate to swamp the DAQ (maximum throughput $\sim$30 Hz) and maximize the number of triggers corresponding to pulser events when it is operating.

5.1.3 Measurement of Environmental Backgrounds

The primary signature for which the CoGeNT experiment is searching is coherent neutrino scattering, a signature that disappears when the reactor is off. Simultaneously with the operation of the germanium detector, measurements of the relative thermal neutron, gamma and muon flux are made in the Tendon Gallery. The purpose of these measurements is to rule out the possibility that a fluctuation in backgrounds is correlated to a fluctuation in the rate in the detector. This is a remote possibility due to the high quality of the shielding. Nevertheless, the measurements are performed for the sake of completeness. Given that the detector is operating 25 m from the core of a nuclear reactor, it is easy to imagine that there could be a correlation of the thermal neutron or gamma rate with reactor operation. The measured rates are not easily correlated to absolute fluxes. Instead they are most useful as relative measurements where a search for correlations to the state of the reactor is possible. The following measurements indicate no such correlation, a likely result of the fact that the experiment is underground and outside of containment (a 5 ft thick concrete wall).

Thermal Neutrons

The relative flux of thermal neutrons is measured by a ^{3}He ionization tube that was used to measure the thermal neutron flux at three depths at the University of Chicago. The relationship between the rate of neutron capture, from thermal neutrons, and the level of overburden behaves as expected [Heusser, 1995]. The average rate of thermal neutron captures in the ^{3}He tube is 0.0014 cps. See 5.1.4 for a more detailed discussion.

The ^{3}He detector is also used to search for any thermal neutron backgrounds that might be related to the operation of the reactor. As can be seen if figure 5.2, there is no apparent change in the count rate of thermal neutrons when the reactor was turned on in May of 2008. This has been observed for several other reactor transitions as well.

Gammas

A relative measurement of the rate of environmental gammas was performed with a Bicron Brilliance-350 scintillating crystal. The crystal diameter is 0.75 in., and it is 1 inch long. To

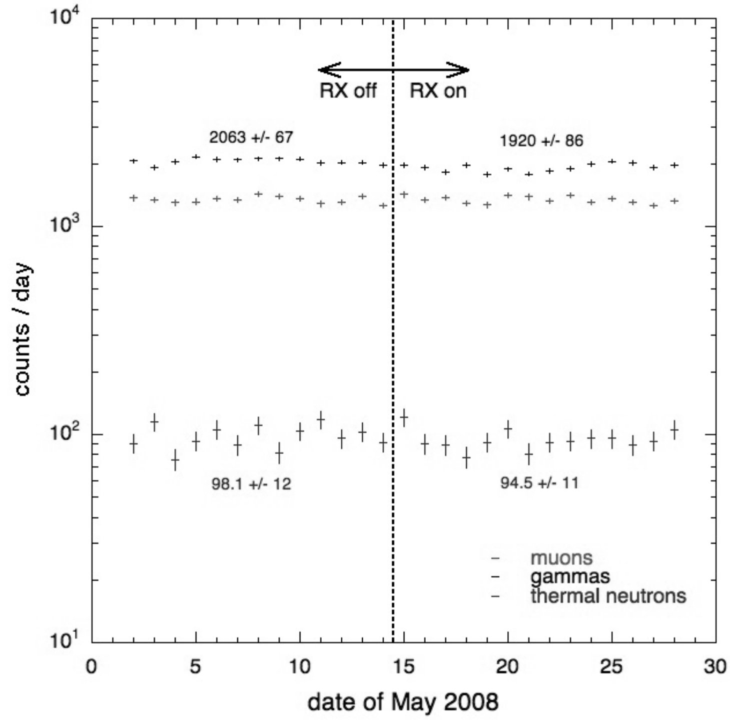

Figure 5.2: The behavior of several potential sources of backgrounds are measured near the shielding at the SONGS reactor. As is demonstrated here, there has been no observed change in the gamma or thermal neutron flux with reactor operation. Figure courtesy of J. I. Collar.

avoid counting the crystal's own intrinsic gamma (1.435 MeV) from ^{138}La, a DAQ threshold is set at 1.5 MeV. The upper level that defines the region of interest for counting environmental gammas is set at 3 MeV. This window is sufficient for measuring gamma backgrounds from ^{232}Th, for instance, while avoiding gammas internal to the crystal. It also excludes most muons passing through the crystal. The measurements show no apparent correlation of the gamma backgrounds with reactor operation (figure 5.2). This is not unexpected, as the Tendon gallery is outside of reactor containment and well shielded by many feet of dirt and concrete.

Muons

The measurement of the relative muon flux is also performed with the Brilliance-350 crystal scintillator by counting events that are out of range. These are events that are greater than 6 MeV, which is well above any naturally occurring gamma radiation. For a crystal of this size, most events from muons traversing the crystal pass this threshold. As can be seen in figure 5.2, there is clearly no significant change in the muon rate during the month of May, 2008. While no correlation with the operation of the reactor can be expected, the measurement can rule out changes in the muon flux, which can potentially cause fluctuations in the background.

5.1.4 Overburden

Deploying the experiment to the Tendon Gallery at the SONGS reactor provides a modest overburden to reduce backgrounds from cosmic ray sources (for a thorough treatment of the subject see [Heusser, 1995]). These backgrounds include muon induced neutrons and cosmic secondary neutrons. In order to simulate the expected contribution to the background from these sources, it is important to have an idea of the level of overburden, described in

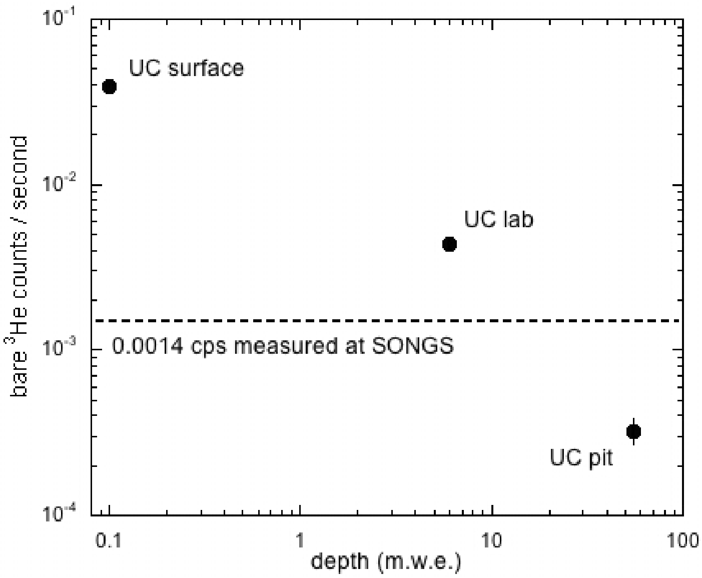

Figure 5.3: The thermal neutron capture rate in the ^{3}He detector is shown for a few levels of overburden at the University of Chicago, measured as part of a summer REU project by Robynne Hooper. Also depicted is the rate of thermal neutron captures in the Tendon Gallery at the SONGS nuclear reactor, suggesting an overburden there of approximately 20–30 m.w.e. This agrees well with estimates based on the depth of the gallery [Heusser, 1995]. Figure courtesy of J. I. Collar.

meters-water-equivilent (m.w.e.). Estimates for this value based purely on the depth of the experiment are rough because the experiment is so shallow, the terrain is irregular, there is a dependence on the composition of the overburden, and because there is a preponderance of large concrete buildings that comprise part of the reactor containment.

Instead, the overburden in the Tendon Gallery was estimated using measurements of the muon and thermal neutron flux. The raw rates do not correlate to an absolute flux, but are instead compared to rates at known depths to establish the overburden. In the case of the measurements of the muon rate using the crystal scintillator, and the thermal neutron rate using the ^{3}He detector, a comparison can be made to rates measured in Chicago at overburdens of 0 and 6 m.w.e. The resulting estimate of the overburden is $\sim$30 m.w.e.

Thermal Neutron Rate

Determining the flux of thermal neutrons as a function of the level of overburden is not a straightforward task, as there are many sources of neutrons that contribute. At the very shallowest depths, the population of thermal neutrons is dominated by the cosmic secondaries. This is very quickly overtaken by muon induced neutron production in nearby rock and heavy equipment, as the cosmic neutrons are attenuated but the muons are much more penetrating. This persists until the dominant source of low energy and thermal neutrons are (α, n) processes and natural fission in the rock walls [Heusser, 1995].

For the purposes of this experiment, the measurement of the neutron capture rate at several locations at the University of Chicago is used as a rough calibration for the rate versus the depth. These locations are a top floor office, a laboratory in a lower level basement, and a pit that extends down another 50 ft from the basement floor, with overburdens of 0.1, 6 and 55 m.w.e. respectively. As can be seen in figure 5.3, the rate measured in the SONGS Tendon Gallery corresponds to about 30 m.w.e. overburden. There are many factors that can contribute to the neutron flux at sea level [Ziegler, 1998], making the estimate very uncertain. It is far less rigorous than the estimate from the relative muon flux, and should only serve as ancillary evidence of the level of overburden at this location.

Muon Rate

The rate of muon events in the Brilliance-350 crystal scintillator in the Tendon Gallery was measured to be 16.6% of the rate measured on the surface at the University of Chicago. At shallow depths, muons are attenuated with a characteristic length of 2 kg$\cdot$cm^{-2} [Heusser, 1995]. A more accurate reduction can be estimated using the functional form for the dependence of muon flux on depth for shallow sites from [Bogdanova et al., 2006], from which an overburden of 32 m.w.e. is estimated. This is consistent with the measurement of thermal

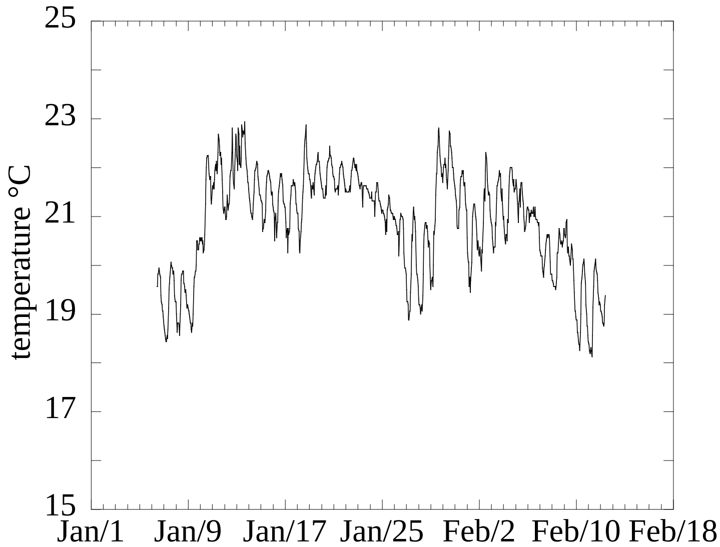

Figure 5.4: The temperature in the SONGS Tendon gallery was measured hourly. Daily fluctuations are clear, as are the changes due to outside weather conditions.

neutrons, and with estimates based on the construction of the gallery.

5.1.5 Ambient Temperature Measurements

The temperature measured in the SONGS Tendon Gallery outside the detector shielding is plotted in figure 5.4. There are daily modulations that are evident along with some dramatic shifts that are likely due to the day/night temperature variations and outside weather patterns, as the Tendon Gallery does not have any temperature control. This effect is smaller than the actual daily and yearly modulations of the outside temperature because the gallery is slightly insulated from the surface. The relative humidity was also recorded during the experiment. Condensation was observed around the detector endcap at $\sim 18^{\circ}$ dew point.

5.1.6 Liquid Nitrogen Generation

The location of the experiment in the Tendon Gallery is reached via a narrow ladder that makes delivering liquid nitrogen to the experiment nearly impossible. As a result, the liquid nitrogen must be produced next to the experiment. This was achieved with an Elan2 liquid nitrogen generator. The installation and maintenance of the unit was the responsibility of our colleagues at Sandia National Laboratories, who had regular access to the Tendon Gallery. The power consumption of the unit is low enough to operate under the 1 kW power limit. The LN2 is produced and temporarily stored in a 20L Dewar, at a rate between 3 and 7 L/day depending on the condition of the unit. Automatic transfers are made to the germanium cryostat Dewar approximately every 3 days in order to minimize transfer losses in the latex tube connecting the systems, while maintaining an adequate level of LN2 in the detector Dewar. The computer that controls the LN2 production and transfer system is isolated from the detector system to minimize ground loops and compressor noise from creeping into the signal.

5.2 Radioactive Backgrounds and Simulations

The following is an enumeration of several background spectra expected in the Coherent Germanium Neutrino Technology (CoGeNT) experiment at the SONGS reactor. Simulations for cosmic secondary neutrons, muon induced neutrons and internal gamma backgrounds using the MCNP-Polimi [Pozzi et al., 2003] Monte-Carlo framework are described. These should all be considered rough guides, as the final arbiter is always the experiment itself. Also described is a background in the low energy region from thermal neutron activation, producing ^{71}Ge, which arises from partial charge collection at the intersection of the active region and the lithium drifted dead layer. Finally, several peaks from cosmogenic activation of the germanium crystal are reviewed.

5.2.1 Cosmic Secondary Neutrons

The spectrum of cosmic secondary neutrons produced in the atmosphere is commonly referred to as the Hess spectrum [Hess et al., 1959]. These Hess spectrum neutrons are suppressed with a modest level of overburden. The effect of the CoGeNT shielding at reducing what remains at 30 m.w.e. was simulated using MCNP-Polimi [Pozzi et al., 2003], which is a version of the MCNP neutron propagation code that is modified in order to perform full analog simulations. MCNP-Polimi allows the exploration of coincidences between multiple detectors, as well as the identification of the spatial location, time and type of interaction. This ability is particularly useful for studying neutron backgrounds in this experiment because the NaI(Tl) anti-Compton veto is used as an anti-coincidence veto for the neutrons. Polimi provides information identifying the nuclear species involved in each interaction as well as the energy of each recoil, allowing a more accurate accounting of the light output from Na and I recoils in the veto. A cross section of the geometry used in these simulations can be seen in figure 5.5.

These simulations require an accurate knowledge of the ionization or scintillation produced in the germanium and NaI(Tl) detectors, respectively. For germanium recoils, the resulting ionization produced is based on a parameterization of the Lindhard theory for the quenching factor for nuclear recoils ($k = 0.2$), the measurement of which was reported on in chapter 4. In the case of Na and I recoils in the anti-Compton veto, the scintillation produced was estimated with a parameterization of the relative scintillation efficiency [Spooner et al., 1994]. Because of light losses in the NaI(Tl), and inefficiencies in light collection by the PMTs, an assumption must be made for the required level of scintillation to create a veto in the discriminator units. For these simulations this threshold is estimated to be a conservative 10 keV. As a result of the uncertainties in the parameterizations for the light output, and the somewhat arbitrary choice of the 10 keV threshold to produce a veto, this

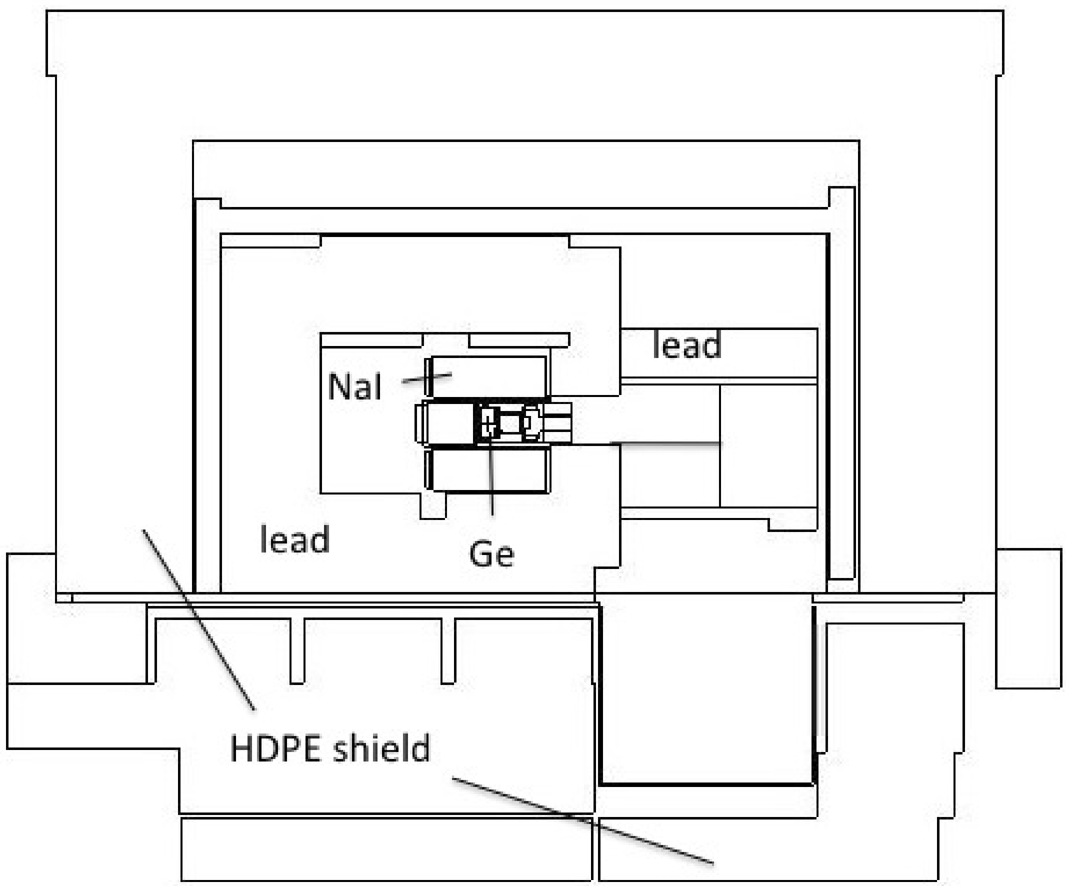

Figure 5.5: A cross section of an MCNP-Polimi [Pozzi et al., 2003] geometry is shown that was used in simulations of cosmic secondary neutrons, muon induced neutrons in the shielding materials, and gamma backgrounds from internal sources. The BEGe-1 germanium detector in its cryostat canister is located at the center. Also depicted are the NaI(Tl) anti-Compton veto, 20 cm of lead, the internal muon veto, and the HDPE neutron moderator.

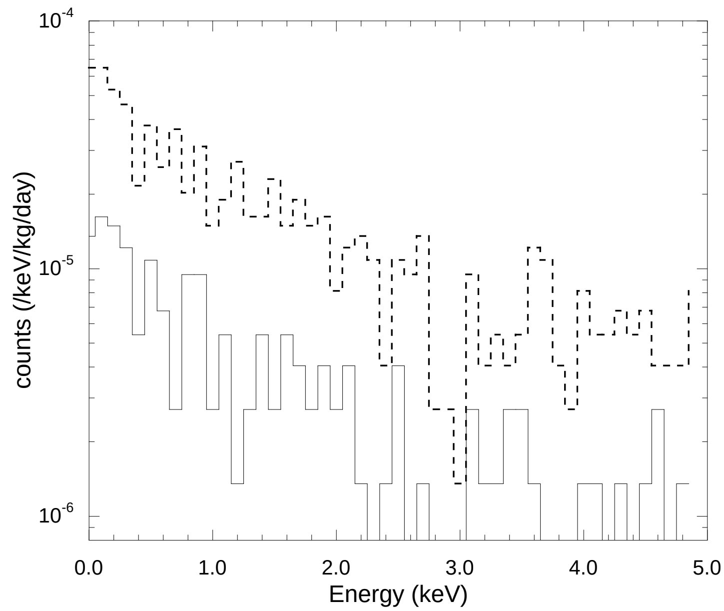

Figure 5.6: Simulation of cosmic secondary neutrons (i.e. the Hess spectrum) for the BEGe-1 germanium detector inside the full shield at 30 m.w.e. The dashed line is the raw spectrum assuming the NaI(Tl) anti-Compton veto has no effect on the neutrons. The solid line is the same, with a 10 keV threshold on the NaI(Tl), operating it in anti-coincidence mode for neutron scatters. These cosmic secondary neutrons are clearly not the dominant background at this depth, having been attenuated by at least a factor of 10^6. [Heusser, 1995; Bogdanova et al., 2006]

cut should be considered only an estimate of the effect of the NaI(Tl) anti-Compton veto on background neutrons.

In the energy range of interest, 1–20 MeV, the Hess spectrum obeys a simple power law [Hess et al., 1959]. The flux of cosmic secondary neutrons at sea level is taken to be 0.006432 $\mathrm{cm}^{-2}\mathrm{s}^{-1}$, although there is some variation over time and at different locations. It is attenuated with a characteristic length between 165–200 $\mathrm{g{\cdot}cm}^{-2}$ [see Heusser, 1995; Bogdanova et al., 2006]. This value is material dependent and is closer to 165 $\mathrm{g{\cdot}cm}^{-2}$ for concrete [Ziegler, 1998]. Therefore, at a depth of 30 m.w.e., the estimated cosmic secondary neutron flux lies within the range of 8.2×10^{-11} to $2.0\times10^{-9}\mathrm{cm}^{-2}\mathrm{s}^{-1}$. For these simulation estimates, the larger flux estimate is used as the more conservative value. The neutrons are best described by an isotropic flux distribution that was incorporated using a "cookie cutter" source built in a thin spherical shell surrounding shielding in the MCNP geometry. The rate these induce in the germanium detector can be seen in figure 5.6. Clearly, at the depth of this experiment, the surviving cosmic secondary neutrons are not the dominant source of background.

5.2.2 Muon Induced Neutrons in the Shielding

At the shallow depth of this experiment (30 m.w.e.), the dominant source of neutron backgrounds are from muon-induced neutrons. These cosmic tertiary neutrons (muons themselves being secondary) can be produced in the walls of the reactor and in heavy equipment near the experiment; but the most problematic interactions are those that occur in the shielding material very near to the detector. The problem is exacerbated for high Z materials, making the Pb shield the largest source of background neutrons in this experiment [Heusser, 1995]. Simulations of muon induced neutrons in the Pb shield and HDPE neutron moderator were made for an overburden of 30 m.w.e., again using MCNP-Polimi [Pozzi et al., 2003].

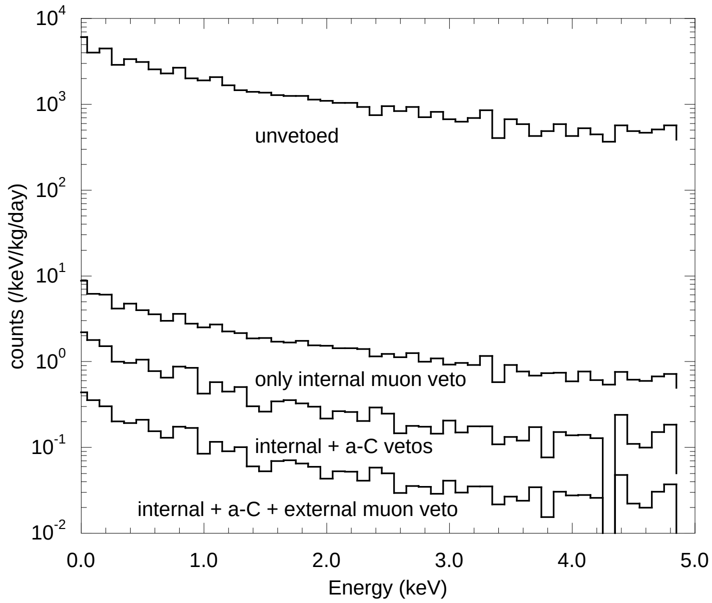

Figure 5.7: A simulation of signals in the germanium from muon induced neutrons in the Pb and HDPE shielding at 30 m.w.e is shown. The estimated effects of the vetoes are shown (10 keV NaI(Tl) threshold, 99.9% efficient internal and 80% efficient external muon vetoes). In the case were all vetoes are active, it is assumed that the 80% efficient external muon veto acts to enhance the veto efficiency of the internal 99.9% muon veto for muons that traverse the Pb.

The NaI(Tl) anti-Compton veto was again used to veto neutrons via an anti-coincidence technique. The background reduction from the operation of the two muon vetoes was also incorporated based on estimates of the muon detection efficiencies.

The neutrons were randomly and uniformly distributed throughout the Pb and HDPE shielding. The neutron trajectories were isotropic with estimated production rates of 2.55×10^{-6} g^{-1} s^{-1} for the Pb and $2.11\times10^{-7}g^{-1}s^{-1}$ for the HDPE, which is corrected for the density of carbon. Hydrogen does not contribute to this process. These production rates were estimated based on the measured production rate of neutrons in Fe, as measured by Gorshkov & Zyabkin [1973]. The attenuation as a function of the level of overburden for the 20–150 m.w.e. range can be well described by the power law: $R[g^{-1}s^{-1}] = 0.000111x^{-1.4294}$, where x is in m.w.e [Heusser, 1995]. The material dependence of the production rate is subject to some uncertainty, either $< A >^{0.9\pm0.23}$ or $< A >^{0.76\pm0.01}$ [Gorshkov & Zyabkin, 1973]. For these simulations, the value giving the largest production rate, which is the most conservative estimate of backgrounds, was used for Pb and C targets. The same values of the quenching factor in germanium and relative scintillation efficiency in NaI(Tl) that were used in the Hess spectrum simulation were used for the muon induced neutrons.

The spectrum for muon induced neutrons has two components, evaporative production and direct production. The magnitude and range over which each term is valid can change slightly, depending on the target. A complete treatment can be found in [da Silva et al., 1995; Formaggio & Martoff, 2004, and the references therin]. The dependence of the rates on the target are incorporated in these simulations, while the spectral dependencies are not because they are very small. As a result, the spectrum for Fe was used for both the Pb shield and the HDPE moderator.

The results in figure 5.7 indicate that at approximately 30 m.w.e., there should be little background in our signal region. This should be taken as a guide only because of the many uncertainties in the parameters used to generate this Monte Carlo estimate. To reiterate, there are large uncertainties in the actual threshold for detection of nuclear recoils in the NaI(Tl) veto. There are mild uncertainties regarding the actual overburden of this experiment. Within the literature, there are a range of estimates and measurements for the production rate of muon induced neutrons, and their dependence on the target. The spectrum of production, and its dependence of target species, is the least well understood aspect of this process. Where possible, the most conservative parameters were used to generate these estimates. This includes, but is not limited to, the efficiencies of the vetoes, the attenuation of muons by the overburden, and the production rates of neutrons in the target nuclei.

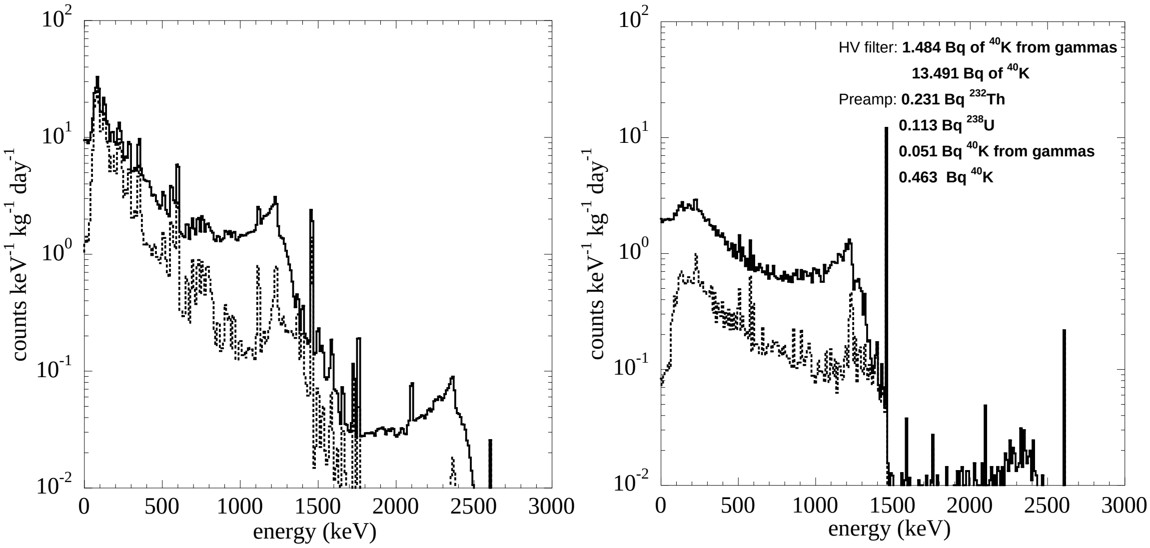

Figure 5.8: Simulations of gamma backgrounds from sources in the detector cryostat. The estimated contribution from high background aluminum in the cryostat endcap is shown (left), along with the effect of the NaI(Tl) anti-Compton veto. Also shown is the contribution from the electronic components in the preamplifier box (right), for which the level of radioactivity was characterized separately. (see A)

5.2.3 Background Gammas from Internal Sources

Sources of gamma radiation from natural radioactivity near the detector can cause low energy backgrounds from highly forward-peaked Compton scattering. These background gammas, typically from ^{40}K and the ^{238}U and ^{232}Th decay chains [Hess et al., 1959], are able to be suppressed by an order of magnitude by the NaI(Tl) anti-Compton active veto. Nevertheless, large contaminations in construction materials can lead to higher than desired background levels. MCNP-Polimi [Pozzi et al., 2003] simulations were performed to characterize some of these background sources, as well as to determine the effectiveness of the anti-Compton veto.

It is instructive to consider the most dominant sources of background as they were addressed during the course of this experiment. Typically, the sources closest to the detector will contribute the most. The PPC-1 detector was initially constructed out of a standard aluminum cryostat, including the can, crystal holder and the additional aluminum parts attached to the cold finger. These can be seen in figure 2.5. As was reported in [Barbeau et al., 2007b], the initial backgrounds were very high, which are a result of high levels of radioactive contamination in the standard aluminum. This was quickly remedied by the replacement of the parts with low background aluminum by the vendor. A simulation was performed to study what backgrounds would result from PPC-1 if the additional aluminum parts were still made with standard stock. The results, seen in figure 5.8, show the still high levels even after the can and crystal holder no longer contribute. While the effect of the anti-Compton veto is dramatic, the resulting backgrounds are still very high. In addition, the simulation only included gammas with branching ratios greater than 0.01, and it completely ignored the contribution from Bremsstrahlung photons from the many beta decays in the aluminum. Materials within the cryostat, as well as those touching the crystal, clearly need to be clean. The next largest source of background gammas from PPC-1 comes from the electronics in the rear of the cryostat, as they have a line of sight directly to the detector (also illustrated in figure 2.5). Duplicates of the preamplifier and high voltage filter were counted in the low background counting facility at the University of Chicago, reported in appendix A. The resulting simulated contribution to the background can be seen in figure 5.8. It is significantly lower than the contribution from the additional aluminum parts, but it is still relatively high. The effect of the anti-Compton veto is to reduce the level of backgrounds sufficiently in order to perform a coherent neutrino scattering experiment ($\sim$ 1–5 counts kev^{-1} kg^{-1} day^{-1}). Without it, however, the background level is prohibitively high.

As a result of these simulations, steps were taken to ameliorate these backgrounds with the deployment of the BEGe-1 detector in the same shielding. First, all of the internal metal parts are now made of OFHC copper, eliminating even the low background aluminum (<2 ppb U, Th). Another benefit of the BEGe-1 detector is that the preamplifier box is offset from the main body of the cryostat. As a result, low background lead bricks were placed between the electronics and the crystal, eliminating the line of sight to this source of backgrounds.

Beyond these closest sources, it is difficult to account for further sources of gamma backgrounds. The next closest is the construction material of the anti-Compton veto. While it was refurbished to reduce backgrounds, replacing the inner cavity aluminum wall with thin stainless steel, there are many other potential sources of unknown activity. These include screws, epoxy, reflective powder near the NaI(Tl) crystal, and the NaI(Tl) scintillator itself. We are able to estimate the contribution from the lead bricks that make up the shield. It is exceedingly difficult to simulate the backgrounds from Bremsstrahlung gammas produced in the Pb shielding from ^{210}Pb because of the large number of computations that is required to track the slowing down of the betas in the lead. Such a simulation has been performed in Vojtyla [1996] for a detector with a shield geometry very similar to the one described here. Making the comparison to this experiment, where the Pb bricks that make up the shield are estimated to have 14 Bq/kg of ^{210}Pb, gives an estimate of 1–2 counts keV^{-1}kg^{-1}day^{-1}. This does not account for the fact that the anti-Compton veto is located between the detector and the lead in most directions. Estimating a solid angle for the direct line of sight to the lead bricks of ∼10% gives results of 0.1–0.2 counts keV^{-1}kg^{-1}day^{-1} before any consideration of the effect of the active veto. Therefore, the expected background from ^{210}Pb is negligible.

In fact, there is unlikely to be any single source of gammas that can be easily blamed for the majority of the backgrounds. Instead, any further reduction of backgrounds will likely come from a more complete abatement program, such as those considered in $0\nu\beta\beta$ decay experiments (Majorana , Gerda).

5.2.4 Thermal Neutron Activation: ^{71}Ge

There is a particular background in the low energy region for this experiment that is caused by partial charge collection at the dead layer of the germanium crystal. The effect causes radiation from electron capture isotopes to contribute to the lowest energy backgrounds that would otherwise not be an issue. One of the most dominant of these electron capture peaks is caused by the thermal neutron activation to ^{71}Ge. ^{70}Ge makes up about 21% of the natural abundance of germanium, and it has a high cross section for thermal neutron absorption ($\sim 3\times 10^{-24}$ cm^2) [Jen, 1997]. During fabrication on the surface and transportation via plane, a normal germanium detector can be exposed to a copious amount of thermal neutrons. The capture produces ^{71}Ge nuclei, which decay with an 11.43 day half life via electron capture. A peak in the spectrum of the germanium detector is produced by a cascade of x-rays and Auger electrons after the capture of either a K-shell or L-shell electron. The energy of the cascades adds up to 10.3 and 1.30 keV, i.e., the binding energy of the K and L-shells of ^{68}Ga. The L-shell peak comprises $\sim$ 12% of the electron-capture decays [Genz et al., 1973; Abdurashitov et al., 1999] .

While the peaks pose a moderate problem as a background, see 5.2.5, this is more than made up for by their usefulness as low energy calibration points. The real background problem arises because of the nature of the p-type germanium detector. If a decay occurs near or within the Li-drifted dead layer of the detector, there is a chance that only a portion of the ionization produced by the decay drifts out of the dead region. This leads to a plateau in the spectrum below the 1.3 and 10.3 keV peaks, which represents $\sim$ 2–4% of the total number of decays. This correlates roughly with the fractional volume of the dead region. Depending on the level of exposure to thermal neutrons, this plateau from partial charge collection can be the dominant background. This is exhibited in figure 5.9, where the PPC-1 detector was inadvertently exposed to a large flux of thermal neutrons prior to its deployment

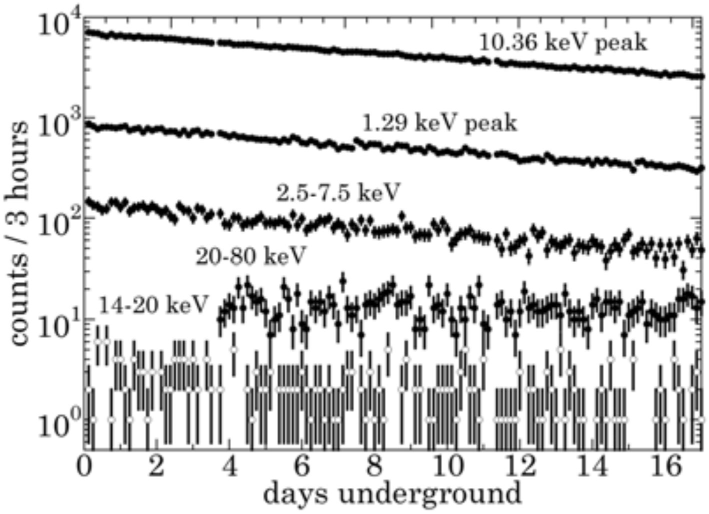

Figure 5.9: The low energy plateau from incomplete charge collection was conclusively identified with the thermal neutron activation of PPC-1. The region between 2.5–7.5 keV below the K shell peak from ^{71}Ge decayed with the same 11.4 day half-life as the peak, indicating that 3–4% of all events in the K-shell will suffer from partial charge collection. This partial charge collection can be seen in the spectrum in figure 8.15 The effect is attributed to partial charge collection at the intersection of the active and lithium drifted dead regions. Figure courtesy of J. I. Collar.

to SONGS.

The most obvious solution to background problem from thermal neutron activation is to wait for the detector crystal to deactivate for several half-lives. The 11.43 day half-life of ^{71}Ge makes this a reasonable option even for experiments that have stringent time constraints, like the current deployment to the SONGS reactor. However, it is important to always protect the detector with thermal neutron absorber during manufacture, transport, and storage in order to minimize the amount of time required. Even then there is a limit to the lowest rate achievable that is imposed by the decay of ^{71}Ge in equilibrium with its production from thermal neutron activation within the detector shield. However, even if thermal neutrons could be eliminated there is still the much longer lived decay of ^{68}Ge, from cosmogenic activation, which produces the same background spectrum. Depending on the level of exposure on the surface, and the length of the deactivation period, other electron capture peaks will also come into play.

5.2.5 Backgrounds from Cosmogenic Activation

Cosmogenic activation of detector materials is a source of unwanted signals that needs to be considered for most low background experiments. The activation from cosmic secondaries typically occurs on the surface, or in air transport, where there are ∼150 times more neutrons of the same hardness at 30,000 ft. This experiment is focused on signals in the low energy region, and thus the backgrounds of interest are those that occur in the 0–20 keV region. While there are many radionuclides that can decay with the emission of a beta, these events are unlikely to affect this experiment because of the narrow energy region of interest, close to the threshold. It is the electron-capture decays that constitute the background, resulting in the emission of a cascade of x-rays and Auger electrons equal to the energy of the captured electron shell for the daughter nucleus. The result is a population of peaks in the low energy spectral region.

A compilation of likely sources of background peaks can be seen in tables 5.1 and 5.2. The radionuclides with intermediate half-lives are the most bothersome. They do not decay away immediately, but their half-lives are not so long that the detector would rarely see a decay. Some radionuclides, like ^{71}Ge, decay directly into their ground state, where the only indication of the decay is the existence of the peak itself. For most of the rest, there is a significant branching ratio to decay into the ground state; however, they also have non-zero branching ratios from electron capture that coincide with the emission of a de-excitation gamma from the daughter nucleus. For these decays, several things can occur. The first is that the gamma can escape the germanium crystal and also avoid the NaI(Tl) anti-Compton veto, leaving the peak in the spectrum as the only signature of this decay. There is also the possibility that a coincident gamma interacts with the germanium crystal, contributing to the energy deposition of the peak. These events never tally under the peak, but instead add to the continuum background at higher energies. The final possibility is that the coincident gammas escape the germanium crystal without depositing energy, but then interact with the NaI(Tl) anti-Compton veto. This causes the peak to show up in the spectrum of coincidences. The energies of these coincident peaks and their branching ratios from electron capture are also recorded in tables 5.1 and 5.2.

Simulations using MCNP-Polimi [Pozzi et al., 2003] were performed for events that coincide with gamma emission for the BEGe-1 detector, the results of which are reported in table 5.1. A simulation was also performed for a the deployment of the PPC-1 detector in the shield, the results of which are reported in table 5.2. The percentage of electron capture decays that coincide with the veto, and that are anti-coincident with the veto, were determined. These percentages do not add to 100% because of the possibility that the gamma interacts with the germanium. Using these percentages, the ratio of vetoed peak events to unvetoed peak events is listed. This signature is key in the experiment because it verifies that the detectors behave as expected. As an example, for ^{65}Zn decay, the size of the peak in the coincident veto spectrum is $\sim$0.48 that of the peak in the unvetoed spectrum, in agreement with the expectation, which is listed in table 5.1.

In addition to the gamma coincident signature, there are half-life signatures in the decays of these radionuclides that can be exploited. An example is the 67.8 m time correlation between the decay of ^{68}Ge via electron capture and the subsequent decay of its daughter, ^{68}Ga. In the decay of ^{73}As, 100% of the decays are via electron capture to the $1/2^-$ excited state, which decays with a half-life of 0.499 s with the emission of a 54.4 keV gamma. The gamma will almost never escape the crystal, meaning nearly every measured decay of ^{73}As in the germanium will be promptly followed by another event in the germanium. In this experiment, the second decay appears as an event out of range, but otherwise unvetoed.

Table 5.1. Veto Efficiencies for Cosmogenic Peaks in BEGe-1

			Coincident γ's		Simulated Veto Efficiencies		
Isotope	half-life (days)	Peaks (keV)	Energy (keV)	BR from EC (%)	Vetoed Peaks (%)	Unvetoed Peaks (%)	Ratio
^{40}K	1.25×10^{9} Y	3.206	1,460.9	98.15	51.3 (58.0)[a]	12.5 (18.2)[a]	4.17 (3.19)[a]
			···	1.84			
^{51}Cr	27.70	5.478	320.1	9.9	3.6	90.6	0.039
			···	90.0			
^{57}Co	271.74	7.128	122.1, 136.5	99.8			
^{58}Co	70.86	7.128	810.8	98.8	47.3	6.3	7.47
			864.0 + 810.8	0.7			
			1,674.7	0.5			
^{65}Zn	244.06	8.980	1,115.5	50.6	25.8	53.6	0.48
			···	49.4			
^{68}Ga	67.71 M	9.668	1,077.4	3.4	1.7	96.9	0.018
			···	96.6			
^{68}Ge	270.95	1.298, 10.368	···	100	···	100	···
^{71}Ge	11.43	1.298, 10.368	···	100	···	100	···
^{73}As	80.30	11.113	53.4 + 13.3	100			
^{74}As	17.77	11.113	595.9	89.3	40.6	15.3	2.65
			···	10.7			

[a]The value in parenthesis was calculated assuming a point source of ^{40}K that was 4 cm from the point contact electrode.

Table 5.2. Veto Efficiencies for Cosmogenic Peaks in PPC-1

			Coincident γ's		Simulated Veto Efficiencies		
Isotope	half-life (days)	Peaks (keV)	Energy (keV)	BR from EC (%)	Vetoed Peaks (%)	Unvetoed Peaks (%)	Ratio
^{40}K	1.24×10^{9} Y	3.206	1,460.9	98.15	52.0	13.3	3.85
			⋯	1.84			
^{51}Cr	27.70	5.478	320.1	9.9	3.8	90.4	0.042
			⋯	90.0			
^{57}Co	271.74	7.128	122.1, 136.5	99.8			
^{58}Co	70.86	7.128	810.8	98.8	47.0	6.2	7.69
			864.0 + 810.8	0.7			
			1,674.7	0.5			
^{65}Zn	244.06	8.980	1,115.5	50.6	25.7	53.9	0.48
			⋯	49.4			
^{68}Ga	67.71 M	9.668	1,077.4	3.4	1.7	96.9	0.017
			⋯	96.6			
^{68}Ge	270.95	1.298, 10.368	⋯	100	⋯	100	⋯
^{71}Ge	11.43	1.298, 10.368	⋯	100	⋯	100	⋯
^{73}As	80.30	11.113	53.4 + 13.3	100			
^{74}As	17.77	11.113	595.9	89.3	41.8	14.8	2.86
			⋯	10.7			

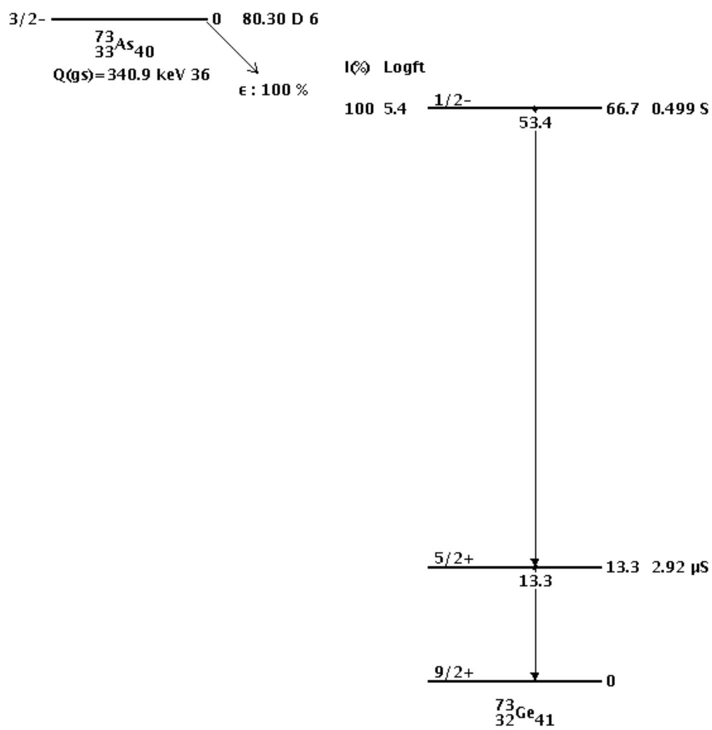

Figure 5.10: The decay scheme for ^{73}As produced by cosmogenic activation in the germanium detector. The time correlation between the 11.1 keV k-shell peak after the electron capture and the events in the germanium detector from the 53.4 keV gamma is used to help identify this radionuclide background. This diagram was obtained from [Nuc, 2009].

The short half-life of the intermediate state makes detecting this time correlation possible because the trigger rate of events above 20 keV is not prohibitively large. Also, the detection of this decay in significant numbers indicates that the germanium crystal has suffered from proton activation as well as neutron activation from cosmic secondaries [Barabanov et al., 2006].

Table 5.1 also includes the simulated veto percentages from a point source of ^{40}K that is 4 cm from the electrode. There is no reason to believe that there is any ^{40}K contamination in the germanium crystal, or the nearby cryostat components, at detectable levels. If there were, a significant peak would be visible in the anti-Compton coincident spectrum.

5.3 Microphonic Background Suppression Scheme

Microphonic background noise in germanium detectors arises from vibration induced changes in the capacitance of the electronics of the detector. The result is typically an excess of low energy background near threshold. Microphonic events can be caused by acoustic noise produced near the detector, vibrations transmitted to the detector from nearby equipment, and also by vibrations induced in the detector cryostat from LN2 boiling during and immediately after refills.

5.3.1 Vibration Reduction

The significant thickness of the HDPE and lead shield tends to reduce the effect of acoustic noise. Reduction of backgrounds from nearby equipment, such as the compressors used in the LN2 generation, is achieved by separating the cryostat and Dewar from the shield with a vibration damping pad. The pad is made of alternating layers of 1 cm thick aluminum sheet and 1.3 cm thick cork board. During the construction of the shielding, great care was taken to prevent the detector cryostat and Dewar from touching any parts of the shield other than the damping pad, reducing the transmission of vibrations to the detector.

It also is possible to suppress microphonic background in the data analysis using several techniques. These were extensively developed and studied in Morales et al. [1992]. The first and easiest technique is to eliminate data sets that correspond to periods of time during and immediately after refilling the Dewar with LN2, when there is a lot of vibration caused by the boiling of the LN2. In this experiment, this is simply done by keeping track of the times of the refills.

5.3.2 Analog Filtering

Another method developed by Morales et al. [1992] involves using two amplifiers with different shaping times for the conditioning of the signal. The technique is based on the assumption that signals from microphonic noise have a fundamentally different time structure than real signals from the preamplifier. While real events are amplified similarly in each amplification channel, microphonics can lead to completely different amplitudes. It is this difference which provides a parameter that helps to differentiate bad events. The Particle Identification (PID) parameter is the ratio of the peak amplitudes of the 6 μs shaping amplifier to the 10 μs amplifier. The ratio should be $\sim$1 for good events, but can be dramatically different for microphonic events.

The second handle on microphonic events comes from the observation that they tend to occur in bunches. The time correlation, generally long-lived compared to the shaping time of the electronics, is likely due to the nature of the vibration causing the background signal. The low event rate in this experiment makes suppressing this population fairly straightforward. This method was seen to be completely complementary to the use of the PID parameter mentioned above. All of these techniques for microphonics suppression are used in the construction of this experiment and analysis of the data, which is covered in more detail in section 6.3.

There is another method for reducing microphonic backgrounds, which may or may not already be removed by the application of analog filtering techniques. It was developed in the IGEX experiment to further reduce the low energy component of their background [Irastorza et al., 2003]. The idea involves using wavelet analysis on the recorded waveforms to identify potential signal peaks sitting on a background of noise. When a candidate pulse is identified, the measured width of the pulse is compared to the width expected from real ionization events. Microphonic signals, which can have larger characteristic widths, are suppressed by requiring that the widths be within a narrowly defined window. Wavelet analysis was tested for this experiment, but was not seen to offer enough benefit in further background reduction, while imposing an unacceptable penalty in the CPU time associated to the analysis. It remains an option for future work.

CHAPTER 6

ANALYSIS OF SONGS DATA

An overview of the data analysis from the deployment of the BEGe-1 detector at the SONGS nuclear reactor is presented. This is a unique instrument deployed in a unique environment which enables searches for new physics. The experiment was deployed for ~230 days before it was required to be removed from the Tendon Gallery because of a scheduled reactor upgrade. Several unexpected incidents limited the operating time to only ~110 days, at intermittent intervals. The experiment commenced when it was still suffering from high backgrounds due to cosmogenic activation during transport, which resolved over time. Power was occasionally lost in the gallery, which prevented access to the experiment, and therefore there were very often periods without sufficient LN2 production to operate the detector. All of these factors significantly affected the operating time of the experiment. The result is a total of four data runs that are operated under varying conditions and that began and were terminated at odd intervals. These are described below in detail. This chapter covers the analysis of the recorded waveforms to determine event energy, as well as the identification and removal of radioactive and microphonic background events. Also covered are the many in-situ measurements, including the live time fraction determination and energy calibrations using several low energy internal background peaks. Finally, the resulting energy spectra are presented for further analysis in the context of specific physics applications performed in later chapters.

6.1 Description of Data Sets

The data files contain the recordings of the four waveforms from the scope cards. The recording time for each file is approximately 3 hours. Every two hours the DAQ turns on the test pulser for a minute in order to measure the veto live time fraction. The data files are saved and transferred to an external hard drive at intervals up to three weeks apart, because neither a continuous presence nor a high bandwidth data connection is possible at the reactor site.

There are four main categories of data recorded that are characterized by the state of the experiment or the reactor. They are enumerated as Runs 1–4. There are also sub-categories, which will be delineated, that are a result of changes in the operation of the experiment, which were made in order to perform cross checks or eliminate systematics.

The first set of data (Run 1) witnessed fairly flawless operation. The only draw-back was that the detector still suffered from significant cosmogenic activation obtained during transport. Unfortunately, after 3 weeks of operation, the detector was shut down because of difficulties with the LN2 production. It remained off for another month until production could be restored. The data from Run 1 have proven extraordinarily useful because of the availability of six cosmogenic lines below 10 keV that are used for low energy calibrations. The fast decay for some of the isotopes meant that some peaks quickly disappeared and were not apparent in later data sets.

When the experiment was restarted, it was observed that the anti-Compton veto was not performing correctly. It was determined that the origin of this was in the failure of one of two NIM logic units in the intervening time between runs. It was soon replaced. While many of the background peaks had decayed by this time, the partially functioning veto compensated for the reduction in backgrounds, leaving them high. Approximately two weeks of data (Run 2) were recorded before the faulty unit could be replaced. This second set of data is fairly useless on its own in comparison to the other data runs. Furthermore, during the early days of this set the LN2 level was so low that it provided minimum cooling to the cryostat. As the detector warms up, the leakage current increases, thus the detector suffered an enhanced sensitivity of the electronic noise to the ambient temperature of the gallery for several days, as well as a noticeably higher detector noise.

Table 6.1. Data Runs for the BEGe-1 Detector at the SONGS Reactor

Run	Live Time (days)	Dates Operated	Reactor State	Notes
Run 1	20.86	11/13/08–12/4/08	OFF	High background from activation
Run 2	17.05	1/6/09–1/8/09 and 1/12/09–1/27/09	ON	Broken A/C veto logic
Run 3 (Ch1)	39.61	1/28/09–2/27/09	ON	LN2 low → poor threshold
Run 3 (Ch2)	33.77	1/28/09–2/27/09	ON	$\sim$ 6 days at higher dynamic range
Run 4	28.49	6/1/09–6/30/09	ON	Low backgrounds and low threshold

The third set of data (Run 3) begins with the repair of the logic unit and the restoration of the full background rejection capability of the anti-Compton veto. Eventually it too was stopped due to poor production rates of LN2. By this time, the short lived backgrounds had decayed away. It is during Run 3 that several temporary adjustments were made in order to characterize the behavior of different aspects of the detector and veto system. For the first week of this set, the range of the high energy waveform (Ch2) was increased to measure depositions as high as 60 keV. While this cannot be easily included in any spectra produced from Ch2, channels 0 and 1 were not adjusted and are therefore perfectly valid measurements. Thus these channels experienced about a week more live time than Ch2 during this low background data set, which is reflected in the tabulated live time (table 6.1). After the first week, the range of Ch2 was returned to a maximum of 15 keV, operating as it was originally intended for the next two weeks. During the week following this, the magnitude of the test pulser was reduced to two-thirds of its initial value; it was still easily observed in all three channels. The pulser was then turned off for a week in order to rule out any contamination of the low background spectrum from untagged pulser events, the same reason why it was reduced in the first place. It was subsequently restored to its two-thirds value for the remainder of the deployment. Unfortunately, liquid nitrogen production was sporadic for the full run, resulting in an extremely poor electronic noise threshold for this data set.

The last data set (Run 4) lasted for $\sim$28.5 days, had very low background levels, and had sufficient LN2 in the Dewar to maintain a low energy threshold ($\sim$0.5 keV). Some of the best results for this deployment come from the analysis of Run 4. Unfortunately, it too was ended prematurely due to a misbehaving LN2 generation unit that could not be fixed because the exhaust fans were shut down to the Tendon Gallery. This was the last set of data at this site because the experiment had to be removed due to construction activities at the reactor (steam generator replacement).

6.2 Waveform Analysis

Analysis of the data files containing the event waveforms was performed by a code written in Python within the ROOT framework (PyROOT) [Brun & Rademakers, 1997]. The goal of this initial analysis was to determine the peak height of events in all three channels and to record the type and timing of the three active vetoes. The results were recorded in the form of ROOT n-tuples to provide easy access to the salient signal characteristics on an event-by-event basis with a secondary code. Also recorded were several ancillary pieces of information including the name of the data file for the event, the event number within its data file, the date and time of the event with ms precision, and a flag indicating whether or not the automatic pulser was operating. A separate independent analysis of the data was performed using labVIEW, as a cross-check of the software and hardware cuts to the data.

6.2.1 Peak Height Determination

Particular care must be taken when determining event energies because of the proximity of the signal to the noise threshold. In order to eliminate the effects of digitizer noise in the 8-bit cards, the waveforms from channels 0–2 were sent through a software median filter of degree 2. This smoothed out any high frequency "hairs" in the waveform. The magnitude of the event peak is determined in each waveform by subtracting the maximum voltage of the event from the waveform baseline. The uncertainty in the determined peak amplitude is strongly coupled to any transient deviations in the measured baseline, requiring pre-trace information that is as long as reasonable. A sample waveform can be seen in figure 6.1. The search for the peak maximum is limited to the last 100 μs, and the mean of the baseline is determined in the first 300 μs of the waveform obtaining a very precise value.

In addition to recording the voltage magnitude of asymptotic signals, events that are due to artifacts of the detector or DAQ must be identified and eliminated. For this experiment,

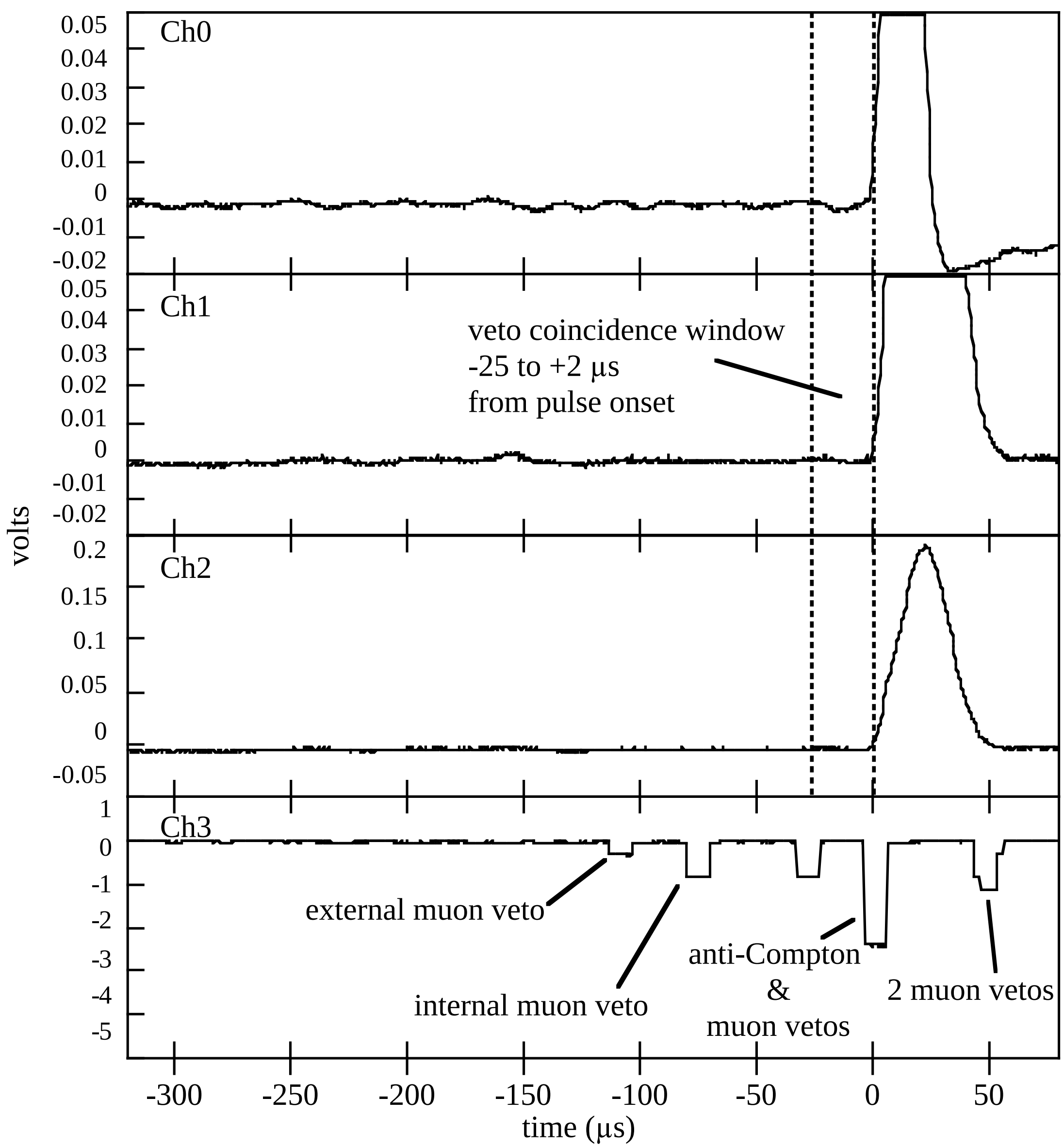

Figure 6.1: An example waveform from the DAQ, measured at the SONGS reactor. This particular event is out of range of the low energy channels (0, 1), but is measurable in the high energy channel (2). Several veto events are recorded, though only one causes the event to be vetoed, falling within the coincidence window.

there are two types of anomalous signals that must be discarded that are due to the pulsed resets of the preamplifier. A cut was used to remove any event with a large negative excursion in the waveforms that occured with the pulse reset of the preamplifier. The second, more subtle artifact, is a result of a linear gate that was used to reduce the number of event triggers due to resets. The linear gate, upon receiving an inhibit signal from the preamplifier that a reset is imminent, gates off the signal from Ch0 and thus prohibits an event trigger. Unfortunately, the level of the gated baseline does not always match the level of the un-gated waveform baseline. Thus, there is an occasional waveform recorded were a portion of the first 300 μs contains two distinct levels in the baseline because the linear gate was removed some time during the waveform. This causes a misidentification of the baseline, and thus the peak amplitude of Ch0. Such an occurrence is rare enough that it was only ever identified with events from the pulser run, when the trigger rate was intentionally maximized. An accurate measurement of the peak height from Ch0 and Ch1 are vital for accurate rejections of microphonic events, thus any event exhibiting this two-level baseline is eliminated.

6.2.2 Vetoes

Identification of vetoed events is not as straightforward as the determination of the peak height because the three veto signals must be de-convoluted from the waveform in Ch3. Each veto has a 10 μs width, but a different characteristic pulse height. An example containing all three distinct veto types, as well as some combinations of vetoes, is displayed in figure 6.1. The smallest pulse, from the external muon veto, is $\sim$ -0.4 V. Next is the internal muon veto at $\sim$ -0.9 V and the anti-Compton Veto at $\sim$ -1.6 V. When combinations of veto events to occur there is no ambiguity because the pulse heights for all possible combinations are unique.

With the identification of the types of veto events in hand, the next step was to determine whether any of the vetoes were coincident with the signal from the germanium detector. This was achieved by performing a search on the Ch3 waveform for the onset of a veto pulse and measuring the time difference between each veto event and the onset of the signal from the germanium detector. Only the time difference between the signal onset and the nearest veto is recorded for all three veto types. It is this time difference that is used to determine if an event is vetoed. An event is in coincidence with a pulse from the anti-Compton detector if the veto arrives within 25 μs before and 2 μs after the onset of the germanium signal. This is based on a data run taken in the lab in a similar shield where there was clear evidence for neutron straggling within 25 μs. The conservative 2 μs excess after the germanium signal onset ensures that no delays of the signals, or slight misidentifications of the signal onset, can cause events to go unvetoed. The same time coincidence window is used for the internal muon veto signals. The coincidence window for the external muon veto is smaller, extending to only 10 μs before the onset of the germanium signal. This is because its event rate is very high and would otherwise cause too much dead time. The elimination of events that are coincident with the vetoes has a dramatic effect in reducing the overall backgrounds in this experiment, as can be seen in figure 6.2. In addition, the separation of the vetoes into three different types provides a useful way to study the types of energy depositions that are associated with each veto. Specifically, those coincident with the anti-Compton veto allow the study of compound decays from radioactive isotopes in the germanium detector that also interact with the NaI(Tl) crystal surrounding it (see 5.2.5).

There is a significant ($\sim$10%) accidental identification of vetoed events resulting from the nearly single photon thresholds set on all of the veto PMTs. The percentage of dead time incurred is characterized in section 6.4.3 using the periodic pulser measurements.

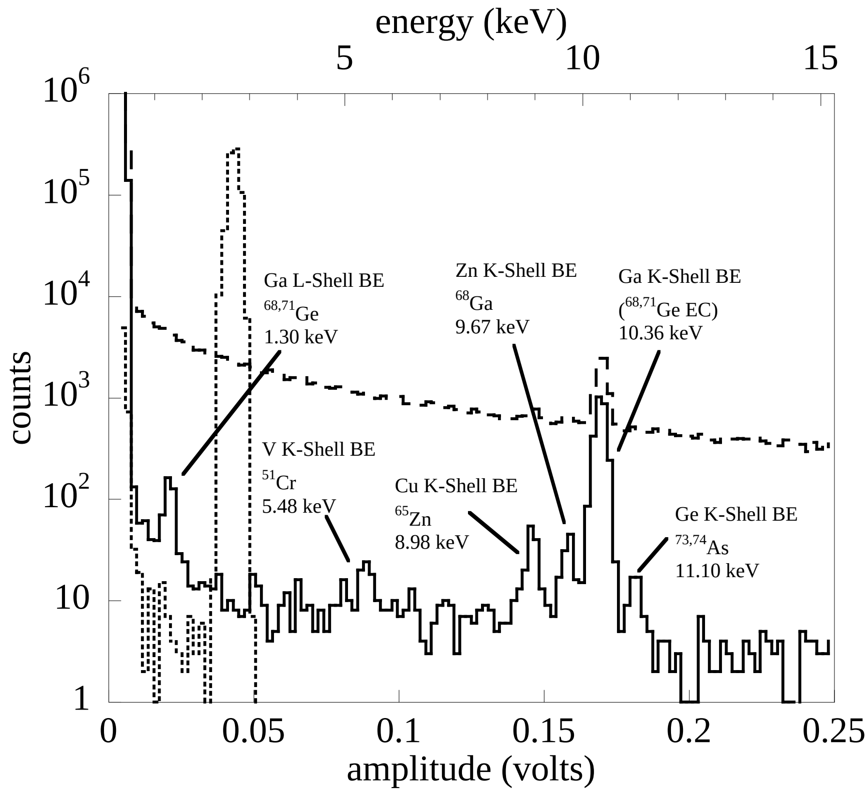

Figure 6.2: Background spectrum used to calibrate the high energy channel (Ch2), collected during the first 21 days of operation. A number of cosmogenic peaks are apparent. Several of them are observed for the first time in a germanium detector experiment by virture of the excellent energy resolution of PPCs. The pulser peak is shown (dotted line), as is the unvetoed spectrum displaying the dramatic reduction in backgrounds from the triple active veto. This level of backgrounds is not yet sufficient for a measurement of coherent neutrino-nucleus scattering.

6.3 Suppression of Microphonic events

Steps were taken in the construction of the detector shielding to reduce the occurrence of microphonic backgrounds by isolating the detector cryostat from environmental vibrations. While this is effective, it is unable to eliminate all microphonic backgrounds, specifically those resulting from the boiling of LN2 in the detector Dewar. The identification and removal of these microphonic events is discussed below.

6.3.1 Particle Identification

The first method that was used to remove microphonic events utilizes a Particle Identification parameter (PID) that is the ratio of peak amplitudes from amplifiers with two different characteristic shaping times. The technique [Morales et al., 1992; Goulding, 1972; Goulding & Landis, 1982] relies on there being a fundamental difference between legitimate signals and the microphonic background that is reflected in the value of the PID parameter, resulting in an anomalous ratio for microphonic events. A scatter plot of the peak amplitude of Ch1 (in Volts) versus the PID parameter can be seen in figure 6.3. The data was obtained for a group of events generated by a pulser that was scanned over the range of Ch1. The ratio of Ch0/Ch1 is centered around a value of 0.9, reflecting the slightly mismatched gain of the two amplifiers. For lower energies, the distribution of the measured ratio broadens because of the increased impact of the electronic noise on the two peak amplitudes. The low energy reach of this population, below the nominal threshold of 0.007 V, is achieved by maximizing the rate from the pulser so that the DAQ is predominantly triggered by these pulser events instead of baseline noise.

The population of events in figure 6.3 helps define the window of PID values for which an event is considered acceptable. A similar scatter plot, in figure 6.4, displays events that were coincident with the anti-Compton veto (solid dots), and are thus true radiation induced

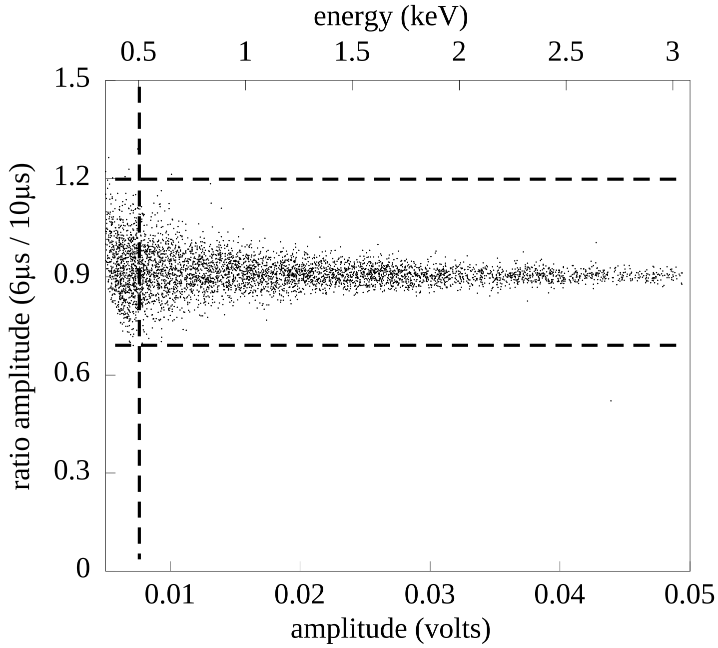

Figure 6.3: The distribution of PID values versus energy is shown for events created by a test pulse generator. Events pass the PID software cut if they fall within the dashed lines.

events. The lobe at low energies (open circles) for PID values < 0.7 is populated with microphonic backgrounds that evidently give rise to an anomalous ratio. A cut is placed to reduce the contribution from these signals that eliminates all events with a PID value < 0.7 or > 1.2. This window eliminates some of these backgrounds, but it is clear by inspecting the population of asymptotic events from the scanned pulser data set that above the nominal threshold of 0.007 there are no such events eliminated.

We can see that many of these anomalous events are related to the refilling of the LN2 Dewar from figure 6.6, where there is an excess of anomalous PID events that occur within minutes of a refill. These originate in vibration of detector from the boiling of LN2 on the warm cold-finger. The number of low energy events above threshold is plotted in a histogram as a function of the fractional time between LN2 refills for both the raw data set, as well as the data with the PID cut applied. Many of the events removed by the PID cut occurred immediately after a LN2 refill. Unfortunately, we cannot reliably throw out all 3 hr data sets after LN2 refills due to the loss of some of the information on LN2 fill times. Neither would this eliminate all microphonic events, such as those from individual bubbles in the Dewar that can continue to occur well after the refill.

It must be noted that the measurement of the PID parameter is only possible for events whose maxima fall completely within the range of Ch0 and Ch1. Larger signals that are recorded in Ch2 do not have PID cuts applied to them. However, for the spectra produced from Ch2, events with maxima that fall fully within all three ranges do have the PID cuts applied. The low energy portion of the spectra produced from Ch2 is consistent with the low energy spectra produced from just Ch0 and Ch1.

6.3.2 Event Bunches

A second characteristic of microphonic backgrounds in germanium detectors is their tendency to arrive in bunches [Morales et al., 1992]. The histogram in figure 6.5 displays the time separations between events above threshold, with and without the PID cut applied. The large excess of events with short time separations are removed with the PID cut. Furthermore, figure 6.4 displays a scatter plot of the peak height in Ch1 versus the PID parameter for the events that are bunched within 6 seconds. With a few exceptions, most fall outside of the acceptable window of PID values, validating the choice of those cuts.

6.4 Stability Measurements

The stability of the experiment and DAQ were tested by taking advantage of the activation of the germanium detector with long lived ^{68}Ge isotopes, as well as by utilizing the periodic operation of the pulse generator.

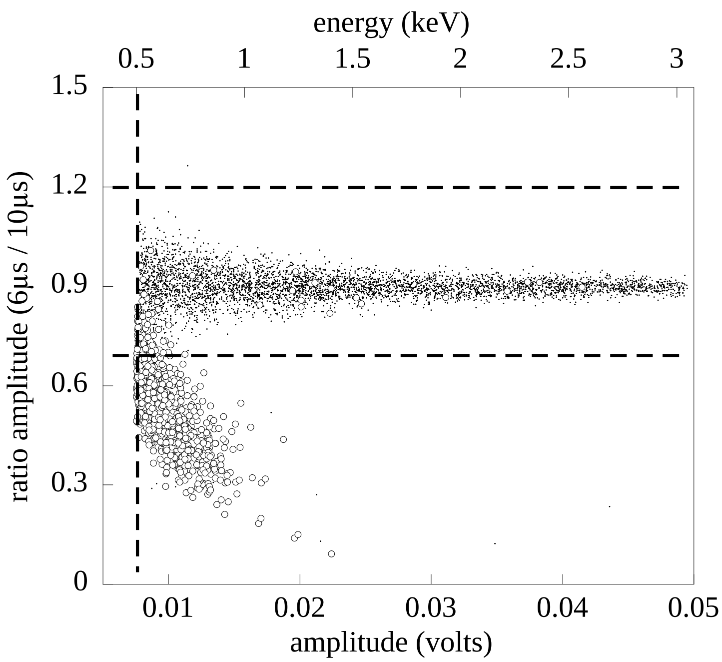

Figure 6.4: The distribution of PID values versus energy is shown for recorded events. The solid dots, which fall within the PID cuts, are events from interactions in the detector that are coincident with the NaI(Tl) anti-Compton veto. Also depicted are events (circles) that arrive in bunches (within <4 s of another event), which are likely due to microphonic events. The PID values for these low energy events mostly lie outside the cuts and are removed by software.

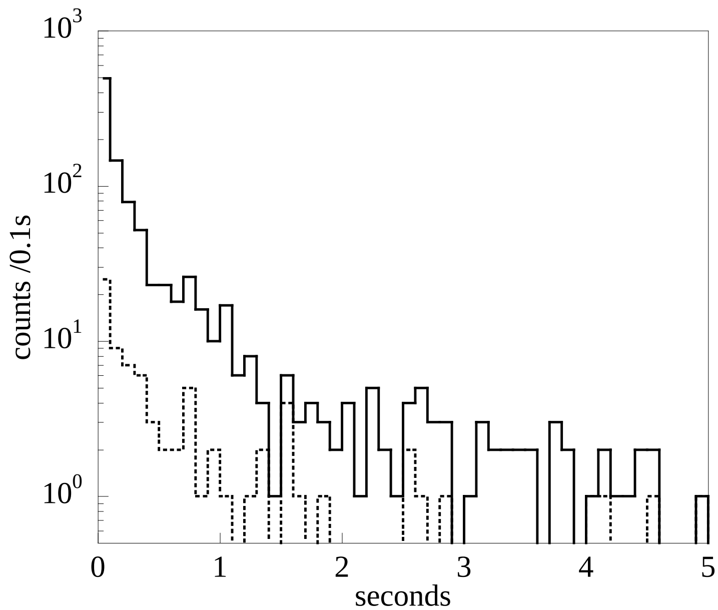

Figure 6.5: Histograms of the time separation between events above threshold are compared when a PID cut is applied. The solid line is for all events, while the dotted line is what remains after the application of PID cuts, shown in figure 6.4. The application of the PID cuts and a time bunching cut eliminates a significant number of low energy microphonic events.

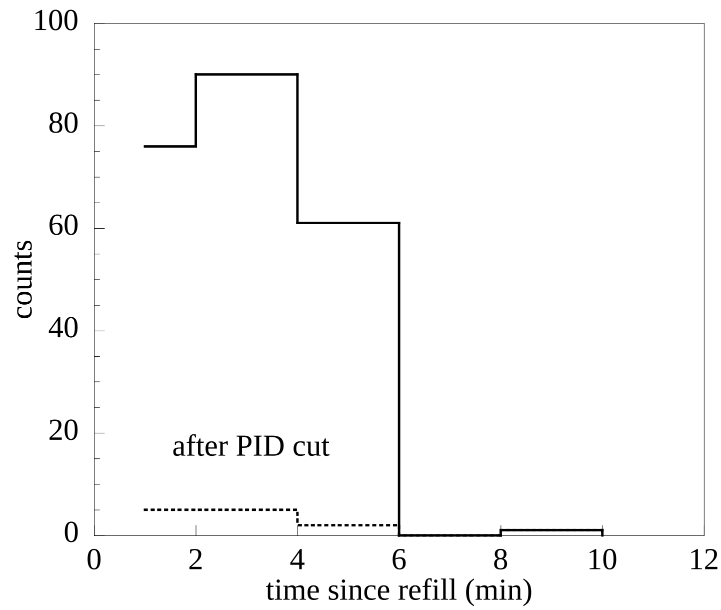

Figure 6.6: An illustration of the effect of the PID cut on the number of low energy events (0.5–3 keV) that occur immediately after a LN2 refill. Clearly the boiling of the LN2 in the Dewar is a significant source of microphonics.

6.4.1 Energy Shifting with the 10.3 keV Ga K-shell peak

The 10.3 keV peak from ^{68}Ge and ^{71}Ge is the dominant background peak in the high energy spectrum (figure 6.2). While the initial rate under the peak decays rapidly after deployment underground, it reaches an approximately steady rate of decay at later times, presumably as a result of longer lived isotopes (^{68}Ge) or thermal neutron capture inside the shielding. This is discussed in more detail later in this chapter and is illustrated in figure 6.18. The continued presence of this peak at later times makes it possible to measure the shift in the peak position as a function of time. The peak centroid was measured using time bins of three days. A plot of the peak position versus time can be seen in figure 6.7. Also shown are the linear fits for each data period (Runs 1–4) used to compensate for the change in the offset. The errors on the peak positions are statistical, worsening with the decay of the isotopes. For both Runs 1 and 4, there are clear trends of increasing offset versus time. While there is no conclusive evidence suggesting the source of this shift, it is possibly due to the change in the LN2 level in the detector Dewar. This argument is supported by the increase of the detector noise with time in these two runs, which is well correlated with the known loss of LN2 for the experiment. In addition, during Runs 2 and 3, the LN2 level was known to be extremely low, to the point that the detector noise suffered, which is possibly responsible for the elevated but unchanged offset for these runs. The corresponding rate in the L-shell background peak (1.298 keV) is $\sim$1/10th of the K-shell, thus the shifting of this peak is measured with much longer time bins. The position of the 1.298 keV peak is measured for the four data sets, and the resulting peak change with respect to its initial position is also plotted in figure 6.7 (solid circles). The energy shift of the L-shell peak tracks that of the higher energy K-shell, with the possible exception of Run 4, suggesting that the change in the peak position is due to a change in the offset of the peak, and not to a change in the gain. The position of the L-shell peak is used to correct for the offset as a function of time prior to the energy calibration displayed in figure 6.5.

6.4.2 Pulser Width

The level and stability of the electronic noise of the germanium detector can be measured using the periodic operation of the pulse generator. Every two hours the pulser turns on, for a minute, producing a peak in the spectrum that is within the range of all three channels (0–2). For each short run, the pulser events in Ch0 and Ch1 are fit with a gaussian distribution. The FWHM of the fitted peak is plotted versus time in figure 6.8 for Ch1. The values were converted to units of eV using the energy calibration described in section 6.5. There is no noise measurement during the week when the pulser was turned off. With a few exceptions due to the warming up of the detector, the electronic noise is consistent about its mean value of 161 eV FWHM. This stability should enable a future measurement of coherent neutrino

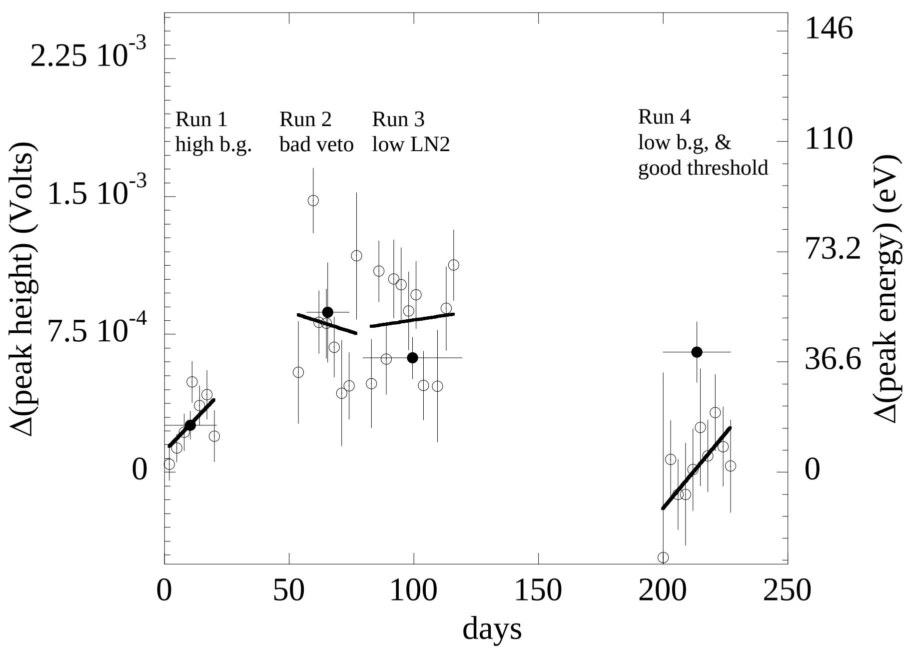

Figure 6.7: The drift of the two most prominent background peaks from cosmogenic activation. The 10.36 keV peak from the Ga K-shell has enough statistics to provide a regular 3 day measurement (open circles), while the 1.298 keV (filled circles) peak from the Ga L-shell is measured over much longer periods (∼20 days). Both show a noticeable drift that seems anti-correlated to the the level of LN2 in the Dewar. The L and K-shell peaks track each other, indicating a shift in the energy offset instead of the more familiar gain drift. The solid lines are fits to the peak shift for the different data runs, which are used to compensate for the peak drift over time.

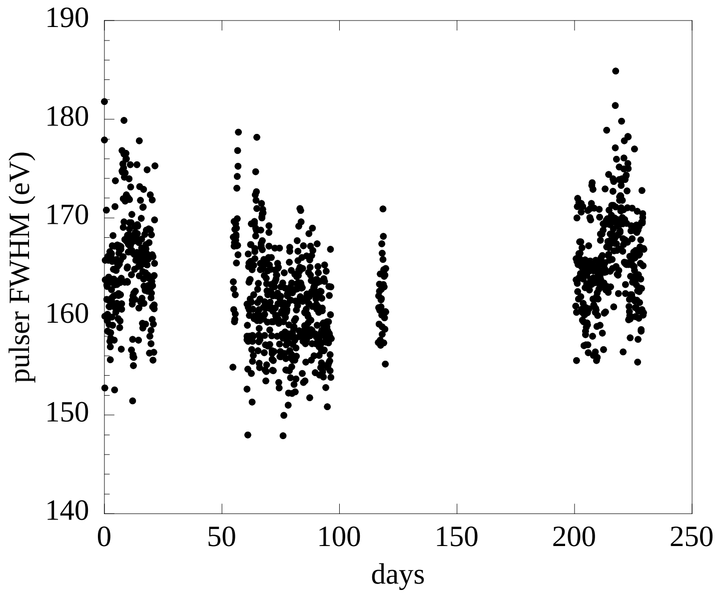

Figure 6.8: Fluctuations in the electronic noise of the BEGe-1 detector at the SONGS reactor. The largest excursions are due to poor cooling–a result of low levels of LN2 in the Dewar.

scattering at a reactor site similar to the Tendon Gallery at SONGS.

6.4.3 Spurious Veto Fraction

In addition to measuring the electronic noise, the pulser is also useful in the measurement of the dead time incurred by the muon and anti-Compton vetoes. During operation, the pulse generator is set to its maximum rate, which completely overwhelms the data acquisition (DAQ). During this time, the events that are recorded can be considered to be entirely due to the pulser. With the exception of the period during Run 2 when part of the veto logic malfunctioned, the relative fraction of pulser events that are accidentally coincident with the vetoes is measured to be $\sim 19.4\%$. The rate dropped during Run 2, but as this data period is unused it is inconsequential. During the week when the pulser was turned off, the dead fraction is assumed to be constant and equivalent to the measurements immediately before and after it was turned off.

6.5 In-situ Calibrations

6.5.1 High and Low Energy Channels

The energy spectrum is calibrated using six cosmogenic peaks from Run 1, before most of them decayed away. The source isotopes are listed in table 5.1. The peak fits to the energy spectra can be seen in figure 6.2, providing a very linear calibration for the high energy range spectrum.

The two lowest energy channels are calibrated with the help of the pulser peak, whose position is fixed with reference to the calibration for the high energy channel. The pulser peak is observed in both low energy spectra, as is the 1.298 keV peak from ^{68}Ge and ^{71}Ge. These two peaks are fit in figure 6.9, and a two point energy calibration is performed for these channels.

6.5.2 Fano Factor Measurement

Using the peak widths measured by the fits for the energy calibration, a measurement of the Fano factor in this germanium detector was performed. The Fano factor is a measure of the dispersion of a probability distribution. In detectors, it is a result of the energy loss in collisions not purely described by a statistical process [Fano, 1947]. The equation describing the gaussian peak width for a Fano factor F is:

$$FWHM = 2.35(\sigma_{noise}^2 + 2.96EF)^{1/2} \tag{6.1}$$

where E is the mean energy of the peak, 2.96 eV is the energy required to create an electron-hole pair in germanium at 77K, and σ_{noise}=70.3 eV is the rms electronic noise. The fit to

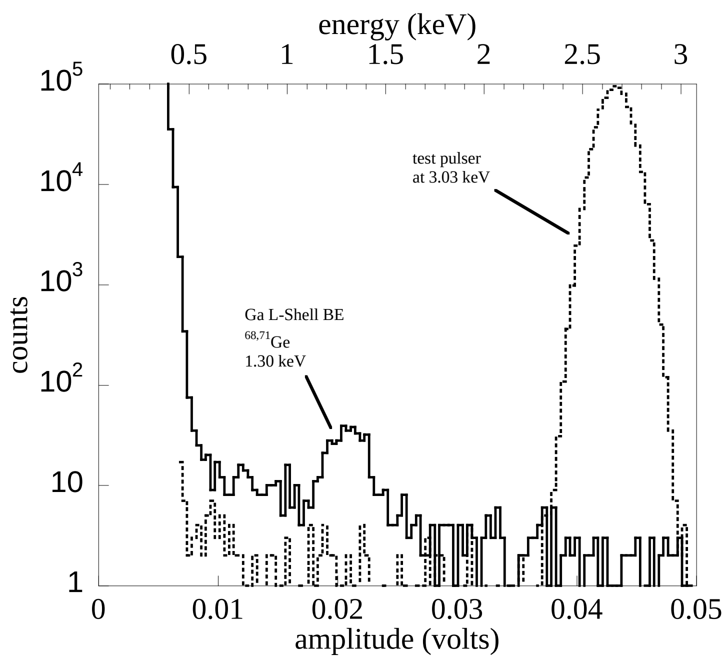

Figure 6.9: Background spectrum (solid line) and pulser spectrum (dotted line) used to calibrate the low energy channel (Ch1). Both the pulser peak and the 1.298 keV peak are used.

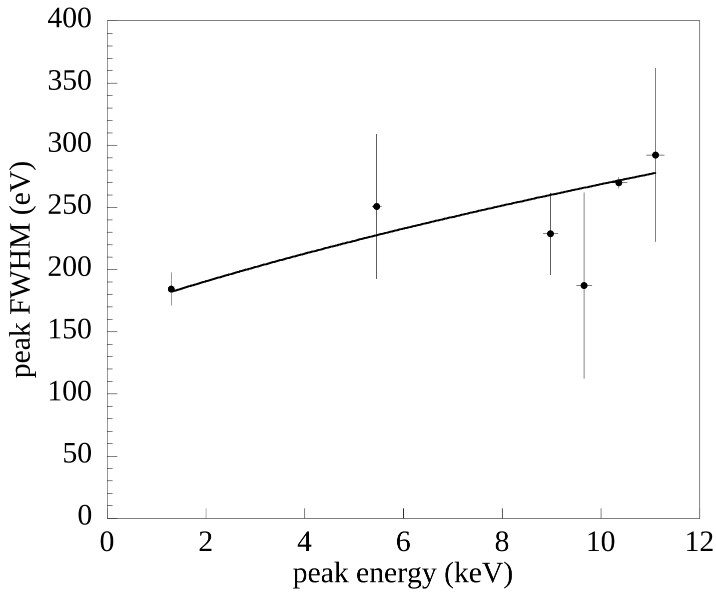

Figure 6.10: Measurement of the peak resolution as a function of the peak energy for the calibration peaks shown in figure 6.2. The measurement can be used to determine an effective Fano factor for this detector. The solid line is a fit to the data using equation 6.1, which gives a measured Fano factor of F=0.274 $\pm$ 0.015 for this detector.

the measured peak widths is shown in figure 6.10, where the best fit value was determined to be F=0.274 $\pm$ 0.015. Knowledge of this is critical for analysis methods that search for a gaussian peak of a defined width at various energies, such as will be performed in section 8.3 and chapter 9.

This measurement of the Fano factor does not take into account the effect of charge trapping on the peak resolution, as the simpler functional form is sufficient for predicting peak widths in our region of interest. In addition, the charge losses due to trapping are low for these detectors, as was discussed in section 2.7.

6.6 ^{73}As Coincidence Cut

There are several background peaks in the spectra, resulting from cosmogenic activation of the detector, that are not removed by the vetoes or the microphonic cuts. While the backgrounds exist they are very useful for energy calibrations of the detector. The SONGS deployment did not have the luxury of waiting until they had all decayed away, meaning that some of the physics results were sub-optimal. There is one long lived background from ^{73}As that can be removed by studying the time structure of events in the detector. The removal of this background is useful for improving the electron decay limits (chapter 9). As mentioned in section 5.2.5, the electron capture decay is followed by the emission of a 53.4 keV gamma with a half-life of 0.499 s. The gamma will rarely escape the germanium crystal meaning that a cut can be made on any background event that is soon followed by another larger signal, in this case a signal that is out of range of the DAQ. A histogram of the time difference between events in a window around the 11.1 keV peak and overflow events that would otherwise pass all of the veto cuts can be seen in figure 6.11. The statistically limited sample has a half-life that is consistent with the 0.499 s half-life from ^{73}As. This background is removed with a timing cut such that an event of any energy followed within 4 s by an overflow (unvetoed) event is thrown out. The rate of overflow events is low enough that the number of accidental vetoes is insignificant. Incidentally, the background resulting from ^{73}As electron capture also gives a peak at the L-shell (1.41 keV), which must, in principle, also be removed by this cut; however, the rate is low enough, and the background large enough, that this is not observed.

6.7 Energy Spectra

6.7.1 High Energy Range

The useful energy spectra resulting from this analysis include the high and low energy ranges for Runs 1, 3 and 4. The data taken in Run 2, with the malfunctioning logic unit, suffer from high backgrounds that were unable to be removed by the anti-Compton veto.

The high energy range spectra can be seen in figures 6.12 and 6.13 after all of the veto,

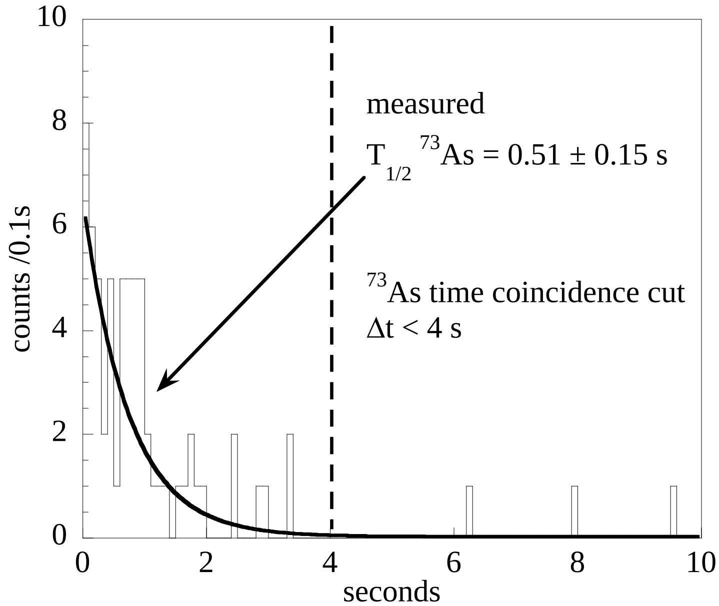

Figure 6.11: Histogram of the time separation between events under the 11.1 keV peak due to ^{73}As and the detection of a higher energy event that corresponds to the decay (see figure 5.10). A fit to this decay (solid line) agrees with the half-life expected from the decay ($T_{1/2}$=0.49 s as seen in figure 5.10). A cut is placed (dashed line) on this time coincidence signature, eliminating events that occur within a time window of 4 s.

PID, and timing cuts have been applied. The data were normalized to the measured exposure and also shifted according to the fits in figure 6.7.

6.7.2 Low Energy Range

The low energy spectra for the useful data periods (Runs 1, 3 and 4) are displayed in figures 6.14 and 6.15 after all of the cuts, the energy shift, and exposure normalization have been applied. The spectra have been re-binned to ~100 eV widths. The nominal bin size, determined by the 8 bit digitizer card, is 25 eV widths. It is an unnecessarily small value considering the observed energy shifts (~ 70 eV). The low energy spectra from the Run 3 data set have six more days of exposure than the high energy range during that period, which were accrued when the range of Ch2 was increased in order to measure energies up to 60 keV.

6.8 Discussion of Backgrounds

Nearly all of the background peaks that were present in the first data set had decayed significantly in the subsequent data sets. With time, it is likely that the background level between 3 and 8 keV will continue to drop, potentially to the level above 11 keV. The backgrounds in the region <3 keV may continue to drop as the activation cools. On the other hand, it could be due to neutrons or some other unidentified background, in which case no improvement can be expected. There has been a dramatic improvement in the level of backgrounds in comparison to the previous deployment to the TARP facility [Aalseth et al., 2008] that was brought about by several detector improvements, as can be seen in figure 6.16. The figure combines the low background results for the high energy spectrum from Runs 3 and 4 in order to improve the statistics on the low background portions of the spectrum; the poor threshold of Run 3 is ignored for this purpose. The results are also compared to

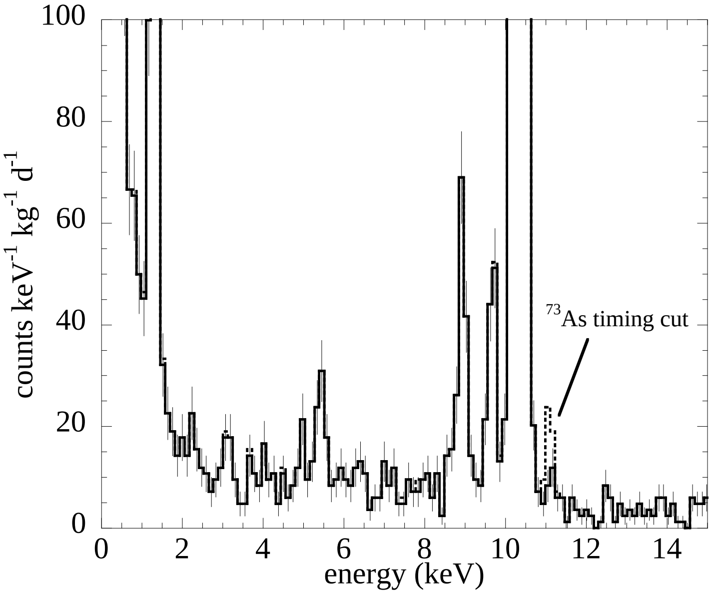

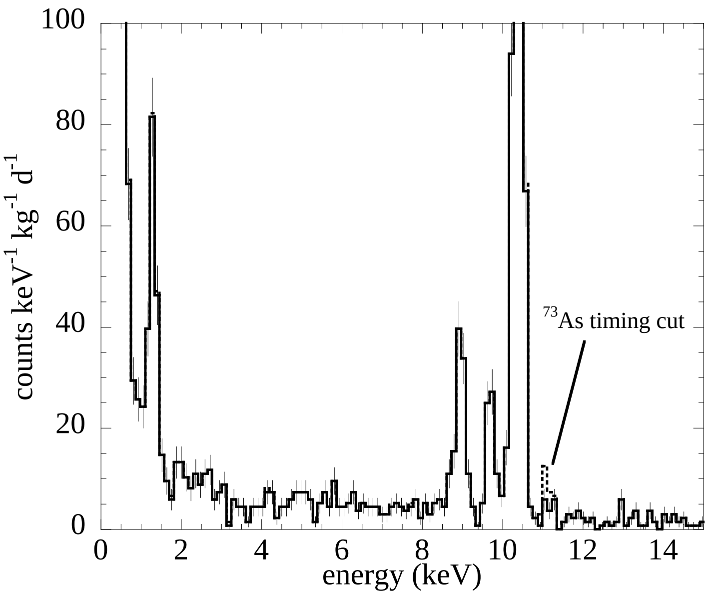

Figure 6.12: High energy background spectra (Ch2) obtained for Run 1 (top) and Run 3 (bottom). The results of the ^{73}As timing cut are also evident on the 11.1 keV peak. The 5.48 keV x-ray peak from ^{51}Cr has noticeably decayed away by Run 3 ($T_{1/2}$ 27.7 days). The activity of the other background peaks has also dropped noticeably.

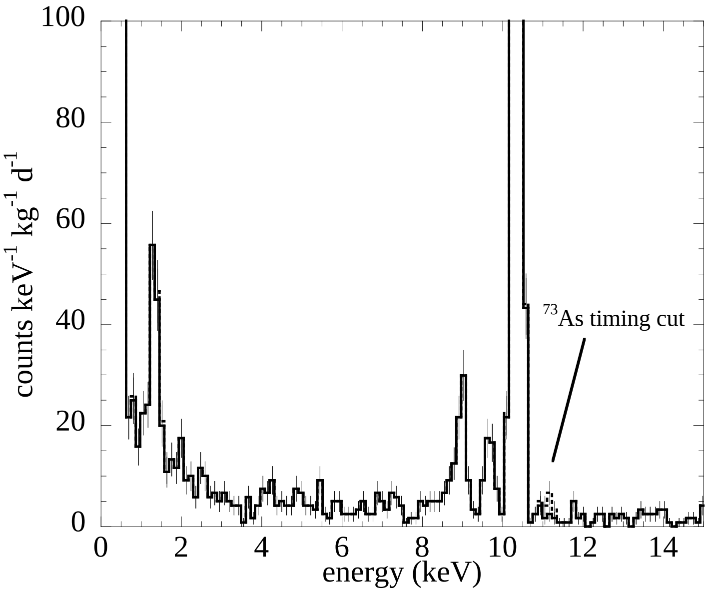

Figure 6.13: High energy spectra (Ch2) obtained for Run 4.

recent result from the CDMS collaboration [Ahmed et al., 2009b], where the discrimination against minimum ionizing backgrounds has not been applied, being ineffective below 5 keV in that experiment. Remarkably, the background level achieved with the BEGe-1 detector at 30 m.w.e. are only slightly worse than those achieved by the CDMS experiment at a much deeper site. It must be noted that this analysis of the CDMS data maintains the sensitivity to both nuclear recoils as well as electron and photon backgrounds. A redeployment to a deeper site, along with further elimination of background sources near the detector may reduce the background well below the level displayed in figure 6.16.

It is interesting to consider the spectrum of background signals that was vetoed by the anti-Compton NaI(Tl) crystal, shown for the full data set in figure 6.17. To begin with, there is a significant component of the spectrum that is due to accidental coincidences with the veto. This is best illustrated by the large peak at 10.36 keV from ^{68,71}Ge. One feature that is not from accidentals which is readily evident is the peak from ^{65}Zn. As was discussed in chapter 5.2.5, a significant fraction of the decays under this peak are expected to occur

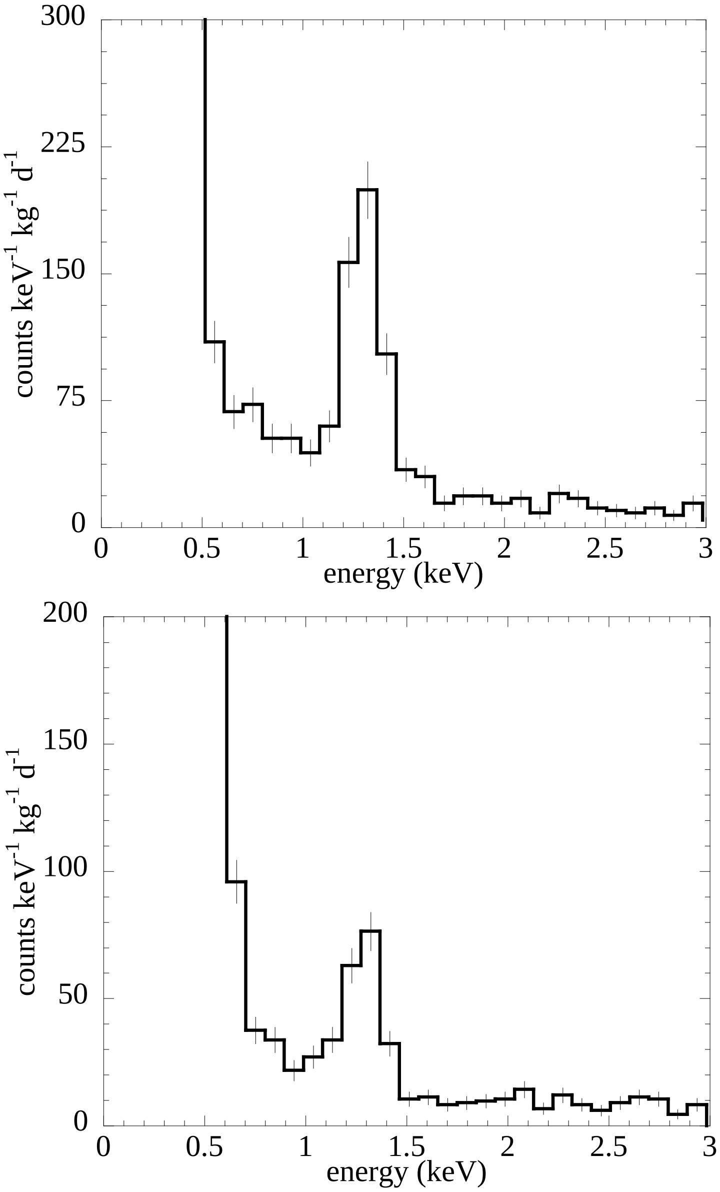

Figure 6.14: Low energy background spectra (Ch1) obtained for Run 1 (top) and Run 3 (bottom). The low threshold but high backgrounds are evident for Run 1, while the poor threshold and lower backgrounds for Run 3 are also clear. Notice the different vertical scales in these figures and 6.15.

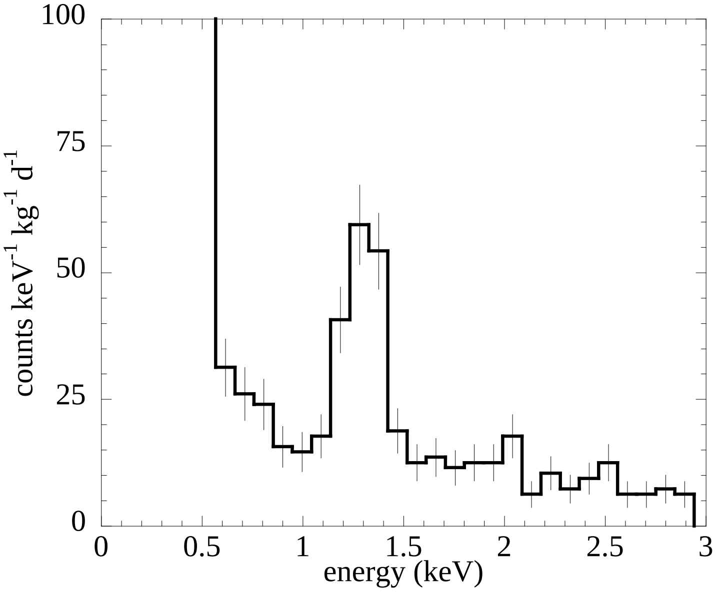

Figure 6.15: Low energy background spectra (Ch1) obtained for Run 4. This run maintained a low threshold and achieved the lowest background measured at SONGS. Notice the different vertical scale between this figure and those in 6.14.

in coincidence with the emission of a high energy gamma. Based on the results of Monte Carlo simulations, recorded in table 5.1, the peak in the coincidence spectrum should contain ∼50% of the events in the unvetoed spectrum. This expectation is plotted in figure 6.17, where reasonable agreement is found. It is also worth considering the background peak at 11.1 keV. It has already been established in section 6.6 that this is dominated by ^{73}As cosmogenic background. It is clear from figure 6.12 that this timing cut does not eliminate all of the events in this peak. While this is likely due to the escape of the coincident x-ray from the germanium crystal, the question as to whether it can be ascribed to ^{74}As is a valid one, as it has a cosmogenic origin as well ($T_{1/2}$=17.77 days) and can produce the same signature. Assuming that the entire excess left over after the timing cut is ascribed to this decay, and using the detection efficiency determined from the Monte Carlo simulation reported in table 5.1, it is possible to estimate the rate of events in the vetoed spectrum. This is also plotted in figure 6.17, where it is clearly illustrated that ^{74}As does not play a significant role in the

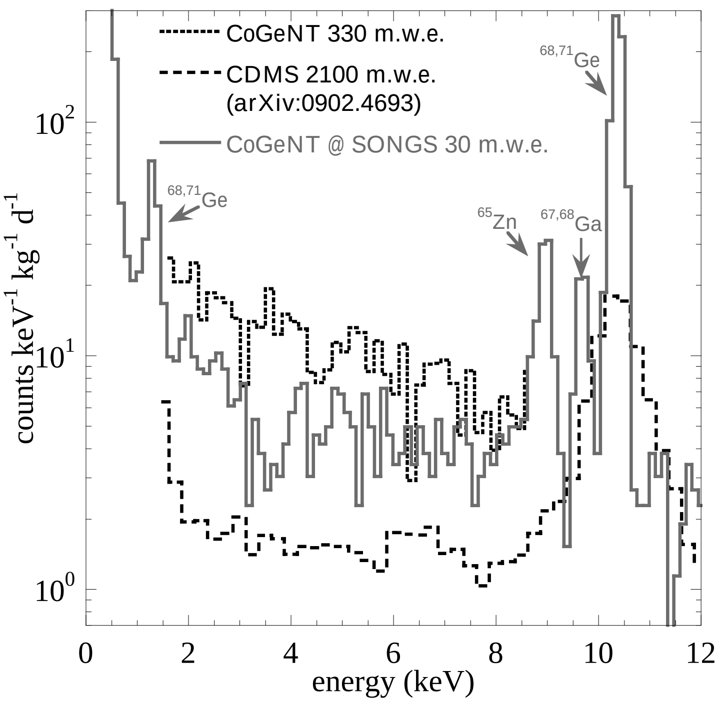

Figure 6.16: The background spectra obtained from Runs 3 and 4 are compared to the results from the TARP deployment, where significant improvement is seen after the removal of some internal sources. A comparison is also made to a run from the CDMS experiment for which no cuts against minimum ionizing backgrounds have been applied [Ahmed et al., 2009b].

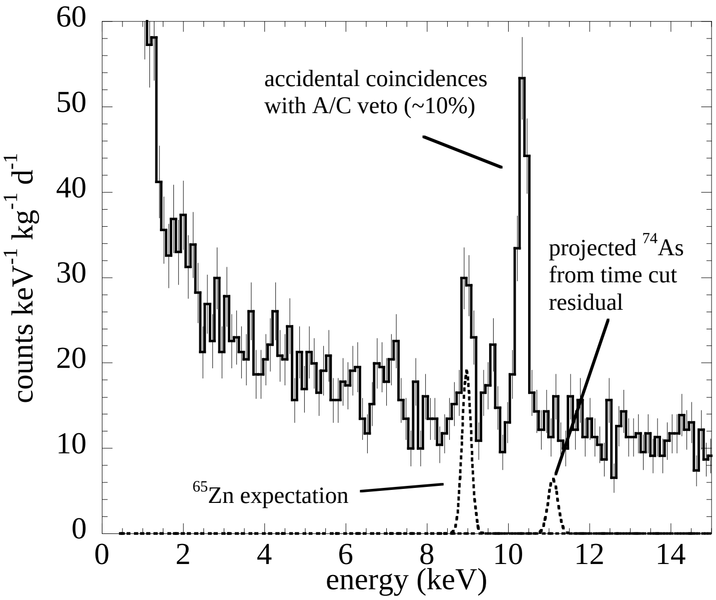

Figure 6.17: The spectrum of events coincident with only the NaI(Tl) anti-Compton veto is shown. The expected signal from the decay of ^{65}Zn, determined from the unvetoed spectrum and a Monte Carlo simulation, is shown to be in reasonable agreement with the data. Similarly, it is demonstrated that the residual counts under the 11.1 keV peak in the unvetoed spectrum cannot be dominated by ^{74}As decays (see text).

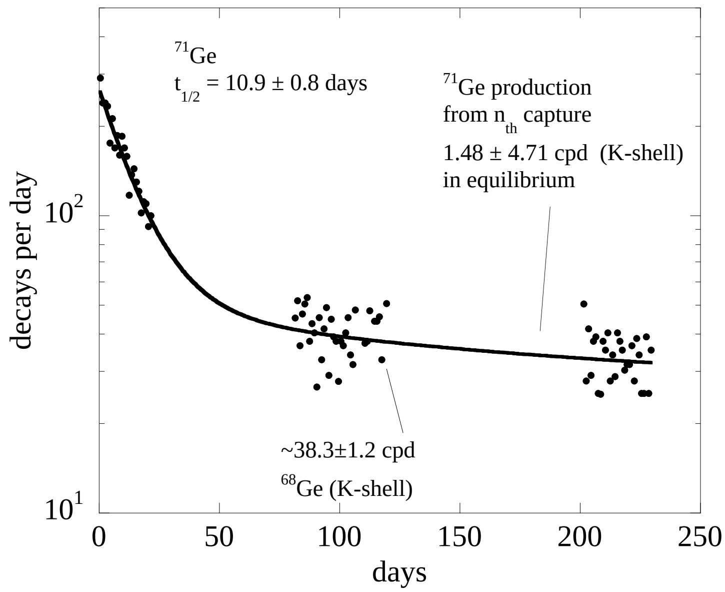

Figure 6.18: The decay of the count rate from events under the 10.3 keV peak over time is shown; events from Run 2 have not been included. The contribution from thermal neutron capture producing ^{71}Ge clearly dominates early. Using the event rate under the 9.6 keV peak (^{68}Ga) it is shown that the peak is dominated by ^{68}Ge decay, at later times, and not by a residual rate of thermal neutron capture in the detector. This is further supported by the long decay half-life of the 10.36 keV peak (t > 70 days). Most thermal neutrons are expected to be absorbed in the boron and cadmium filled materials that are part of the radiation shield.

backgrounds.

While the backgrounds are universally lower, and the exposure longer in the spectra from Run 3, the threshold has increased due to low levels of liquid nitrogen in the detector Dewar and a correspondingly high leakage current. It reduces the reach of Light WIMP searches, because much of the leverage comes from the lowest energy region. Fortunately, for the data collected in Run 4, this is not the case.

6.8.1 ^{71}Ge Thermal Neutron Activation

The most apparent feature in the remaining background spectra is from the K and L-shell peaks of gallium daughters and the corresponding partial energy depositions. The two offending parent isotopes are ^{68}Ge from cosmogenic activation, and ^{71}Ge from thermal neutron activation. It is possible to identify the parent isotope by looking for characteristics of the decay. For example, figure 6.18 displays the decay rate of events under the 10.36 keV peak, where it is clear that ^{71}Ge dominates early from the characteristic 11.43 day half-life. Clearly, the crystal was exposed to a non-negligible thermal neutron flux, which was removed sometime prior to the beginning of operation within the radiation shield. It was likely a result of the transportation, or storage above ground, even though the detector had modest protection against thermal neutrons.

It is unlikely that the radiation shield in the SONGS Tendon Gallery completely eliminates thermal neutrons. There is likely some equilibrium rate of decay of ^{71}Ge at later times. In addition to this, there is also some component from ^{68}Ge, which has a half-life of 270.8 days. The decay rate under the K-shell peak at later times is depicted in figure 6.18. The fraction of events in the K-shell from ^{68}Ge can be estimated by measuring the decay of ^{68}Ga which follows (67.7 m half-life), with a K-shell peak at 9.67 keV. The electron capture decay of ^{68}Ga leads to a peak at 9.67 keV for 8% of the 10.36 keV peak decays, whereas the balance decay via β^+, and are not observed in our spectrum. The short lived cosmogenic isotope of ^{67}Ga ($\sim$3 days) necessitates using the later data (Run 3) to characterize this rate. There were 99.5$\pm$12.3 counts in the K-shell from ^{68}Ga decay in Run 3. This suggests that there should be 1,243.5$\pm$153.9 counts under the 10.36 keV peak from ^{68}Ge decays, which compares well to the 1308.7$\pm$40.7 counts measured. The estimated rate from ^{71}Ge is then 1.94$\pm$4.71 cpd, indicating that backgrounds from equilibrium thermal neutron capture in the germanium crystal are low.

CHAPTER 7

REACTOR NEUTRINO EXPERIMENTS WITH PPC DETECTORS

The deployment of a PPC detector to a location that is 25 m from the core of a $\sim$3 GW (thermal) power reactor has provided the opportunity to perform three experiments using reactor neutrinos. The original impetus for this deployment was an attempt to measure coherent neutrino-nucleus scattering by taking advantage of the low threshold of the BEGe-1 germanium detector. The very large flux of neutrinos from the power reactor and the $\sim$MeV energy scale of the neutrinos is ideal for the measurement because all of the neutrinos can undergo coherent neutrino-nucleus scattering. The measurement has not yet been achieved but progress has been made towards this goal, which is reported on below.

There are two other experiments that take advantage of the large neutrino flux, the low backgrounds and the unique characteristics of PPC detectors. The first is an attempt to improve the limits on the magnetic moment of the neutrino, using neutrino-electron scattering. Modest limits were obtained for this deployment by taking advantage of the low energy threshold of PPC detectors and the $1/T$ spectral shape of the scattering contribution (T is the recoil energy) from μ_ν [Vogel & Engel, 1989]. Unfortunately, because of the brevity of this deployment, the results are limited to data sets that were obtained with the reactor ON. High background levels early in the deployment prohibited the use of the the data set from Run 1 that was obtained with the reactor OFF, which reduces the quality of the results. A more complete deployment will likely improve on the limits placed by the TEXONO collaboration [Wong et al., 2007], with their higher threshold conventional HPGe detector, by running for longer and establishing backgrounds with the reactor OFF. The third experiment described here places a limit on the continuous energy deposition due to a putative electromagnetic interaction of the reactor neutrinos with the BEGe-1 germanium detector. A significant improvement, more than two orders of magnitude, on the previous limits [Castera et al., 1999] is reported . Every effort was made to take full advantage of this deployment considering the rarity of such an experiment with low backgrounds, located near such a high flux of neutrinos and using PPC detectors, which have such unique capabilities.

7.1 Status of the Coherent Neutrino-Nucleus Scattering Measurement

The measurement of coherent neutrino-nucleus scattering has been a holy grail in neutrino physics since its prediction more than 30 years ago [Freedman, 1974]. To date, the failure to measure the cross-section, for which the signature is typically a sub-keV nuclear recoil, can be attributed to the scarcity of detector technologies with a large enough mass (>1 kg), low enough backgrounds and a low enough threshold that is required to observe it. This is not for a lack of trying; many potential detector technologies have been proposed or explored. As an interesting example, the early experimental efforts with the detectors that comprise the Cryogenic Dark Matter Search (CDMS) were part of an attempt to measure coherent neutrino scattering [Cabrera et al., 1985]; their use for dark matter detection would come only later. The recent development of the low threshold PPC detectors indicates that the first observation of coherent neutrino-nucleus scattering may be near. This section describes this significant progress towards the measurement using the low background, low threshold PPC detectors at the San Onofre Nuclear Generating Station.

7.1.1 Coherent Neutrino-Nucleus Scattering

The coherent scattering of neutrinos off nuclei is an uncontroversial standard model process that was predicted following the discovery of weak neutral currents [Freedman, 1974]. The process is analogous to the coherent scattering of photons off atoms involving the elastic scattering of a neutrino off the nucleons in a target nucleus. The process occurs via the neutral current and benefits from a coherent enhancement to the cross-section that is proportional to the square of the number of neutrons in the nucleus [Drukier & Stodolsky, 1984]. Full coherence (which leads to a cross section $\propto N^2$) occurs when the momentum transfer wavelength is sufficiently long to probe the entire nucleus, which causes all of the nuclei to recoil in phase. An equivalent statement is that the nucleus is a point-like object in the interaction. In other words, $q \ll (1/R)$ where q is the momentum transfer and R is the radius of the nucleus. This condition is most easily maintained by using a source of low energy neutrinos ($E_\nu <$ 10's of MeV), for which the momentum transfer must be small. However, as was discussed in the seminal paper on the subject [Freedman, 1974], it is possible for higher energy neutrinos to forward scatter and partially benefit from the coherent enhancement as well. In this case the total cross-section is then proportional to $N^{4/3}$. The second coherence condition requires that the initial and final states of the interaction be indistinguishable. Thus, to maintain full coherence, the scattering must be elastic and must occur via the neutral current. A change in the number of neutrons and protons in the final state accompanying a charged current interaction would destroy coherence. The signature that results from a coherent neutrino-nucleus interaction is a low energy nuclear recoil that can be produced by all known neutrino types, with cross-sections that are expected to be essentially the same.

For point-like scattering the form factor in the cross-section is approximated to be unity. The cross-section is then given by:

$$\frac{d\sigma}{dT} = \frac{G_F^2 Q_W^2}{4\pi} m_N \left(1 - \frac{m_N T}{2E_\nu^2}\right) \tag{7.1}$$

where G_F is the Fermi Constant, T is the recoil energy of the nucleus, E_ν is the energy of the neutrino and m_N is the mass of the target nuclei. Q_W is the weak nuclear charge and is defined as:

$$Q_W = N - Z(1 - 4\sin^2\theta_w) \tag{7.2}$$

where θ_w is the weak mixing angle, N is the number of neutrons and Z the number of protons in the nucleus. Taking $\sin^2\theta_w \sim 0.23$, the contribution from the protons in the nucleus can be seen to play a sub-dominant role. This leads to the approximation that $\sigma \propto N^2$. The total cross section is then:

$$\sigma_{tot} = \frac{G_F^2 Q_W^2 E_\nu^2}{4\pi} \tag{7.3}$$

Notably the cross-section is proportional to E_ν^2. In the expression for the differential cross-section (equation 7.1) there is a small, incoherent contribution from the spin-dependent axial current that has been neglected. As was discussed in Horowitz et al. [2003], there is a small modification to the weak nuclear charge in order to estimate the cross-section for nuclei that are nearby $J = 0$, $Z = N$. For a target with an atomic number A, the effective weak nuclear charge is then:

$$Q_{eff}^2 = 3g_a^2\delta_{A,odd} + Q_W^2 \tag{7.4}$$

where $\delta_{A,odd} = 1$ for odd A, $\delta_{A,odd} = 0$ for even A, and $g_a = 1.26$.

To establish a perspective on the energy of the nuclear recoil it is helpful to consider the maximum energy that a target nucleus can obtain [Drukier & Stodolsky, 1984]:

$$T_{max} = \frac{2E_\nu^2}{M_N + 2E_\nu} \tag{7.5}$$

where M_N is the mass of the target nucleus. For a 10 MeV neutrino scattering off a germanium nucleus, this gives a maximum recoil energy of 2.95 keV. To this one must apply the quenching factor, leading to a detectable ionization energy of 0.62 keV. Clearly, the higher neutrino energies gives rise to larger cross-sections and higher energy recoils that are easier to detect. It is worth noting that increasing the neutrino energy to improve a search for coherent neutrino scattering only works as long as all of the recoiling nuclei satisfy the condition that $q \ll (1/R)$. Similarly, reducing the mass of the target nuclei will increase the recoil energy of the target and make it easier to detect, but it also decreases the coherent enhancement and lowers the maximum neutrino energy that can undergo coherent scattering.

There are several neutrino measurements that can be facilitated by a detector that is capable of observing coherent neutrino-nucleus scattering. To begin with, coherent scattering is the dominant cross section in the dynamics of supernovae [Freedman et al., 1977]. An experimental confirmation of the expected cross-section would validate those models. Also, because it is a neutral current process, a large enough detector could be used to efficiently detect neutrinos of all species from a nearby supernovae [Giomataris & Vergados, 2006; Scholberg, 2007; Horowitz et al., 2003]. Such a detector could determine the oscillation pattern of the neutrinos and thus the total energy and temperature of the supernovae [Beacom et al., 2002]. Also, because the detector is blind to neutrino flavor, searches for oscillations into sterile neutrinos can be performed, which would be aided by the coherent enhancement [Latimer et al., 2007]. As a result of coherence, a precision measurement of the cross-section can also provide a sensitive test of weak nuclear charge [Krauss, 1991]. With detectors composed of different target nuclei (e.g. Ge and Si) it is also be possible to probe the effect of non-standard neutrino interactions (NSI) such as flavor changing or non-universal neutral current scattering [Barranco et al., 2005]. Finally, the interaction cross-section is critically dependent on the magnitude of the neutrino magnetic moment [Dodd et al., 1991]. Just as the weak contribution to this scattering has a coherent enhancement, so does the contribution from the electromagnetic component due to a larger than expected μ_ν (see figure 7.3). A measurement of the recoil spectrum can potentially improve the current limits on the magnitude of the neutrino magnetic moment. A more detailed discussion of the neutrino magnetic moment is given in section 7.2 with the discussion of a search for it using neutrino-electron scattering.

Special thought must be given to the choice of source used in any experiment attempting to measure coherent neutrino-nucleus scattering. The neutrino source must emit neutrinos with enough energy to produce a significant number of observable nuclear recoils, while at the same time not exceeding the constraints imposed by the coherence condition that $q \ll (1/R)$. The condition must hold for very heavy target nuclei, where the coherent enhancement is maximized. At the same time, the source must emit a large enough flux of neutrinos so that the experiment can operate with a reasonable detector mass and operate for a reasonable period of time. There have been proposals to use the neutrinos from spallation sources, such as the SNS, for coherent neutrino scattering experiments [Drukier & Stodolsky, 1984; Scholberg, 2006; Efremenko & Hix, 2009]. These have two main advantages. The first is that the neutrino energies are relatively high (~30 MeV), which results in high cross-sections and high recoil energies (~1 keV). The second advantage is that the neutrino events are pulsed, so that the contribution from coherent scattering can be separated out from the environmental backgrounds. This source also provides the intriguing possibility of studying the interaction using different neutrino flavors. For example, with the stopped pion beam at the SNS, different neutrino and anti-neutrino flavors arrive at the detector at different times after a spill. Unfortunately, the neutrino flux is low ($\sim 10^7$ ν cm^{-2} s^{-1} at 20 m), meaning that a detector with a significant mass may be required. Also, the backgrounds from neutrons at the spallation source are expected to be pulsed as well, negating much of the benefit of the background rejection, unless a relatively massive neutron shield is used. There have also been similar suggestions to use beta-beams to measure the cross-section [Bueno et al., 2006], though these can suffer many of the same hurdles as an experiment at the SNS. As has already been discussed, the neutrinos from a nearby supernovae would scatter coherently in a detector, because the neutrinos have energies in the range ~20–30 MeV. Unfortunately, a fairly large detector ($\gg$ 10 kg) would need to be deployed until another Supernova is observed [Drukier & Stodolsky, 1984]. It is better to consider this source as an application for a detector that has already been proven capable of observing coherent scattering. Perhaps the best source for neutrinos is a nuclear power reactor. While the neutrino energies are a bit lower than those at a spallation source, peaking at ∼2 MeV and dying off at ∼ 10 MeV, it is possible to reach very high neutrino fluxes at locations close to the reactor ($\sim 10^{13}$ ν cm^{-2} s^{-1}) [Drukier & Stodolsky, 1984; Beda et al., 2007]. Additional advantages include the ability to observe the neutrino interactions cease when the reactor is shut down for periodic refueling and the ability to locate a detector underground at some reactors, but still close (∼20 m) to the core, where the flux is a large $\sim 10^{13}\nu$ cm^{-1} s^{-1} [Bowden et al., 2008], in order to benefit from the modest level of overburden (∼30 m.w.e.) and reduce backgrounds. Solar neutrinos are another potential source; however the majority of recoils have even lower energies, and the flux is significantly lower than what is available at a power reactor [Drukier & Stodolsky, 1984].

7.1.2 Other Detector Concepts

Throughout the years, there have been several detector concepts that have been proposed to attempt to measure coherent neutrino scattering. The underlying requirements for all of them can be summed up as follows: they need to have a low threshold, low backgrounds and large masses ($\geq$ 1kg). Without any one of these the measurement is not possible and hence the relative difficulty. For example, for experiments at reactors like the one described in this dissertation, a sub-keV detector threshold for nuclear recoils is required. While this experiment does not require the backgrounds of the most modern dark matter experiments, background levels that are on the order of a few counts keV^{-1} kg^{-1} d^{-1} should be achieved. A detector with a mass in the range of 1–10 kg is likely needed for a reactor experiment. As has already been mentioned, the development of a capable bolometer detector was attempted but the detector thresholds were insufficient [Cabrera et al., 1985]. Modern incarnations of this effort to use bolometer detectors include an attempt to utilize the Neganov-Trofimov-Luke [Neganov & Trofimov, 1985; Luke, 1988] effect to amplify the heat signal and, thus, reduce the threshold [Gütlein et al., 2008]. Another early, but unsuccessful attempt used superheated superconducting grains (SSGS) [Stodolsky, 1991] to attempt to achieve low thresholds. There have also been proposals for constructing micropatterned gas detectors, using either Micromegas or GEMs to amplify the few electrons that are ionized by a low energy nuclear recoil [Collar & Giomataris, 2001; Barbeau et al., 2003a; Giomataris & Vergados, 2006]. One such attempt served as the beginnings of this research program. The use of gas detectors suffers from the evident difficulties with deploying compact experiments with enough mass. Also the potential sources of single electron backgrounds are not well studied. There is a program to build a dual phase liquid argon detector which could potentially get around the problem of the detector mass [Hagmann & Bernstein, 2004]. The detector has some potential backgrounds from contamination of ^{39}Ar, an isotope yielding beta decay that is present in the detector. The proposed CLEAN experiment is a liquid Neon detector that is intended to be used for dark matter and Solar neutrino physics which can also potentially observe coherent neutrino scattering from a nearby supernova [Horowitz et al., 2003]. The TEXONO collaboration has conceived of building a large $\sim$kg scale detector using a large array of small 5 g germanium detectors (ULEGEs, a commercial brand of Canberra Industries) which individually have sub-keV thresholds [Wong et al., 2006]. The experiment has run into some difficulties with low energy backgrounds that are likely a result of the N-type ULEGe detectors that are used, which are sensitive to low energy x-rays or betas from surrounding materials. Thus, while that experiment has achieved relatively low thresholds, it is likely both limited in the total mass that can be deployed and the ultimate level of backgrounds that can be achieved.

The experiment described here has progressed the farthest of all of these attempts by deploying a low background, large mass PPC detector to the Tendon Gallery of the SONGS reactor (see chapter 2 for a description of the BEGe-1 detector). As has already been discussed, PPC detectors have achieved sub-keV thresholds with massive (∼0.5–1 kg) detectors. In addition, contrary to some of the previously mentioned detector concepts, the quenching factor for low energy recoils has been measured which provides an accurate identification of the true threshold for nuclear recoils (see chapter 4). HPGe crystal detectors are inherently very low in backgrounds, as they are one of the purest materials known to mankind, an advantage that is enhanced by the use of radio-clean construction materials and a high quality radiation shield that surrounds the detector. In addition, because the detectors are P-type, the outer 0.5 mm of Li-drifted germanium is largely unresponsive to radiation, which serves to shield the active volume from low energy backgrounds. It is the progress with this detector which is described below. The deployment of the detector with its shielding was described in chapter 5.

It should be noted that the TEXONO collaboration has recently transitioned, following our work, to using the same large mass P-type Point Contact detectors, also produced by Canberra Industries to attempt to measure coherent neutrino-nucleus scattering at the Kuo-Sheng nuclear reactor [Wong, Rome 2009].

7.1.3 BEGe-1 Detector at SONGS

A comparison of the expected recoil spectrum from coherent neutrino-nucleus scattering to the measured background spectrum from the BEGe-1 detector can be seen in figure 7.1. The effect of the quenching factor and detector resolution have been accounted for. Evidently, a measurement of the cross-section is not currently possible. A detector with this threshold (∼0.5 keV) might expect a signal on the order of ∼0.5 counts keV^{-1} kg^{-1} d^{-1}, but the background is ∼20 keV^{-1} kg^{-1} d^{-1}, thus a measurement is still unrealistic. However, the

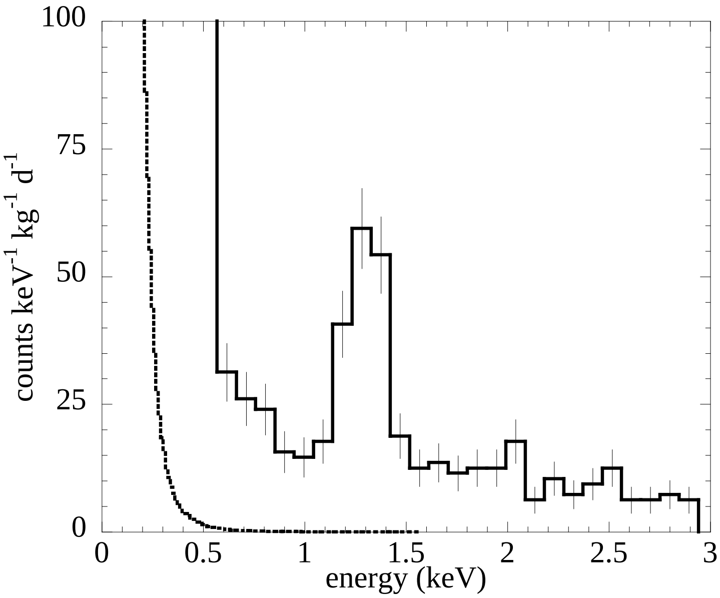

Figure 7.1: The expected signal from coherent neutrino-nucleus scattering for the BEGe-1 detector (dashed line) is compared to the lowest background and lowest threshold spectrum recorded of Run 4 (solid histogram). The recoil spectrum was calculated by Juan Collar.

results displayed in figure 7.1 are a dramatic and significant improvement over all previous attempts.

7.1.4 Prospects

While the detection of coherent neutrino-nucleus scattering has not yet been achieved there is a clear path towards this goal using PPC detectors deployed at nuclear power reactors. The reduction to the current level of backgrounds is already a significant achievement, but there is no reason to believe that this will improve further; it is possible that the detector is beginning to be affected by background neutrons. A reduction of the threshold to 200 eV would increase the detectable signal to as high as 100 keV^{-1} kg^{-1} d^{-1} at the lowest energies and allow the measurement of coherent neutrino-nucleus scattering. This is a realistic goal considering that significantly lower thresholds ($\sim$50 eV) have been achieved with low mass

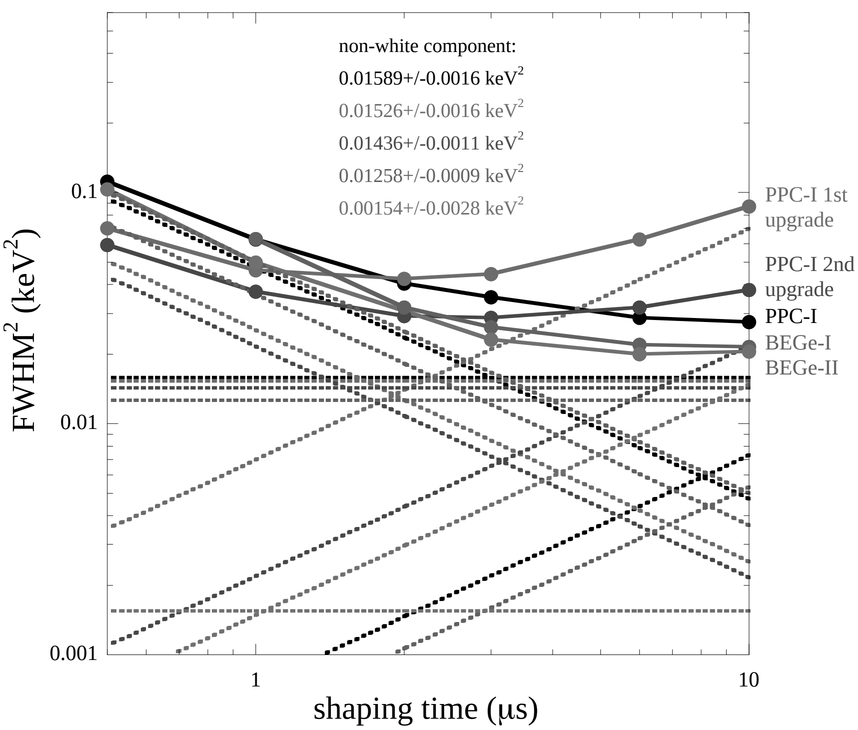

Figure 7.2: This figure encapsulates some of the efforts to reduce the electronic noise in PPC detectors by upgrading the PPC-1 detector, or by using different configurations of newer detectors. There are possible signs of a recent reduction of the non-white component, which is currently the limiting factor. Figure courtesy of J. I. Collar.

$\sim$1 pF x-ray detectors.

In light of this, there has been a campaign to identify and remove sources of electronic noise using various configurations of various detectors and, thus, reduce the threshold. These efforts are encapsulated in the noise corner plots in figure 7.2, where it can be observed that improvement is being impeded by a source of non-white noise. As was discussed in chapter 2, there is some indication that this source of noise may have been alleviated in the BEGe-2 detector. Unfortunately, the detector also suffered from a relatively high leakage current, compared to some earlier detectors and was unable to achieve the lowest level of noise that is dictated by the non-white component. There is some uncertainty as to the validity of this improvement because of the poor leverage in the fit that determines the noise components at larger shaping times. If this improvement in the non-white component has actually been achieved, then a detector with a detector threshold of $\sim$200 eV is right around the corner, and so is the first measurement of coherent neutrino-nucleus scattering.

7.2 Limit on μ_ν with Reactor $\bar{\nu}_e$'s

While the primary purpose of the deployment of this PPC detector to the SONGS nuclear reactor was to attempt to measure the coherent neutrino-nucleus scattering of reactor anti-neutrinos, it is also possible to take advantage of the high flux of neutrinos to obtain limits on the magnitude of the neutrino magnetic moment using neutrino-electron interactions. The low background, large mass and low energy threshold make this detector a particularly useful upgrade over similar neutrino magnetic moment experiments. Unfortunately, the brief period of deployment described in this dissertation prohibits the comparison of spectra with the reactor both ON and OFF, a common technique that is used to account for backgrounds which are unrelated to the operation of the reactor [Daraktchieva et al., 2005; Beda et al., 2009; Li et al., 2003]. As such, the limits obtained are not as strong as those that can be obtained in a full experimental campaign (∼5 reactor cycles). In lieu of this, it is possible to project the expected sensitivity of a complete experiment in such a campaign. The limits obtained from this run, as well as these projected limits are presented below.

7.2.1 The Neutrino Magnetic Moment

Within the framework of the Standard Model, the neutrino is massless and has no magnetic moment (see [Kozlov et al., 1997; Ellis, 2001; Wong, 2007] and references therein for complete reviews on the subject). Recent results from the Super-Kamiokande and SNO experiments, as well as from long baseline neutrino experiments, indicate that neutrinos oscillate [Araki et al., 2005; Eguchi et al., 2003; Aharmim et al., 2005; Ahmad et al., 2002; Aliu et al., 2005; Ashie et al., 2005], which in turn leads to the conclusion that they have a finite mass. The Minimally Extended Standard Model then allows for a finite electromagnetic interaction of the neutrino. If the neutrinos are of the Dirac type, then the neutrino magnetic moment is proportional to the mass of the neutrino and can be expressed as:

$$\mu_\nu = 2.3 \times 10^{-19} \mu_B \left(\frac{m_\nu}{1eV} \right) \tag{7.6}$$

where it is parameterized in terms of the Bohr magneton, μ_B. There is also a potential neutrino charge radius [Bernabéu et al., 2000] but this is neglected in the discussions that follow.

Given current limits on the mass of the neutrinos, this value is far to small to be of any astrophysical or experimental consequence. For Majorana neutrinos a value as large as $\mu_\nu \sim 10^{-10} - 10^{-12} \mu_B$ is possible [Okun et al., 1986; Fukugita & Yanagida, 1987; Pakvasa & Valle, 2004; Gorchtein et al., 2007; Bell et al., 2006]. In principle, a measurement of this would provide a method for distinguishing whether or not the neutrino is a majorana particle [Beda et al., 2007]. It is important to note that because Majorana neutrinos are their own antiparticles, such a neutrino cannot have a neutrino magnetic moment. This is not the case for Dirac neutrinos. However, both types of neutrinos are allowed to have transition magnetic moments for scattering between neutrino flavors ($\nu_j \rightarrow \nu_k$ where $i \neq j$) [Nieves, 1982; Kayser, 1982]. Another mechanism that gives rise to an enhancement of the neutrino magnetic moment is the existence of large extra dimensions [Mohapatra et al., 2004]. As a point of interest, one consequence of a non-zero neutrino magnetic moment is the necessary existence of neutrino radiative decay [Raffelt, 1989].

7.2.2 Existing μ_ν Bounds

The strongest bounds on the neutrino magnetic moment come from astrophysical arguments. A historically intriguing consequence of a large neutrino magnetic moment ($\sim 10^{-11}\mu_B$ [Kopeikin et al., 1997]) is that of the transformation of left-handed neutrinos in Solar Magnetic fields to right-handed neutrinos via the Spin Flavor Mechanism [Barranco et al., 2002]. For Dirac neutrinos, this would result in the production of sterile neutrinos that escape the Sun and account for the Solar neutrino deficit. This has been restricted to a sub-dominant contribution to the Solar neutrino problem by neutrino oscillation measurements [Balantekin & Volpe, 2005]. More stringent limits come from the analysis of the Solar neutrino spectrum, where $\mu_\nu < 0.54 \times 10^{-10}\mu_B$ [Arpesella et al., 2008]. These are difficult to compare directly to the results from experiments using ν_e because the solar neutrinos would involve a change of flavor. The strongest bounds come from astrophysical arguments of late stage helium burning stars and are of the order of $\sim 10^{-11} \rightarrow 10^{-12}\mu_B$, though these are model dependent. Despite this, concrete experimental results with sensitivities $\sim 10^{-11}\mu_B$, lacking model dependencies, carry more weight.

Competing in sensitivity with the Solar neutrino spectral distortion limits are those obtained with reactor $\bar{\nu}_e$'s. It should be noted that because of neutrino oscillations, as well as the primary flavor composition of Solar neutrinos, the two types of measurements can be complementary. For reactor experiments, one of the more important tasks is background reduction. The recent MUNU experiment (μ_{ν_e} <$9\times10^{-11}\mu_B$) addressed this problem by utilizing a large shielded gas detector, where the direction of the electron recoils could be identified [Daraktchieva et al., 2005]. This allowed a rough reconstruction of the direction of the incoming neutrino and thus allowed the separation of the reactor related signal from the isotropic background. The TEXONO experiment, which has produced the most stringent experimental limits (μ_{ν_e} <$7.4\times10^{-11}\mu_B$), utilizes a low background conventional germanium detector [Li et al., 2003]. In this case the threshold of 10 keV is utilized, in combination with the characteristic $1/T$ spectral shape expected from the neutrino magnetic moment scattering in order to increase the strength of the limits. The GEMMA experiment has similar results (μ_{ν_e} <$3.2\times10^{-11}\mu_B$), further reducing their threshold to as low as 3 keV while simultaneously increasing the flux of neutrinos by deploying to a location that is 13.9 m from the core of a 3 GW (thermal) reactor, although it does not appear the most conservative approach was taken in the analysis to produce the limits [Beda et al., 2009]. The experimental limits described in this dissertation do not have this proximity advantage; however, the detector threshold is even lower at 0.5 keV. The improvement from this advance alone is enough to provide competitive limits from just ∼12 kg-days of data that were taken with the reactor ON.

7.2.3 EM $\bar{\nu}_e$–e^- Scattering

Experiments searching for neutrino-electron scattering attempt to identify the process by searching for the spectral shape in the background that is expected from a contribution of a neutrino magnetic moment. The expected spectral shapes are a function of the differential cross-section for the process as well as the spectrum of neutrino energies. Limits are placed

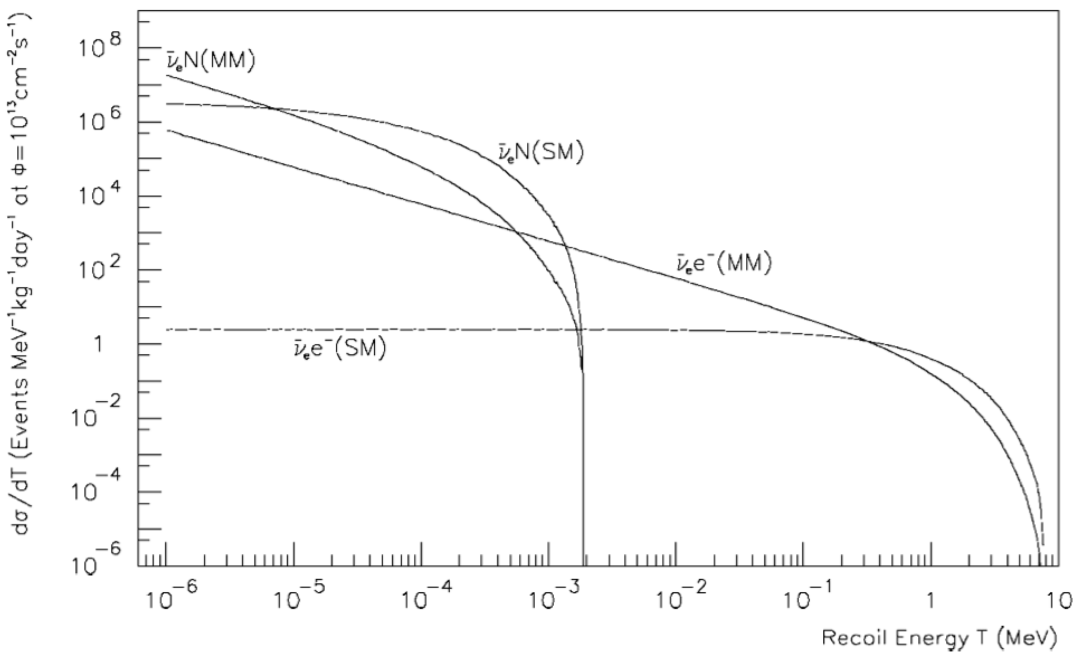

Figure 7.3: This plot, which was produced by the TEXONO collaboration [Wong, 2005], shows the differential cross-section for neutrino-electron scattering and coherent neutrino-nucleus scattering in a germanium detector. Also shown are contributions from the differential cross-sections due to a hypothetical neutrino magnetic moment of $\mu_\nu = 10^{-10}\mu_B$, in units of Bohr magnetons. SM refers to the expected Standard Model contribution to the cross-section, while MM denotes the contribution from the putative magnetic moment scattering contribution.

on the magnitude of the electromagnetic interaction cross-section above the standard model cross-section that is due to the weak interaction. For the standard model weak interaction the cross-sections are:

$$\frac{d\sigma_W}{dT} = \frac{G_F^2 m_e^2}{2\pi}\left[(g_V - g_A)^2\left(1 - \frac{T}{E_\nu}\right)^2 + (g_V + g_A)^2 + (g_A^2 - g_V^2)\frac{m_e T}{E_\nu^2}\right] \tag{7.7}$$

where T is the recoil energy of the electron, θ_W is the weak mixing angle, and E_ν is the energy of the incoming neutrino. For the electromagnetic interaction:

$$\frac{d\sigma_{EM}}{dT} = \frac{\pi \alpha_{em}^2 \mu_\nu^2}{m_e^2} \left[\frac{1}{T} - \frac{1}{E_\nu} \right] \tag{7.8}$$

where μ_ν is the neutrino magnetic moment. The advantage of using low threshold detectors comes from the characteristic $1/T$ energy dependence of the recoil spectrum. The increase at lower energies with respect to the Standard Model cross-section is due to the absence of an interference term that is a result of the change in the handedness of the neutrino. Folding in the energy spectrum of the reactor neutrinos, and assuming a neutron flux of $\sim 10^{13}$ ν_e cm^{-2} s^{-1}, the recoil energies expected by reactor anti-neutrinos in a germanium detector are depicted in figure 7.3 (obtained from [Wong, 2005]).

For low-energy recoils, the $\frac{1}{E_\nu}$ terms can be approximated to be zero and the details of the energy spectrum of reactor neutrinos are unimportant [Beda et al., 2007]. The differential cross-section, using the notation of [Beda et al., 2007], is then described in terms of the total neutrino flux at the detector. The cross-section approximates to:

$$\frac{d\sigma_W}{dT} = 1.06 \times 10^{-46}\ cm^2\ MeV^{-1} \tag{7.9}$$

and

$$\frac{d\sigma_{EM}}{dT} = \chi \frac{2.495 \times 10^{-45}}{T}\ cm^2\ MeV^{-1} \tag{7.10}$$

where $\chi \equiv \left(\frac{\mu_\nu}{10^{-10}\mu_B} \right)^2$ and μ_B is the Bohr magneton. The expected signal in a given detector, as a function of the recoil energy, is given by the equation

$$S(T) = \frac{d\sigma}{dT} N_e \Phi_\nu R \tag{7.11}$$

with N_e the number of electrons in the active volume of the detector and Φ_ν the flux of neutrinos. The R term accounts for the effects of the binding energies of the various target electrons. If the energy transfered q to the nucleus is less than the binding energy of the electrons on a shell, those electrons cannot take part in the interaction. This is described by the equation

$$R(q) = \frac{1}{Z}\sum_i n_i \theta(q - \epsilon_i) \tag{7.12}$$

with Z=32 for germanium, n_i the number of electrons at the i shell, and ϵ_i the binding energy at the i shell. The term $\theta(q-\epsilon_i) = 1$ if $q > \epsilon_i$ and is zero otherwise. For recoil energies greater than the K-shell binding energy, $R = 1$. Between the L and K-shell energies, $R = 0.9375$. It drops even further for energies below the L-shell. An example of the expected low energy spectrum that takes the binding energies into account can be seen in figure 7.4.

The expected spectrum from the electromagnetic interaction is then compared to the measured background spectra to obtain limits on the magnitude of the neutrino magnetic moment.

7.2.4 μ_{ν_e} Limit from the SONGS Deployment

A limit can be placed on the magnetic moment of reactor anti-neutrinos using the brief operational period of the BEGe-1 detector at the SONGS reactor. The limit is pleasently strong considering the relatively small exposure ($\sim$ 12 kg days) compared to the limits obtained from leading experiments ($\sim$100–1000 kg days). The neutrino flux is comparable (0.98×10^{13} $\bar{\nu_e}$ cm^{-2} s^{-1}) at the SONGS reactor to the most competitive experiments [Wong et al., 2007; Beda et al., 2007; Daraktchieva & for the MUNU Collaboration, 2003]. The data taking periods have been regularly interrupted because of the lack of availability of LN2, power failures in the Tendon Gallery and the failure of some components of the veto logic. The results reported here are negatively affected by the fact that there were elevated backgrounds from cosmogenic activation of the germanium crystal during the only period when the reactor was OFF. Some sensitivity is recovered due to the low threshold characteristics of PPC detectors, because the contribution from the neutrino magnetic moment is most dominant at low energies (see equation 7.10).

One characteristic that makes reactor experiments easier than searches for dark matter, for example, is that the signature should disappear when the reactor is turned off. These reactor OFF periods typically last for about a month: long enough to replace fuel rods or perform maintenance. While these periods are short in comparison with the reactor ON periods, for the TEXONO and GEMMA and MUNU collaborations, they allow the subtraction of backgrounds, which improves the sensitivity of the experiment. That has not been possible for the results presented below because during the reactor OFF period of this deployment (Run 1) many backgrounds from cosmogenic activation had yet to decay. There is no reliable way to estimate the low energy backgrounds in the reactor ON period using the data set from Run 1. This problem is only a result of the specific timing and reactor schedule of the current deployment and should not bother future experiments. It is also worth noting that the results also suffer from a lack of exposure, another factor that is easily remedied in a future experiment. The limit reported here is obtained by determining the maximum allowable neutrino magnetic moment that can contribute to the background spectrum in Run 4, because it had the lowest backgrounds and the best threshold of all runs (figure 7.4). No attempt is made to assume a spectral shape for the background, as was done in [Beda et al., 2009], and thus a comparatively much more conservative limit is reported here.

The low energy spectrum from Run 4 is fit in the energy window between 0.5–3 keV, where the advantages of the low threshold PPC detectors and low background deployment at SONGS come into play. No attempt was made to obtain limits at higher energies, as the backgrounds are similar to those achieved by the TEXONO collaboration and would suffer from the significantly less exposure. The fit includes the functional form expected

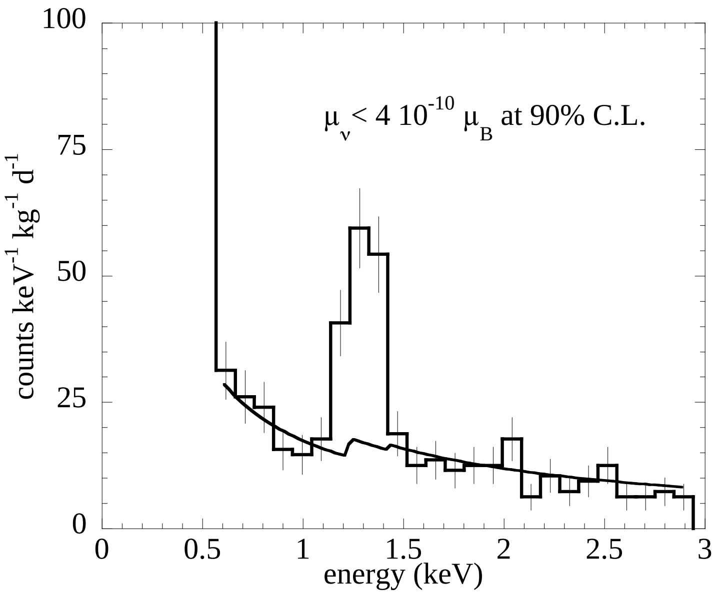

Figure 7.4: The maximum allowable contribution to the background spectrum (Run 4) due to a neutrino magnetic moment is shown ($4 \times 10^{-10}\mu_B$). The kinks in the spectrum at ∼1.4 keV result from a loss of sensitivity due to the binding energy of the L-shell electrons in germanium [Beda et al., 2007].

from neutrino-electron scattering contribution from a magnetic moment, which is described by equation 7.11. Also included is a gaussian peak centered at 1.298 keV, that accounts for the background from ^{68}Ge, using the appropriate peak resolution. The tiny contribution to the expected spectrum from the weak interaction is neglected because it does not to play a significant role, as can be seen in figure 7.3. In addition, an exponential background contribution is also assumed. The resulting limit for the magnetic moment is $\mu_\nu < 4 \times 10^{-10}\mu_B$ at a 90% C.L., in units of Bohr magnetons (factor of 12.5 above GEMMA bound). The expected signal from this neutrino scattering is included in figure 7.4. Apparent in the fit is the role played by the function R. Already, below 11.1 keV, the two K-shell electrons in germanium are unavailable for scattering because of their binding energy; the further loss of the L-shell target electrons clearly reduces the sensitivity at energies below 1.4 keV.

7.2.5 Projected Sensitivity of a Complete Reactor Experiment

It is possible to project the future sensitivity of such an experiment if it were conducted under conditions similar to the two leading experiments TEXONO and GEMMA. It can safely be assumed that a larger, 1 kg version of this detector can be deployed without any degradation of the threshold or change in the backgrounds. As an example of this, the BEGe-2 detector, described in chapter 2, has twice the mass of the BEGe-1 detector with similar energy resolution and threshold. It is also safe to assume that such an experiment would operate for several reactor cycles. The SONGS reactor, for example, cycles off for one month approximately every 18 months. A hypothetical experiment might realistically run for five reactor OFF periods (~150 days), and four reactor ON periods (~2,160 days). This will allow the use of the same background subtraction techniques that are used in other experiments in order to improve the sensitivity. As a conservative measure, it will be assumed that the low energy backgrounds currently measured in Run 4 are the best that will be achieved. Much worse backgrounds at energies <5 keV have been achieved by the TEXONO and GEMMA collaborations, both of which deployed germanium detectors to shallow locations near the reactors.

Using these assumptions, a Monte Carlo simulation of the reactor ON and OFF spectra were produced in the energy range between 0.5–7 keV. The spectra can be seen in figure 7.5. The reactor OFF spectrum is amplified by ×10, for clarity. The Monte Carlo was produced using ROOFIT [Verkerke & Kirkby, 2003], and assuming an exponential and a gaussian peak background spectrum, which was based on a fit of the spectra in figure 7.4. The residual of these two simulated data sets is also shown. This residual is fit with the functional form expected from the electromagnetic scattering of reactor neutrinos, using equation 7.11. The allowed, projected spectrum at 90% C.L. is also depicted. The region around the 1.298 keV peak from ^{68}Ge is explicitly avoided in the fit. This background will be present at significant

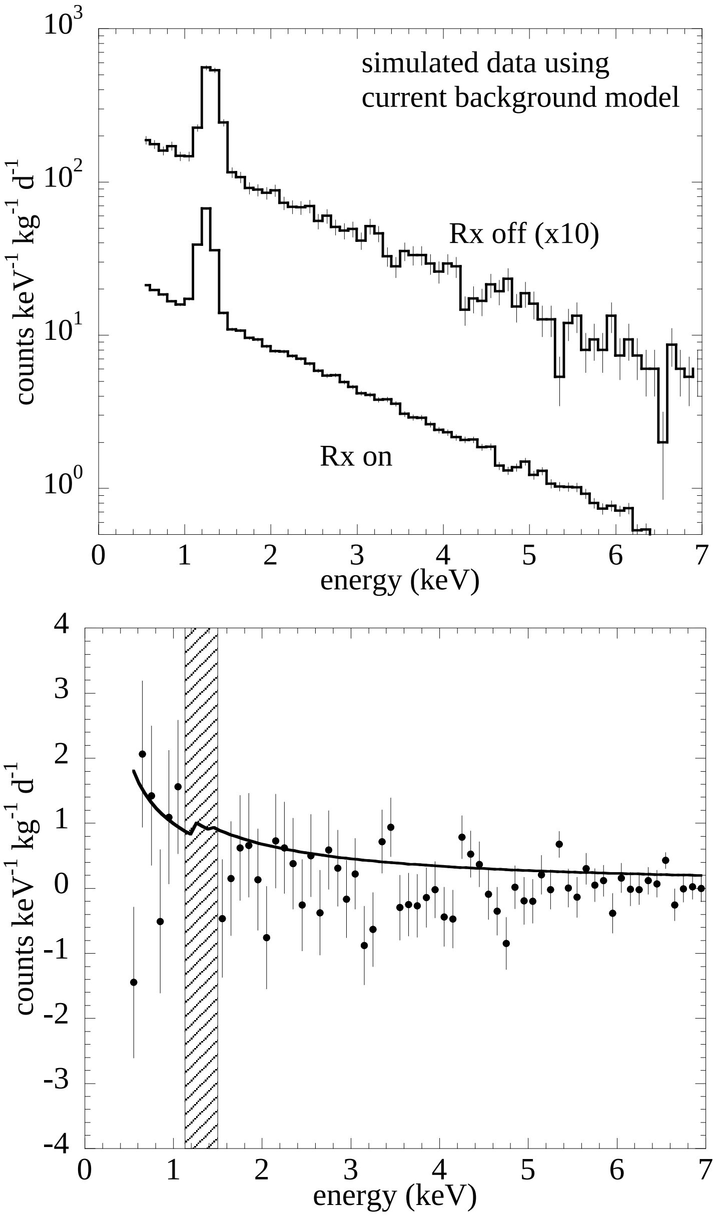

Figure 7.5: The results of a Monte Carlo simulation for a full campaign to search for a hypothetical neutrino magnetic moment with PPC detectors at a nuclear power reactor is shown. The background spectra (top) assume six months of reactor OFF measurements and 90 months with the reactor ON, assuming a level of backgrounds equal to the best reported here. A fit on the residual spectrum (bottom) suggest an achievable sensitivity of $6{\times}10^{-11}\mu_B$ Bohr magnetons.

levels because throughout any experiment because of its long 270.8 day half-life, and must be accounted for.

The projected limit achievable with a 1 kg germanium detector after 4 cycles and roughly 6 years is $\mu_\nu < 6.5 \times 10^{-11}\mu_B$. These estimates do not incorporate any leverage that might be achievable at energies >11 keV, where the TEXONO and GEMMA experiments have operated. While stronger projections are possible, this projection is conservative. It is a slight improvement over the limits obtained for electron recoils above 10 keV by the TEXONO collaboration. While the naive expectation would be a much larger improvement resulting from the larger expected signal at low energies, the observed increased background at low energies significantly reduces this advantage.

7.2.6 Discussion

The limit on the neutrino magnetic moment for this deployment ($\mu_\nu < 4 \times 10^{-10}\mu_B$) is remarkably strong, considering the short exposure obtained as well as the inability to subtract backgrounds. This is due primarily to reduced threshold of PPC detectors. From this reduction alone, one might expect a significant improvement in the limits; however, the backgrounds at low energies continue to rise along with the expected signal. A similar trend to increase in the low energy backgrounds has been observed in both the GEMMA [Beda et al., 2009] and TEXONO [Wong et al., 2007] experiments, and is possibly a result of the shallow overburden that exists for reactor experiments near the surface.

There is potential for improving the low energy threshold of PPC detectors to as low as 50–100 eV [Barbeau et al., 2007b]. While this will likely benefit many proposed measurements with the detectors, it is unlikely to significantly help with bounding the neutrino magnetic moment with neutrino-electron scattering. This is because below $\sim$0.4 keV, the cross-section from coherent neutrino nucleus scattering begins to dominate. The cross-sections, depicted in figure 7.3, are shown as a function of the target recoil energy. There is some reprieve due to the fact that the ∼20% quenching factor for Ge recoils shifts the onset of the coherent neutrino scattering down from ∼2 keV. While discrimination between electronic and nuclear recoils has been achieved [Cabrera et al., 1985], at these low energies it is unlikely. Improved sensitivity is, however, possible with a detector capable of measuring coherent neutrino scattering, where the contribution from a putative neutrino magnetic moment can also benefit from the coherent enhancement , as was mentioned in 7.1.

The limit on the achievable sensitivity to μ_ν depends weakly on the exposure of the detectors in these experiments. The generic behavior can be described by the equation [Wong et al., 2007],

$$\mu_\nu \propto \frac{1}{\sqrt{N_\nu}} \left(\frac{B}{Mt} \right)^{1/4} \tag{7.13}$$

where N_ν is the number of signal neutrino events, B is the background level, M is the mass of the detector and t is the measurement time. The fastest way to improve the sensitivity is to increase the number of measured neutrinos. This can be achieved by increasing the neutrino flux or by reducing the energy threshold, as long as the backgrounds do not increase dramatically as well.

7.3 Limit on Continuous Energy Depositions by Neutrinos

The two neutrino experiments at the SONGS reactor that have already been discussed are fairly conventional experiments. A coherent neutrino-nucleus interaction is an expected Standard Model interaction that has likely not yet been seen simply because of technological challenges. The search for a neutrino magnetic moment, while not strictly within the confines of the Standard Model, is a very active area of research in the field. The unconventional experiment described in this section is a search for an energy deposition by neutrinos in matter that does not occur via the weak interaction. The hypothetical process makes no claims on the nature of the interaction other than it would manifest as a continuous energy deposition ($\frac{dE}{dx}$) in the detector volume [Vannucci, 1999]. A similar experiment was recently performed that obtained a limit on the interaction using muon neutrinos [Castera et al., 1999], which are less likely to undergo an electromagnetic interaction. For the work described here, the unique electronic noise and mass of PPC detectors and the high flux of reactor neutrinos improves on the previous limit by more than two orders of magnitude.

7.3.1 Interaction Signature

This non-standard neutrino interaction involves the deposition of small amounts of energy in matter. The energy deposition is assumed to occur by a method other than via the standard weak interaction such as that discussed in [Kuznetsov & Mikheev, 1997], where the interaction from a small electromagnetic component of a neutrino is amplified in the large magnetic field of a target nucleus. Unlike typical neutrino experiments the signature of the interaction is not a single event, but is instead the sum of many smaller interactions. It is then proportional to the pathlength of the neutrino in a detector. The analysis ignores large, independent energy depositions that are due to standard weak interactions. There is a lower bound on the energy of the observable quanta in the germanium semiconductor detector. It must exceed the energy required to create an electron-hole pair ($\sim$2.9 eV). Such depositions are too small to measure. Therefore, the experimentally observable signature is actually an increase in the apparent leakage current of the germanium detector that would result from many small quanta of energy being deposited [Castera et al., 1999].

7.3.2 Experiments

The previous experiment [Castera et al., 1999] utilized a low background germanium detector in a high energy ν_μ beam. The experimenters searched for an increase in the leakage current of the germanium detector that occurred in coincidence with the passage of the neutrinos. It was determined that $< 10^{-5}$ eV cm^{-1} was lost in the germanium for muon neutrinos. It is noted that this sets a maximum of 10 keV that can be lost by ν_μ's passing through the earth's diameter. It was suggested there that a better limit may be achieved by deploying the experiment to a nuclear reactor where there is a much greater flux of neutrinos, or also by upgrading to more sensitive technology.

For the deployment of the CoGeNT detector to the SONGS nuclear reactor there has been progress on both fronts. The neutrino flux is much greater, at $\sim 0.98 \times 10^{13}$ $\bar{\nu}$ cm^{-2} s^{-1} [Bowden et al., 2008]. In addition, the very low noise of the BEGe-1 detector allows for very sensitive measurements of the leakage current, which is also very small ($\sim$1 pA). By quantifying the maximum allowable increase in the leakage current that is correlated to the reactor operation, an improved limit is placed on this hypothetical process.

7.3.3 Limit on the Induced Leakage Current from Reactor $\bar{\nu}_e$'s

A conservative limit on the continuous energy deposition of neutrinos in matter was obtained by comparing the maximum allowable difference in the leakage current of the BEGe-1 detector in the SONGS Tendon gallery between periods when the reactor was ON and OFF. The underlying assumption is that any exotic mode of neutrino energy loss would contribute to an excess in this current. Only the data recorded during the $\sim$21 days of Run 1 occurred during a reactor outage, therefore, only Run 1 is used to characterize the leakage current during an OFF period. All of the other data runs were recorded during reactor operation. A few exceptional periods with the reactor ON are ignored because they had low levels of liquid nitrogen and the detector was not operating correctly.

The limit was obtained by determining the maximum allowable excess leakage current in the BEGe-1 detector that can be attributed to reactor anti-neutrinos passing through the

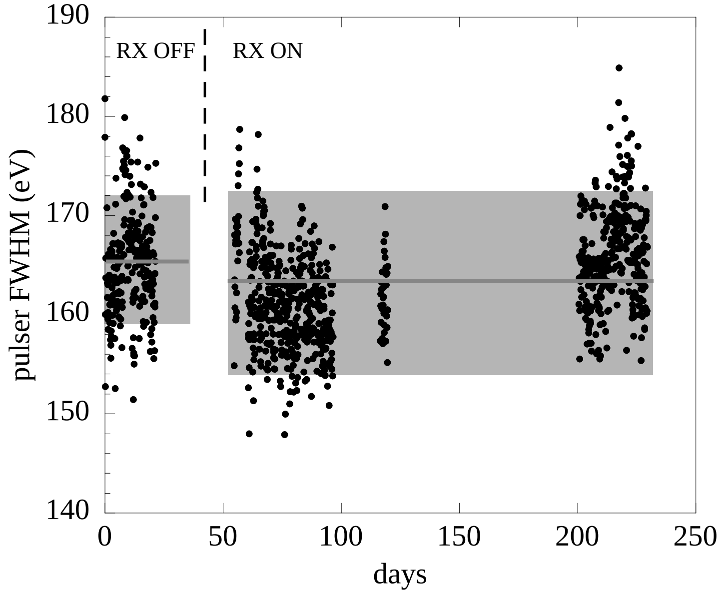

Figure 7.6: Detector noise, as measured with a pulser, during the various periods of operation is shown. Also shown is the mean (line) of the measurements and the 1 σ standard deviation (band).

germanium crystal. The leakage current was measured using the periodic pulser measurements illustrated in figure 7.6. Recalling equations 2.4 and 2.6, it is possible to characterize the leakage current I_L of the detector by comparing the electronic noise at several different characteristic shaping times. For these purposes, the noise is only measured using the channel that records the 10 μs shaped pulse. While the large shaping time minimizes the contribution to the noise from the white series component there is still a significant contribution from the non-white (flat) component. Thus, the leakage current is conservatively overestimated by assuming that it is entirely responsible for the measured noise at 10 μs shaping. From equation 2.4, the estimate is given by:

$$I_L = \frac{ENC^2}{0.67 \times q\tau}, \tag{7.14}$$

where ENC is the equivalent noise charge, q is the charge of an electron, τ is the shaping time of the amplifier, and the coefficient 0.67 is due to the triangular shaping (table 2.1).

The electronic noise measurements from the pulser have a significant spread that exceeds the uncertainties of the individual measurements. This variation is likely due to temperature changes that effect the operation of the detector and amplifier system. Sources of this variation include changes in the ambient temperature (figure 5.4), which affect the amplifiers in the DAQ, as well as low liquid nitrogen levels, which causes a warming of the germanium crystal and, therefore, an increas of the leakage current. As a result of the variation the electronic noise is taken to be the mean of the pulser measurements during a given period, while the uncertainty is taken to be the variance of these measurements. This is illustrated in figure 7.6. For the reactor OFF period, the detector noise was determined to be 165.5 eV $\pm$ 6.6 eV FWHM; while for the reactor ON period 163.46 eV $\pm$ 9.1 eV was measured. Using the average energy per electron-hole pair (2.96 eV at 77 K), this corresponds to an $ENC =$ 23.8 $\pm$ 0.9 electrons for the reactor OFF period and 23.5 $\pm$ 1.3 electrons for the reactor ON period. While the noise is larger with the reactor OFF, it is compatible within statistics, and does not prevent a determination of the maximum allowable contribution that is correlated to the presence of reactor anti-neutrinos. Using equation 7.14 the leakage current is:

$$I_L^{OFF} = \frac{566.44e^2}{0.67 \times e \times 10\mu s} = 8.5 \times 10^7 e^- s^{-1} \tag{7.15}$$

$$\sigma I_L^{OFF} = \frac{2 \times 23.8e^2}{0.67 \times e \times 10\mu s} \times 0.9 = 6.4 \times 10^6 e^- s^{-1} \tag{7.16}$$

for the reactor OFF period, and

$$I_L^{ON} = \frac{552.27e^2}{0.67 \times e \times 10\mu s} = 8.2 \times 10^7 e^- s^{-1} \tag{7.17}$$

$$\sigma I_L^{ON} = \frac{2 \times 23.5e^2}{0.67 \times e \times 10\mu s} \times 0.7 = 4.9 \times 10^6 e^- s^{-1} \tag{7.18}$$

for the reactor ON period. The difference between the reactor ON and reactor OFF periods is $\Delta I_L = -3 \times 10^6 \pm 8 \times 10^6$ e s^{-1}, which corresponds to -0.50 pA ± 1.3 pA. Therefore, the maximum leakage current due to reactor neutrinos is less than 1.63 pA, at a 90% C.L., which corresponds to a large fraction of the observed noise and is therefore a conservative limit. It is equivalent to 10.2×10$^6 e^-$ s^{-1}, which is 3.02×10^{7}eV s^{-1} in the germanium detector.

The next step is to determine the average pathlength and total flux through the detector of the reactor anti-neutrinos. The BEGe-1 detector is oriented such that the axis of the detector is perpendicular to the direction of the reactor core. This means that the average pathlength of a neutrino through the detector is $\frac{4}{3}r = 3.93$ cm, where the radius of the active germanium volume is r = 2.95 cm. It also means that for the approximately parallel rays of neutrinos, the detector exhibits a cross-sectional area of 2.9 cm × 5.9 cm = 17.1 cm^2. The estimated neutrino flux 25 m from the reactor core is 9.8 ×10^{12} ν cm^{-2} s^{-1}, which gives a total of 1.68 ×10^{14} ν s^{-1}.

Putting all this information together, a limit on the maximum continuous energy deposited in the active volume of the germanium detector is obtained:

$$\frac{dE_{em}}{dx} < \frac{3.02 \times 10^7 eV s^{-1}}{1.677 \times 10^{14} s^{-1} \times 3.93 cm} = 4.6 \times 10^{-8} eV cm^{-1} \tag{7.19}$$

where $\frac{dE_{em}}{dx}$ is the energy deposited per unit pathlength via an electromagnetic interaction for the reactor anti-neutrinos.

7.3.4 Discussion

This limit is a significant improvement over the previous results of $\frac{dE_{em}}{dx} < 10^{-5} eV cm^{-1}$ [Castera et al., 1999]. This corresponds to an energy loss of ≤45 eV passing through the diameter of the earth for neutrinos with ∼MeV energies.

Future improvements in the electronic noise of PPC germanium detectors will likely improve the quality of this limit. A better measurement of the leakage current is possible by measuring the electronic noise with several longer shaping times, where the noise is dominated by the leakage current. It is also possible to obtain a high quality measurement of the leakage current by measuring the average reset rate of the germanium preamplifier, during periods without any large energy depositions. However, no matter how accurate a measurement is made, the limitation is likely to be due to the lowest possible leakage current achievable and the variation of that leakage current due to changes in the temperature of the crystal. It is not the accuracy of the noise measurement that drives the limit, but the stability of the leakage current itself. There is some promise for improvement as these detectors have been observed to have lower noise and more stable operation in controlled circumstances in the laboratory, for instance, by ensuring a constant topping off of the LN2 Dewar.

As with most measurements of this type, improvements are made possible with increased exposure to neutrinos. In this case, the use of a larger detector will increase the pathlength and the number of neutrinos within the germanium. Both have the effect of increasing the contribution to the leakage current. Thus, a volume increase of the detector mass would lead to an improvement as long as similar leakage currents are maintained. This does not likely extend to the deployment arrays of smaller detectors, because the detrimental temperature effects on the stability of operation would likely correlate between detectors, which causes a larger fluctuation in the total measured leakage current.

CHAPTER 8

DARK MATTER SEARCHES WITH PPC DETECTORS

The primary purpose of the BEGe-1 deployment to the SONGS reactor was to attempt to measure coherent neutrino-nucleus scattering. As such, the steps taken to reduce backgrounds are commensurate with the location: at a depth of 30 m.w.e. little improvement of the backgrounds beyond a few counts kev^{-1} kg^{-1} d^{-1} can be expected in the low energy region. This is high compared to the backgrounds from experiments like the CDMS experiment [Ahmed et al., 2009a] which can discriminate between nuclear and electron recoils. However, because of the unique capabilities of PPC detectors, even results with comparatively high backgrounds can make an impact in a dark matter search: the low energy threshold leads to constraints on dark matter models where few detectors are sensitive. This chapter deals with the application of the data recorded at the SONGS reactor to two dark matter searches. The first application is a search for light mass WIMPs (<10 GeV c^{-2}), while the second is a search for pseudoscalar dark matter candidates. The limits obtained are competitive with the sensitivities of more conventional dark matter experiments.

The results are especially remarkable because of the level of background as well as the limited exposure for the data sets. To explore the full capabilities of PPC detectors for these searches, the low energy background for the 60 kg Majorana demonstrator experiment has been projected. The module will consist of 60 kg of germanium PPC detectors with the same, or better, low noise characteristics as PPC detectors described here. Based on the estimated background spectra, sensitivities are projected for the WIMP and pseudoscalar searches described here and are presented below.

8.1 The Dark Matter Problem

Baryonic matter accounts for only a small fraction of the total mass of the Universe. The vast majority of the mass of the universe is composed of dark matter, so called because the only evidence for its existence has come via its gravitational interaction. The first indications of this missing matter came in the early 1930's with observations by Fritz Zwicky of the velocity dispersion of galaxies in the Coma cluster [Zwicky, 1933]. The velocity components of the galaxies, estimated using the Doppler effect, was found to be significantly higher than expected based on the estimated size of the cluster from optical observations. Zwicky inferred that the cluster was much larger than could be determined by optical measurements and must be dominated by an unseen matter.

This interpretation failed to gain acceptance for many years; however, more recent measurements of the rotational velocities of galaxies at large radii support his argument. These measurements, first extended to large radii by [Rubin & Ford, 1970] and [Roberts & Rots, 1973], indicate that the outermost regions of galaxies are rotating far faster than can be expected if the mass distributions followed the light distribution. The evidence suggested that the galaxies exist within an extended spherical halo distribution of matter that is non-luminous. Further evidence for dark matter comes from estimates of the total masses of galaxy clusters by measuring the hot intergalactic gas. The gas is captured in the gravitational wells of the clusters and serves to map the distribution of mass. The heated gas emits x-rays from thermal bremsstrahlung which is detected by orbiting x-ray telescopes such as Chandra and XMM-Newton. Observational measurements of the mass distributions of clusters can also be obtained from gravitational lensing [Schneider et al., 1992; Narayan & Bartelmann, 1996]. Light from background sources is warped by the gravity of the cluster, giving rise to the appearance of smeared rings or arcs, such as can be seen in figure 8.2. It is possible to estimate the distribution of mass within a cluster by analyzing this lensing effect.

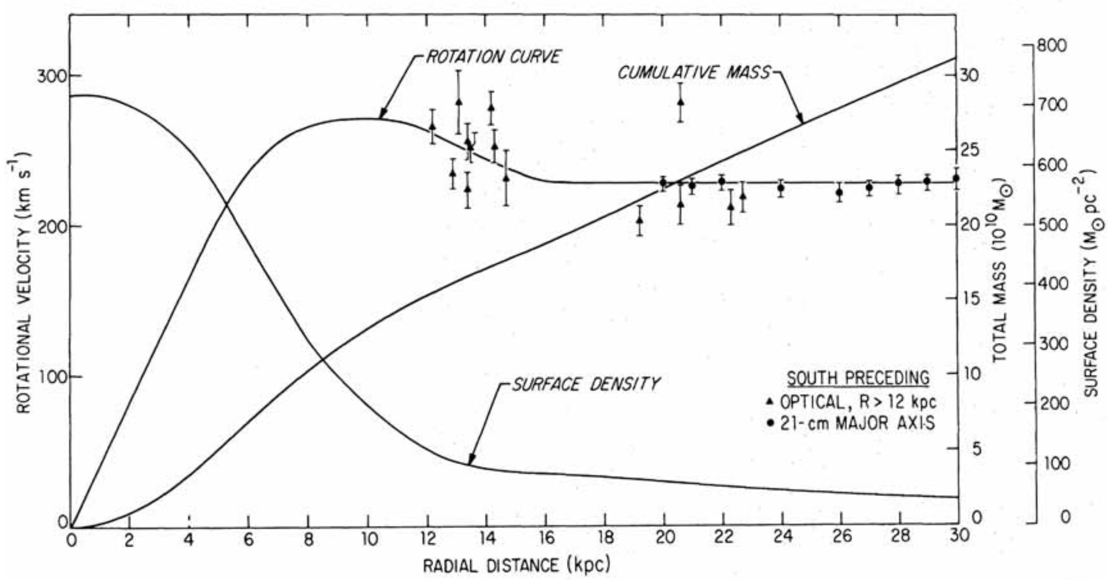

Figure 8.1: The rotation curve of the M31 galaxy. The unexpectedly high velocities at large radii indicate a possible extended dark halo of matter. This figure was obtained from [Rubin & Ford, 1970].

Some of the most compelling evidence comes from the studies of colliding galaxies. The three types of measurements already discussed (optical, x-ray and lensing) can be combined in observations like those of the Bullet cluster (figure 8.3) [Clowe et al., 2006]. In this figure, two sub-clusters have apparently passed through each other without significant interaction. X-ray measurements, however, indicate that the populations of hot gas from the two clusters have interacted and have been heated and slowed down so that the centers of x-ray luminosity are significantly less separated than their optically luminous counterparts. This sets up a test to determine if the total mass of the cluster is dominated by the inter-cluster gas or by some other non-interacting mass component. The comparison, overlaid in the figure, is made using measurements of the total mass distributions using gravitational lensing from which it is shown that the dominant mass follows the luminous matter. The bulk of the cluster's mass is non-interacting, which is consistent with the dark matter halo model.

As far as the nature of the dark matter is concerned, other astrophysical measurements

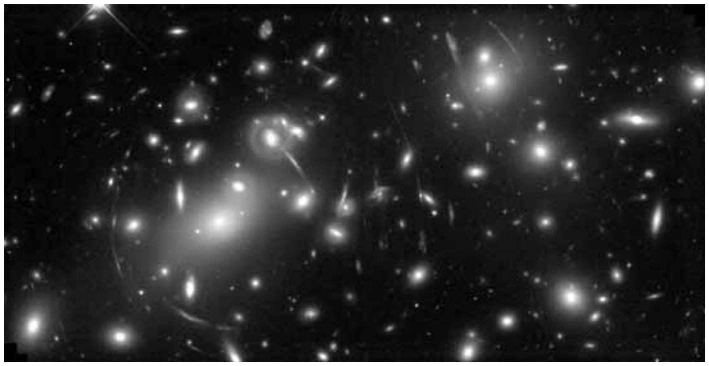

Figure 8.2: Gravitational lensing of light from the Abell 2218 cluster. This figure is from the Space Telescope Science Institute and was obtained from [Filippini, 2008].

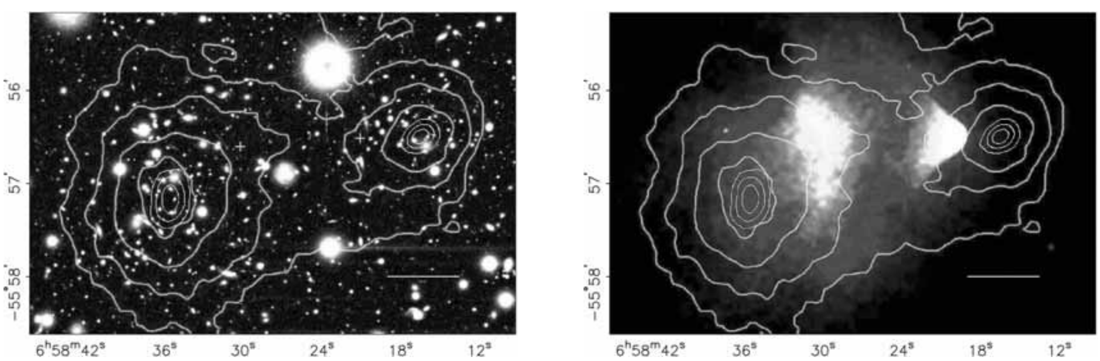

Figure 8.3: Three measurements of the mass distribution of theBullet cluster are depicted: optical (left) from the Hubble Space telescope, lensing (contours) and x-ray (right) from the Chandra X-ray Observatory. The lions share of the mass of the cluster is non-interacting and dark. The figure was obtained from [Clowe et al., 2006].

have established that it is predominantly non-baryonic. The amount of baryonic matter in the universe today is connected to the ratio of Baryons to photons during Big Bang nucleosynthesis. This ratio can be characterized primarily through measurements of the cosmic abundance of light elements like deuterium [Cyburt et al., 2003; Olive et al., 2000]. Combined with knowledge of the photon temperature at the surface of last scattering from measurements of the cosmic microwave background radiation this ratio can be determined. This is shown in figure 8.4. It can be further constrained with measurements of anisotropies in the Cosmic Microwave Background (CMB), the effect of which is also shown in figure 8.4. The resulting conclusion is that the matter content of the universe is dominated by non-baryonic dark matter.

The most natural candidates for the dark matter come from non ad-hoc theories, the existence of which is motivated by some other physics. Ordinary matter in the form of MAssive Compact Halo Objects (MACHOs) such as large planets have been considered. Microlensing studies, however, have ruled them out as the main contributor to the dark matter [Tisserand et al., 2007]. Massive neutrinos, which are another dark matter candidate, are also considered to be subdominant because the currently accepted ΛCDM model for the expansion of the universe suggests that the dark matter must be cold, while the neutrinos would be relativistic (see [Kolb & Turner, 1990] for example). One good candidate that comes from Minimal Supersymmetric Models is the Lightest Supersymmetric Particle (the neutralino in many constructions) which is stable and weakly interacting. It is referred to as a WIMP (Weakly Interacting Massive Particle). A complete review of supersymmetric dark matter can be found in [Jungman et al., 1996]. There are two forms of WIMP searches: indirect and direct experiments. Indirect WIMP experiments search for WIMP annihilation products such as neutrinos, gamma rays, positrons, etc. While annihilation can occur in the galactic halo, one of the most convincing signatures would be the emission from the center of the Earth or the Sun, where the WIMPs collect at the center of the gravitational wells.

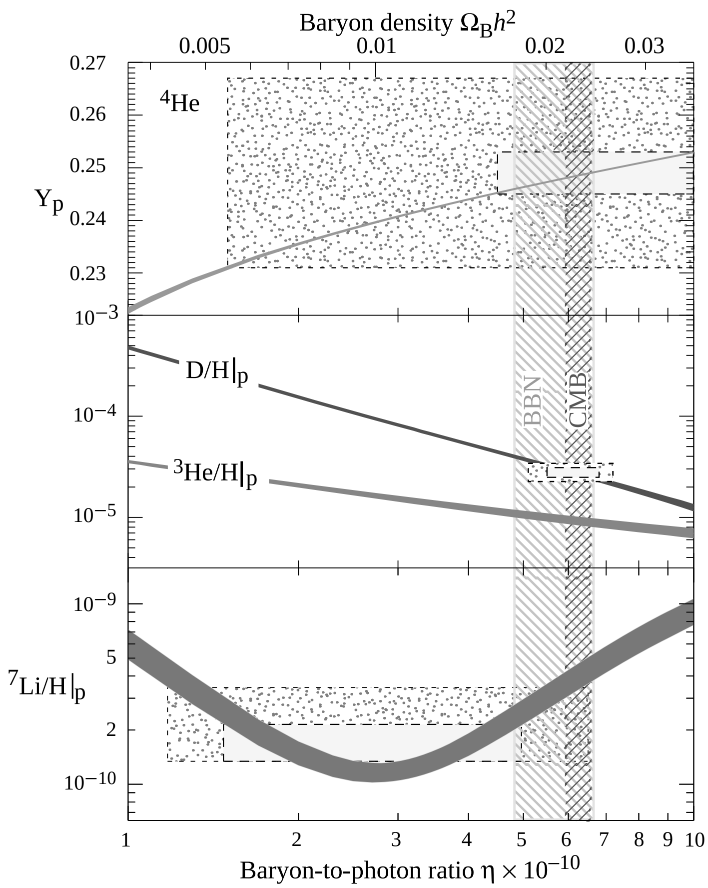

Figure 8.4: The primordial cosmological abundances of ^{4}He, D, ^{3}He and ^{7}Li as a function of the baryon-to-photon ratio. The small boxes indicate 2σ observations, while the bands indicate the 95% C.L. allowed region from CMB and nucleosynthesis arguments. This figure was obtained from Olive et al. [2000].

WIMP induced nuclear recoils can also be detected directly in low background radiation detectors in the laboratory. The characteristic interaction is a nuclear recoil with a spectral shape that is a function of the galactic escape velocity, the mass of the WIMP, the mass of the target nuclei, the Halo density and the coupling cross-section. Another well motivated candidate is the axion-like dark pseudoscalar [Pospelov et al., 2008] which can be searched for as well [Bernabei et al., 2006; Aalseth et al., 2008; Ahmed et al., 2009b]. In this case, the dark matter interacts with the electrons in a detector via the axio-electric effect where the spectral signature is a function of the mass of the pseudoscalar and the halo density.

8.2 Light WIMP Search

The first dark matter limits that are imposed using the low background spectra from the SONGS deployment are on light WIMPs. WIMP-nucleon interactions fall into two distinct types: spin-independent and spin-dependent. For low momentum transfers the scattering amplitudes off each nucleon can add coherently and result in a cross-section proportional to the square of the mass number, A^2 [Lewin & Smith, 1996]. This is analogous to the coherent neutrino-nucleus cross-section (see chapter 7.1). On the other hand, the spin-dependent interaction is an axial vector coupling to the spin of the nucleons. The scattering amplitudes from the paired and opposite spins of the nuclei interfere and thus the cross-section does not benefit from a coherent enhancement. Instead, it is a function of the total spin of the target nuclei (either protons or neutrons) and can be a significantly smaller cross-section than for spin-independent scattering. While there are some experiments designed to be maximally sensitive to spin-dependent interactions (e.g. COUPP) [Behnke et al., 2008], the limits presented here are only for spin-independent scattering. For ionization-only detectors such as PPC germanium detectors only a fraction of the low energy recoil is detectable as ionization, meaning the quenching factor for nuclear recoils must be well characterized. For a more complete discussion of the quenching factor and the results of a measurement with PPC detectors, see chapter 4.

WIMP experiments search for interactions from dark matter from the galactic halo: in order to compare results from different experiments, a standard galactic isothermal halo model is typically assumed. One of the experimental signatures that results is a modulation of the WIMP-nucleon interaction rate due to changes in the velocity of the earth relative to the Halo as it orbits the Sun [Lewin & Smith, 1996]. In the absence of any detection of candidate events or modulation, the experiments place limits on the interaction cross-section of the WIMP as a function of its mass. Limits are expressed in a two-dimensional phase space of the cross-section versus the mass. This is because the interaction rate of dark matter in the detector is a function of the interaction cross-section and the particle mass, with a particle number density constrained by the Halo density (0.3 GeV cm^{-3}). Experiments have been able to place ever stronger limits and have begun approaching the sensitivities required to test the most popular dark matter models [Behnke et al., 2008; Ahmed et al., 2009a]. The DAMA and DAMA-LIBRA collaborations, however, have claimed evidence for the detection of the WIMP annual modulation [Bernabei et al., 2008b]. The experiment is a low background deployment of NaI(Tl) scintillating crystals [Bernabei et al., 2008a]. Much of the allowable region of phase space that would explain this modulation has already been excluded by other experiments. However, for low mass WIMPs (<10 GeV c^{-2}), these experiments do not have the sensitivity of the DAMA detectors [Savage et al., 2004; Gondolo & Gelmini, 2005; Savage et al., 2009]. This is primarily due to the light Na nuclei which can have a higher recoil energy than their counterparts in other detectors. This is not a big concern for many of the Minimal Supersymmetric Models (MSSM) of dark matter as most of them they do not make predictions for such light mass WIMPs. On the other hand, there are recent, well motivated predictions of Next-to-Minimal Supersymmetric Models that produce ample populations of WIMP candidates at these low masses [Cerdeno & Seto, 2009; Aalseth et al., 2008] (see figure 8.19). These provide further motivation for light WIMP searches beyond the possible refutation or confirmation of the DAMA claim.

There are a number of experiments other than the DAMA collaboration that search for the spin-independent interaction of WIMPs. Usually, the experiments utilize some form of discrimination power from their detectors to eliminate unwanted backgrounds. Events that are due to nuclear recoils are kept while interactions from minimum ionizing backgrounds such as gammas are thrown out. One of the most successful experiments to date has been the CDMS experiment [Ahmed et al., 2009a]. It uses bolometric germanium detectors capable of measuring the ionization deposited from an event, which is affected by the quenching factor, as well as the total energy deposited, which is measured by the heat deposited. The ratio of these two measurements provides the ability to discriminate against minimum ionizing backgrounds such as gammas and betas. Another flavor of experiment is typified by the XENON [Angle et al., 2008] and LUX [Kastens et al., 2009] collaborations which use a two phase (gas and liquid) Xenon detector. In this case, discrimination between nuclear recoils and minimum ionizing backgrounds is achieved by comparing the ionization produced in the liquid to the primary scintillation generated. Such experiments are theoretically capable of massive increases in target mass. A third type of experiment is exemplified by COUPP detectors which utilize bubble chambers that are sensitive to nuclear recoils, but are operated in a regime of operational parameters that makes them insensitive to minimum ionizing backgrounds [Behnke et al., 2008]. Unlike all of these detector technologies, PPC detectors do no provide any discrimination against minimum ionizing backgrounds. As such, they do not compete with these experiments in searching for more conventional WIMPs that have masses between 10–100 GeV c^{-2}, where the energy region of interest is typically 10–100 keV (ionization energy). Instead, the lower threshold in PPC detectors provides the ability to place strong limits on light mass WIMP candidates (1–10 GeV c^{-2}) for which no other experiments are sensitive. This is because the lighter the mass of the WIMP, the lower the energy of the recoil. Also, a light WIMP concentrates the signal into a small energy region which leads to a larger differential rate and therefore a larger signal to background ratio than in a more conventional dark matter experiment. WIMP limits obtained with PPC detectors are complementary to those of other experiments.

The claimed observation by the DAMA collaboration for low mass WIMPs, and the existence of models that produce low mass WIMPs, provide further justification for more experiments that are sensitive to this region of phase space. The results reported from the first deployment of PPC detectors to the TARP facility [Aalseth et al., 2008] finally ruled out the conventional WIMP hypothesis for the observed DAMA annual modulation signal. The results presented below benefit from lower backgrounds and a longer exposure and serve to reinforce that conclusion.

8.2.1 Spin-Independent Limits from the SONGS Deployment

Limits on the spin-independent WIMP cross-section versus WIMP mass were obtained from three distinct data runs at the SONGS reactor. The first set of data is from the initial 3 weeks of operation (Run 1), which has a low threshold but suffers from contamination due to cosmogenic backgrounds. The low threshold of this data set provides strong limits for the light WIMP masses (<6 GeV c^2). The second spectrum used is from Run 3. While the threshold is higher because of problems maintaining LN2 levels, many of the cosmogenic backgrounds had already decayed, providing for better limits at slightly higher WIMP masses. The limits from these two runs are combined as if they were separate experiments [Lewin & Smith, 1996] in order to improve the overall sensitivity. These combined limits are surpassed, however, by those obtained from Run 4, which had the lowest backgrounds as well as a low threshold. In all cases it is the low energy spectra that are used to determine the limits (figure 8.5), where these detectors are most competative. The Run 2 data set is unused because it suffers from a high threshold, high elevated backgrounds due to a malfunctioning veto and a short exposure.

The limits were obtained by comparing the measured spectra with all background cuts applied, to the expected spectra of nuclear recoils from the standard isothermal WIMP halo. The recoil spectra were determined, following the formalism of [Lewin & Smith, 1996], with the differential rate given by the equation:

$$\frac{dR}{dE_R} = 0.997\frac{R_0}{E_0 r}[0.751e^{-0.567E_R/E_0 r} - e^{-\upsilon_{esc}^2/\upsilon_0^2}] \tag{8.1}$$

where R_0 is the total event rate, $E_0 = \frac{1}{2}M_D\upsilon_0^2$ is the most likely recoil energy, r is a kinematic factor given by $4M_DM_T/(M_D^2 + M_T^2)^2$, $\upsilon_0 = 230$ km s^{-1} is the halo velocity dispersion and $\upsilon_{esc} = 650$ km s^{-1} is the galactic escape velocity. M_D ($<$ 10 GeV c^{-2}) and $M_T = 0.932 < A >= 67.7$ GeV c^{-2} are the WIMP mass and target mass, respectively. In the determination of the limits, the local WIMP density is assumed to be $\rho_{DM} = 0.3$ GeV cm^{-3}. No accounting is made for any annual modulation of the dark matter interaction rate.

The spectra of nuclear recoils, from equation 8.1, are converted to spectra of ionization energy (in units of keVee or "electron equivalent energy") using the measured quenching factor that was reported in chapter 4. Using the value of k=0.2, from equation 4.1, that seems to provide good agreement with measurements of the quenching factor performed with PPC-1 (chapter 4), 20.8% of the energy of the nuclear recoil is detected as ionization. This causes the signal to appear at a lower energy but with a higher differential rate. The nuclear form factor correction is neglected for the range of WIMP masses probed by this measurement because the momentum transfer is low enough that it can be approximated to be ∼1. Also, because of the excellent energy resolution, there is no need to account for its effect on the spectra of WIMP induced recoils, as is suggested by Lewin & Smith [1996].

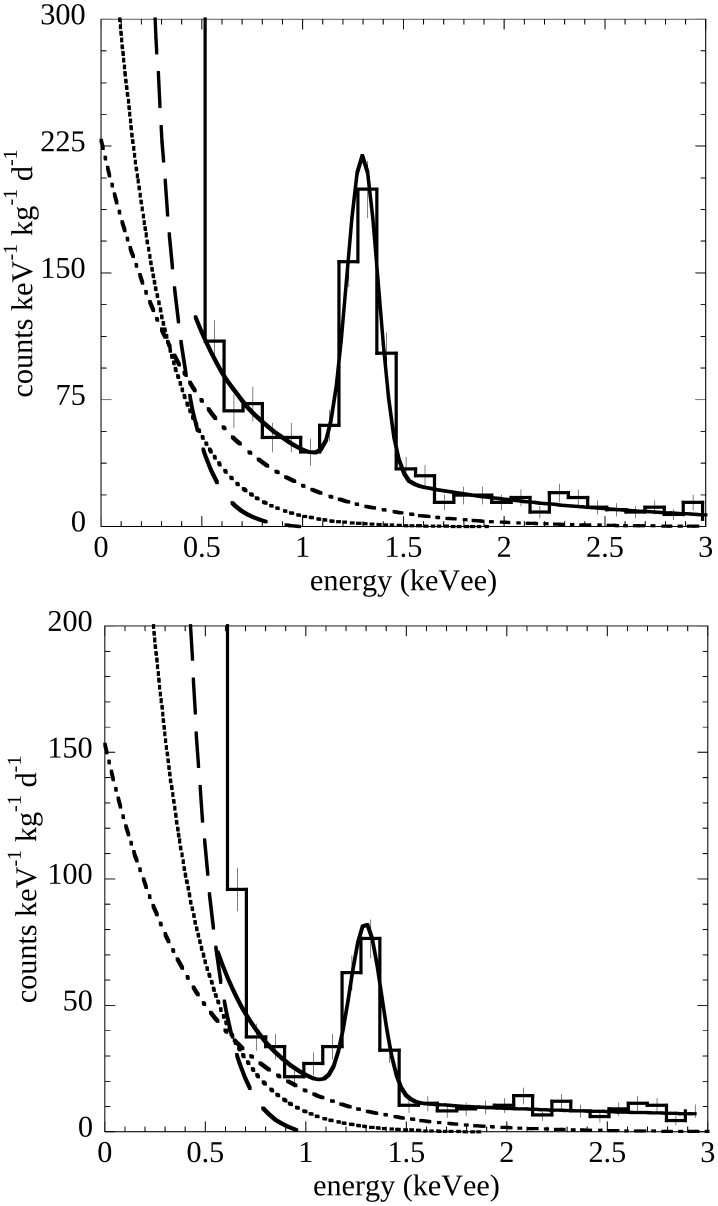

Figure 8.5: Low energy background spectra from Run 1 (top) and Run 3 (bottom). Notice the different scales. The solid lines are fits to the data assuming a contribution from a light WIMP interation, an exponential background and a gaussian peak at 1.298 keV from the cosmogenic activation of ^{68,71}Ge, with the appropriate energy resolution. Also shown are the expected spectra for several excluded (90% C.L.) candidate WIMP masses of 5 (dashed), 7 (dotted) and 10 (dash-dotted) GeV c^{-2}. The cross-sections are, in that same order: (top) 1.9×10^{-3} pb, 5×10^{-4} pb, 3×10^{-4} pb and (bottom) 3.7×10^{-3} pb, 4.7×10^{-4}, 2×10^{-4}.

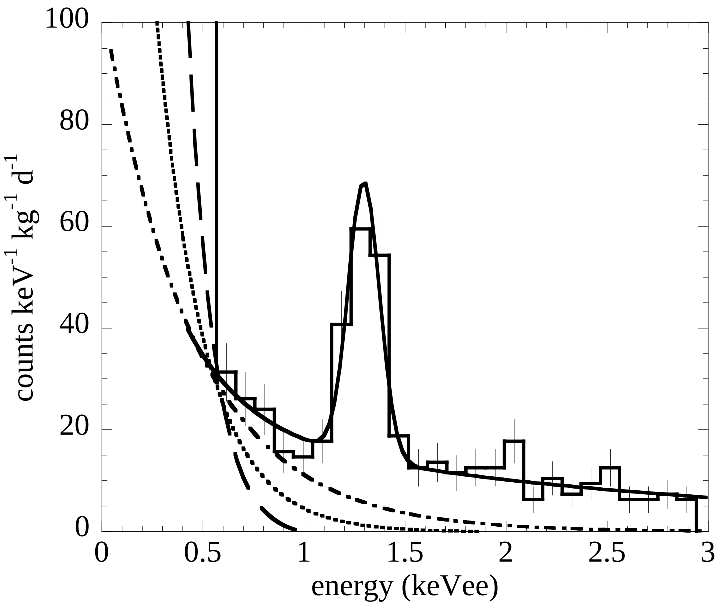

Figure 8.6: Low energy background spectra from Run 4. Notice the different scale compared to figure 8.5. The solid lines are fits to the data assuming a contribution from a light WIMP interaction, an exponential background and a gaussian peak at 1.298 keV from the cosmogenic activation of ^{68,71}Ge, with the appropriate resolution. Also shown are the expected spectra for several excluded (90% C.L.) candidate WIMP masses of 5 (dashed), 7 (dotted) and 10 (dash-dotted) GeV c^{-2}. The cross-sections are, in that same order: 1.6×10^{-3} pb, 2.5×10^{-4} pb, 1.2×10^{-4} pb.

The effect of this was seen to be negligible. The differential rate is then:

$$\frac{dR}{dE_{ioniz}} = 0.997\frac{R_0}{E_0 r}[3.61e^{-2.73E_R/E_0 r} - e^{-v_{esc}^2/v_0^2}] \tag{8.2}$$

Limits are obtained at 90% C.L. by determining the maximum WIMP signal, along with a reasonable background that is compatible with the spectra from the data runs. The background spectrum is composed of a gaussian peak at 1.298 keV with a free amplitude and a resolution fixed by measurements of the Fano factor, as well as a simple exponential to represent the continuum of backgrounds. For each WIMP mass, the expected spectral shape is included with a free normalization that is proportional to the spin-independent WIMP cross-section. The A^2 coherent enhancement to the cross section for these low momentum transfer interactions is included, following the prescription of [Lewin & Smith, 1996]. Example fits for all data runs can be seen in figure 8.5. The best fit that was obtained was to the null hypothesis. Also included in the figure are several excluded recoil spectra for WIMP masses of M_D =5, 7 and 10 GeV c^{-2}.

The WIMP-nucleon couplings excluded at the 90% C.L. are plotted in figure 8.7 and compared to results from several other experiments, including the region compatible with the claimed observation from the DAMA collaboration [Gondolo & Gelmini, 2005].

In this case, the results from Runs 1 and 3 were combined in order to benefit from the increased leverage for low mass WIMPs in Run 1 and the lower backgrounds in Run 3. The exceptional results from Run 4 are presented separately, as the spectra has both an excellent threshold and low backgrounds. Runs 1 and 3 are treated as two separate experiments, which is a valid assumption considering the dramatic differences (i.e. the decreased background from cosmogenic activation and larger threshold possibly resulting from sub-optimal levels of LN2 in the Dewar). Also, the different runs were separated by a significant number of

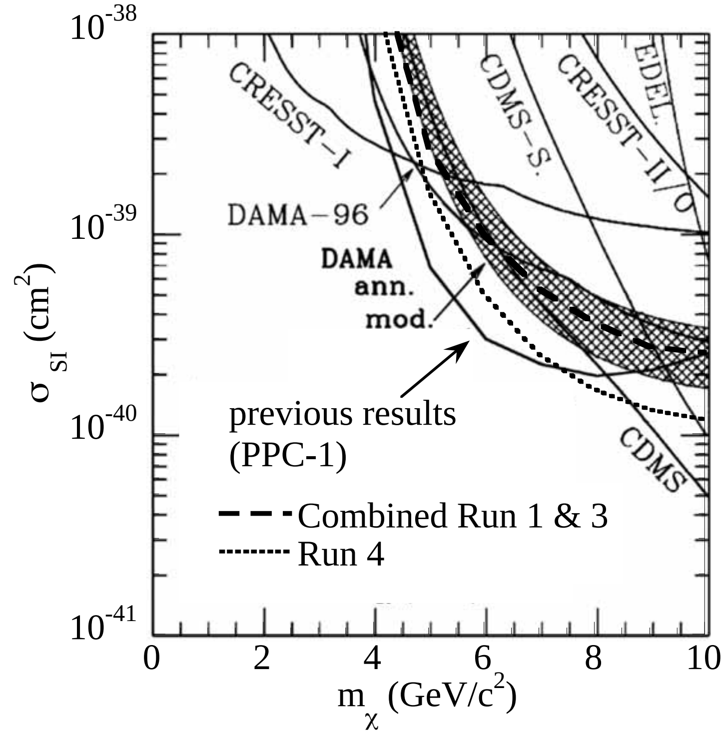

Figure 8.7: Exclusion limits obtained from this deployment for the combination of Runs 1 and 3 (dashed line) are shown, as well as the much improved limits from Run 4 (dotted line). They are compared to the previous limits obtained with the TARP deployment of the PPC-1 detector [Aalseth et al., 2008], as well as several other dark matter searches. The hatched area is the 90% C.L. allowed region for the DAMA annual modulation signal. This figure is adapted from [Aalseth et al., 2008].

days. The results are combined following the prescription of [Lewin & Smith, 1996], where:

$$\widehat{R} = \frac{1}{w}\sum_{i=1}^{N} w_i R_i \tag{8.3}$$

$$\widehat{S} = 1/\sqrt{w} \tag{8.4}$$

where $w_i = 1/S_i^2$, $w = \sum_{i=1}^{N} w_i$, for N different estimates of the rate, R_i, and standard deviations of the rates S_i.

8.2.2 Discussion

The limits presented here, specifically those obtained from Run 4, reinforce the results of the first light WIMP search performed with PPC detectors [Aalseth et al., 2008]. While the backgrounds are lower than those achieved at the TARP facility, the spectral shape of the backgrounds has changed significantly. Specifically, the exponential term used in the background model has a shallower decay for the SONGS results than previously. The result is that it more closely mimics the expected spectral shape from the WIMP interactions, which decreases the sensitivity of the limits for light masses. This effect is clearly seen in figure 8.7. Modifications made to the internal parts and a different contamination from the neutrons at these markedly different depths could be responsible for this. If the active vetoes are not working with their expected efficiency (see simulations in chapter 5), it is possible that the low energy backgrounds at SONGS are from muon induced neutrons, which were not as prevalent at the deeper location. The solution to this is to redeploy the detector to a much deeper site such as the Soudan mine, a project which is in the works at the time of this dissertation.

The channeling of low energy nuclear recoils in the NaI crystals of the DAMA experiment has been proposed as a method for the allowed region to escape the constraints imposed on it [Drobyshevski, 2008; Petriello & Zurek, 2008; Bernabei et al., 2008d; Avignone et al., 2008b]. The effect results in a recovery of the signal lost to the quenching factor for recoils that travel through axial or planar channels in the crystal, increasing the sensitivity of the experiment to lower energy nuclear recoils. It has been pointed out that if this effect occurs in NaI [Graichen et al., 2002], it must also necessarily occur in a single HPGe crystal [Bernabei et al., 2008d], such as with PPC detectors. Thus these detectors would benefit from an increased sensitivity similar to the DAMA experiment.

8.3 Search for Dark Pseudoscalars

The DAMA collaboration has pointed out that the standard hypothesis of an isothermal galactic WIMP halo is not the only possible explanation for the measured annual modulation signal in their detectors. They have suggested that axion-like dark pseudoscalars can be responsible and have offered a corresponding favored region, in terms of the pseudoscalar-electron coupling strength as a function of its mass, that is able to explain the effect [Bernabei et al., 2008b,c]. This is not without controversy however. The formalism utilizes a term in the Hamiltonian that is independent of the velocity of the pseudoscalar, which when multiplied by the flux gives rise to an annual modulation of the signal. This is not the case, as was discussed in [Pospelov et al., 2008], because the correct term in the Hamiltonian is inversely proportional to the velocity, which does not give rise to a velocity dependence of the interaction rate [Pospelov et al., 2008; Collar & Marino, 2009]. Thus, there should be no annual modulation signature. However, the correct calculation suggests that the sensitivity of the DAMA experiment is greater than was originally reported. This effect on the allowed region from the DAMA experiment was estimated in [Collar & Marino, 2009] and is reproduced in figure 8.12.

Despite this controversy, dark pseudoscalars, sometimes referred to as SuperWIMPs, remain a viable candidate for the dark matter [Pospelov et al., 2008]. The signature for the interaction is a peak in the spectrum at an energy that is equal to the rest mass of the particle. PPC detectors excel at such a search because of their excellent energy resolution at low energies (<15 keV). Limits have already been obtained from the previous deployment of a PPC detector to the TARP facility, which were reported in Aalseth et al. [2008]. Similarly, limits have been reported by the CDMS collaboration, where they study only the electronic component of the energy deposited in their detectors [Ahmed et al., 2009b]. While a modest improvement is obtained by CDMS for higher masses, the comparative sensitivity of PPC detectors is remarkable considering the different approaches to background reduction for the two experiments. The effect of the improved resolution and the comparable level of backgrounds is evident in figure 8.10 and figure 6.16, where the results from TARP, SONGS, and CDMS are displayed. The limits presented below benefit from a significant reduction in backgrounds with respect to the TARP run, as well as from an increased exposure.

Leaving aside the experimental constraints, there are also bounds on the axio-electric coupling that are based on astrophysical arguments [Gondolo & Raffelt, 2009]. These are displayed in figure 8.12. The "Solar neutrino" bound relies on the flux of Solar neutrinos as measured by the SNO experiment to limit the energy lost from the Sun, in the form of putative new particles, to less than 10% of its photon luminosity. Bounds are obtained on the axio-electric cross-section because the production and resulting escape of the pseudoscalars with a given cross-section would exceed the limit on such a non-standard energy loss for the Sun [Gondolo & Raffelt, 2009]. The "globular cluster" limit is based on similar arguments arising from the lifetimes of horizontal branch stars in globular clusters [Gondolo & Raffelt, 2009].

8.3.1 Detecting Dark Matter with the Axioelectric Effect

For the class of experiments described here, the dark matter pseudoscalars interact with radiation detectors via the phenomenon known as the axioelectric effect [Avignone et al., 1987]. The process is akin to the photoelectric effect. A diagram of the process can be seen in figure 8.8. The non-relativistic incoming axion interacts with the electrons in the detector, resulting in a recoiling electron which deposits energy in the detector that is equal to the rest mass of the axion.

The dark matter pseudoscalars that are searched for in this experiment have non-relativistic velocities. The result of this is that the energy deposited in the target detector can be ap-

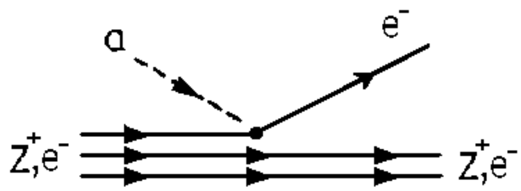

Figure 8.8: Feynman diagram for the axioelectric effect. The mass of the non-relativistic incoming axion (or pseudoscalar) is converted into energy, which is deposited in a detector by the recoiling electron. This figure was obtained from [Bernabei et al., 2006].

proximated by the mass of the axion. Searching for this interaction then becomes an exercise in searching for anomalous peaks in the spectrum at $\sim$ keV energies. The energy resolution of the peak is dominated by the electronic noise and the charge creation statistics of the detector. The energy dependence of the Fano factor must also be taken into account. Contrary to the claims made by the DAMA collaboration in Bernabei et al. [2008b,c], there is no annual modulation of the signal [Pospelov et al., 2008], a fact which simplifies the search.

There are many components to the interaction rate calculation, but for the experimenter the two most important aspects are its proportionality to the product of the axion mass and the photoelectric cross-section of the target material. Following [Pospelov et al., 2008], the complete axion interaction rate from pseudoscalars in a dark matter halo, for an axion mass m_a, is described by the equation:

$$R[kg^{-1}d^{-1}] = 1.2 \times 10^{19} A^{-1} g^2_{a\bar{e}e} m_a \sigma_{pe} \tag{8.5}$$

where R is the total rate, A =72.64 is the average atomic number of the target, $g_{a\bar{e}e}$ is the axion-electron coupling strength and σ_{pe} is the photoelectric cross section in barns/atom. A plot showing the event rate in germanium for an example coupling constant $g_{a\bar{e}e} = 10^{-10}$ can be seen in figure 8.9. The plot illustrates the potential importance of using different

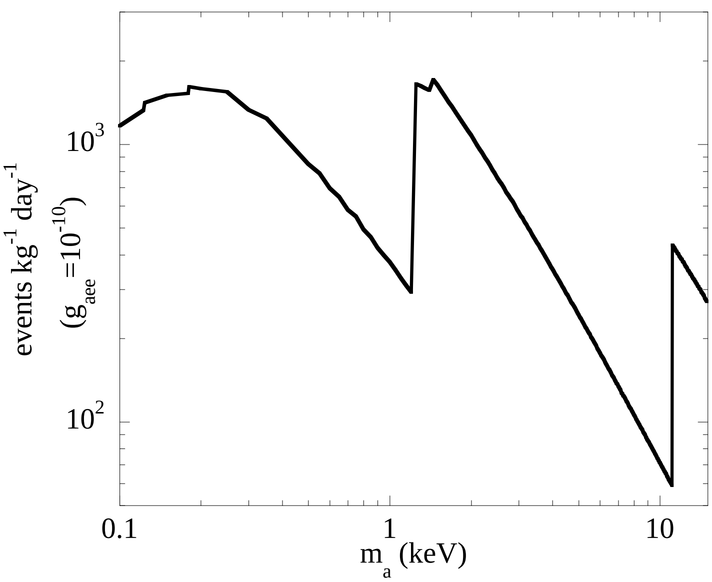

Figure 8.9: Expected rate in a germanium detector as a function of the mass of the dark matter pseudoscalar, assuming an axioelectric coupling strength of $g_{a\bar{e}e}$=10^{-10}. The event rate is proportional to the product of the photoelectric cross section and the mass of the pseudoscalar. The jagged edges come from the binding energies of the K and L shell electrons.

detector targets with complementary sensitivities in order to cover the entire energy range more completely.

Interestingly, the axioelectric effect is a direct measurement of the interaction of axions, or pseudoscalars, with electrons and provides a direct measurement of $g_{a\bar{e}e}$. This is rare for axion experiments, where many search for interactions of axions with photons, such as via Primakoff effect [Zioutas et al., 2005; Avignone et al., 1987; Cebrian et al., 1999; Creswick et al., 1998], .

8.3.2 Limits on Pseudoscalar Dark Matter

Limits on the coupling strength of dark Galactic axions to electrons ($\mathrm{g}_{a\bar{e}e}$) were obtained for axion rest masses (m_a) between 0.5–15 keV. The high energy spectra from the Runs 1, 3 and 4 were used, after the background cuts were applied. As discussed earlier, the backgrounds from cosmogenic activation in Run 1 were still dominant, thus the results from the 9.2 kg-days of that run are less significant. The Run 3 data set, which had an exposure of 14.9 kg-days, has lower backgrounds and better statistics over this energy range and produces strong limits. It benefits greatly from the previous ∼75 days of underground storage, protecting it from cosmogenic activation: several peaks in the 4–9 keV energy range have had the chance to decay away. Unfortunately, the threshold was poor due to low levels of LN2 in the detector Dewar and, thus, the sensitivity to low axion masses suffers. The Run 4 data set has all of the benefits of both Runs 1 and 3, with a low background, a reasonable exposure (12.5 kg-days) and a low threshold. The data set from Run 2 is again unusable for this analysis because of the high backgrounds introduced due to the malfunctioning anti-Compton veto logic unit.

Limits are obtained at the 90% C.L. by fitting the expected signal, along with a reasonable background model, to the unbinned spectra using a maximum likelihood fitting routine.

The expected spectral shape for a pseudoscalar interaction is a gaussian peak located at an energy corresponding to m_a, having a peak resolution determined by the electronic noise of the detector and the measured Fano factor (equation 6.1). The background spectrum model used was composed of an exponential and a linear term. Also included in the background model were K-shell peaks that correspond to the observed electron-capture decays of ^{73,74}As, ^{71}Ge, ^{68}Ga, ^{65}Zn as well as the L-shell peak from ^{71}Ge decay (11.113, 10.368, 9.668, 8.980 and 1.298 keV respectively). There are likely less significant background peaks due to cosmogenic activation in the spectrum that are not included in the fit. While the ^{73,74}As peak is very small, it is included in the background model because it is the remnant of a much larger and well characterized (figure 6.11) population of events, some of which were thrown out using the ^{73}As cut (section 6.6). Finally, the background model included an error function that represented the partial energy depositions (discussed in chapter 5.2.4) of the 10.36 keV peak to the left of the centroid. Its role is clearly visible in figure 8.10. The position of the test peak corresponding to a putative pseudoscalar is scanned over the mass range, where the maximum rate under the peak (at 90% C.L.) is determined and converted to an excluded cross-section using equation 8.5. This is performed for Runs 1, 3 and 4, as if they were separate experiments, a valid approximation considering the significant change in the background model and threshold levels between them, and the large time spans separating them (table 6.1).

A plot showing the excluded couplings as a function of pseudoscalar mass (m_a) is shown in figure 8.12. The limits from the data runs were combined using equation 8.3, the same method as with the light WIMPs [Lewin & Smith, 1996]. The results from a similar search performed by the CDMS collaboration are also depicted, as is the corrected allowed region for the DAMA signal [Collar & Marino, 2009]. The astrophysical bounds are also depicted.

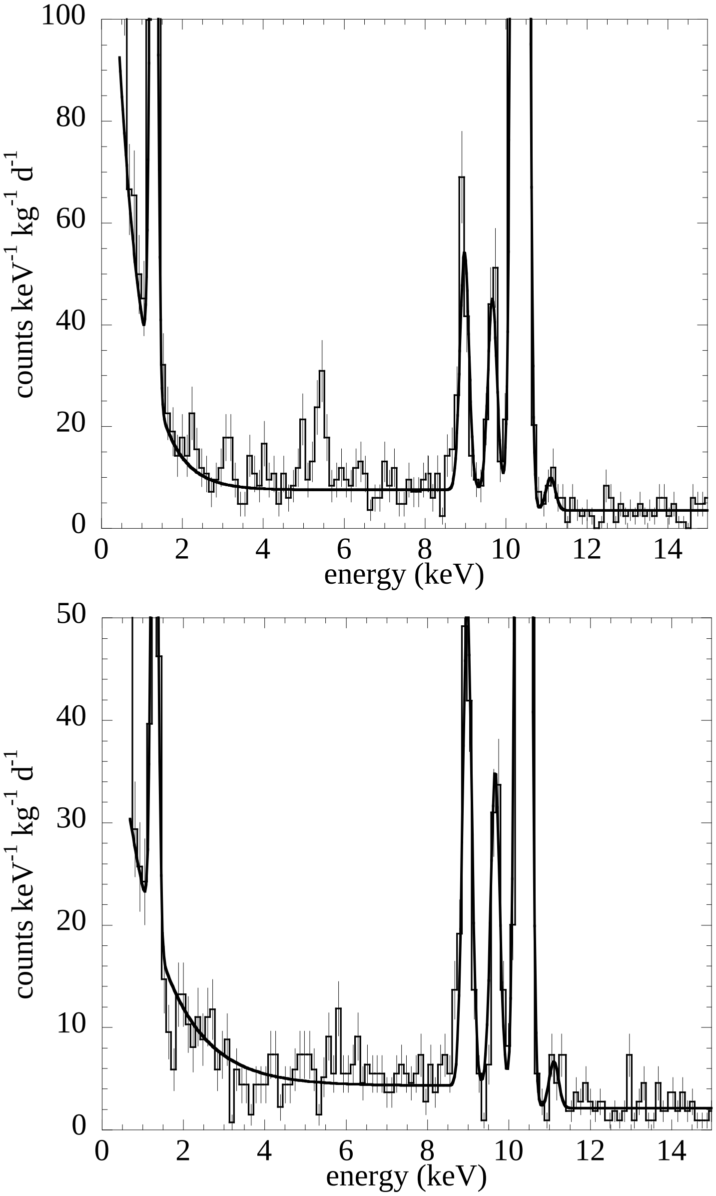

Figure 8.10: The background model used in the search for dark matter pseudoscalars is overlaid on the spectra from Run 1 and 3. The background model includes five gaussian peaks for the well characterized cosmogenic backgrounds as well as a linear and exponential contribution. Also included is an error function to account for the plateau below the 10.3 keV peak from partial energy deposition in the active region (chapter 5.2.4).

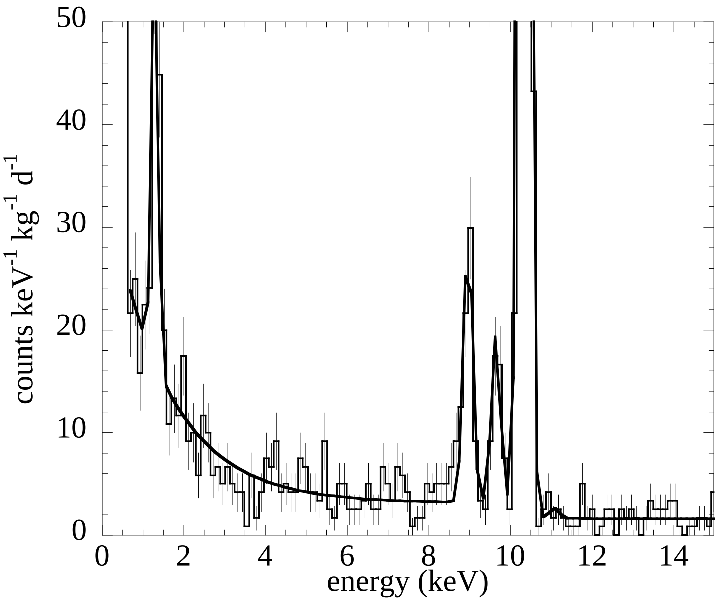

Figure 8.11: The background model used in the search for dark matter pseudoscalars is overlaid on the spectrum from Run4. The background model includes five gaussian peaks for the well characterized cosmogenic backgrounds as well as a linear and exponential contribution. Also included is an error function to account for the plateau below the 10.3 keV peak from partial energy deposition in the active region (chapter 5.2.4).

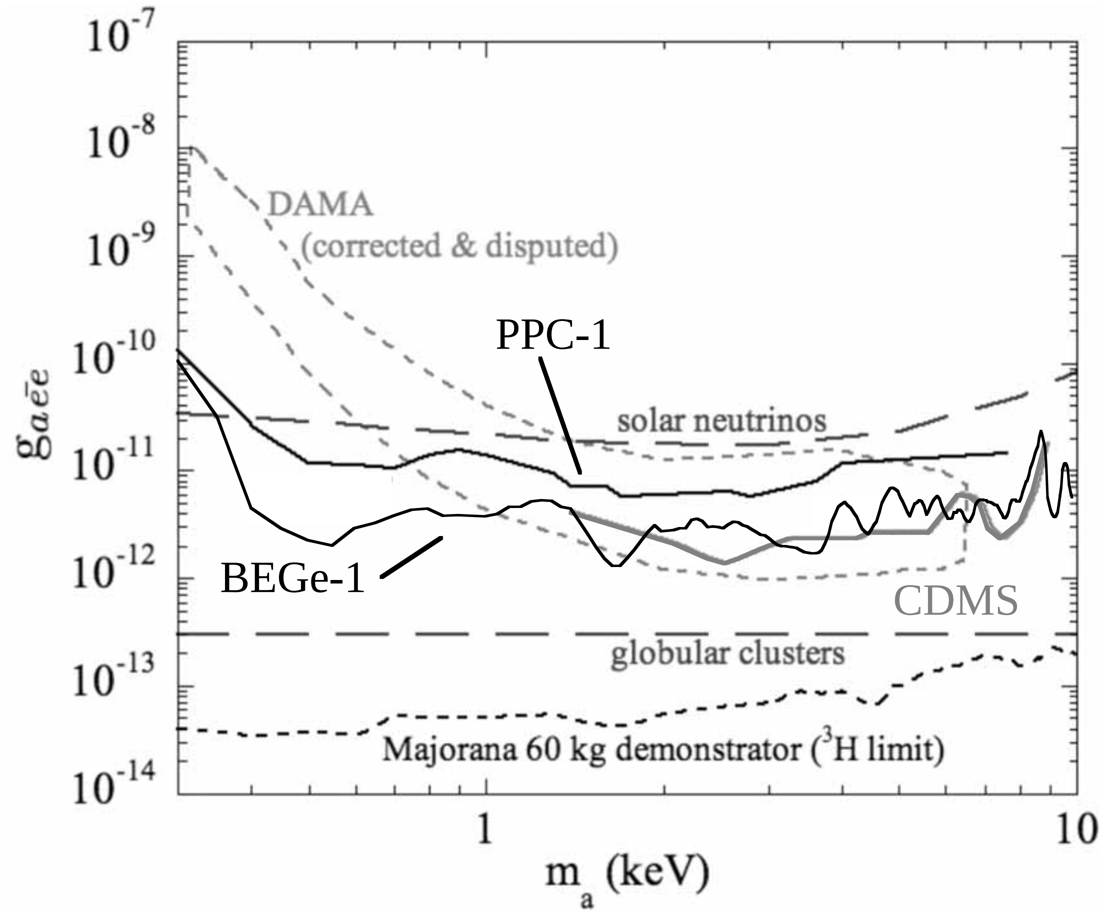

Figure 8.12: The bounds obtained on the axioelectric coupling of a dark pseudoscalar as a function of its mass are shown. The results from this experiment are compared with the previous TARP deployment of PPC-1, as well as recent results from the CDMS collaboration. Also included are the projected limits that can be obtained with the 60 kg MAJORANA demonstrator. The enclosed region represents the allowed region of phase space that is compatible with DAMA observation, a claim which is itself controversial [Pospelov et al., 2008; Gondolo & Raffelt, 2009]. This plot was adapted from [Collar & Marino, 2009].

8.3.3 Discussion

The results obtained for the SONGS deployment are a significant improvement over the those from the earlier TARP deployment, as can be seen in figure 8.12. The results from a recent search by the CDMS collaboration are depicted as well as very competitive with the limits from the SONGS deployment, though only for axion masses >1.5 keV. A redeployment of a PPC detector to a deeper site may benefit from the point of view of lower backgrounds and an increased exposure, and has the potential to improve on the limits reported here. Also shown in the figure is an estimate of the expected sensitivity of the MAJORANA experiment. These are based on simulations of the cosmogenic background for the experiment and are described in more detail in the next section.

8.4 Projected Backgrounds for the 60 kg MAJORANA Demonstrator

The limits presented above for dark matter WIMP and pseudoscalar candidates illustrate the extraordinary strength of PPC detectors for such searches. While the backgrounds for the deployment of the BEGe-1 detector at the SONGS reactor are very low, considering the modest overburden, they are not low by the standards of conventional dark matter or double beta decay experiments. Even so, the limits presented are superior to or competitive with dedicated dark matter searches, again an effect of the improved energy threshold and resolution. It is interesting to consider the limits that could be achieved with a properly deployed low background dark matter experiment such as the 60 kg MAJORANA demonstrator. This section is concerned with the estimation of the low energy backgrounds (<15 keV) for that experiment. It is demonstrated that at these low energies, many of the usual sources of backgrounds are not dominant, such as those from neutrons and gammas. A potential background at the lowest energies from the coherent scattering of Solar Neutrinos is also addressed and shown to be sub-dominant. In fact, the dominant source of events at these lowest energies is from cosmogenic backgrounds. These include the background spectrum from ^{3}H, a beta decay isotope that has an endpoint energy of ~18 keV, as well as the background spectra from a number of expected cosmogenic isotopes that decay via electron-capture, such as ^{68}Ge. The expected background spectrum for the 60 kg Majorana demonstrator is calculated based on several reasonable assumptions about the above ground crystal exposure to cosmic ray neutrons, as well as the depth and duration of the experiment. The effect of the detector energy resolution, as well as an important partial charge collection observed near the lithium-drifted dead layer (chapter 5.2.4), are accounted for in the production of the estimated background spectrum. Dark matter limit projections for light WIMPs and pseudoscalars are then obtained using the same analysis routines described above.

8.4.1 Neglecting Backgrounds from Gammas and Neutrons

Based on the planned surface exposure to cosmogenic activation for the germanium crystals in the 60 kg Majorana demonstrator, and the backgrounds that result from it below ~15 keV, the contribution to the background spectrum from environmental neutrons can be neglected. It is possible to show this by comparing the expected rates from neutron backgrounds, based on a simulation and experimental campaign performed by the IGEX collaboration, to a reference level of backgrounds which is less than the calculated background rate from cosmogenic activation in the energy window below 15 keV. There are four main problem sources of neutrons for underground, low background germanium experiments. These are: neutrons from spontaneous fission and (α, n) in the rock; (μ, n) interactions in the rock, resulting in very high energy neutrons; (μ, n) in the surrounding lead shield; and (α, n) interactions in the lead shield. Normally, characterization of this background would involve in-depth simulations for all of these sources, but this is avoided in this case by utilizing the results from the IGEX collaboration, a previously operated low background germanium detector experiment, which characterized these sources [Cebrián et al., 2005]. The reference level of backgrounds, for which the cosmogenic backgrounds are always larger, is chosen to be 0.2 counts keV^{-1} kg^{-1} y^{-1}, which is based on calculations of the cosmogenic activation and a Monte-Carlo simulation of the resulting background spectra (this choice will be covered in more detail in section 8.4.3).

The IGEX experiment was a deep underground germanium dark matter and double beta decay experiment located in the Canfrac underground laboratory (2450 m.w.e.) in [Morales et al., 2000]. The collaboration performed a systematic study of neutron backgrounds using GEANT4 and FLUKA simulations in tandem with background measurements with the 2 kg germanium detector by varying the neutron moderator thickness (0–80 cm Polyethylene) for the shield [Cebrián et al., 2005]. The results of the study suggest that the experiment was limited in the low energy region (4–10 keV) due to cosmogenic production of ^{3}H. For the purposes of these projections, estimates of the neutron backgrounds are extended to 0.1–15 keV, and where appropriate, translated to a laboratory depth of 4850 m.w.e., which is the depth of the Homestake underground laboratory. Based on the spectral shape of the neutron backgrounds that were simulated and measured, a conservative approximation is made here for the backgrounds in the 0.5–4 keV energy window and is taken to be double that in the 4–10 keV window reported for each type of neutron background by the IGEX collaboration. This estimate is made because of the monotonically increasing level of backgrounds with decreasing energy that is typical of these neutron backgrounds, evident in figure 8.13, which was obtained from Cebrián et al. [2005]. As can be seen in the figure, the highest rates from neutron backgrounds occur at the lowest energies. It is these rates that are compared to our 0.2 keV^{-1} kg^{-1} y^{-1} reference level, which was chosen based on the lowest rates in the cosmogenically activated background spectrum (see figure 8.16) at higher energies ($\sim$15 keV). Thus, the comparisons should be considered very conservative.

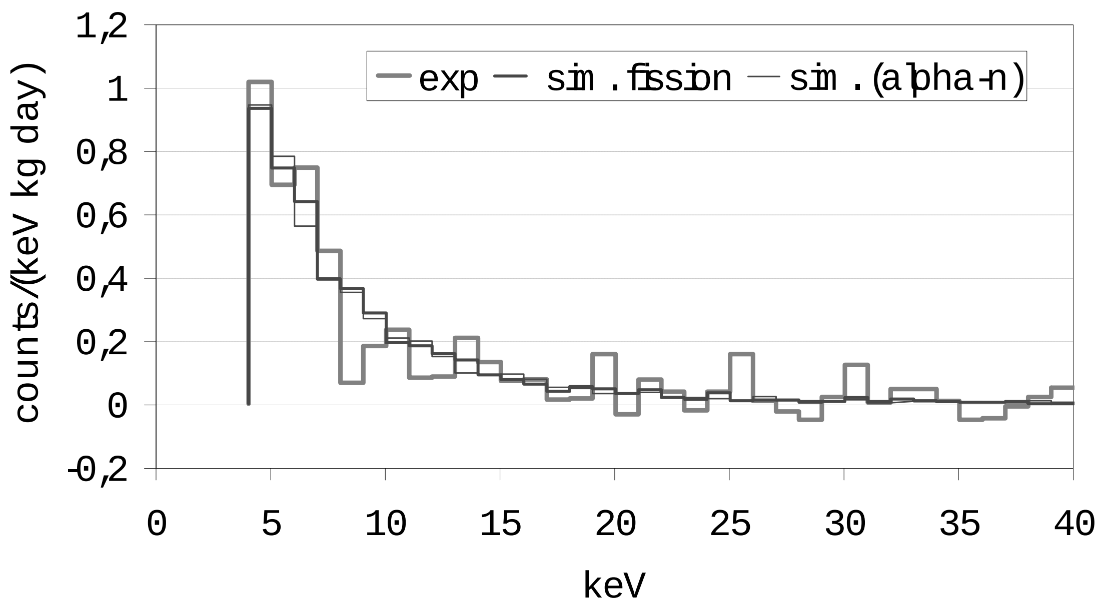

Figure 8.13: A comparison of the simulated energy deposited in the IGEX detector from fission (thick blue line) and (α,n) in the rock (thin blue line) is made to the measured spectra with detector (red line). These results did not incorporate any neutron moderator in the detector shield. Notice the monotonic increase in rate with decreasing energy, a characteristic which is shared by other neutron background sources such as (μ,n). This plot was obtained from Cebrián et al. [2005].

The IGEX collaboration determined that with 40 cm of polyethylene neutron moderator, the contribution to the background from fission and (α, n) in the rock was $\sim$0.064 keV^{-1} kg^{-1} y^{-1} in the range 4–10 keV. This is extrapolated to a conservative estimate of $\sim$0.13 keV^{-1} kg^{-1} y^{-1} in the range 0.5–4 keV. While this approaches our previously mentioned reference level of 0.2 keV^{-1} kg^{-1} y^{-1}, it should be noted that in the energy range (0.5–4 keV), where this neutron background is the largest, the backgrounds from cosmogenic activation are much larger than our reference level (see figure 8.16). Furthermore, it was determined that at 80 cm of moderator, there was a completely negligible contribution from neutrons from the surrounding rock, which will likely be the case for the 60 kg Majorana demonstrator as well, with its planned shielding.

It is noted in Cebrián et al. [2005] that backgrounds from (α, n) in the shielding material contribute three orders of magnitude less than the measured background of 0.078 keV^{-1} kg^{-1} y^{-1} in the range 4–10 keV, for the IGEX experiment. This is extrapolated to a conservative estimated contribution in the 60 kg Majorana demonstrator of 0.16 keV^{-1} kg^{-1} y^{-1} in the range 0.5–4 keV, which also approaches our previously mentioned reference level of 0.2 keV^{-1} kg^{-1} y^{-1}. Again, it should be noted that in the energy range (0.5–4 keV) where this neutron background is the largest the backgrounds from cosmogenic activation are much larger than our reference level (see figure 8.16). While this cannot be attenuated with neutron moderator, as is the case with the neutron backgrounds from fission and (α, n) in the rock, it is unlikely that this will exceed the backgrounds from cosmogenic activation (see figure 8.16).

In addition to neutrons produced from natural radioactivity in the rock, the IGEX collaboration also studied the contribution from (μ, n) in the rock. For 40 cm of polyethylene neutron moderator, the neutrons contributed in the 4–10 keV energy window at the level of 0.32 keV^{-1} kg^{-1} y^{-1}, and for 80 cm the contribution was 0.21 keV^{-1} kg^{-1} y^{-1}. The conservative extrapolation for the 60 kg Majorana demonstrator would then be 0.42–0.64

keV^{-1} kg^{-1} y^{-1} in the range (0.5–4 keV). However, Canfranc has significantly less overburden than the proposed site at Homestake, which reduces the contribution in the 60 kg MAJORANA demonstrator by a factor of $\sim$20, to negligible levels.

Finally, the backgrounds produced from (μ, n) interactions in the lead shielding of the IGEX experiment were determined to contribute $\sim$57 keV^{-1} kg^{-1} y^{-1} in the range 4–10 keV. This extrapolates to a conservative value of $\sim$114 keV^{-1} kg^{-1} y^{-1} in the range 0.5–4 keV. This did not include any reduction that would occur from the use of a muon veto. If a veto is used with very reasonable $\sim$ 99% efficiency for eliminating muons, the conservative estimate for the contribution to the backgrounds in the 60 kg MAJORANA demonstrator becomes 1.2 keV^{-1} kg^{-1} y^{-1} in the range 0.5–4 keV. Again, this is dramatically reduced (by a factor of $\sim$20) with the increased overburden at Homestake, to a level that is easily below our reference of 0.2 keV^{-1} kg^{-1} y^{-1}, and thus it is also sub-dominant compared to the backgrounds from cosmogenic activation.

Similarly, low energy backgrounds from gammas due to natural radioactivity surrounding a low background germanium detector have been extensively simulated by the GENIUS collaboration [Baudis et al., 1999]. The proposed experiment consisted of 100 kg of germanium detectors submerged in liquid nitrogen to search for dark matter and $\beta\beta$ decay. While the construction and deployment of the experiment differs from that proposed for the 60 kg MAJORANA demonstrator, there are enough similarities to make a reasonable comparison, which avoids the need to fully simulate the gamma backgrounds at these low energies. For the lowest energies, the simulations made by the GENIUS collaboration take into account gamma backgrounds from cosmogenic activation but the contribution from ^{3}H production was inadvertently neglected. When background gammas from natural radioactivity in the construction materials are included, the simulated backgrounds at $\sim$ 15 keV do not exceed 0.04 keV^{-1} kg^{-1} y^{-1}. Extending this below 15 keV, and acknowledging that the contribution from this background are nearly flat there [Collar Colmenero, 1992], it is clear that the environmental gammas do not exceed our reference level of 0.2 keV^{-1} kg^{-1} y^{-1} anywhere in the energy window.

Based on previous measurements and Monte Carlo simulations of similar low energy, underground germanium experiments, we can conclude that the contribution of neutron and gamma backgrounds are sub-dominant below 15 keV when compared with other cosmogenic sources able to generate at least 0.2 counts keV^{-1} kg^{-1} y^{-1}.

8.4.2 Neglecting Backgrounds from Solar Neutrino Coherent Scattering

Another potential background in the low energy region that has received some discussion recently [Monroe & Fisher, 2007] is from the coherent neutrino-nucleus scattering of Solar neutrinos. A complete description of the effect can be seen in chapter 7.1, where the original intentended use of PPC detectors as part of a coherent neutrino scattering experiment at a nuclear reactor is described.

The expected rate of recoils from coherent neutrino-nucleus scattering due of Solar neutrinos in a germanium have already been calculated in an early paper by Drukier & Stodolsky [1984]. From this it is possible to see that, for a recoil energy threshold of 0.5 keV, approximately 10^{-3} counts kg^{-1} d^{-1} are expected above threshold. This threshold is chosen based on the potential improvement of the electronic noise threshold to 0.1 keV, accounting for the expected quenching factor for nuclear recoils at the lowest energies of 20%. A discussion of the low energy quenching factor for nuclear recoils can be found in chapter 4. An inspection of the pertinent graph, reproduced in figure 8.14, suggests that these recoils are distributed over a conservatively small energy window of 0.5 keV. Thus, a rate at the very lowest energies of $\sim$0.7 keV^{-1} kg^{-1} y^{-1} is expected. While this just exceeds our previously discussed reference level of 0.2 keV^{-1} kg^{-1} y^{-1}, a quick inspection of figure 8.16 shows that below 0.5 keV, this rate is still dominated by the expected backgrounds from cosmogenic production

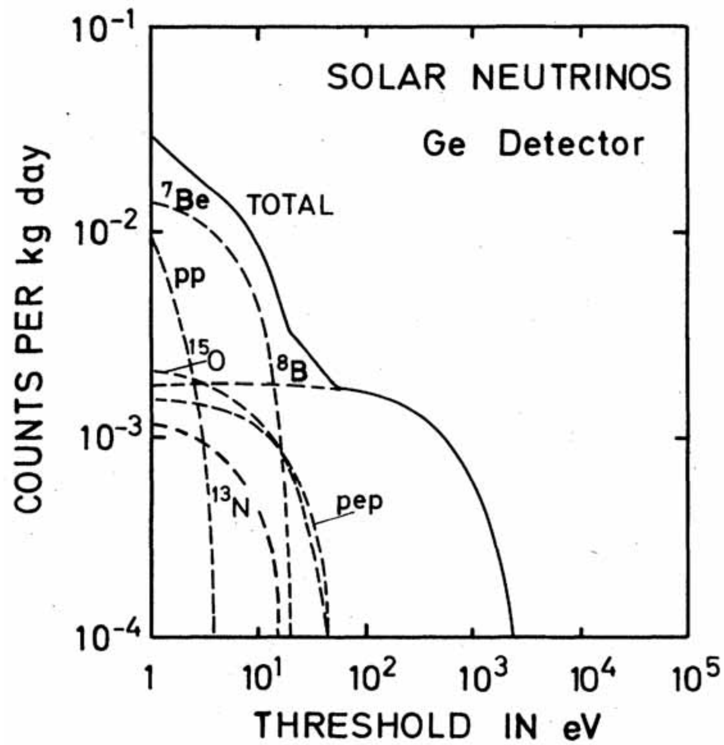

Figure 8.14: The calculated rate of nuclear recoils, above threshold, from coherent neutrino-nucleas scattering of Solar neutrinos. This plot was obtained from Drukier & Stodolsky [1984] .

of ^{3}H.

8.4.3 Background Spectrum from Cosmogenic Activation

The only remaining backgrounds in the low energy region, once neutrons and gammas are neglected, are from the cosmogenic production of tritium and a handful of isotopes that decay via electron capture (see table 8.1). Background spectra were generated for the Majorana experiment assuming the eventual deployment of 40 kg of unenriched PPC germanium detectors. It is assumed that the crystals have been exposed to 15 days of cosmogenic activation during fabrication and transportation, stored underground for 1 year, and then operated for 3 years in a low background cryostat and radiation shield. The realities of the production chain make it essentially impossible that all of the crystals should arrive simultaneously and the 1 year delay is a reasonable estimate.

The expected spectrum from ^{3}H decay in the germanium crystals is simulated using the spectrum derived from [Morita, 1973]. For other cosmogenic contributors undergoing electron-capture decays, the usual signatures are peaks at the K and L shell energies of the daughter atom, where the ratio of K:L decays is ∼10:1. For certain of these nuclei, there is a finite branching ratio for a decay involving the emission of a coincident gamma that can also deposit energy in the germanium detector, which increases the total energy detected for the decay and potentially removes the event from the energy region of interest [Baudis et al., 1999]. Some of these decays can also be easily identified when they interact in more than one crystal, though the fraction for which this occurs depends on the detector array geometry. These effects are neglected in this calculation in order to generate the most general background spectra. In addition, because of charge losses that are likely due to the dead layer, the background model also includes a partial energy deposition effect (figure 8.15) with an additional flat tail below the peak centroid (chapter 5.2.4). Previous measurements have indicated that as much as 4% of the events from electron capture in a shell occur in this continuum, which is consistent with the fractional volume of the Li drifted dead layer of the detectors. An example of such a tail can be seen in figure 8.15 for spectra taken just after the PPC-1 detector was exposed to a large flux of thermal neutrons that lead to a copious number of ^{71}Ge decays. The dead layer for the 60 kg Majorana demonstrator PPC detectors is planned to be half as thick as in PPC-1; as a result, an estimated 2% of the decays that correspond to each electron-capture peak are assumed to be in the lower energy flat continuum.

The background spectra were produced using the Monte Carlo generation capabilities of ROOFIT [Verkerke & Kirkby, 2003]. Probability Density Functions (PDFs) were created for the characteristic spectra of each isotope. While the ^{3}H PDF follows the familiar form

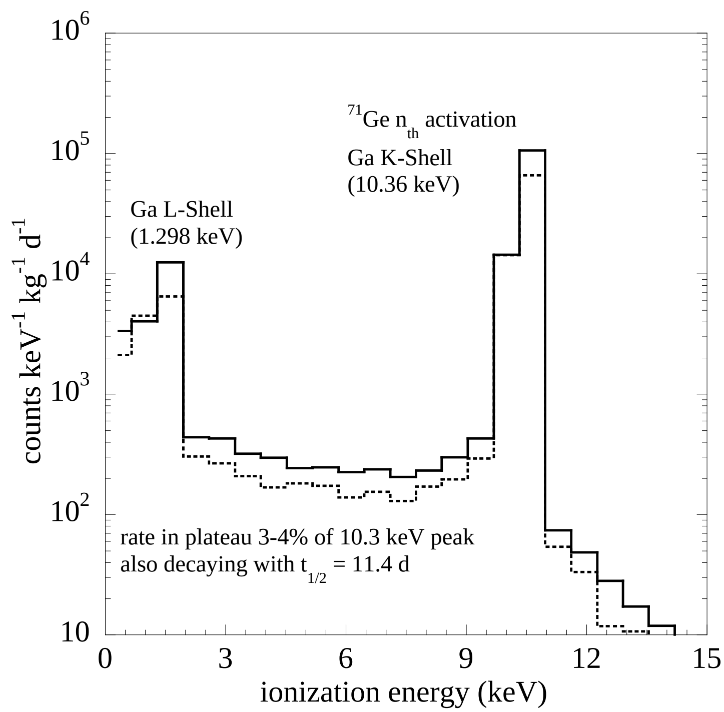

Figure 8.15: The low energy plateau from incomplete charge collection, seen below 10.3 keV in the figure, was conclusively identified with the thermal neutron activation of PPC-1. This was demonstrated in figure 5.9. The region to the left of the K shell peak from ^{71}Ge decayed with the same 11.4 day half-life as the peak, indicating that 3–4% of all events in the K-shell will suffer from partial charge collection. The effect is attributed to partial charge collection at the intersection of the active and lithium-drifted dead regions.

Table 8.1. Cosmogenic Activation of Isotopes Affecting Low Energy Backgrounds in Majorana

Isotope	Peak Energy K-shell keV	L-Shell keV	$T_{1/2}$ days	Cosmogenic Production[a] Rate Nat. (Enr.) kg^{-1} day^{-1}	N_0	Decayed yrs 1–4
^{68}Ge	10.36	1.298	270.95	41.3 (7.2)	6.45×10^5	2.42×10^5
^{68}Ga	9.668	1.194	67 m	8% E.C. per ^{68}Ge	⋯	19,409
^{65}Zn	8.98	1.096	244.26	37.1 (20.0)	22,260	7,713
^{57}Co	7.128	0.846	271.79	13.5 (6.7)	8,100	3,053
^{55}Fe	6.539	0.769	2.73 y	8.6 (3.4)	5,160	2,134
^{54}Mn	5.989	0.695	312.3	2.7 (0.87)	1,620	665
^{3}H	⋯	⋯	12.33 y	27.7 (24.0)	16,620	2,438

[a]For 15 days exposure to activation on the surface [Mei et al., 2009].

of the beta decay with an endpoint at 18.6 keV, those for the electron capture decays are more complicated. The electron capture PDFs contain gaussian peaks at the K and L-shell energies that have widths that are determined by the electronic noise and Fano factor of the detector. The appropriate relative amplitudes (10:1) between the two peaks is also maintained [Siegbahn, 1966]. In addition, for each peak the flat background is approximated by an error function centered at the peak energy and having the same characteristic width as the peak. The number of events that make up each plateau portion of the PDFs comprise 2% of the K or L-shell decays, as explained above. As a result, the plateau components of the lower energy L-shell peaks pack more decays per energy bin than those at higher energies from the K-shells. The threshold of the detector is taken into account by cutting off the spectra at the appropriate low energy point. All of these PDFs are then combined with the appropriate magnitudes reflecting the expected number of decays, per isotope, in the 3 year operational period assuming 15 days of exposure to cosmogenic activation on the surface.

There have been many attempts to calculate and measure the rate of cosmogenic activation of isotopes in germanium detectors through the years [Collar Colmenero, 1992; Avignone et al., 1992; Mei et al., 2009]. For the purpose of these projections, the production rates on the surface from the calculations in Mei et al. [2009] will be used. The production rates for the offending longer lived isotopes are reproduced in table 8.1 along with their corresponding peak energies and half-lives. With the exception of ^{68}Ge, the numbers of unstable nuclei produced after a time t are calculated using the following equation:

$$N = \frac{R}{\lambda}(1 - e^{-\lambda t}) \tag{8.6}$$

where $\lambda = \frac{ln2}{T_{1/2}}$, R is the rate of production and $T_{1/2}$ is the half-life of the isotope. The estimated number of atoms in 40 kg of unenriched germanium crystals after 15 days on the surface are also recorded in table 8.1. During fabrication, the germanium material is purified using a process called zone refinement, which removes chemically dissimilar impurities from the crystal. The process also removes many of the isotopes that were built up in the germanium material from cosmogenic activation. After this, the cosmogenic activation of the germanium crystals must be kept to a minimum. In the case of ^{68}Ge, the isotope is not removed in the zone refinement process, and thus the assumption must be made that the isotope is in equilibrium in the crytsal. The number of atoms of ^{68}Ge prior to storage underground is then:

$$N(\infty) = \frac{R}{\lambda} \tag{8.7}$$

which is also recorded for ^{68}Ge in table 8.1.

The number of decays included in the background for each isotope is then calculated from the operational period between years 1 and 4 after the detectors were activated and placed underground. The governing equation is:

$$N_{decayed} = N_0 \times (e^{-\lambda t_1} - e^{-\lambda t_2}) \tag{8.8}$$

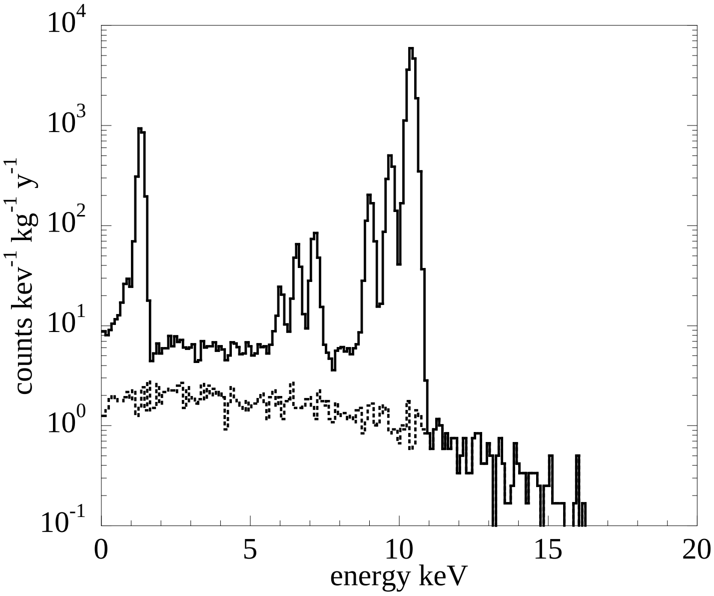

Figure 8.16: The results of a Monte Carlo simulation for the projected low energy backgrounds for the Majorana demonstrator experiment are shown. For energies less than 15 keV the backgrounds are dominated by cosmogenic activation of ^3H (dotted line), as well as several nuclei that decay via electron capture (solid line). See text for details. The detector energy resolution and incomplete charge collection near the lithium-drifted dead layer are accounted for (chapter 5.2.4).

where t_1 is the beginning of operation and t_2 is the end.

The decay of ^{68}Ge is swiftly followed by the decay of its daughter ^{68}Ga with a half-life of 67 m. The large majority of these decay with the emission of a β^+, which has a Q value of 2921 keV. The energy deposition for the events is so spread out that it does not compete as a background in the low energy region. However, $\sim$ 8% decay via electron capture. A PDF for this decay is included in the background model with peaks at the K and L-shell energies of Zn (8.98 and 1.096 keV respectively) with a rate that is 8% of the rate from ^{68}Ge.

Combining all of this information, for the low energy region, the result of a Monte Carlo simulation of the expected dominant backgrounds is shown in figure 8.16. In this case, a detector noise resolution of 160 eV FWHM is assumed. This corresponds to a conservative detector threshold of 0.5 keV. Simulations were also performed assuming a much improved detector threshold of 100 eV, which is potentially within reach for the detector technology. In this case, only the cosmogenically activated backgrounds for the 40 kg of unenriched germanium in the MAJORANA demonstrator module were projected. The case for the intended 20 kg of enriched (86% ^{76}Ge) germanium crystals is less simple to pin down. To begin with, it can no longer be assumed that the ^{68}Ge is in equilibrium. In addition, the cosmogenic production rates for nearly every isotope are less than those for the unenriched crystals. The sole exception to this is rate of production from ^{3}H. Indeed, a detector configuration can be envisioned where, after a sufficient deactivation period, the only low energy backgrounds are from the beta decay of ^{3}H. Thus, the final estimated background projection for the MAJORANA demonstrator is taken to be due to this alone, and is also depicted in figure 8.16. For the sake of simplicity, the ^{3}H spectrum from the 40 kg of unenriched germanium crystals is used, providing a modest improvement of the experimental exposure.

Returning briefly to the justification for neglecting neutron and gamma backgrounds, it is clear that the background rate indicated in figure 8.16 exceeds 0.2 keV^{-1} kg^{-1} y^{-1} everywhere below 15 keV, the reference level used above. The background due to ^{3}H alone cannot be easily avoided because of the long half-life of the isotope ($T_{1/2}$=12.33 y).

8.4.4 Projected WIMP Sensitivity

The potential reach for dark matter WIMP limits is explored using the projected low energy spectra for the 60 kg MAJORANA demonstrator, which is to be built with 40 kg of unenriched PPC detectors. The remaining 20 kg is intended to be built with enriched detectors. As discussed above, the dominant backgrounds below 15 keV are assumed to result from cosmogenic activation of the germanium crystals. Specifically, it is the production of ^{3}H and ^{68}Ge that cause the most problems. The contribution of the ^{3}H decay can be seen in figure 8.17 (dotted line). ^{68}Ga produces two main features that affect these limits. The first is a very dominant L-shell peak at 1.298 keV, while the second is the flat component contributions to the backgrounds that arise from partial charge collection of events near the dead layer of the detector. As discussed above (section 8.4.3), the flat components are assumed to comprise $\sim$2% of the decays for the K and L-shell peaks, thus there is a larger differential rate from this flat background component below 1.298 keV than below the 10.368 keV peak.

Fits to the Monte-Carlo projected spectra were performed using equation 8.2 to generate a WIMP component. Limits on the maximum number of counts allowed to be due to dark matter interactions were obtained assuming the current level of electronic noise of 160 eV FWHM for a threshold of 500 eV, as well as for the goal threshold of 100 eV. The projected 90% C.L. exclusion limits are plotted in figure 8.19 along with the limits achieved in this deployment, for comparison. As is illustrated in figure 8.17, the region near threshold is crowded with L-shell peaks from the various cosmogenic isotopes, obscuring the threshold and limiting the strength of the WIMP fits for 160 eV FWHM detector noise. An improvement is possible with the reduction of the electronic noise for the goal threshold of 100 eV, where greater sensitivity at low energies is available. It is possible that most of the backgrounds, other than the continuum for ^{3}H, can be reduced either through analysis techniques specific to the detector layout (see Baudis et al. [1999] for example), or by waiting for activation products to cool down. In light of this, the projected light WIMP limits in a detector that is contaminated only with ^{3}H were estimated and are included in figure 8.19. This can be considered the limiting reach of such an experiment for the spin-independent WIMP cross-section without performing a more sophisticated annual modulation analysis, or producing the germanium detectors underground away from all activation.

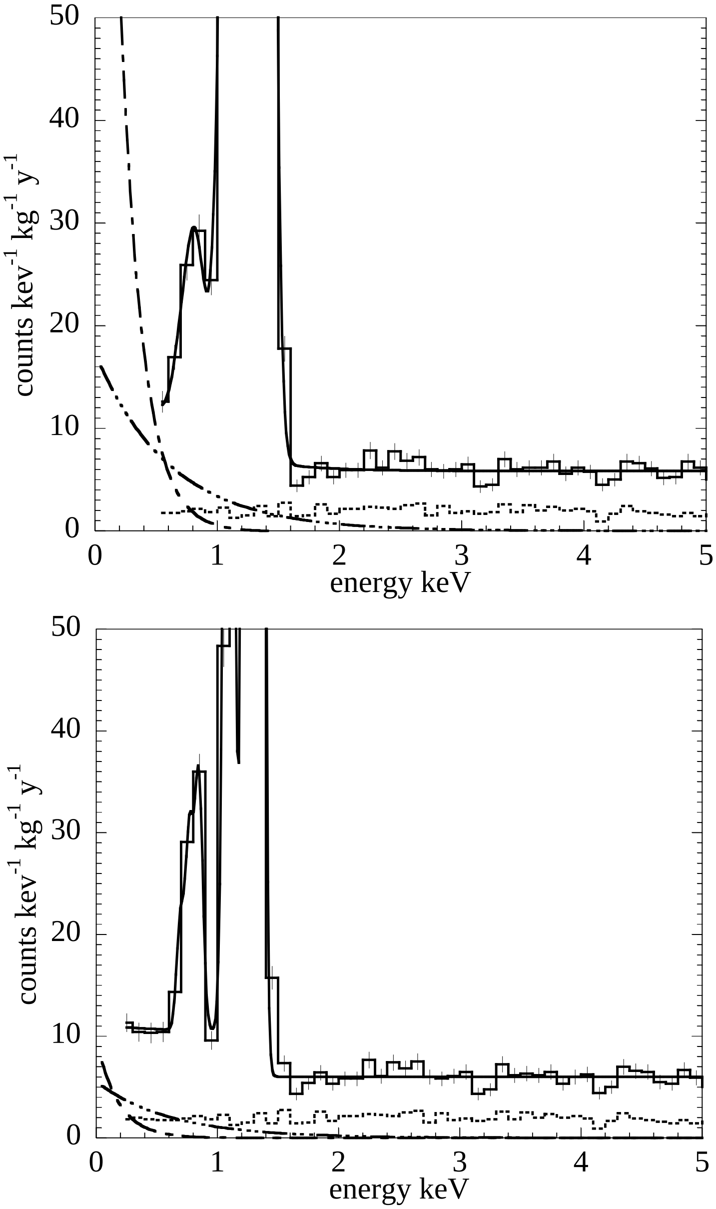

Figure 8.17: This figure illustrates the fits of the background model to the projected background spectra from the MAJORANA demonstrator that were used to project the sensitivity for light WIMP searches. The model accounts for the estimated energy resolution and threshold, 160 eV FWHM (top) and 50 eV FWHM (bottom). Also included are the expected spectra for 6 (dash-dotted) and 12 (dash-triple-dotted) GeV c^{-2} WIMP masses, corresponding to cross-sections (excluded at 90% C.L.) of (top) 3×10^{-7} pb, 7×10^{-8} pb and (bottom) 1.7×10^{-8} pb, 2×10^{-8} pb.

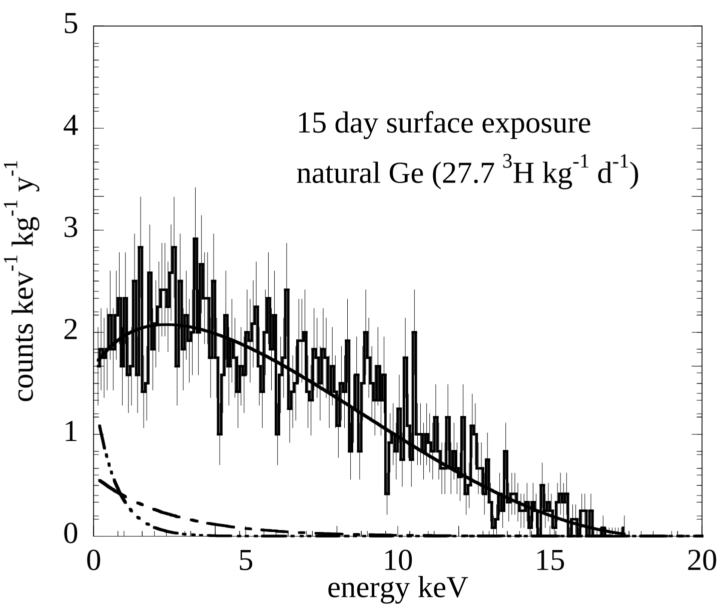

Figure 8.18: This figure illustrates the fits of a background model to the estimated "lower limit" background level, dominated only by the cosmogenic activation of ^{3}H, with a detector threshold of 100 eV. The solid line represents the spectral shape of the ^{3}H beta decay spectrum used to generate the data. This is potentially achievable if a significant time has passed ($\sim$ 5–10 years) with the detectors underground, enough to have the other cosmogenic products decay away. Also shown are the expected recoil spectra from WIMPs with masses of 6 (dash-triple-dotted) and 13 (dash-dotted) GeV c^{-2} with cross-sections of 2.7×10^{-9} pb, 2.2×10^{-9} pb respectively.

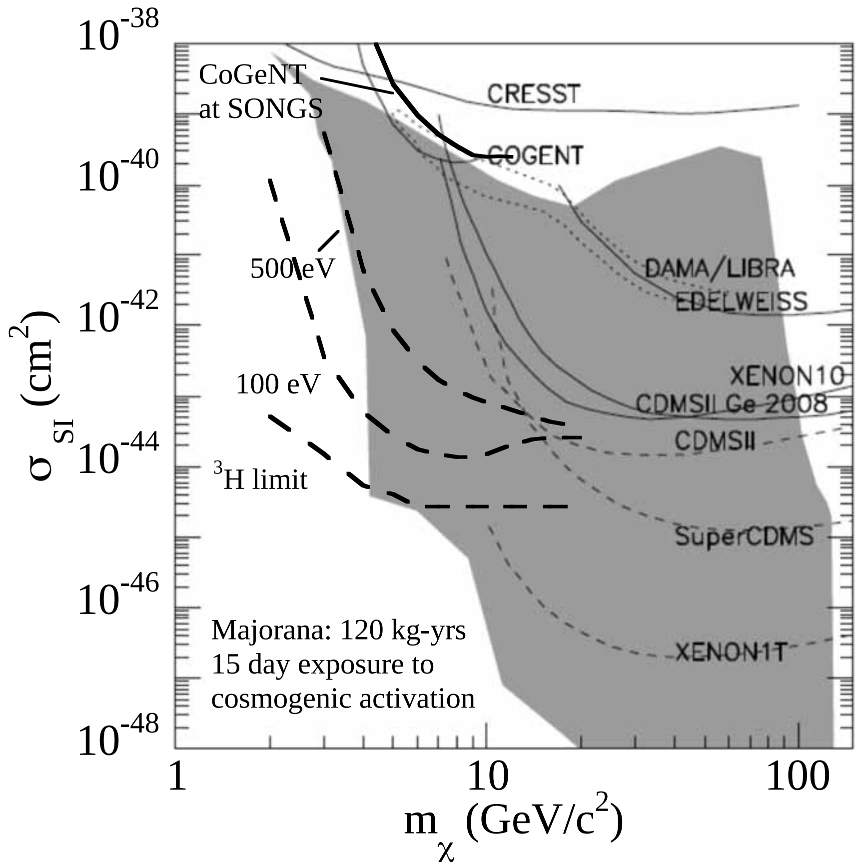

Figure 8.19: Projected limits that can be obtained for light WIMPs by the 60 kg MAJORANA demonstrator. Limits from other experiments are depicted with solid lines, while projections are dashed. Also shown is a shaded region of phase space for models of light WIMPs that are generated by the NMSSM theories. A clear discovery possibility exists for the MAJORANA demonstrator in a region of phase space where other experiments are limited because of their higher thresholds. This plot was adapted from [Cerdeno & Seto, 2009].

8.4.5 Projected PseudoScalar Sensitivity

Limit projections for such a dark pseudoscalar search with the 60 kg Majorana demonstrator can be made using the "lower limit" background estimate that is dominated only by cosmogenic ^{3}H decay seen in figure 8.19. Furthermore, the projected limits assume that the deployed detectors have achieved thresholds of 100 eV. The analysis described in section 8.3 was performed on the ^{3}H background spectrum depicted in figure 8.12. Projected limits were calculated using a fitting routine by scanning the position of the pseudoscalar peak on the unbinned data, depicted in figure 8.19 by the black dotted lines. The appropriate energy dependent peak width was used, as is determined by equation 6.1, which incorporates the Fano factor and an electronic noise of 32 eV FWHM. These assumptions provide the most aggressive projections because of the low background level and excellent signal to background ratio of the peak. The low threshold also provides for strong limits at the lowest energies. The resulting projected limit, depicted in figure 8.12, should be considered the limiting reach for this measurement with the Majorana demonstrator experiment. The possibility to impose experimental limits that significantly surpass all of the astrophysical constraints exists in principle.

CHAPTER 9

CONSTRAINING ELECTRON DECAY WITH PPC DETECTORS

The deployment of the BEGe-1 detector to the SONGS nuclear reactor was part of an attempt to measure coherent neutrino scattering. While this was not achieved in this experiment, significant progress did occur towards this goal. In addition, two experimental limits were placed using the high flux of reactor anti-neutrinos, discussed in chapter 7. Similar to the case of the dark datter searches, discussed in chapter 8, the low background environment can be used as an early test of alternate applications of the large mass, low background PPC detectors within the MAJORANA experiment. One ancillary experiment which is common in low background experiments is a search for the decay of electrons in the detector via either $e^- \rightarrow \nu_e \gamma$ or $e^- \rightarrow \nu_e \bar{\nu}_e \nu_e$ [Belli et al., 1999; Aharonov et al., 1995]. It is the second one, which has been justified as the most likely decay signature, which is described in this chapter. While the backgrounds in the SONGS deployment are not ideal, the uniquely large mass and low noise of this detector result in a surprisingly good sensitivity to the process. The results from the current deployment are compared to the limits from the DAMA experiment, which set the leading lower limits on the lifetime of the electron [Belli et al., 1999]. A similar measurement is to be performed as part of the MAJORANA demonstrator experiment [Majorana, 2003]. The expected sensitivity for the search is estimated using the projected MAJORANA backgrounds discussed in chapter 8.4.

9.1 Violation of Electric Charge Conservation

The electron is the lightest known charged particle, thus a search for electron decay is a search for the violation of conservation of electric charge. There is a connection between the existence of electron decay and the non-zero mass of the photon. In fact, there is a famous theorem by Weinberg that forbids electron decay if the photon is massless, within the framework of quantum electrodynamics [Weinberg, 1964]. Therefore, if electron decay is observed, then the photon must have a finite mass. It should be pointed out that there is no expectation that the electric charge is not conserved. In fact, unlike the case in some GUT theories which violate baryon number conservation and lead to the decay of the proton [Primakoff & Rosen, 1981; Georgi & Glashow, 1974], there have not been any self consistant theories that would provide for electron decay [Belli et al., 1999]. This is not a compelling reason, however, to avoid highly sensitive experiments such as those described here. Aside from the possible discovery of "new physics", further backing of the accepted model would add weight to theoretical arguments.

There are two decay channels that are employed to look for electron decay. The first is the "invisible" decay of the electron to three neutrinos $e^- \rightarrow \nu_e \nu_e \bar{\nu_e}$. The second is the decay $e^- \rightarrow \nu_e \gamma$, which is easier to observe for many detector technologies because of the emission of a 255.5 keV gamma. As a result, the second type of decay achieves more stringent limits on the lifetime of the electron than do typical searches for the "invisible" decay mode.

There are strong theoretical arguments against the existence of electron decay (see Aharonov et al. [1995] and references therein). Some have argued that the explicit violation of electric charge in both types of decay would lead to the delayed emission of very large numbers of longitudinal bremsstrahlung photons with very tiny energies. The photons would rob energy from the gamma in the $e^- \rightarrow \nu_e \gamma$ scheme, eliminating the decay signature. Some have argued that in the "invisible" decay, because the result of the decay is the prompt rearrangement of the electrons in the source atom and the emission of a cascade of x-rays and Auger electrons, the emission of the Bremsstrahlung photons does not have time to inhibit the experimental signature [Aharonov et al., 1995]. The conventional wisdom is that while both unlikely, the "invisible" decay is the more acceptable of the two. As a note of caution, there are strong theoretical arguments against this decay mode as well, the most dramatic of which suggests that a decay of an electron bound in an atom would be accompanied by the decay of all higher energy bound electrons in the universe [Okun et al., 1986; Aharonov et al., 1995], though some assumptions are made that may invalidate the arguments. In the spirit of adventure, limits on this decay mode, which are historically less restrictive of the electron lifetime, are reported on here.

It is interesting to compare the limits on the mass of the photon to what are implied from the limits on the lifetime of the electron. Following the example of [Belli et al., 1999], the electron lifetime τ_e, is given by:

$$\tau_e \simeq 10^{-25}(m_Z/m_\gamma)^2 \; yr \tag{9.1}$$

with the mass of the Z boson m_Z=91.2 GeV, τ_e is the lifetime of the electron and m_γ is the photon mass. To date, the current best experimental limits on the lifetime of the electron do not compete with the sensitivities achieved from the limits on the mass of the photon (equation 9.1).

9.2 $e^- \rightarrow \nu_e \nu_e \bar{\nu}_e$ Decay Signature

Experiments looking for the “invisible” decay of $e^- \rightarrow \nu_e \nu_e \bar{\nu}_e$ use the detecting medium as the source for the decaying electrons. The process is difficult to observe because the resulting neutrinos escape the detector, carrying away the bulk of the energy. The signature of the decay is then due to the hole in a K-shell or L-shell in the germanium detector, which results in a cascade of x-rays and Auger electrons with a total energy that equals the binding energy of the electron. The energy is then deposited in the active volume of the germanium detector as ionization. It is characterized by a gaussian peak with a centroid at the binding energy and a peak width that is determined by the energy resolution of the detector. These peaks are searched for in the low background energy spectra from the detectors and bounds are placed on the process.

The bounds are reported in terms of the lifetime of the electron. The estimate for the mean life is given by the equation:

$$\tau(e^- \to \nu_e \nu_e \bar{\nu_e}) > N\epsilon\ t/A \tag{9.2}$$

where N is the number of on-shell electrons in the germanium crystal, ϵ is the peak efficiency at the specified energy, t is the observation time and A is the number of counts under the peak as determined by a fitting routine. Clearly, the sensitivity of these limits increase with larger detectors, lower backgrounds and longer exposure times.

The peak efficiency is also important, as not all of the energy from the cascade may deposit itself in the active volume of the detector. As has already been shown with PPC-1, there is a significant fraction of the energy that is deposited due to the cascade from the electron capture in ^{68}Ge that is only partially collected (see chapter 8.4). Thus a reasonable estimate of the efficiency ϵ for observing the total energy deposition from electron decays in the entire detector must be made, otherwise the limits obtained will not be conservative.

9.3 Experiments

The pioneering experiment searching for the "invisible" decay of the electron, reported by Goldhaber & Geinberg [1959], was performed using NaI(Tl) scintillation detectors. The cascade resulting from the decay of an electron in a K-shell deposits 33.2 keV, easily above the threshold of a NaI(Tl) scintillator. Aside from the relatively large energy signature, the experiment had the advantage of a large number of electrons in a detector that was relatively massive. The best limits on the lifetime of the electron today come from the low background NaI(Tl) array in the DAMA dark matter experiment [Belli et al., 1999]. The experiment benefits from a dramatic increase in the mass of the detector, state-of-the-art low background crystals and a lower energy threshold. This last point allows the DAMA collaboration to increase the number of electrons that can decay to include all of those in the L-shell as well ($\sim$ 5 keV). There are also very strong limits which come from a deployment of a large low background liquid Xe experiment [Belli et al., 1996], which has an isotope that similarly produces high energy cascades which are easier to detect above threshold.

Both of these techniques begin to suffer, however, because of the poor energy resolution of these detectors and thus the poor separation of the signal from background. Experiments that have performed better in this respect, such as [Aharonov et al., 1995], have utilized HPGe detectors. While the binding energy of the K-shell in germanium is lower (at $\sim$10 keV) than the equivalent in iodine or xenon, HPGe detectors typically have lower energy thresholds that still allow the search to be performed. In addition, the energy resolution is far superior in a germanium semiconductor detector, providing enhanced separation of the signal from the background. Using the advantages of PPC detectors, similar limits are obtained here, even in the presence of relatively high backgrounds and using short exposures.

9.3.1 Advantages of PPC Detectors

The primary advantage over previous experiments when using PPC detectors for this measurement is the superior energy resolution for low energy peaks. For example, as was mentioned in [Aharonov et al., 1995], the COSME detector was used to determine the limits on the decay of $e^- \rightarrow \nu_e \nu_e \bar{\nu_e}$ instead of the TWIN detectors because the lower mass (0.253 kg) detector had the best electronic noise. This allowed easier separation of the signature 11.1 keV peak from the nearby 10.3 keV gallium K-shell than was possible with the TWIN detectors. The BEGe-1 detector has a larger mass than the COSME detector and also has a lower electronic noise. Therefore, there is less crowding of the energy window from the high energy tail of the very large 10.3 keV peak.

Combine this with the fact that an improved electronic noise will undoubtably improve the signal to background and the advantage is clear. It is this last point which allows these detectors to provide competitive results with respect to the lower background NaI(Tl) [Belli et al., 1999] and Xe [Belli et al., 1996] experiments. For the results described below, PPC detectors are stationed at a very shallow 30 m.w.e. depth and have been operated for a relatively short exposure of ∼30 kg-days. In comparison, the dark matter experiment DAMA obtains lower background spectra, with excellent statistics because of a far greater exposure (428 kg yr) [Belli et al., 1999]. This provides fairly tight limits on any excess signal due to electron decay in their region of interest, despite the relatively poor energy resolution of the NaI(Tl) scintillators. Nevertheless, the initial BEGe-1 results described below are competitive because of the enhanced ability to extract a signal from the continuous ~ 1 keV^{-1} kg^{-1} d^{-1} background.

In addition, the DAMA limits are improved by searching for the decay of electrons in the K-shell as well as the L-shell of iodine. This is possible in the NaI(Tl) detectors because of the high energy ∼20 keV of the L-shell binding energy, well above the threshold (~ 2 keV). The benefit comes from the fact that there are four times more electrons at the L-shell than at the higher energy K-shell. An L-shell search is not possible with the COSME detector, which had a threshold (~ 1.5 keV) above the binding energy of the L-shell. It also had significantly increased backgrounds at low energies. PPC detectors have a significantly lower threshold and are capable of performing a measurement using the L-shell electrons.

PPC detectors combine the virtues of these two experimental approaches for such a measurement. These are the improved signal to noise due to the excellent energy resolution and inclusion of the L-shell electron decays due to the lower energy threshold. This provides a pathway for significant improvement of the limits on charge conservation using the $e^- \rightarrow \nu_e \nu_e \bar{\nu_e}$ channel.

9.4 Experimental Limits from the SONGS Deployment

A bound was placed on the lifetime of the electron for the decay $e^- \rightarrow \nu_e \nu_e \bar{\nu_e}$ by searching for the characteristic K and $L_{1,2,3}$ peaks of the decay in the data sets from Runs 1, 3 and 4, after all of the background cuts have been applied. Once again, the Run 2 data set proves of little use as it suffered from a higher level of background due to a malfunctioning veto logic unit.

Limits on the lifetime of the electron at 68% C.L. (and 90% C.L.) were obtained for the K-shell electrons using an extended maximum likelihood fit for a gaussian peak at 11.1 keV (the binding energy in germanium) plus a background model on the unbinned data sets. The peak resolution was determined from equation 6.1 and the peak intensity was kept as a free parameter. Also included in the fit are gaussian peaks at 8.98 keV, 9.67 keV and 10.36 keV, corresponding to the cosmogenic activation peaks that were found in the data sets, with the appropriate width, and a linear fit to the background continuum. The maximum allowable peak rate at a 68% C.L. is plotted in figure 9.1 for the K-shell electrons. It corresponds to an allowed event rate of 14.7±5.4 counts in 20.86 days in Run 1; 11.0±5.2 in 33.8 days in Run 3; and for Run 4, 3.8±3.5 counts in 28.5 days. This does not account for the 19.4% dead time incurred from accidental coincidences with the active vetoes (chapter 6). Limits on the lifetime of the electron are obtained using equation 9.2. An estimate for the peak detection efficiency is required in order to obtain accurate limits. This has been done for a germanium detector with similar dimensions to PPC detectors, in [Aharonov et al., 1995], where a value of ϵ=0.93 was calculated. We observed that only 96% of events from electron-caputre decays deposit their full energy, which is a result of the lithium-drifted dead layer (see chapter 5.2.4), thus the efficiency of ϵ=0.93 is taken as a conservative estimate. There are 7.87$\times 10^{24}$ K-shell electrons in the active volume of BEGe-1 detector, thus the 68%(90%) C.L. bounds for Runs 1, 3 and 4, in this same order, are:

$$\tau_K(e^- \rightarrow \nu_e \nu_e \bar{\nu_e}) > 1.72(1.46) \times 10^{22} yr \tag{9.3}$$

$$\tau_K(e^- \rightarrow \nu_e \nu_e \bar{\nu_e}) > 3.46(2.89) \times 10^{22} yr \tag{9.4}$$

$$\tau_K(e^- \rightarrow \nu_e \nu_e \bar{\nu_e}) > 6.53(4.66) \times 10^{22} yr \tag{9.5}$$

which are added in quadrature to give:

$$\tau_K(e^- \rightarrow \nu_e \nu_e \bar{\nu_e}) > 7.59(5.67) \times 10^{22} yr \tag{9.6}$$

Further bounds are placed on the lifetime of the electron by performing a fit in the lower region of the spectrum to determine the maximum number of counts that can be attributed to electron decay from the L-shell. An extended maximum likelihood fit is performed for gaussian peaks at 1.142 (L_3), 1.248 (L_2) and 1.414 keV (L_1), having widths determined by equation 6.1. The peak amplitudes are fixed at a ratio of 4:2:2, reflecting the number of electrons populating the L_3, L_2 and L_1 shells, respectively. The fit allows the overall normalization of the three peaks to float. The background model includes an exponential decay, as well as a gaussian peak at 1.298 keV that is attributed to ^{68}Ge decay, which has a width determined as above. The maximum allowable rates under the three peaks at a 68% C.L. are plotted in figure 9.3. The corresponding counts under all three peaks for Run 1 are 0$\pm$35.4 in 20.86 days; 23.0$\pm$21.6 counts in 33.8 days for Run 3; and 10.7$\pm$18.2 counts in 28.49 days for Run 4. Again, this does not account for the 19.4% dead time incurred from the vetoes. There are 3.15$\times 10^{25}$ L-shell electrons in the detector, therefore, the 68%(90%)

C.L. bounds on the lifetime of the electron for Runs 1, 3 and 4 are:

$$\tau_L(e^- \to \nu_e \nu_e \bar{\nu_e}) > 3.91(2.38) \times 10^{22} yr \tag{9.7}$$

$$\tau_L(e^- \to \nu_e \nu_e \bar{\nu_e}) > 5.02(3.83) \times 10^{22} yr \tag{9.8}$$

$$\tau_L(e^- \to \nu_e \nu_e \bar{\nu_e}) > 6.53(4.66) \times 10^{22} yr \tag{9.9}$$

which are, when added in quadrature,

$$\tau_L(e^- \to \nu_e \nu_e \bar{\nu_e}) > 9.11(6.48) \times 10^{22} yr \tag{9.10}$$

It is possible to improve the overall limits by adding those obtained from the K-shell and L-shell electrons in quadrature, as was done in [Belli et al., 1999]. The resulting 68%(90%) C.L. overall bound on the lifetime of the electron is,

$$\tau_{K+L}(e^- \to \nu_e \nu_e \bar{\nu_e}) > 1.2(0.86) \times 10^{23} yr \tag{9.11}$$

9.5 Projected Sensitivity of 60 kg MAJORANA Demonstrator

Similar to the limits obtained for dark matter searches, it is possible to project the sensitivity achievable with the 60 kg MAJORANA demonstrator for constraining the lifetime of electron. The projected background spectra for the MAJORANA demonstrator experiment were analyzed using the same extended maximum likelihood routine as above.

The projected limits from the decay of an electron from the L-shell are strongly affected by the cosmogenic continuum from ^{3}H decay and the plateau of partial energy deposition from the 10.3 keV peak. However, as can be seen in figure 8.16 and again in 8.19, at this

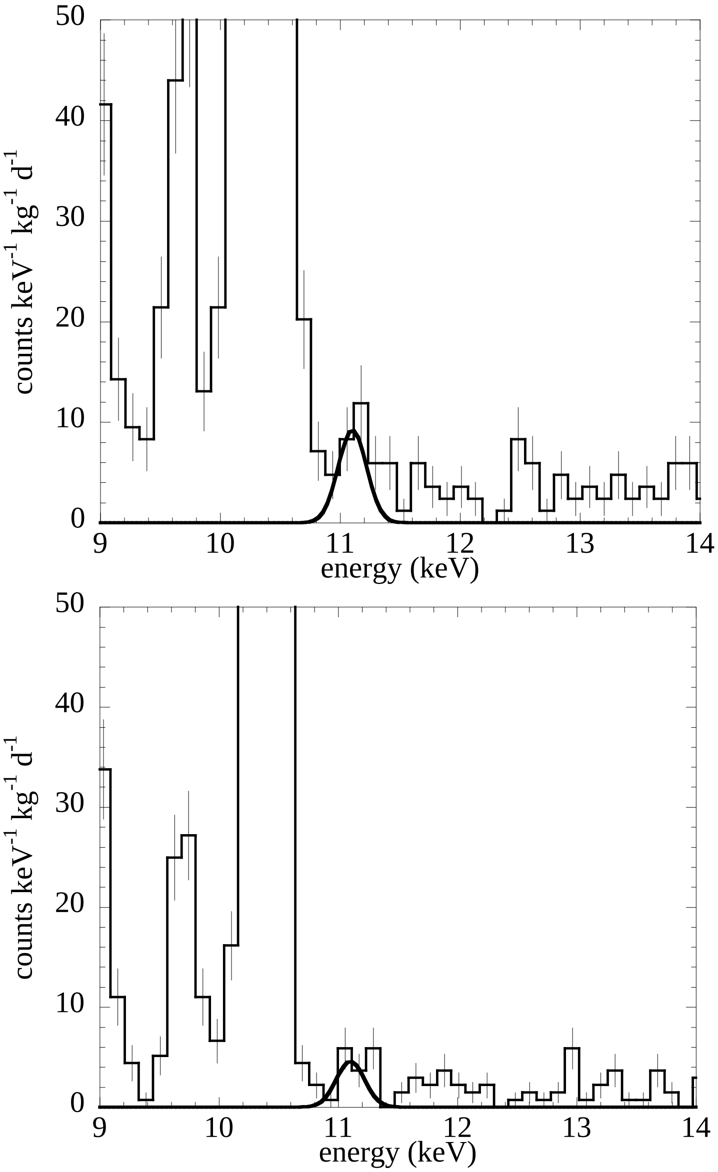

Figure 9.1: The solid line shows the maximum allowed amplitude at 68% C.L. for the gaussian peak centered at 11.1 keV for Run 1 (top) and Run 3 (bottom), which is the signature for the "invisible" decay of an electron from the K-shell of Ge.

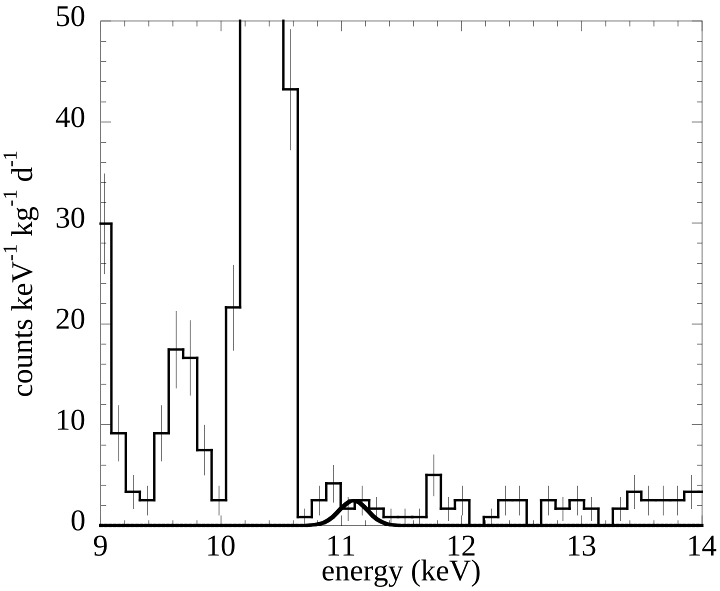

Figure 9.2: The solid line shows the maximum allowed amplitude at 68% C.L. for the gaussian peak centered at 11.1 keV for Run 4, which is the signature for the "invisible" decay of an electron from the K-shell of Ge. A residual activity of cosmogenic ^{73}As is still evident in this run.

energy ($\sim$ 1.2 keV), the dominant backgrounds are from the L-shell peaks of the electron capture backgrounds. Just as in the measurement described above, the limits peaks obscure the expected L-shell peak signature for germanium. Some improvement can be found if the detectors have a further reduced electronic noise because of the increased signal to background ratio of the peaks, as well as the improved separation of the background peaks. The projected sensitivities, assuming an electronic noise of 160 eV FWHM and 50 eV FWHM, are then

$$\tau_{L,160eV}(e^- \to \nu_e \nu_e \bar{\nu_e}) > 1.3(0.8) \times 10^{26} yr \tag{9.12}$$

$$\tau_{L,50eV}(e^- \to \nu_e \nu_e \bar{\nu_e}) > 7.0(4.3) \times 10^{26} yr \tag{9.13}$$

The dramatic improvement in the limits for 50 eV FWHM noise is mostly a result of the reduced spillage of the 1.298 keV gallium L-shell into the region of interest around the 1.4

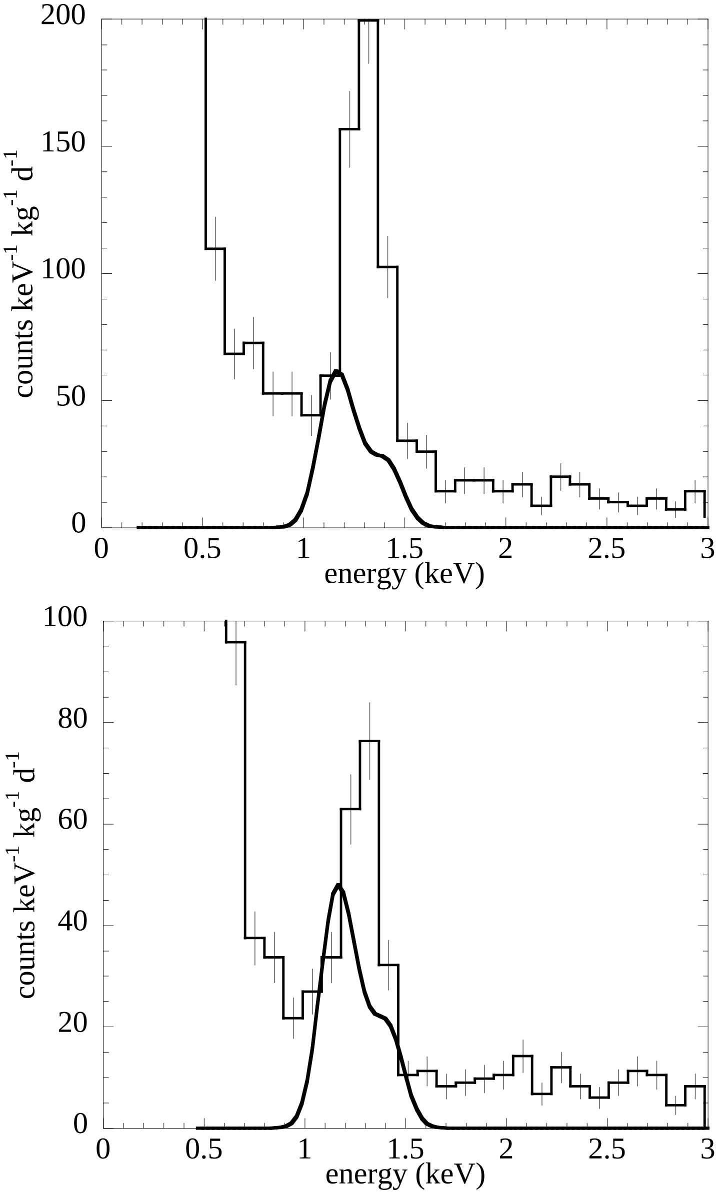

Figure 9.3: This solid line shows the maximum allowed amplitude at 68% C.L. for a gaussian peak centered ∼1 keV for Run 1 (top) and Run 3 (bottom), which is the signature for the "invisible" decay of an electron from the $L_{1,2,3}$-shells of Ge.

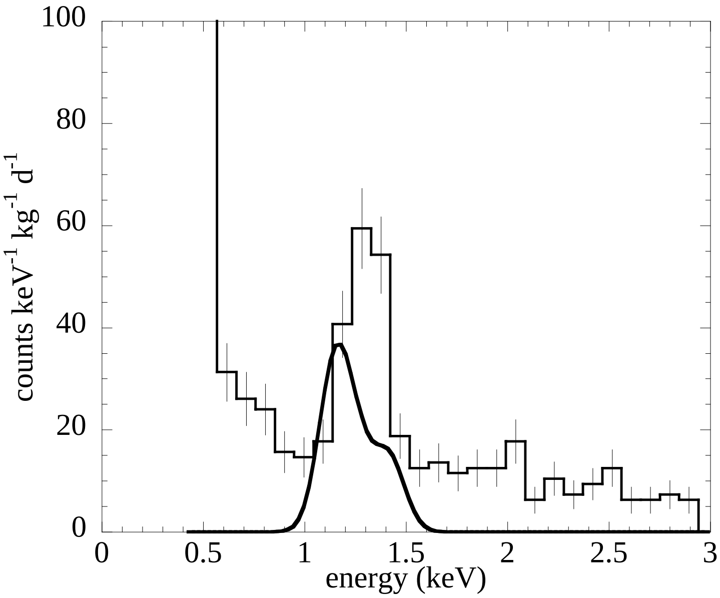

Figure 9.4: The solid line shows the maximum allowed amplitude at 68% C.L. for a gaussian peak centered ∼1 keV for Run 4, which is the signature for the "invisible" decay of an electron from the $L_{1,2,3}$-shells of Ge.

keV L_1 germanium peak. As such, nearly all of the strength of the fit results from the two electrons in the L_1 shell, nullifying the advantage from the factor of 4 increase in the number of electrons in the L-shell.

Unlike the projections at ∼1.2 keV, the only background that contributes to the projected MAJORANA spectrum at 11.1 keV is from the ^{3}H continuum. While the BEGe-1 detector did experience some cosmogenic proton activation of ^{73}As, which reduced the quality of the limit, no significant level of this activation is expected in the MAJORANA demonstrator experiment. The projected sensitivity from the decay of electrons in the K-shell of germanium was determined by applying the same extended maximum likelihood fit used above on the Monte Carlo data. For a detector noise of 160 eV FWHM, the potential sensitivity is:

$$\tau_{K,160eV}(e^- \rightarrow \nu_e \nu_e \bar{\nu_e}) > 1.40(0.86) \times 10^{26} yr \tag{9.14}$$

Similarly to the limits obtained above, the nearby presence of the 10.3 keV peak from ^{68}Ga decay spills into the the region of interest about 11.1 keV, limiting the sensitivity. On the other hand, the estimates for detectors with 50 eV FWHM noise improve greatly due to the increased signal to noise ratio, and most importantly, the improved separation from the Ga K-shell at 10.368 keV. The projected limit is,

$$\tau_{K,50eV}(e^- \rightarrow \nu_e \nu_e \bar{\nu_e}) > 2.83(1.83) \times 10^{26} yr. \tag{9.15}$$

Contrary to a naive expectation, the most sensitive measurement of electron decay in the Majorana experiment is projected here to be due to the 11.1 keV K-shell electrons. This is a direct result of the L-shell electron-capture backgrounds at low energies, which obscure that other region of interest. In addition, the background continuum from ^{3}H is significantly lower at the K-shell binding energy (11.1 keV) than it is at the L-shell binding energy (1.4 keV). Significant improvement is also possible with lower noise detectors resulting from the improved identification and separation of the background peaks.

9.6 Discussion

The results presented here do not begin to compete with the results from the DAMA experiment though they are beginning to approach the sensitivity of the COSME HPGe detector. This is a result of two problems with the experiment. The first, and most obvious, is the existence of a remaining background from ^{73}As, which was produced from cosmogenic proton activation. The second problem is the lack of exposure for the experiment, which was a result of the regular interruptions due to lack of power or LN2. While the experiment does not improve the limits on the lifetime of the electron, it is the first germanium experiment to search for this decay from the L-shell.

Despite the high backgrounds, and poor exposure of the SONGS deployment, the limits are surprisingly strong. This is due to the fact that the energy resolution of PPC detectors is far superior to all other technologies that have performed these measurements. It can be expected that for a proper ultra low background deployment, as would occur for the Majorana demonstrator experiment, a dramatic leap in sensitivity would take place, resulting in an improvement on the current limits by more than a factor of 500 [Belli et al., 1999].

CHAPTER 10

SUMMARY

As a general rule in nuclear and particle physics, the development of a new detector technology brings about new physics opportunities. There is no doubt that such an event has occurred with the development of the P-type point contact (PPC) high purity germanium detector. A number of physics experiments that can be performed with PPC detectors have been explored in this thesis. The following results were presented:

- The quenching factor for nuclear recoils in germanium was measured to be ~20% for recoil energies between 0.6–1.2 keV, which is consistent with the theory as well as previous measurements.

- The low energy backgrounds for a deployment to a nuclear power reactor were assessed and the progress towards a measurement of coherent neutrino-nucleus scattering was described.

- A limit on the magnitude of the neutrino magnetic moment ($\mu_\nu < 4 \times 10^{-10}\ \mu_B$) was obtained. A projected limit ($\mu_\nu < 6 \times 10^{-11}\ \mu_B$) for a longer (~6–8 years), dedicated experiment using PPC detectors was estimated.

- A limit on the continuous energy deposition by reactor neutrinos in matter ($\frac{dE_{em}}{dx} < 4.6 \times 10^{-8} eV\ cm^{-1}$) was obtained, an improvement on a previous limit by over two orders of magnitude.

- Limits on light WIMPs that constrain the physical explanation for the DAMA claimed observation of dark matter were obtained. They are the leading constraints for 8 GeV cm^{-2} mass WIMPs, for which the spin-independent cross-section of WIMP-nucleon scattering must be less than 1.6×10^{-40} cm^2. Projected limits for a similar search using the 60 kg MAJORANA demonstrator experiment where also calculated to reach a level of 3×10^{-44} cm^2 for WIMP masses between 1–20 GeV c^{-2}.

- Limits on dark pseudscalars that also constrain the physical explanation for the DAMA claimed observation of dark matter were obtained. For pseudoscalar masses between 0.3–1.4 keV they are the leading results, for which the axioelectric coupling strength is: $g_{a\bar{e}e} < 2 \times 10^{-12}$. Projected limits for a similar search using the 60 kg MAJORANA demonstrator experiment where also calculated ($g_{a\bar{e}e} < 4 \times 10^{-14}$–$1.4 \times 10^{-13}$) for pseudoscalar masses between 0.3–10 keV.

- A bound on the lifetime of the electron was obtained and found to be $\tau(e^- \rightarrow \nu_e \nu_e \nu_{\bar{e}}) > 8.6 \times 10^{23}$ yr (at 90% C.L.), which is significantly less constraining than the leading result [Belli et al., 1999]. The sensitivity of the 60 kg MAJORANA demonstrator experiment was also calculated to reach a level for a limit on the electron lifetime of $\tau(e^- \rightarrow \nu_e \nu_e \nu_{\bar{e}}) > 1.83 \times 10^{26}$ yr (at 90% C.L.).

APPENDIX A

MEASUREMENTS OF INTERNAL RADIOCONTAMINATION IN DETECTOR COMPONENTS

Low level radioactivity measurements of detector components were made using a low background germanium detector counting facility at the University of Chicago. For the purposes of this experiment, the cleanest materials are not necessary, but it is prudent to characterize the contamination of ^{238}U, ^{232}Th, ^{40}K and ^{60}Co to avoid any unforeseen backgrounds.

The central elements of the counting facility is an Ortec GEM10 low background germanium detector. The detector has a 1.5 mm thick low background magnesium endcap. The crystal is 4.66 cm in diameter and 4.46 cm long, with an estimated 0.05 cm thick dead layer. The detector is recessed within a gamma shield with a large inner volume (30 cm $\times$ 30 cm $\times$ 30 cm). The inner cavity is surrounded by 10 cm of low ^{60}Co steel that supports the $\sim$30 cm of lead bricks all around. It also seems to attenuate gamma backgrounds from ^{210}Pb in the bricks. The detector is located in a laboratory with a moderate 6 m.w.e. overburden. For some measurements, a plastic scintillator muon veto was erected around the lead castle to further reduce backgrounds. Two configurations of the muon veto were used, one designated a "partial" muon veto that only covered the top of the lead castle, and the other "full" veto that surrounded all sides of the castle. The "full" veto, while providing more coverage, is not hermetic, leaving some muon induced gamma backgrounds unaffected. The background spectra measured in these three configurations are displayed in figure A.1. The "full" muon veto reduces the background rate by $\sim$85%, which is consistent with the estimated geometrical coverage of the lead castle. The general effect is to reduce the continuum backgrounds and improve sensitivity to some of the lower energy and lower intensity gamma lines, specifically from the ^{238}U and ^{232}Th decay chains. Spectra from the relevant samples, as well as the background spectra, were obtained over periods of 3–4 days to reduce the effect of a

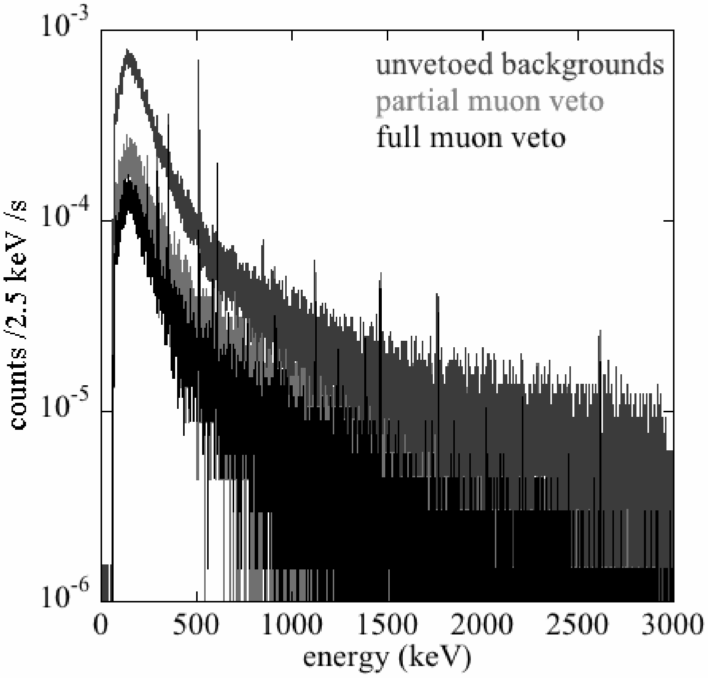

Figure A.1: The measured background spectra in the underground, low background counting facility at the University of Chicago. The germanium detector and shielding were surrounded by two different muon vetoes, the effects of which are also shown.

modulation of the Rn backgrounds in the air from daily ambient pressure changes, which is a background that could be alleviated with a gas tight acrylic box, and nitrogen gas radon displacement. The lab, however, exhibits less than 0.3 pCi L^{-1}, or fresh air levels.

The radioactive contaminations of the samples are estimated by comparing the rates above background for several characteristic gamma peaks with the simulated peak efficiency for complete energy deposition in the crystal. The MCNP geometry used has been well characterized for this detector. Estimating the activity of a radioactive isotope like ^{40}K is straightforward because of the 10.9% of the decays that occur via electron capture, nearly all of them involve the emission of a 1,461 keV gamma. Isotopes like ^{238}U and ^{232}Th involve a chain of decays that leads to very complicated spectra. For the cases measured below, it is assumed that the decay chains are in equilibrium.

A.1 High Voltage Filter

A sample HV filter, of the same type used in PPC-1, was counted using this detector. The spectrum was swamped by the continuum associated to the 1461 keV line from ^{40}K. As such, the sensitivity to the other interesting isotopes is lost because the germanium detector is most sensitive to gamma lines with energies within the continuum. Under the peak, a rate of $0.02\pm1.2\times10^{-1}$ cps above background is measured. The peak efficiency was determined to be 0.0135, with a standard 15% uncertainty assigned from the Monte Carlo. This gives a measured rate of gamma emission of $1.48\pm$ 0.22 Bq, corresponding to a total ^{40}K decay rate of 13.5 ± 2.0 Bq. This is used to estimate the effect of the filter on the gamma backgrounds of the PPC-1 detector when deployed in its radiation shield (chapter 5). MCNP-polimi [Pozzi et al., 2003] simulations were performed using these activity levels of the detector components.

A.2 Preamplifier

Unlike the high voltage filter, the preamplifier for PPC-1 is not dominated by ^{40}K. This allows the measurement of contaminations from the ^{238}U and ^{232}Th decay chains as well. Because the preamplifier is a disperse object, being composed of several electronic boards, it was placed far from the germanium detector (5 cm) in order to make the geometry more point-like. Otherwise, individual components that may have been closer to the germanium detector would have dominated the sample counting measurement. While this necessarily reduced the sensitivity of the measurement, the preamplifier is high enough in activity that the measurement can still be performed in a reasonable amount of time. The measurements indicate a rate of: 0.113 ± 0.010 Bq from ^{238}U; 0.231 ± 0.044 Bq from ^{232}Th; and 0.463 ± 0.069 Bq of ^{40}K. It was assumed that the decay chains are in equilibrium. These values are also used in simulations of background gammas from the difficult-to-shield preamplifier in PPC-1

5.8.

A.3 Lead Bricks

There are three types of lead bricks that were used in the radiation shield of this experiment (chapter 5). The three types are characterized by their levels of contamination of ^{210}Pb, a chemically similar isotope in the bricks that leads to the emission of Bremsstrahlung photons, which can be a background for many experiments. The first type of lead bricks to be mentioned are ultra low background ancient bricks that were cast from ingots using a careful low background technique. There is also a group of lead bricks, that has been stamped "Low Level Radioactivity Lead" (referred to as the stamped bricks) that is found in our lab, that we assume was a result of a similar, but less successful casting using the ancient lead ingots. The last type of lead bricks, referred to as normal lead, are standard commercial bricks found in the laboratory. No assumptions are made of their level of contamination, initially, but as we shall see, they are seen to have an activity of $\sim$100 Bq kg^{-1}. Characterizing the contamination of ^{210}Pb in the bricks that were used is not as straightforward as it is for typical contaminants. For these measurements, we measure the rate of these Bremsstrahlung photons from the ^{210}Bi β^- in lead bricks with an unknown contamination and interpolate between bricks that are better known.

The ultra low background lead (ULB) bricks that may have been recently cast from old ingots have been determined to have <0.02 Bq/kg of ^{210}Pb using ultra low background alpha spectroscopy following radiochemical preparation methods at Pacific Northwest National Laboratory. The second population, the stamped bricks, are assumed to be less contaminated than normal, commercial lead because they were cast from the same old lead ingots, but with less success than the most recent casting. In all three cases, the lead bricks where etched in a nitric acid and still-water solution to remove the outer layers that may have had long exposures to Rn. For each type of lead, the equivalent of 6 standard size (2×4×8 inch) bricks were piled around the germanium detector inside the cavity so that the detector saw only these bricks. This maximizes the efficiency for measuring the Bremsstrahlung photons while further suppressing backgrounds inside the larger lead castle. Because the same thickness of lead was used for each type, the attenuation of backgrounds from the castle is equal. These measurements were performed with the full muon veto in place.

For all three setups, the number of events between 100 keV and 1 MeV were counted, in the energy region where the Bremsstrahlung photons dominate the background. For the conventional lead bricks, the continuum of backgrounds in this energy region was seen to be consistent with a level of $\sim$100 Bq kg^{-1} of ^{210}Pb, by comparing the spectrum to a simulated spectrum from a similar sized germanium detector [Vojtyla, 1996].

It is assumed that even the spectra from the ULB lead are contaminated in this region by events that are not a result of ^{210}Pb. Because the only difference between these three setups is the type of lead used, the contamination is equal in all of them. Thus, by subtracting the counts from the ULB lead run from the others, it is possible to interpolate the activity of the stamped bricks. The excess rate in this energy window from the normal lead, as compared to the ULB lead, was measured to be 0.050±0.002 cps, whereas for the stamped bricks, the excess rate was $0.0074\pm8.0\times10^{-4}$ cps. Interpolating:

$$\frac{R_{known} - R_{ULB}}{R_{standard} - R_{ULB}} = 14.8\% \pm 1.7\% \tag{A.1}$$

With activity of the standard lead bricks estimated to be 100 Bq/kg of ^{210}Pb, and the ULB bricks approximated to have none, the stamped lead bricks can be estimated to have $\sim$15 Bq/kg. The largest uncertainty in this estimate is from the assumed activity of the standard lead bricks, which can range well higher than 100 Bq/kg. For this measurement at SONGS, it is enough to know that these stamped bricks have a significantly lower contamination than normal bricks, and that it is advantageous to have them line the inner layer of the lead shielding described in 5.1.1.

REFERENCES

1997, JENDL-3.2 (Japan Atomic Energy Research Institue Nuclear Data Center)

2009, National Nuclear Data Center, Brookhaven National Laboratory

Aalseth, C. E., et al. 2008, Phys. Rev. Lett., 101, 251301

Abdurashitov, J. N., et al. 1999, Phys. Rev. C, 60, 055801

Aharmim, B. et al. 2005, Phys. Rev. D, 72, 052010

Aharonov, Y. et al. 1995, Phys. Rev. D, 52, 3785

Ahmad, Q. R. et al. 2002, Phys. Rev. Lett., 89, 011301

Ahmed, Z. et al. 2009a, Phys. Rev. Lett., 102, 011301

Ahmed, Z., et al. 2009b, arXiv:0902.4693 [hep-ex]

Aliu, E. et al. 2005, Phys. Rev. Lett., 94, 081802

Angle, J., et al. 2008, Phys. Rev. Lett., 101, 091301

Araki, T. et al. 2005, Phys. Rev. Lett., 94, 081801

Arnaboldi, C. et al. 2008, Phys. Rev. C, 78, 035502

Arpesella, C. et al. 2008, Phys. Rev. Lett., 101, 091302

Ashie, Y. et al. 2005, Phys. Rev. D, 71, 112005

Assamagan, K., et al. 1996, Phys. Rev., D53, 6065

Avignone, F. T., , Elliott, S. R., & Engel, J. 2008a, Reviews of Modern Physics, 80, 481

Avignone, F. T. 2008, Journal of Physics: Conference Series, 120, 052059 (3pp)

Avignone, F. T. et al. 1992, Nuclear Physics B Proceedings Supplements, 28, 280

Avignone, F. T., Brodzinski, R. L., Dimopoulos, S., Starkman, G. D., Drukier, A. K., Spergel, D. N., Gelmini, G., & Lynn, B. W. 1987, Phys. Rev. D, 35, 2752

Avignone, F. T., Creswick, R. J., & Nussinov, S. 2008b, arXiv:0807.3758 [hep-ph]

Balantekin, A. B., & Volpe, C. 2005, Phys. Rev. D, 72, 033008

Barabanov, I., et al. 2006, Nucl. Instrum. Meth. B

Barate, R., et al. 1998, Eur. Phys. J., C2, 395

Barbeau, P., Collar, J., & Whaley, P. 2007a, Nucl. Instrum. Meth. A, 574, 385

Barbeau, P., Collar, J. I., Miyamoto, J., & Shipsey, I. 2003a, IEEE Trans. Nucl. Sci., 50, 1285

Barbeau, P. S., Collar, J. I., & Tench, O. 2007b, JCAP, 2007, 009

Barbeau, P. S., et al. 2003b, Nucl. Instrum. Meth., A515, 439

Barranco, J., Miranda, O. G., & Rashba, T. I. 2005, JHEP, 12, 021

Barranco, J., Miranda, O. G., Rashba, T. I., Semikoz, V. B., & Valle, J. W. F. 2002, Phys. Rev. D, 66, 093009

Baudis, L., et al. 1999, Nucl. Instrum. Meth., A426, 425

Beacom, J. F., Farr, W. M., & Vogel, P. 2002, Phys. Rev., D66, 033001

Beda, A. G., et al. 2007, arXiv:0705.4576v1 [hep-ex]

—. 2009, arXiv:0906.1926v1 [hep-ex]

Behnke, E. et al. 2008, Science, 319, 933

Bell, N. F., Gorchtein, M., Ramsey-Musolf, M. J., Vogel, P., & Wang, P. 2006, Phys. Lett., B642, 377

Belli, P. et al. 1999, Phys. Lett. B, 460, 236

Belli, P., Bernabei, R., & Di Nicolantonio, W. 1996, Astrop. Phys., 5, 217

Benoit, A., et al. 2007, Nucl. Instrum. Meth., A577, 558

Bernabei, R. et al. 2008a, Nucl. Instrum. Meth. A, 592, 297

—. 2006, International Journal of Modern Physics A, 21, 1445

Bernabei, R., et al. 2008b, Eur. Phys. J., C56, 333

—. 2008c, Mod. Phys. Lett., A23, 2125

—. 2008d, Eur. Phys. J., C53, 205

Bernabéu, J., Cabral-Rosetti, L. G., Papavassiliou, J., & Vidal, J. 2000, Phys. Rev. D, 62, 113012

Bertuccio, G., & Pullia, A. 1993, Rev. Sci. Instrum., 64, 3294

Bettini, A. 2007, Nucl. Phys. B Proc. Suppl., 168, 67 , proceedings of the Neutrino Oscillation Workshop

Blair, J., Beckedahl, D., Kammeraad, J., & Schmid, G. 1999, Nucl. Instrum. Meth. A, 422, 331

Bogdanova, L. N., Gavrilov, M. G., Kornoukhov, V. N., & Starostin, A. S. 2006, Phys. Atom. Nucl., 69, 1293

Bowden, N. S., et al. 2008, arXiv:0808.0698 [nucl-ex]

Briesmeister, J. F., ed. 1993, MCNP, A General Monte Carlo N-Particle Transport Code, LA-12625-M (Los Alamos National Laboratory,)

Brun, R., & Rademakers, F. 1997, Nucl. Instrum. Meth. A, 389, 81 , new Computing Techniques in Physics Research V

Budjas, D., Heider, M. B., Chkvorets, O., Schonert, S., & Khanbekov, N. 2008, arXiv:0812.1735v1 [nucl-ex]

Bueno, A., Carmona, M. C., Lozano, J., & Navas, S. 2006, Phys. Rev., D74, 033010

Cabrera, B., Krauss, L. M., & Wilczek, F. 1985, Phys. Rev. Lett., 55, 25

Caldwell, D. O. et al. 1990, Phys. Rev. Lett., 65, 1305

Castera, A., Dumarchez, J., Lachaud, C., & Vannucci, F. 1999, Phys. Lett., B452, 150

Cebrián, S. et al. 2005, Nucl. Phys. B Proc. Suppl., 138, 65

Cebrian, S., et al. 1999, Astropart. Phys., 10, 397

Cerdeno, D. G., & Seto, O. 2009, arXiv:0903.4677

Chasman, C., Jones, K. W., Kraner, H. W., & Brandt, W. 1968, Phys. Rev. Lett, 21, 1430

Chasman, C., Jones, K. W., Ristinen, R. A., & Sample, J. T. 1967, Phys. Rev., 154, 239

Clowe, D., et al. 2006, Astrophys. J., 648, L109

Collar, J. I., & Giomataris, Y. 2001, Nucl. Instrum. Meth., A469, 249

Collar, J. I., & Marino, M. G. 2009, arXiv:0903.5068

Collar Colmenero, J. I. 1992, PhD thesis, University of South Carolina, uMI-93-07926

Creswick, R. J., Avignone, F. T., Farach, H. A., Collar, J. I., Gattone, A. O., Nussinov, S., & Zioutas, K. 1998, Phys. Lett. B, 427, 235

Cyburt, R. H., Fields, B. D., & Olive, K. A. 2003, Phys. Lett., B567, 227

da Silva, A. et al. 1995, Nucl. Instrum. Meth. A, 354, 553

Danilov, M. et al. 2000, Phys. Lett. B, 480, 12

Daraktchieva, Z. et al. 2005, Phys. Lett. B, 615, 153

Daraktchieva, Z., & for the MUNU Collaboration. 2003, arXiv:hep-ex/0305057

Dodd, A. C., Papageorgiu, E., & Ranfone, S. 1991, Phys. Lett., B266, 434

Drobyshevski, E. M. 2008, Mod. Phys. Lett. A, 23, 3077

Drukier, A., & Stodolsky, L. 1984, Phys. Rev. D, 30, 2295

Efremenko, Y., & Hix, W. R. 2009, J. Phys. Conf. Ser., 173, 012006 (6pp)

Eguchi, K. et al. 2003, Phys. Rev. Lett., 90, 021802

Elliott, S. R. et al. 2009, J. Phys. Conf. Ser., 173, 012007 (9pp)

Elliott, S. R., Gehman, V. M., Kazkaz, K., Mei, D.-M., & Young, A. R. 2006, Nucl. Instrum. Meth., A558, 504

Ellis, J. R. 2001, Nucl. Phys. Proc. Suppl., 91, 503

Fano, U. 1947, Phys. Rev., 72, 26

Ficenec, D. J., Ahlen, S. P., Marin, A. A., Musser, J. A., & Tarlé, G. 1987, Phys. Rev. D, 36, 311

Filippini, J. P. 2008, PhD thesis, University of California, Berkeley

Firestone, R. B. 1996, Table of Isotopes, cd rom edition edn. (Wiley-Interscience)

Formaggio, J. A., & Martoff, C. J. 2004, Annu. Rev. Nucl. Part. Sci., 54, 361

Freedman, D. Z. 1974, Phys. Rev. D, 9, 1389

Freedman, D. Z., Schramm, D. N., & Tubbs, D. L. 1977, Ann. Rev. Nucl. Part. Sci., 27, 167

Fukugita, M., & Yanagida, T. 1987, Phys. Rev. Lett., 58, 1807

Gatti, E., Manfredi, P. F., Sampietro, M., & Speziali, V. 1990, Nucl. Instrum. Meth. A, 297, 467

Genz, H., Wood, R. E., Palms, J. M., & Venugopala Rao, P. 1973, Zeitschrift fur Physik, 260, 47

Georgi, H., & Glashow, S. L. 1974, Phys. Rev. Lett, 32, 438

Giomataris, Y., & Vergados, J. D. 2006, Phys. Lett., B634, 23

Goldhaber, M., & Geinberg, G. 1959, Proc. Natl. Acad. Sci. USA, 45, 1301

Gondolo, P., & Gelmini, G. 2005, Phys. Rev., D71, 123520

Gondolo, P., & Raffelt, G. 2009, Phys. Rev., D79, 107301

Gonzalez, D., et al. 2003, Nucl. Instrum. Meth., A515, 634

Gorchtein, M., Bell, N. F., Ramsey-Musolf, M. J., Vogel, P., & Wang, P. 2007, AIP Conf. Proc., 903, 287

Gorshkov, G. V., & Zyabkin, V. A. 1973, Atomic Energy, 34, 269

Goulding, F. S. 1972, Nucl. Instrum. Meth., 100, 493

Goulding, F. S., & Landis, D. A. 1982, IEEE Trans. Nucl. Sci., NS-29, 1125

Graichen, J., Maier, K., Schuth, J., Siepe, A., & von Witsch, W. 2002, Nucl. Instrum. Meth., A485, 774

Gütlein, A. et al. 2008, J. Low Temp. Phys., 151, 629

Hagmann, C., & Bernstein, A. 2004, IEEE Trans. Nucl. Sci., 51, 2151

Hellmig, J., & Klapdor-Kleingrothaus, H. V. 2000, Nucl. Instrum. Meth. A, 455, 638

Hess, W. N., Patterson, H. W., Wallace, R., & Chupp, E. L. 1959, Phys. Rev., 116, 445

Heusser, G. 1995, Ann. Rev. Nucl. Part. Sci., 45, 543

Hoppe, E. Pacific Northwest National Laboratory, Private Communication

Horowitz, C. J., Coakley, K. J., & McKinsey, D. N. 2003, Physical Review D, 68, 023005

Irastorza, I. G., et al. 2003, Astropart. Phys., 20, 247

Jones, K. W., & Kraner, H. W. 1971, Phys. Rev., C4, 125

—. 1975, Phys. Rev., A11, 1347

Jungman, G., Kamionkowski, M., & Griest, K. 1996, Phys. Rept., 267, 195

Kastens, L. W., Cahn, S. B., Manzur, A., & McKinsey, D. N. 2009, arXiv:0905.1766

Kayser, B. 1982, Phys. Rev. D, 26, 1662

Klapdor-Kleingrothaus, H. V., Dietz, A., Harney, H. L., & Krivosheina, I. V. 2001, Mod. Phys. Lett., A16, 2409

Kolb, E. W., & Turner, M. 1990, The Early Universe (Frontiers in Physics. Westview Press)

Kopeikin, V. I., Mikaelyan, L. A., Sinev, V. V., & Fayans, S. A. 1997, Physics of Atomic Nuclei, 60, 1859

Kozlov, Y. V., Martem'yanov, V. P., & Mukhin, K. N. 1997, Physics-Uspekhi, 40, 807

Kraus, C., et al. 2005, Eur. Phys. J., C40, 447

Krauss, L. M. 1991, Phys. Lett., B269, 407

Kuznetsov, A., & Mikheev, N. 1997, Physics Letters B, 394, 123

Latimer, D. C., Escamilla, J., & Ernst, D. J. 2007, Phys. Rev. C, 75, 042501

Lewin, J. D., & Smith, P. F. 1996, Astropart. Phys., 6, 87

Li, H. B. et al. 2003, Phys. Rev. Lett., 90, 131802

Lindhard, J., & Scharff, M. 1961, Physical Review, 124, 128

Luke, P. N. 1988, j. Appl. Phys., 64, 6858

Luke, P. N., Goulding, F. S., Madden, N. W., & Pehl, R. H. 1989, IEEE Trans. Nucl. Sci., 36, 926

Majorana. 2003, arXiv:nucl-ex/0311013v1

Majorovits, B., & Klapdor-Kleingrothaus, H. V. 1999, Eur. Phys. J. A, 6, 463

Mei, D. M., Yin, Z. B., & Elliott, S. R. 2009, arXiv:0903.2273 [nucl-ex]

Messous, Y. 1995, Astropart. Phys., 3, 361

Mohapatra, R. N., Ng, S.-P., & Yu, H. 2004, Phys. Rev. D, 70, 057301

Monroe, J., & Fisher, P. 2007, Phys. Rev. D, 76, 033007

Morales, A., et al. 2000, Phys. Lett., B489, 268

Morales, J., et al. 1992, Nucl. Instrum. Meth., A321, 410

Morita, M. 1973, Beta decay and muon capture (W. A. Benjamin, Reading MA)

Narayan, R., & Bartelmann, M. 1996, arXiv:9606001 [astro-ph]

Neganov, B., & Trofimov, V. 1985, USSR Patent No 1037771, Otkrytia i Izobreteniya 146, 215

Nieves, J. F. 1982, Phys. Rev. D, 26, 3152

Nilsson, L. 1983, Nucl. Instrum. Meth., 216, 306

Okun, L. B., Voloshin, M. B., & Vysotsky, M. I. 1986, Sov. Phys. JETP, 64, 446

Olive, K. A., Steigman, G., & Walker, T. P. 2000, Phys. Rep., 333, 389

Pakvasa, S., & Valle, J. W. F. 2004, Proc. Indian Natl. Sci. Acad., 70A, 189

Petriello, F. J., & Zurek, K. M. 2008, Journal of High Energy Physics, 2008, 047

Petry, F. 1994, Prog. Part. Nuc. Phys., 32, 281

Petry, F., et al. 1993, Nucl. Instrum. Meth., A332, 107

Pospelov, M., Ritz, A., & Voloshin, M. 2008, Phys. Rev. D, 78, 115012

Pozzi, S. A., Padovani, E., & Marseguerra, M. 2003, Nuclear Instruments and Methods in Physics Research Section A: Accelerators, Spectrometers, Detectors and Associated Equipment, 513, 550

Primakoff, H., & Rosen, S. P. 1981, Annu. Rev. Nucl. Part. Sci., 31, 145

Radeka, V. 1988, Ann. Rev. Nucl. Part. Sci., 38, 217

Raffelt, G. G. 1989, Phys. Rev. D, 39, 2066

Roberts, M. S., & Rots, A. H. 1973, A&A, 26, 483

RSICC. SPEC-4, Calculated Recoil Proton Energy Distributions from Monoenergyetic and Continuous Spectrum Neutrons., RSICC peripheral shielding routine collection

Rubin, V. C., & Ford, W. K. J. 1970, ApJ, 159, 379

Savage, C., Freese, K., Gondolo, P., & Spolyar, D. 2009, arXiv:0901.2713

Savage, C., Gondolo, P., & Freese, K. 2004, Phys. Rev., D70, 123513

Schneider, P., Ehlers, J., & Falco, E. E. 1992, Gravitational Lenses (Springer-Verlag)

Scholberg, K. 2006, Phys. Rev. D, 73, 033005

—. 2007, arXiv:astro-ph/0701081v1

Shizuma. 1989, Radioisotopes, 38, 516

Shutt, T. et al. 1992, Phys. Rev. Lett., 69, 3425

Siegbahn, K. 1966, American Journal of Physics, 34, 275

Smith, D. M., Shapshak, M., Campbell, R., Primbsch, J. H., Lin, R. P., Luke, P. N., Madden, N. W., & Pehl, R. H. 1988, in American Institute of Physics Conference Series, Vol. 170, Nuclear Spectroscopy of Astrophysical Sources, ed. N. Gehrels & G. H. Share, 484–489

SNO+. 2007, AIP Conference Proceedings, 942, 101

Spooner, N. J. C., et al. 1994, Phys. Lett., B321, 156

Statham, P. J. 1977, X-ray Spectroscopy, 6, 94

Stodolsky, L. 1991, Physics Today, 44, 24

Sudarshan, M., & Singh, R. 1991, Meas. Sci. Tech., 2, 1192

Tisserand, P., et al. 2007, Astron. Astrophys., 469, 387

Vannucci, F. 1999, Nucl. Phys. B Proc. Suppl., 70, 199 , proceedings of the Fifth International Workshop on topics in Astroparticle and Underground Physics

Verkerke, W., & Kirkby, D. 2003, The RooFit toolkit for data modeling

Vogel, P., & Engel, J. 1989, Phys. Rev. D, 39, 3378

Vojtyla, P. 1996, Nucl. Instrum. Meth. B, 117, 189

Weinberg, S. 1964, Phys. Rev., 135, B1049

Weinheimer, C., et al. 1999, Phys. Lett., B460, 219

Wong, H. T. 2005, Nucl. Phys. Proc. Suppl., 138, 333

Wong, H. T. 2007, in The Standard Model and Beyond, ed. T. Aliev, N. K. Pak, & M. Serin

Wong, H. T. Rome 2009, in Topics in Astroparticle and Underground Physics (TAUP)

Wong, H. T., Li, H.-B., Li, J., Yue, Q., & Zhou, Z.-Y. 2006, J. Phys. Conf. Ser., 39, 266

Wong, H. T. et al. 2007, Phys. Rev. D, 75, 012001

Ziegler, J. F. 1998, IBM J. Res. Dev., 42, 117

Zioutas, K., et al. 2005, Phys. Rev. Lett., 94, 121301

Zwicky, F. 1933, Helvetica Physica Acta, 6, 110